

NTA-400

IN-05
259100

FEASIBILITY STUDY FOR A MICROWAVE-POWERED OZONE SNIFFER AIRCRAFT

VOLUME I

(NACA-CP-108660) FEASIBILITY STUDY FOR A
MICROWAVE-POWERED OZONE SNIFFER AIRCRAFT
U.S. Thesis (Worcester Polytechnic Inst.)
540 p

CSCL 91C

N90-27307

Uncl:is

93/05 0249107

**FEASIBILITY STUDY FOR A
MICROWAVE-POWERED
OZONE SNIFFER AIRCRAFT**

Project #: MSG-89A1

Major Qualifying Project Report
Submitted to the Faculty
of the

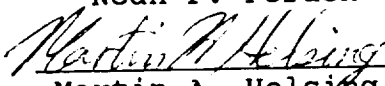
Worcester Polytechnic Institute

in partial fulfillment of the requirements
for the
Degree of Bachelor of Science

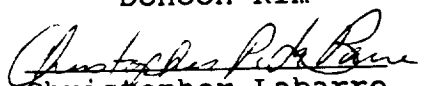
by



David F. Botros

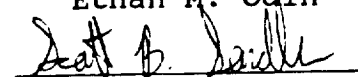

Charlotte K. Cody

Noah P. Forden

Martin A. Helsing

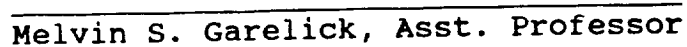

Thomas H. Jutras

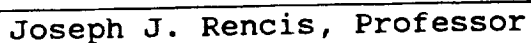
DoHoon Kim

Christopher Labarre


Ethan M. Odin


Scott B. Sandler

Approved By:


Melvin S. Garelick, Asst. Professor


Joseph J. Rencis, Professor

Abstract

The preliminary design of a high-altitude, remotely-piloted, atmospheric-sampling aircraft powered by microwave energy beamed from ground-based antenna has been completed. The vehicle has a gross weight of 6720 pounds and is sized to carry a 1000 pound payload at an altitude of 100,000 feet. The underside of the wing serves as the surface of a rectenna designed to receive microwave energy at a power density of 700 watts per square meter and the wing has a planform area of 3634 square feet to absorb the required power at an optimum Mach number $M = 0.44$. The aircraft utilizes a horizontal tail and a canard for longitudinal control and to enhance the structural rigidity of the twin fuselage configuration. The wing structure is designed to withstand a gust-induced load factor $n = 3$ at cruise altitude but the low-wing loading of the aircraft makes it very sensitive to gusts at low altitudes, which may induce load factors in excess of 20. A structural load alleviation system is therefore proposed to limit actual loads to the designed structural limit. Losses will require transmitted power on the order of megawatts to be radiated to the aircraft from the ground station, presenting environmental problems. Since the transmitting antenna would have a diameter of several hundred feet, it would not be readily transportable, so we propose that a single antenna be constructed at a site from which the aircraft is flown. The aircraft would be towed aloft to an initial altitude at which the microwave power would be utilized. The aircraft would climb to cruise altitude in a spiral flight path and orbit the transmitter in a gentle turn.

Acknowledgements

The members of the project group would like to thank the following people for their support during this project:

Professor M. S. Garelick

Professor J. J. Rencis

Richard L. Kashian

Mr. Roger Luidens

Mr. William Brown

NASA/USRA

Specical thanks to Christopher Gillis and Mark Tobin for providing the Beam Tracking System Analysis.

Table of Contents

Volume I	Page
Abstract	
Acknowledgements	
List of Figures	
1.0 Introduction	1
2.0 Mission Profile	3
3.0 Propulsion	6
3.1 Power Systems	
3.2 Microwave Propulsion	
3.3 Summary of the Propulsion System	
4.0 Aircraft Sizing	12
4.1 Component Weight Estimation	
4.2 Discussion of Parametric Study	
4.3 Selection of Design	
4.4 Comparison with Conventional Aircraft	
4.5 Configuration	
4.5.1 General	
4.5.2 Effects of Planform	
4.5.3 Selection of Planform	
4.6 Summary of Aircraft Sizing	
5.0 Aerodynamics	26
5.1 Airfoil Design	
5.1.1 Elliptical Wing Loading	
5.1.2 Airfoil Design Overview	
5.1.3 Design Procedure	
5.1.4 Airfoil Analysis	
5.1.4 Summary of Airfoil Design and Analysis	
5.2 Wing-Body Analysis	
5.2.1 Twist Distribution	
5.2.2 Compressible Wing-Body Analysis	
5.2.3 Theoretical Drag Calculations	
5.2.4 Summary of Wing-Body Analysis	
6.0 Structural Design and Analysis	42
6.1 Static Analysis	
6.1.1 Summary of Static Structural Analysis	
6.2 Vibration Analysis	
6.2.1 Clamped Free-Beam Analysis	
6.2.2 Preliminary Wing Structural Design	
6.2.3 Revised Wing Structural Design	
6.2.4 Revised Wing With External Brace	
6.2.5 Summary of Vibration Analysis	
7.0 Stability and Control	53
7.1 Static Stability Analysis	
7.1.1 Summary of Static Stability	
7.2 Dynamic Stability	
7.2.1 Summary of Dynamic Stability	
8.0 Weight and Balance	64
8.1 Component Sizes and Locations	
8.2 Mass Properties	
8.3 Summary	
9.0 Performance	67
9.1 Objective	
9.1.1 Power	

9.1.2	Flight Path	
9.1.3	Climb	
9.1.4	Effect of Wind Gust	
9.2	Power Analysis	
9.2.1	Level Flight	
9.2.2	Turning Flight	
9.2.3	Total Transmitted Power	
9.3	Climb Performance	
9.3.1	Climb Rate	
9.3.2	Time to Climb	
9.4	Flight Path	
9.5	V-n Diagram	
9.6	Results	
9.7	Summary of Performance	
10.0	Beam Tracking System	82
10.1	Overview	
10.2	Background	
10.3	Microwave Powered High-Altitude Aircraft	
10.4	Microwave Transmission System	
10.5	Tracking System Model	
10.6	Summary of Tracking System Model	
11.0	Environmental Impact	95
12.0	Cost Analysis	98
13.0	Conclusions	100
14.0	Bibliography	104
15.0	Figures	107

Volume II

Appendices

A.1.	CAD Drawings	A.1.1
A.2.	Wing Generator 1.0	A.2.1
A.3.	Weight Estimation Computer Code	A.3.1
A.4.	Drag Calculations	A.4.1
A.5.	Static Structural Analysis Data	A.5.1
A.6.	Drive Train Sizing Calculations	A.6.1
A.7.	Static Stability Derivation & Analysis Code	A.7.1
A.8.	Dynamic Stability	A.8.1
A.9.	Performance	A.9.1
A.10.	Cost Analysis	A.10.1

List of Figures

- 2.1 Mission Profile Diagram
- 3.1 Rectenna Location
- 3.2 Microwave Transmission Efficiency
- 3.3 Airborne Transmitter Configuration
- 3.4 Multi-Station Ground Transmitter Configuration
- 3.5 Single-Station Ground Transmitter Configuration
- 4.1 Wing Loading vs. Mach Number
- 4.2 Gross Weight vs. Mach Number
- 4.3 Wing Area vs. Mach Number
- 4.4 External Rectenna Area vs. Mach Number
- 4.5 Power Available vs. Mach Number
- 4.6 Wing Span vs. Mach Number
- 4.7 L/D Ratio vs. Mach Number
- 4.8 First Iteration Component Weights
- 4.9 Aircraft Design Concept #1
- 4.10 Aircraft Design Concept #2
- 4.11 Aircraft Design Concept #3
- 4.12 Landing Gear Configuration
- 4.13 Final Design Configuration
- 4.14 Planform Parameters
- 4.15 Planform Geometry
- 4.16 Second Iteration Aspect Ratios and Thicknesses
- 4.17 Second Iteration Component Weights
- 5.1.1 Transition Bubble
- 5.1.2 Sample Pressure Distribution
- 5.1.3 Span Loading
- 5.1.4 L, P & Q Target Pressure Distributions
- 5.1.5 P-Series Pressure Distribution (Designed Airfoil)
- 5.1.6 L-Series Pressure Distribution (Designed Airfoil)
- 5.1.7 Q-Series Pressure Distribution (Designed Airfoil)
- 5.1.8 L1, L2 & L3 Targets
- 5.1.9 L1 Inviscid Pressure Distribution & Geometry
- 5.1.10 L2 Inviscid Pressure Distribution & Geometry
- 5.1.11 L3 Inviscid Pressure Distribution & Geometry
- 5.1.12 L-Series c_l & c_m vs. α (Inviscid Analysis)
- 5.1.13 L-series c_l vs. α (Viscid & Compressible Analysis)
- 5.1.14 Trailing Closure
- 5.1.15 L1 Compressible & Target Pressure Distribution
- 5.1.16 L2 Compressible & Target Pressure Distribution
- 5.1.17 L3 Compressible & Target Pressure Distribution
- 5.1.18 L-Series Drag Polar
- 5.1.19 L1 vs. NACA 4415 Drag Comparison
- 5.1.20 L2 vs. NACA 4412 Drag Comparison
- 5.1.21 L3 vs. NACA 4409 Drag Comparison
- 5.1.22 L1 vs. NACA 4415 Lift Comparison
- 5.1.23 L2 vs. NACA 4412 Lift Comparison
- 5.1.24 L3 vs. NACA 4409 Lift Comparison
- 5.2.1 c_l vs. % Span
- 5.2.2 Airfoil Lift Curve Equations
- 5.2.3 Variation of Lift Curve Slope
- 5.2.4 Variation of Zero Lift Angle of Attack
- 5.2.5 Twist Distribution

- 5.2.6 First Twist Approximation
- 5.2.7 Final Twist Approximation
- 5.2.8 Main Wing Twist and Location
- 5.2.9 Main Wing Side View
- 5.2.10 C_L vs. α
- 5.2.11 Comparison of c_l vs. Span
- 5.2.12 Wing Loading vs. % Span Comparison
- 5.2.13 Untwisted Wing Pressure Distribution $\alpha = -1.0^\circ$
- 5.2.14 Untwisted Wing Pressure Distribution $\alpha = 0.375^\circ$
- 5.2.15 Untwisted Wing Pressure Distribution $\alpha = 2.0^\circ$
- 5.2.16 Untwisted Wing Pressure Distribution $\alpha = 5.0^\circ$
- 5.2.17 Twisted Wing Pressure Distribution $\alpha = -1.0^\circ$
- 5.2.18 Twisted Wing Pressure Distribution $\alpha = 0.2^\circ$
- 5.2.19 Twisted Wing Pressure Distribution $\alpha = 2.0^\circ$
- 5.2.20 Twisted Wing Pressure Distribution $\alpha = 5.0^\circ$
- 5.2.21 C_L vs. C_D
- 5.2.22 C_L vs. Lift-to-Drag Ratio
- 6.1.1 Spanwise & Chordwise Pressure Distribution
- 6.1.2 Average Chordwise Pressure Distribution
- 6.1.3 Model #1 Deflection (isometric view)
- 6.1.4 Model #1 Deflection (side view)
- 6.1.5 Model #1 Shear Stress Plot (bottom view)
- 6.1.6 Model #1 Shear Stress Plot (right I beam)
- 6.1.7 Model #1 Shear Stress Plot (left I beam)
- 6.1.8 Model #1 Shear Stress Plot (top view)
- 6.1.9 Model #1 Principle Stress (bottom view)
- 6.1.10 Model #1 Principle Stress (left I beam)
- 6.1.11 Model #1 Principle Stress (right I beam)
- 6.1.12 Model #1 Principle Stress (top view)
- 6.1.13 I-Beam Properties
- 6.1.14 Front I Beam Properties
- 6.1.15 Middle I Beam Properties
- 6.1.16 Rear I Beam Properties
- 6.1.17 Model #2 Deflection Plot Pressure & Gravity (side view)
- 6.1.18 Model #2 Shear Stress Plot Pressure & Gravity (top view)
- 6.1.19 Model #2 Shear Stress Plot II Pressure & Gravity (top view)
- 6.1.20 Model #2 Shear Stress Plot Pressure & Gravity (bottom view)
- 6.1.21 Model #2 Prin. Stress with Press. & Gravity (top view)
- 6.1.22 Model #2 Prin. Stress with Press. & Gravity (bot. view)
- 6.1.23 Model #2 Prin. Stress with Press. & Gravity (left I beam)
- 6.1.24 Model #2 Prin. Stress with Press. & Gravity (middle I beam)
- 6.1.25 Model #2 Prin. Stress with Press. & Gravity (right I beam)
- 6.1.26 Model #2 Deflection Plot with Brace (side view)
- 6.1.27 Model #2 Shear Stress Plot with Brace (top view)
- 6.1.28 Model #2 Shear Stress Plot with Brace (bottom view)
- 6.1.29 Model #2 Prin. Stress with Brace (top view)
- 6.1.30 Model #2 Prin. Stress with Brace (left I beam)
- 6.1.31 Model #2 Prin. Stress with Brace (middle I beam)
- 6.1.32 Model #2 Prin. Stress with Brace (right I beam)
- 6.1.33 Model #2 Prin. Stress with Brace (bottom view)
- 6.1.34 Pressure & Force Calculations
- 6.1.35 Model #3 Deflection Plot of Half Model (isometric view)
- 6.1.36 Model #3 Deflection Plot of Half Model (side view)
- 6.1.37 Model #3 Shear Stress Plot of Half Model (top view)
- 6.1.38 Model #3 Shear Stress Plot of Half Model (bottom view)

- 6.1.39 Model #3 Prin. Stress of Half Model (top of tail & canard)
- 6.1.40 Model #3 Prin. Stress of Half Model (top view of wing)
- 6.1.41 Model #3 Prin. Stress of Half Model (right I beams)
- 6.1.42 Model #3 Prin. Stress of Half Model (left I beams)
- 6.2.1 Eigenvalue table for preliminary design.
- 6.2.2 1st Mode for Preliminary Design (isometric view)
- 6.2.3 1st Mode for Preliminary Design (front view)
- 6.2.4 1st Mode for Preliminary Design (top view)
- 6.2.5 2nd Mode for Preliminary Design (isometric view)
- 6.2.6 2nd Mode for Preliminary Design (front view)
- 6.2.7 2nd Mode for Preliminary Design (top view)
- 6.2.8 3rd Mode for Preliminary Design (isometric view)
- 6.2.9 3rd Mode for Preliminary Design (front view)
- 6.2.10 3rd Mode for Preliminary Design (top view)
- 6.2.11 4th Mode for Preliminary Design (isometric view)
- 6.2.12 4th Mode for Preliminary Design (front view)
- 6.2.13 4th Mode for Preliminary Design (top view)
- 6.2.14 5th Mode for Preliminary Design (isometric view)
- 6.2.15 5th Mode for Preliminary Design (front view)
- 6.2.16 5th Mode for Preliminary Design (top view)
- 6.2.17 Eigenvalue table for revised design.
- 6.2.18 1st Mode for Revised Design (isometric view)
- 6.2.19 1st Mode for Revised Design (front view)
- 6.2.20 1st Mode for Revised Design (top view)
- 6.2.21 2nd Mode for Revised Design (isometric view)
- 6.2.22 2nd Mode for Revised Design (front view)
- 6.2.23 2nd Mode for Revised Design (top view)
- 6.2.24 3rd Mode for Revised Design (isometric view)
- 6.2.25 3rd Mode for Revised Design (front view)
- 6.2.26 3rd Mode for Revised Design (top view)
- 6.2.27 4th Mode for Revised Design (isometric view)
- 6.2.28 4th Mode for Revised Design (front view)
- 6.2.29 4th Mode for Revised Design (top view)
- 6.2.30 5th Mode for Revised Design (isometric view)
- 6.2.31 5th Mode for Revised Design (front view)
- 6.2.32 5th Mode for Revised Design (top view)
- 6.2.33 Eigenvalue table for revised design w/brace.
- 6.2.34 1st Mode for Design w/Brace (isometric view)
- 6.2.35 1st Mode for Design w/Brace (front view)
- 6.2.36 1st Mode for Design w/Brace (top view)
- 6.2.37 2nd Mode for Design w/Brace (isometric view)
- 6.2.38 2nd Mode for Design w/Brace (front view)
- 6.2.39 2nd Mode for Design w/Brace (top view)
- 6.2.40 3rd Mode for Design w/Brace (isometric view)
- 6.2.41 3rd Mode for Design w/Brace (front view)
- 6.2.42 3rd Mode for Design w/Brace (top view)
- 6.2.43 4th Mode for Design w/Brace (isometric view)
- 6.2.44 4th Mode for Design w/Brace (front view)
- 6.2.45 4th Mode for Design w/Brace (top view)
- 6.2.46 5th Mode for Design w/Brace (isometric view)
- 6.2.47 5th Mode for Design w/Brace (front view)
- 6.2.48 5th Mode for Design w/Brace (top view)
- 7.1.1 C_m vs. α for three arbitrary aircraft
- 7.1.2 Component Contributions to Static Stability
- 7.1.3 Static Stability Analysis Data

- 7.1.4 C_m vs. α ($\delta_c = 0$)
- 7.1.5 C_m vs. α ($\delta_t = 0$)
- 7.1.6 C_m vs. α ($\delta_c = \delta_t$)
- 7.1.7 C_m vs. C_L ($\delta_c = 0$)
- 7.1.8 C_m vs. C_L ($\delta_t = 0$)
- 7.1.9 C_m vs. C_L ($\delta_c = \delta_t$)
- 7.2.1 Response Derivatives
- 7.2.2 Combined Mode Block Diagram
- 7.2.3 Short Period Response at 100,000 feet
- 7.2.4 Long Period Response at 100,000 feet
- 7.2.5 Combined Period Response at 100,000 feet
- 7.2.6 Short Period Response at 25,000 feet
- 7.2.7 Long Period Response at 25,000 feet
- 7.2.8 Combined Period Response at 25,000 feet
- 8.1 Mass Location Diagram
- 8.2 Mass Properties Spreadsheet
- 9.2.1 Net Power Available
- 9.2.2 Power Required
- 9.2.3 Power Available and Required - sea level
- 9.2.4 Power Available and Required - 25,000 feet
- 9.2.5 Power Available and Required - 50,000 feet
- 9.2.6 Power Available and Required - 75,000 feet
- 9.2.7 Power Available and Required - 100,000 feet
- 9.2.8 Angle of Incidence
- 9.2.9 Angle of Incidence - As Flight Radius Increases
- 9.2.10 Angle of Incidence - As Flight Radius Decreases
- 9.2.11 Net Power Available - 25,000 feet
- 9.2.12 Power Required - 25,000 feet
- 9.2.13 Net Power Available - 50,000 feet
- 9.2.14 Power Required - 50,000 feet
- 9.2.15 Net Power Available - 75,000 feet
- 9.2.16 Power Required - 75,000 feet
- 9.2.17 Net Power Available - 100,000 feet
- 9.2.18 Power Required - 100,000 feet
- 9.2.19 Transmitted Power Distribution
- 9.2.20 Parabolic Power Density Distribution
- 9.2.21 Total Transmitted Power Calculation
- 9.3.1 Rate of Climb vs Altitude - wings level flight
- 9.3.2 Rate of Climb vs Mach Number - sea level (level flight)
- 9.3.3 Rate of Climb vs Mach Number - 25,000 feet
- 9.3.4 Rate of Climb vs Mach Number - 50,000 feet
- 9.3.5 Rate of Climb vs Mach Number - 75,000 feet
- 9.3.6 Rate of Climb vs Mach Number - 100,000 feet
- 9.3.7 Time to Climb - wings level flight
- 9.3.8 Time to Climb - turning flight
- 9.4.1 Altitude vs Flight Radius
- 9.4.2 Mach Number vs Altitude
- 9.4.3 Velocity vs Altitude
- 9.4.4 Coefficient of Lift vs Altitude
- 9.4.5 Bank Angle vs Altitude
- 9.4.6 Flight Radius vs Altitude
- 9.4.7 Climb Rate vs Altitude
- 9.4.8 Altitude vs Flight Radius - number of turns
- 9.5.1 Effect of Wind Gust - sea level
- 9.5.2 Effect of Wind Gust - 25,000 feet

- 9.5.3 Effect of Wind Gust - 50,000 feet
- 9.5.4 Effect of Wind Gust - 75,000 feet
- 9.5.5 Effect of Wind Gust - 100,000 feet
- 9.5.6 Load Factor at Maximum and Minimum CL - sea level
- 9.5.7 Load Factor at Maximum and Minimum CL - 25,000 feet
- 9.5.8 Load Factor at Maximum and Minimum CL - 50,000 feet
- 9.5.9 Load Factor at Maximum and Minimum CL - 75,000 feet
- 9.5.10 Load Factor at Maximum and Minimum CL - 100,000 feet
- 9.5.11 Wind Gust Effect (increased load factor range at sea level)
- 9.5.12 Wind Gust Effect (increased load factor range at 25,000 ft)
- 9.5.13 Wind Gust Effect (increased load factor range at 50,000 ft)
- 10.1 Beacon Based Tracking System
- 10.2 Sensor Based Tracking System
- 10.3 Model Block Diagram

Appendix Figures

A.1.1	Canard and Tail
A.1.2	Vertical Tail
A.1.3	Main Wing
A.1.4	Isometric View
A.2.1	Elliptic Load Distribution
A.2.2	Lift Coefficient vs. Span
A.2.3	Forward Swept Wing
A.2.4	Airfoils Side View
A.3.1	Weight Code Constants
A.3.2	Convergence Method Flow Chart
A.3.3	Graphical Convergence Example
A.5.1	Deflection Plot
A.5.2	Shear Stress Plot
A.5.3	Shear Stress Plot (blow up)
A.5.4	Equivalent Principle Stress Plot
A.5.5	Equivalent Principle Stress Plot (blow up)
A.5.6	Load vs Length (uniform load)
A.5.7	Shear vs Length (uniform load)
A.5.8	Moment vs Length (uniform load)
A.5.9	Load vs Length (concentrated load)
A.5.10	Shear vs Length (concentrated load)
A.5.11	Moment vs Length (concentrated load)
A.5.12	Load vs Semi-Span (all load on front I beam)
A.5.13	Shear vs Semi-Span (all load on front I beam)
A.5.14	Moment vs Semi-Span (all load on front I beam)
A.5.15	Load vs Semi-Span (33% on rear I beam)
A.5.16	Shear vs Semi-Span (33% on rear I beam)
A.5.17	Moment vs Semi-Span (33% on rear I beam)
A.5.18	Load vs Semi-Span (66% on front I beam)
A.5.19	Shear vs Semi-Span (66% on front I beam)
A.5.20	Moment vs Semi-Span (66% on front I beam)
A.5.21	Front Spar Properties
A.5.22	Rear Spar Properties
A.5.23	Pressure Distribution over Wing
A.5.24	Pressure Calculations for Wing
A.5.25	Twist Angle vs Semi-Span (beam elements)
A.5.26	Twist Angle vs Semi-Span (bar elements)
A.5.27	Structural Cross-Section
A.5.28	Force Calculations for Wing
A.5.29	Model #2 Deflection Plot with gravity load (side view)
A.5.30	Model #2 Prin. Stress with gravity load (top view)
A.5.31	Model #2 Prin. Stress with gravity load (right I beam)
A.5.32	Model #2 Prin. Stress with gravity load (middle I beam)
A.5.33	Model #2 Prin. Stress with gravity load (left I beam)
A.5.34	Model #2 Prin. Stress with gravity load (bottom view)
A.5.35	Model #2 Deflection Plot with Press. (iso. view)
A.5.36	Model #2 Deflection Plot with Press. (side view)
A.5.37	Model #2 Shear Stress with Press. (bottom view)
A.5.38	Model #2 Shear Stress with Press. (top view)
A.5.39	Model #2 Shear Stress with Press. (top view II)
A.5.40	Model #2 Princ. Stress with Press. (top view)
A.5.41	Model #2 Princ. Stress with Press. (right I beam)
A.5.42	Model #2 Princ. Stress with Press. (middle I beam)

A.5.43 Model #2 Princ. Stress with Press. (left I beam)
A.5.44 Model #2 Princ. Stress with Press. (bottom view)
A.6.1 K-Factor Table
A.6.2 Q-Factor vs. Gearbox Weight
A.7.1 Wing Contribution to Pitching Moment
A.7.2 Horizontal Tail Contribution to Pitching Moment
A.7.3 Control Surfaces
A.8.1 Short Period Mode
A.8.2 Long Period Mode
A.8.3 Combined Mode Data
A.8.4 Combined Mode vs. dw/dt
A.8.5 Combined Mode vs. du/dt

1.0 Introduction

NASA requires an unmanned flight vehicle which can obtain atmospheric samples at an altitude of 100,000 feet to determine the level of constituents such as ozone.

Recent reports about the rapid depletion of the ozone layer have caused much concern among environmentalists worldwide. The ozone layer protects the earth from the harmful radiation of the sun. Preliminary information indicates that fluorocarbons emitted by aerosol products and refrigeration equipment have caused a hole in the ozone layer over the south pole. More recent studies also show signs of ozone depletion around the equator.

Currently there is no method of obtaining accurate atmospheric samples of ozone. Conventional aircraft are unable to operate at the extreme altitudes required for ozone sampling, due the lack of air required for fuel oxidation in an air-breathing engine. Also, the low air - density at altitude causes difficulty in providing sufficient lift. Rockets are able to reach these altitudes, but only for a short duration and at high velocities. In order to make accurate measurements of ozone concentrations the atmosphere must be undisturbed by the aircraft.

The unique requirements of this mission necessitate the design of a long-endurance, high-altitude aircraft.

2.0 Mission Profile

An aircraft is required to fly an atmospheric sampling payload weighing 1,000 lbs. to an altitude of 100,000 feet and loiter for extended periods, possibly on the order of weeks. The high altitude and extended duration of this mission makes a manned vehicle impractical, as life support systems would add a great deal of weight and complexity. Therefore, a remotely piloted design is necessary for the completion of the mission.

The aircraft is equipped with a microwave power system, which receives energy beamed to the aircraft from a single transmitting station on the ground. This power can be transmitted for indefinite periods of time, and allows the vehicle to remain airborne for as long as the mission requires. The microwave power is transmitted in a conical pattern, so the flight path is constrained to a spiralling climb to altitude. A diagram of the flight pattern is shown in Figure 2.1.

The aircraft is designed to be towed to an altitude of 20,000 feet, at which point the entire flight path is contained within the conical microwave beam. With a maximum climb rate of 11.88 ft/sec, it attains cruise altitude within four hours of takeoff. Once at the design altitude of 100,000 feet, the flight path radius is approximately 28,500 feet. The aircraft has the capability to loiter in this condition almost

indefinitely. The cruise speed is at a Mach number of 0.44, which allows operation well below velocities which would induce areas of transonic flow over the aircraft. Atmospheric sampling may then be accomplished before descent.

3.0 Propulsion

3.1 Power Systems

Various types of propulsion system that could be used to power the aircraft were considered. The design requirement for a vehicle capable of flight at 100,000 feet for an extended period of time limited the choice of propulsion systems to solar, hydrazine, diesel, propane, regenerative fuel cells and microwave. A weight estimation program was used to determine the range of power required (see chapter 4).

Light weight diesels will produce peak power at a maximum altitude of only 70,000 feet, which does not meet mission requirements.

Another possible power source was hydrazine. One aircraft design used hydrazine to reach a projected altitude of 100,000 feet (see Ref. 7) but the endurance is limited. The same result was observed with propane powered flight.

One attractive aspect of solar power is the large planform of the wing that can be used for the location of the photo-voltaic cells. Using thin film technology, the vehicle would not have the same altitude limitations as air breathing engines and would also benefit from a low power to weight ratio. Solar power has a projected conversion efficiency of approximately 15%. which results in an expected power density of about 195 watts

per square meter. When the weight estimation program was run using a wing area proportional to this power density, the program would not converge on a solution. It was concluded that solar energy would not meet the initial requirements. Solar power would only provide about 15% of the total power requirement of the vehicle during peak hours of sunlight.

The concept of using microwave energy to power an aircraft involves producing the power at a distance away from the aircraft and then beaming the energy in the form of microwave radiation to the aircraft. The vehicle has a receiving antenna which has rectifying circuitry that converts microwave power into DC power. The current produced is used in an electric motor that drives the propellers. The nature of the system is such that the power obtained is directly proportional to the size of the rectenna. A power density of 700 watts per square meter is presently considered attainable. The microwave energy system weighs approximately 0.79 kilograms per kilowatt of power needed. To maximize received power and minimize aerodynamic drag due to the rectenna, it was decided to place the rectenna on the underside of the wing (see Figure 3.1). This produced a direct relationship between the power density and wing area similar to the solar powered configuration. When the weight estimation program was run using the revised power density, the solution converged.

Another option was solar energy as an addition to the microwave power with both routed into a regenerative fuel cell. This would give additional power from the sun while it was available and the fuel cell would ensure continuous power supply, but this advantage did not compensate for the additional weight of the fuel cell. The most efficient cells available were hydrogen-oxygen regenerative fuel cells, however, the system is only capable of $7\frac{1}{2}$ horsepower, while weighing 500 pounds. Since this power represents only 2 to 5% of the required power for the plane, it became clear that this approach was not feasible.

3.2 Microwave Propulsion

With the elimination of all other alternatives, microwave energy was preferred. With the power source decided, the drive train could be designed.

Energy will be routed directly from the rectenna to the electric motor. The brushless, rare earth magnet electric motors used have a power density of 2 to 4 horsepower per pound and an efficiency of approximately 97%. A frequency of 2.45 gigahertz was selected using data on general power efficiency and degradation as a factor of climate and frequency (see Figure 3.2).

There were four possible methods of implementing the microwave propulsion system. First, it would be

possible to place a satellite or series of satellites in orbit and use massive solar panels to collect energy from the sun and beam it down onto the plane in flight. This idea was not pursued because satellite usage was deemed uneconomical. Another choice involved a second aircraft orbiting at a lower altitude with a large generator and transmitter onboard (see Figure 3.3). This plane would be kept on station using air-to-air refueling and rotate its schedule with other aircraft to provide an around the clock power source to the ozone-sniffer. This system of support aircraft would allow for redeployment of the research aircraft to any point in the world. This alternative was not selected since the size of the transmitting antenna (30 to 50 meters in diameter) would be difficult to accomodate. The third and fourth systems made use of semi-permanent ground stations. One consists of a chain of ground stations linked to provide a corridor in which the plane would fly (see Figure 3.4). The other used only a single source, forcing the vehicle to fly in a circular path to stay within the beam (see Figure 3.5).

The last alternative of providing the microwave energy to the aircraft was selected because the ground stations will be large (approximately 100 meters in diameter) and expensive to build. When the aircraft is in use, it may not be possible to locate the ground stations at every location desired. With only one

station in use, the problem is not as severe. The steady turning flight, however, requires more power than level flight and also reduces the angle of incidence of the microwave beam on the rectenna, thereby reducing available power. This effect is examined in chapter 9 and will not prevent the aircraft from flying.

3.3 Summary of the Propulsion System

The high altitude research aircraft will use microwave energy beamed up from a single ground station that it will circle above. The vehicle will convert the energy into DC power and use that to run an electric motor that will drive a propeller. Other types of propulsion system could be used, but the system chosen was selected as the best possible.

4.0 Aircraft Sizing

In order to provide an initial component weight estimate, a computer code, WEIGHT.BAS, was developed. This program, written in BASIC for IBM compatible PC's, is based on the weight equations given in Reference 24 for light utility aircraft. The sizing is done at the design altitude of 100,000 feet. The fact that the aircraft is microwave powered necessitated modification of the basic equations. The weight of the fuel, which is usually a significant portion of a conventional aircraft's gross takeoff weight, was omitted. In place of the fuel equation, an equation for the weight of the rectenna was derived from data in Reference 6. An additional modification in the form of a correction factor for composite materials has been applied to the final component weights of the wing, fuselage, horizontal and vertical tails. This correction factor is also based on data given in Reference 24. Once the component weights were calculated, an aircraft configuration was determined.

4.1 Component Weight Estimation

Several factors complicated the estimation process. First, there is little available data about sizing high altitude platforms on which to base an initial design. Most initial aircraft sizing is based on a comparison of mission requirements with the mission requirements of

existing aircraft. Without the advantage of hindsight, the initial sizing began by examining the variation of the wing loading (gross aircraft weight divided by the wing planform area) with the Mach number. This calculation is carried out over a range of lift coefficients from .1 to 1.2 as shown in Figure 4.1. At each Mach number the maximum subsonic lift coefficient was determined using the Kármán-Tsien relation given on p. 258 of Reference 1. This subsonic lift coefficient is the maximum value obtainable without local velocities reaching Mach 1.

Only flight velocities less than Mach 1 were considered for this mission, due to the increased power which would be required at transonic or supersonic speeds. Data from several studies of high altitude platform design (References 2,7,16,22) were plotted onto Figure 4.1. The design of Reference 7 was a high altitude, hydrazine powered aircraft while Reference 16 was a microwave powered configuration. Particular note should be made that most designs with liquid fuel were located on the graph in the region of the Reference 7 design. Most aircraft that did not have onboard fuel were in the range near the Reference 16 configuration.

Since all of the component estimation equations in Reference 24 are based on statistical data for conventional aircraft, these equations may not accurately represent the microwave-powered

configuration. At low wing loadings, the wing weight equation is very sensitive to small changes in wing area. The change in wing weight with wing area, dW/dS , varies as approximately $.61S^{-.39}$. However, for lack of a better methodology and statistical equations, the procedure of Reference 24 has been used.

For a microwave powered aircraft, the size of the wing limits the maximum power that the aircraft is capable of absorbing since the wing acts as the rectenna. However, a separate rectenna could be used to absorb any required power in excess of that which is received by the wing. The external rectenna would look similar to the radar dish on an AWACS aircraft except it would be mounted under the fuselage.

4.2 Discussion of Parametric Study

The series of graphs generated from the weight estimation program demonstrated many of the tradeoffs to be considered in the selection of the design parameters of the aircraft. These graphs are shown in Figures 4.2 - 4.7. The output consisted of six graphs. Within each series are graphs of gross weight, wing span, wing area, lift-to-drag ratio, and external rectenna area vs. Mach number for lift coefficients of .5, .6, .7, .8, and .9. Superimposed on these graphs are lines denoting constant external rectenna areas of 0, 500, and 1000 ft²

respectively. Since the design chosen has no external rectenna it must lie on the zero rectenna area line. Each series of graphs represents a different combination of an N_{ult} (Ultimate load factor, the point where failure occurs) of 2, 2.5, or 3 with an aspect ratio of 15 or 25.

The benefit of raising the N_{ult} is that the aircraft structure would be better able to withstand loads induced by gusts or maneuvering. At low altitudes, a small gust of wind can cause a significant increase in the wing loading resulting in deformation or failure of the wing. The tradeoff is that the wing structural weight and aircraft gross weight increase with the ultimate load factor. The effect of this increase is compounded by increased drag and rectenna area. An unexpected effect of reducing the aspect ratio is demonstrated by the graphs. The expected lessening of the lift-to-drag ratio and wing area did not materialize due to the unique relationship of the design parameters. Thus the reduction of the aspect ratio from 25 to 15 does not produce a significant drag increase but results in a reduction of wing weight.

4.3 Selection of Design

A parametric study was conducted using the weight estimation code. All data was generated at a constant

wing thickness-to-chord ratio of 12%. The aspect ratio of the wing was varied from 25 to 15 while the aspect ratio of the horizontal tail was fixed at 25 and the vertical tail was fixed at 5. The ultimate load factor was varied between 2 and 5. Data obtained at higher ultimate load factors (greater than 3) converged only at unrealistically high design lift coefficients ($C_L > 1.0$) which are not obtainable with a low Reynolds number airfoil. The optimum lift coefficient is .6 in level flight.

The maximum acceptable wingspan is limited by the need to keep the wing tip deflections low. Therefore, the wingspan was constrained to a value less than 250 feet. This limitation is based on the total wing weight allotment which is not enough for the heavy structural support needed to accomodate a larger wing span. It was also necessary to have the ultimate load factor as high as possible to maintain structural integrity and damage tolerance. Due to the increase of wingspan with aspect ratio, the final design reflects a compromise in design aspect ratio needed to accommodate the span limitations. The final configuration does not encompass any external rectenna because the parametric study failed to reveal any benefits for such a configuration. However, two drawbacks are evident. First, an external rectenna would produce a large drag penalty and secondly there are structural problems inherent in attaching it to the

aircraft. The wing area is all that is necessary to absorb the power required. The tail area can be used to absorb extra power that will be lost due to the angle of incidence between the beam and rectenna caused by the flight bank angle. The component weights for the first iteration are given in Figure 4.8. These values describe the configuration which has subsequently been analyzed in detail during this project.

4.4 Comparison with Conventional Aircraft

The major difference between this vehicle and a conventional aircraft is the direct relation between the wing area and available power. This connection results in parametric limits which are different than what had been anticipated. The most significant limiting factor on the design has turned out to be the wing span. Fuel constitutes a significant percentage of the weight of a conventional aircraft. There is a direct weight savings from eliminating liquid fuel which also results in a weight savings in the other aircraft components.

The unique relationship between wing area and power available produces another important variation from a conventional vehicle with an air-breathing engine. The optimal Mach number for this aircraft is much lower than what was initially expected. Whereas an air-breathing aircraft flying at 100,000 ft would be expected to

operate most efficiently around Mach .7, our optimum Mach number falls around Mach .45. This is due to the fact that the wing area increases with cruising speed in order to provide sufficient rectenna area to absorb the required power. The wing area is much larger than for an air-breathing aircraft design of comparable weight. At such high altitudes, a large wing area is need to produce enough lift in the low density air at low flight speeds.

4.5 Configuration

The aircraft configuration was chosen after the preliminary weight estimate was obtained. Data was then available on expected cruising speed, altitude and flight duration.

The cruising speed of the aircraft was determined as Mach .44 at an altitude of 100,000 feet. This allowed for a wing with no sweep which also produced a wing weight savings in comparison to the swept configuration required for operation at higher design Mach numbers. The low density of the air at design altitude leads to a large planform with low wing loading. In addition, typical gust velocities of up to 40 feet per second resulted in large normal accelerations (10 to 30 g) at low altitudes.

The mission will require a payload consisting of

sensors that will sample ambient air. It is important that the air not be disturbed by the approach of the aircraft.

4.5.1 General

First, the possibility of an all-wing configuration was considered. An all-wing configuration represents the maximum lifting area possible for an aircraft of a given size. This was important because the rarified air at cruise altitude will reduce lift potential. Since the aspect ratio of the wing is 15 external bracing might be necessary. This issue is discussed in section 6.0.

Figures 4.9 - 4.11 illustrate design concepts with a canard and aft wing. Because of possible directional instability, the wing was relocated further forward and a twin fuselage configuration was used because this arrangement provides greater structural rigidity and internal volume.

The tail configurations examined included butterfly and conventional horizontal-vertical tailplanes and canards. A canard was chosen because of its beneficial lift characteristics and an aft tail was included because of its effect on structural stiffness and pitch control at high altitude. The butterfly tail configuration was dropped when the use of a second

fuselage was made.

The microwave propulsion system does not require fuel on board. The controls will be fly-by-wire, so the control surfaces will use electrical actuators, which means no hydraulics will be needed. The electrical system is representative of the wiring needed to take power from the rectennas to the engine. With a ground control system in use, the avionics will be grouped with the remote control system. The list of components includes the wing, horizontal and vertical tails, the fuselages, electrical wiring, payload, engines, propellers, controls and landing gear.

The next components to be placed were the propellers. Three locations were considered. First, the placement of the propellers at the rear of the fuselages would be beneficial because the atmospheric sensors would be free of the turbulence created by the propellers. The drawback of this configuration is that propellers would be in the slipstream of the main wing and tail surfaces. This will result in propeller vibrations and a reduction in propeller efficiency. The second location would again be aft, but situated atop the vertical tail, free of the wing's wake. In this position the propellers are only affected by the airflow over the tail surfaces, providing a moderate improvement. This location is not considered feasible because of the offset thrust line which would cause a

large negative pitching moment. Another problem would be a complicated drive train because the power would have to be routed from the engine located in one of the fuselages through the vertical tail to the propeller at the top. The last choice was to locate the propellers in the front of the airplane. This allowed for a simple drive train.

The landing gear was positioned fore and aft on each fuselage. Outriggers can be located on the wing tips if needed. A minimum ground clearance for the propellers of 2.25 feet was chosen, permitting a rotation angle of 15° as shown Figure 4.12. The final configuration is reproduced in Figure 4.13.

4.5.2 Effects of Planform

The planform of a wing is collectively comprised of the sweep of the leading edge, aspect ratio, AR, taper ratio and the general shape of the wing as shown in Figure 4.14. The selection of the planform significantly influences the vehicle aerodynamics. The aspect ratio affects the aircraft in two ways. An increased aspect ratio gives improved drag characteristics as demonstrated from the induced drag $C_{Di} \approx C_L^2 / \pi AR$. However, the wing weight is directly proportional to the aspect ratio. This effect is illustrated in the weight estimation computer code which

shows a wing weight variation proportional to $AR^{.57}$. The taper ratio affects the vehicle aerodynamics by approximating an elliptical planform. Such a planform would yield a minimum induced drag. The wing sweep acts to increase the critical Mach number, which is the freestream Mach number where local velocities reach sonic speed. As the Mach number approaches M_{cr} there is an associated rise in drag.

4.5.4 Selection of Planform

The design conditions for the microwave powered aircraft leave limited room for planform selection. For low speed flight there is little advantage to a low aspect ratio or high sweep angle. The operation of this vehicle fits into this category with a subsonic flight speed of Mach 0.44 at cruise altitude. An aspect ratio of 15 was selected based on the data in the weight estimation parametric study. This value represents a compromise between wing weight, aerodynamic efficiency and the limitation of the span length to 250 feet for structural reasons. The planform includes a slight taper on the outer 40% of the semi-span. Figure 4.15 shows the actual planform selected.

4.6 Summary of Aircraft Sizing and Configuration

After an initial analysis was performed by each design group based on the first iteration data, several questions arose. The weights from the first iteration seemed very low. The structures group felt the wing weight allocation was not enough to support a span of 234 feet. The performance group desired more power for climb which would require a larger wing area.

As the design evolved and the first iteration was completed, it became evident that a second iteration of the component weights was necessary. The new configuration contained a canard, two vertical tails and two booms instead of a single fuselage. A standard NACA airfoil of 8% thickness was chosen for the canard and horizontal tail and a NACA 10% thick airfoil was chosen for the two vertical tails.

The weight estimation code was modified as follows to accommodate these changes: The aspect ratios and thicknesses of the canard, horizontal tail plane and vertical tails are based on the first iteration data. The values for these parameters are given in Figure 4.16. An equation similar to the one for a horizontal tail was added to account for the weight of the canard. The fuselage equation weight was doubled to account for two booms each 50 ft. long and 4 ft. in diameter and the vertical tail equation weight was also doubled to account for the two tails. The design condition of $C_L = .6$ and the constraint of having no external rectenna

remain the same, however, the size of the main wing was not fixed due to the fact that it determines the power available to the aircraft.

The second iteration deviates markedly from the initial estimate. The gross weight has more than doubled. This can probably be attributed to the increase in wing size caused by the increased weight and drag of the booms, canard and vertical tails. As mentioned previously, the wing weight equation is very sensitive at low values of wing loading. The overall wing span has also gone up considerably. In the first iteration, the span was fixed at 250 ft. to limit deflections. For this second iteration, the limit is relaxed due to structural findings that deflection are not as great as expected, and the possibility of reinforcing the wings with compression members. The second iteration component weights are illustrated in Figure 4.17.

5.0 Aerodynamics

Using the results of the weight estimation program, it was found that the aircraft lift coefficient needed to range from 0.6 to 1.0, at a design Mach number of 0.44. At low altitudes, the selection of airfoils which meet these requirements is simply accomplished by choosing a standard airfoil. At the design altitude of 100,000 feet, however, due to the rarefied air, the chord Reynolds number is fairly low (about 711,000).

At low Reynolds numbers, the transition of the boundary layer from laminar to turbulent typically involves a transition bubble. The transition bubble consists of a boundary layer separation just before transition, followed by reattachment and turbulent flow as shown in Figure 5.1.1. In the design of airfoils, it is generally desirable to keep the boundary layer laminar for as long as possible, as a laminar boundary layer induces significantly less skin friction drag than a turbulent one. However, a turbulent boundary layer has a much greater resistance to separation and may be advantageous at points where a large adverse pressure gradient exists. Therefore, it is desirable for the boundary layer to transition to turbulent at a point on the airfoil before a large adverse pressure gradient can induce laminar separation. The pressure distribution which the airfoil is designed to match, or the target pressure distribution, shown in Figure 5.1.2, features a flat upper surface in the transition region in order to

minimize laminar separation.

In designing an airfoil for minimum drag, therefore, the target pressure distribution must be such that laminar flow is preserved as far aft as possible. Transition must then be induced before a steep adverse pressure gradient can cause flow separation. This can be accomplished by designing a pressure distribution with a flat rooftop and a long transition ramp before the major pressure recovery as shown in Figure 5.1.2. The transition ramp consists of a very gentle adverse pressure gradient which will induce transition at some point long its length without causing laminar boundary layer separation. In this way, the amount of laminar flow will be maximized, and skin friction drag minimized.

The designed pressure distribution must be as smooth as possible. Otherwise, the resulting airfoil may have irregularities which cause premature transition of the boundary layer. This would result in an undesirable increase in the drag coefficient.

5.1.1 Elliptical Wing Loading

Ideally, an elliptical wing loading would be designed to provide for minimum induced drag. In order to achieve an elliptic wing loading with a non-elliptic planform, the airfoil section lift coefficient must be

varied along the span. The airfoil section lift coefficient is calculated based on the selected wing planform geometry from the classical elliptic lift equation given in Reference 13.

$$c_l = \frac{2\Gamma}{V_\infty c(y)} \sqrt{1 - (2y/b)^2} \quad (5.1)$$

Where Γ is the circulation, y is the location along the semi-span which has a value of zero at the fuselage, V_∞ is the free stream velocity, b is the overall span length and c is the local chord length which may be a function of location.

This expression is evaluated by calculating Γ (circulation) from:

$$\Gamma = \frac{4L}{\rho_\infty V_\infty b \pi} \quad (5.2)$$

Where L is the lift force which equals weight in level flight and ρ_∞ is the air density. Figure 5.1.3 shows the airfoil section lift coefficient variation along the span. This lift distribution has an average value of .6 over the entire span, which is the C_L for this design. Using this figure, three airfoil sections were designed to be installed at specific locations along the span to meet the local airfoil section lift coefficient requirements.

5.1.2 Airfoil Design Overview

The airfoil design procedure is primarily one of trial and error. There is no precise mathematical method from which a good target pressure distribution can be prescribed. The best tool in designing airfoils is an experienced designer and data collected by previous experiments and designs. To begin the airfoil design process, a baseline target pressure distribution was sketched. This target is based on data from References 10, 12, 19, and 23 on low Reynolds number airfoil design.

Figure 5.1.4 shows the baseline airfoil section pressure distribution (L - Series Airfoils), which was then modified twice on the upper surface to produce a total of three variations. The first modification (P-Series Airfoils) features the rooftop further away from the leading edge, a more favorable pressure gradient on the upper surface at the leading edge and a shorter transition ramp. The second modification (Q-Series Airfoils) has the rooftop closer to the leading edge and a longer and steeper transition ramp.

An airfoil section was generated for each of the three target pressure distributions using the computer code CPINVRS.FOR of reference 15. Figure 5.1.5 describes the P-series designed airfoil. Figure 5.1.6 gives a similar description for the L-series airfoil.

Finally, Figures 5.1.7 illustrates the Q-series designed airfoil. Each of these variations has a $c_l = 0.74$, which is the section lift coefficient for the root of the wing. The L, P, and Q airfoils were then analyzed using the computer code Grumfoil of Reference 20. The results of this viscous compressible analysis show that increasing the transition ramp length will decrease drag. Also, a more gentle pressure gradient on the upper surface will delay laminar separation. Using this data, the L-series airfoils were chosen for maximum performance.

Based on the spanwise lift distribution, three spanwise locations were selected and airfoil sections were designed for the appropriate lift coefficients by scaling the initial L-series target. The first section, L1 is designed for the wing root. The next airfoil, L2 is designed for installation at the juncture of the wing inner and outer panels. The final airfoil, L3 is designed for the wing tip. The design lift coefficients for these airfoils are 0.74, 0.59, and 0.40, respectively. Figure 5.1.8 gives the L1, L2 and L3 target pressure distributions. The L1, L2 and L3 geometry is given in Figures 5.1.9-11.

5.1.3 Design Procedure

Each of the three L-series target pressure

distributions was first analyzed using thin airfoil theory to provide an initial estimate of the airfoil shape. The computer program DESIGN.FOR of Reference 13, based on thin airfoil theory, was used for this purpose. The input for DESIGN.FOR is in the form of the upper and lower surface target pressure coefficients specified at locations along the chord. The output airfoil coordinates are then used as a starting airfoil guess for the inverse program CPINVRS.FOR, Reference 15, a thick airfoil design code which uses the Theodorsen method to calculate pressures under the assumption of inviscid, incompressible flow. This program iteratively determines the required airfoil sections, providing airfoil coordinates at 25 chordwise locations on both the upper and lower surfaces.

5.1.4 Airfoil Analysis

The airfoils generated using CPINVRS were first analyzed using a computer code which provided an inviscid, incompressible analysis. Resulting pressure distributions are shown in Figures 5.1.9-11. In order to obtain drag data and more accurate pressure data, the airfoils were then analyzed using Grumfoil, a code which provided a viscid, compressible analysis of the coordinates. In Figure 5.1.12, the lift curves obtained from the inviscid analysis are shown. These are seen to

differ from those found in the viscous analysis, shown in Figure 5.1.13. The nonlinearities in Figure 5.1.13 arise from viscosity and compressibility effects.

Since the design procedure is based on an inviscid, compressible analysis, the airfoil sections were designed with zero thickness trailing edges. In some cases, as in Figure 5.1.14, this induces an abrupt change in surface slope adjacent to the trailing edge, which causes increased drag and unreliable convergence of a viscous, compressible analysis. To avoid this, the airfoil coordinates at points near the trailing edge were extrapolated as seen in Figure 5.1.14. This extrapolation created a trailing edge of finite thickness, which significantly reduced the drag in the viscous compressible analyses.

When analyzed under free transition and at realistic Reynolds numbers, the L-series airfoils were found to have the best lift and drag characteristics at design conditions. This analysis was performed at the design Mach number of 0.44. Grumfoil analysis of sections L1, L2, and L3 shows that the incompressible analysis is fairly accurate, although there are some slight deviations in pressure at the leading edges. Design point pressure distributions for L1, L2, and L3 are shown in Figures 5.1.15-17. Airfoil section drag, shown in Figure 5.1.18, is a significant improvement over the previously designed airfoils.

5.1.5 Summary of Airfoil Design and Analysis

Comparison of the L-series airfoils against typical NACA airfoils of comparable thickness shows that the L designs have significantly lower drag near the design point. Drag polar comparisons are shown in Figures 5.1.19-21. Also, the large amount of camber in the L-series airfoils results in a higher lift per degree angle of attack, as shown in Figures 5.1.22-24. These airfoils provide the necessary performance for the aircraft, although further refinement of the target pressure distribution could give even better airfoil section performance.

5.2 Wing-Body Analysis

The objective of the wing-body analysis was to provide an aerodynamic study of the wing-body lift and drag characteristics. This study was accomplished by selecting a wing planform, integrating the designed airfoil sections into the wing and generating a geometric twist distribution. The wing pressure distributions are analyzed by using the program Flo - 30m. The results approximate an elliptical wing loading and maintain a minimum induced drag.

5.2.1 Twist Distribution

Based on the three airfoil sections designed, a wing twist distribution can be determined. This distribution allows the loading to approach elliptical by varying the effective angle of attack along the span. Once this is done, each airfoil section will produce the lift coefficient described by Figure 5.2.1. For each of the three airfoils designed, the equation for the linear portion of the c_l vs α curve is determined based on the results of the inviscid, incompressible analysis performed with CPDIST.FOR (Reference 14). The general equation for this portion of the graph is given in equation 5.3.

$$c_l = m \alpha_{\text{eff}} + c_{l_{\alpha=0}} \quad (5.3)$$

Here, c_l is the section lift coefficient, m is the lift curve slope, α_{eff} is the effective angle of attack in radians and $c_{l_{\alpha=0}}$ is the zero angle of attack section lift coefficient. Figure 5.2.2 gives the lift curve equations for each of the L-Series airfoils.

Since each airfoil is designed for a specific span location (L1 at root, L2 at .6 semi-span, and L3 at .9 semi-span), the intermediate sections must be approximated. As a first approximation, these sections are evaluated as linear combinations of the two boundary airfoils. As the airfoils vary from root to tip the lift curve slope and the zero angle lift coefficient change. These two important parameters are also calculated using a linear approximation. The equations for the variation of these parameters are given in Figures 5.2.3 and 5.2.4. Substituting the relations from these figures into the general equation for c_l vs. α yielded a single algebraic equation that governs the lift curve over the span. Combining this equation with the section lift coefficient variation gave the effective angle of attack along the wing span as shown in Figure 5.2.5. The effective angle of attack near the root is not accurate since this analysis was performed without regard to fuselage interference effects.

A first order linear approximation of the twist

angle holds the root section fixed at zero twist and varies the twist linearly in a nose down direction to the wing tip as shown in Figure 5.2.6. However, the effects of fuselage interference at the wing root necessitate increasing the root incidence angle to some positive (nose up) value. An elliptical distribution requires the tip section lift coefficient to be zero. Although the tip section is set at the zero lift angle of attack, according to the analysis, lift does remain on the tip.

A second order linear approximation was determined to more closely follow the actual twist distribution as shown in Figure 5.2.7. Figure 5.2.8 shows the actual wing twist of the airfoil sections at several span locations. Figure 5.2.9 shows the airfoil twist variation viewed from the tip to the wing root.

5.2.2 Compressible Wing-Body Analysis

Using the wing geometry, airfoil sections and twist distribution described above, a compressible wing-body analysis was carried out using the program Flo-30m. The input to Flo-30m consists of airfoil sections and twist angles at various span locations. The computer code will interpolate to generate the remainder of the wing sections. After the wing is entered, the body geometry is described in similar fashion. Three iterations were

performed on the wing-body combination in level flight. The first was the untwisted wing geometry. The next two iterations were based on the first and second twist approximations. Only the data for the untwisted and final geometry is presented.

The initial Flo-30m analysis was performed on an untwisted wing geometry. Flo-30m was run over a range of angles of attack from -2.0° to 6.0° . Using the C_L versus α curve (Figure 5.2.10) the geometric angle of attack required to produce the design lift coefficient of .6 was determined ($\alpha = .375^\circ$). By analyzing the wing at this angle and examining the lift coefficient variation along the span a comparison can be made to the elliptical lift variation as illustrated in Figure 5.2.11.

Figure 5.2.11 illustrates the effects of fuselage interference close to the wing root. A large effective angle of attack is needed near the fuselage to approach the desired lift coefficient. The theoretical lift curve slope corrected for Mach number, sweep and aspect ratio for a finite wing was calculated from equation 5.4 given on p 11-2 of Reference 24.

$$\frac{dC_L}{d\alpha} = \frac{m * AR}{2 + \sqrt{[4 + AR^2 B^2 (1 + \tan^2 \theta / B^2)]}} \quad (5.4)$$

Where m is the airfoil lift curve slope corrected for finite span, AR the wing aspect ratio, B is a correction

factor for Mach number given as $\sqrt{1 - M^2}$ and θ is the sweep of maximum thickness line. When the calculation was performed the corrected wing lift curve slope of 6.99 per radian matched the Flo - 30m output.

To improve the results, the wing was analyzed using the second approximation twist distribution. The C_L versus α curve for the twisted geometry is also shown in Figure 5.2.10. The geometric angle of attack corresponding to the design lift coefficient was determined ($\alpha = .2^\circ$). The improvement in the lift distribution can be seen in Figure 5.2.11. The fuselage effects were still prominent. Figure 5.2.12 displays the wing loading for the elliptical, untwisted and twisted geometry. The twisted geometry more closely represents the elliptic wing loading and had a smaller induced drag. The lift curve slope for the twisted wing remained at 6.99 per radian. The twist however shifted the entire lift curve upward (Figure 5.2.10).

The wing-body analysis was performed using level flight conditions. The actual flight path of the aircraft will be circular as described in section 2.0. In a circular flight path the effective wing lift coefficient required to maintain altitude will be slightly higher (see section 9.0).

The Flo - 30m results for the untwisted wing in level flight are given in Figures 5.2.13 - 5.2.16. These figures show the pressure distribution on the wing at

various angles of attack. Similar diagrams for the twisted wing are shown in Figures 5.2.17 - 5.2.20. At the design lift coefficient, where the wing loading is close to elliptical, the pressure distributions are very favorable. At the off-design conditions, especially at high angles of attack, suction peaks develop on the wing tip. These suction peaks are due to the twist distribution being developed for specifically the level flight design C_L and will cause the wing tip to stall.

5.2.3 Theoretical Drag Calculations

Following the methodology in Reference 24, theoretical calculations of the wing-body aerodynamics were carried out. Appendix A.4 gives the details of these calculations. Figure 5.2.21 shows the theoretical wing-body drag polar. The $C_{D\text{MIN}}$ value from this polar was higher than the value used in the weight estimation program. This discrepancy lead to the revision of the drag polar in the weight estimation code for a second weight iteration. The viscous drag factor, K'' , is much greater than the .007 value used in the initial analysis. A larger value of K'' made the drag polar narrower. Therefore a small change in lift coefficient produced a large change in drag. This effect led to rapid drag increases.

Looking at the lift coefficient versus lift-to-drag ratio (Figure 5.2.22) demonstrated the actual L/D ratio is close to the weight estimation code L/D ratio. In fact, the plane would operate at maximum L/D at the level flight design lift coefficient of 0.6. Figure 5.2.22 also confirms the rapid drag increases when deviating from design C_L . The L/D ratio at $C_L = 0.6$ is approximately 25. When in a circular flight path the L/D ratio decreases to 23.5.

5.2.4 Summary of Wing-Body Analysis

The wing-body analysis provided a twist distribution which approximates an elliptical wing loading. From the Flo - 30m analysis, it is clear that the low-Reynolds number wing design will produce enough lift for level flight ($C_L = 0.6$ at $\alpha_{geom} = 0.2^\circ$). Based on the theoretical drag calculations, the aircraft will have a L/D ratio high enough to ensure that the power available will be sufficient to overcome the drag force.

6.0 Structural Design & Analysis

The primary objective of the structural analysis was to design the structural configuration and perform the static and dynamic analysis using the finite element software package ANSYS. The structural analyses consisted of three progressively complex models. The first two models embodied just the wing while the third model embodied the wing, tail, canard and boom. The wing aerodynamic loading distribution on model 1 varied spanwise and was constant chordwise while models 2 and 3 varied spanwise and chordwise as shown in Figures 6.1.1 & 6.1.2.

6.1 Static Analysis

All three models were analyzed statically. The first model consisted of an aluminum skin with an internal structure of graphite - epoxy. It was comprised of 66 nodes, 60 beam elements and 60 plate elements. The chordwise pressure distribution for this run was constant as shown in Figure 6.1.1. For a more detailed discussion on how the first model was developed see Appendix A.5.

After running this model the following results were obtained. A 16.5 foot vertical deflection resulted, as shown in Figures 6.1.3 & 6.1.4. This deflection was small enough be analyzed using small deflection theory, as discussed in Appendix A.5.

The average maximum shear stress was 2184 psi, as shown in Figures 6.1.5 - 6.1.8. This stress was below the ultimate shear strength of aluminum alloy 2014-T6, of 42 ksi. Note that most of the shear is carried in the bottom skin surface due to the upward pressure on the wing.

The average maximum equivalent stress was 33,153 psi, as shown in Figures 6.1.9 - 6.1.12. Again this stress is well below the ultimate tensile strength of aluminum 2014-T6 as well as graphite - epoxy which have strengths of 70 ksi and 69.9 ksi, respectively. Most of the bending stress is carried in the I beams as illustrated in Figures 6.1.10 - 6.1.11. However, small amounts of bending stress are carried by the skin surface, as seen in Figures 6.1.9 & 6.1.12. The skin surface where stress was maximum was located near the centerline.

With this configuration the weight of the wings is 2050 pounds. This is only 76 % of the allocated weight of 2704.6 pounds, allowing for further strengthening of the wing. The wing weight allowance was determined from the weight estimation analysis in Section 4.0.

The first model was then altered to take into account the chordwise pressure distribution as discussed in Appendix A.5. Running these changes with a gravity load produced better results, reducing the vertical deflection to 14 feet. However, the chordwise deflection

was 7.33 inches, which was too high for this model. This deflection was due to the low stiffening in the wing.

Since the first model was too flexible, a second model was developed. The resolution of the second model was increased to 168 nodes, 180 beam elements and 180 plate elements, to more accurately represent the structure. The entire structure was made out of graphite - epoxy. This material was chosen because it reduced wing weight while increasing the strength of the wing. The geometry and wing aerodynamic loading distribution are presented in detail in Appendix A.5 and Figures 6.1.13 - 6.1.16.

Using the second model, four different analyses were run, including a gravity loading of 1g, a pressure loading, a pressure and gravity loading, and an externally braced configuration with both gravity and pressure.

The results of the gravity loading and the pressure loading analyses are presented in Appendix A.5.

For the combined pressure and gravity loading the average maximum equivalent stress was 36,955 psi, the maximum vertical displacement was 9.4 feet, and a maximum horizontal displacement was 5.3 inches, as shown in Figures 6.1.17 - 6.1.25. The horizontal deflections were reduced by 30% and the stresses were still quite reasonable while maintaining the wing weight allocated.

The last case for this model was for an externally braced configuration. The objective of this run was to see if a brace would significantly reduce the stresses and deflections. The brace was modeled using a one element bar with a modulus of elasticity of $20E10$ psi to represent a rigid element. The external brace was connected to the middle I beam at a distance of 40.75 feet out from the root and to the upper tail as shown in Figure 6.1.26. The average maximum equivalent stress was lowered from 36,955 to 27,039 psi. The vertical deflection was reduced from 9.4 to 3 feet. The shear stress was increased to -8866 psi, approximately 5 times as much as without the brace. These results are shown in Figures 6.1.26 - 6.1.33. The compressive forces within the brace were 26.2 kips. These forces tended to produced buckling, as disscussed in Appendix A.5.

In order to construct a brace to withstand the given load, a larger cross - section was needed. The minimum acceptable diameter, using graphite - epoxy, was calculated to be 5 inches. However, this cross - section would generate unacceptable drag. This could be overcome by placing an airfoil around the braces. The airfoil would have a mean chord of about 50 inches. However, this would drastically alter the design of the aircraft.

The third and final model was comprised of the second model plus a canard, tail, and boom. The pressures applied to the canard and tail are shown in

Figure 6.1.34. In this model a pressure with gravity loading was analyzed. The maximum vertical deflection was 8.5 feet, as shown in Figures 6.1.35 & 6.1.36. The maximum shear stress is -1588 psi as seen in Figures 6.1.37 & 6.1.38. The maximum equivalent principal stress is 32,609 psi as shown in Figures 6.1.39 - 6.1.42.

6.1.2 Summary of Static Structural Analysis

All three models show that this aircraft at an altitude of 100,000 feet can structurally withstand flight conditions of 3 g's. However, at sea level, flight conditions were determined to cause a 24 g aerodynamic wing loading. No analysis was performed on a 24 g wing loading, however, one can readily see that the structure would fail before it ever reached such conditions. The only possible way the plane could operate at sea level conditions is if a gust alleviation system is incorporated in the aircraft, as described in Section 9.0.

6.2 Vibration Analysis

Dynamic analysis was required to study the stresses under the unsteady loading conditions and to ensure that flutter is not encountered in the operating envelope of the vehicle. Dynamic analysis was used to determine the natural frequencies and mode shapes of the wing structure. It was important to review this analysis because the vibration, which can be caused by aerodynamic excitations, occurs during flight. The wing will deflect in vibrating motions and can cause a failure in the structural design. In the analysis, three configurations were analyzed by utilizing the computer code, ANSYS. The first wing structural model was the preliminary design, the second wing structural model was a revised design of the first model, and the third model included an external brace.

Major parts of the dynamic analysis are the free vibration analysis of the wing as the clamped free beam and the free-free analysis.

6.2.1 Clamped Free - Beam Analysis

The half wing structural model was developed with ANSYS. A free vibration analysis was performed with the wing as a clamped free beam. The clamped free beam configuration has the same boundary condition as

a cantilever beam. Since the fixed end can not have any displacements, the wing root was fixed by restraining three translations and three rotations. The behavior of the ANSYS model was compared with the results of uniform cantilever beam.

6.2.2 Preliminary Wing Structural Design

The preliminary wing structural design and model consisted of two spars with ten spanwise rib sections, as shown in Figures 6.2.2 - 6.2.16 and as discussed in Section 6.1. The spars, which were modeled as the I-beams, were tapered along the span.

Natural frequencies (Eigenvalue) of the each mode are shown in Figure 6.2.1 - 6.2.16. Figures 6.2.2 - 6.2.4 illustrate the first bending mode of the wing; Figures 6.2.5 - 6.2.7 display the first torsional mode; Figures 6.2.8 - 6.2.10 reveal the second bending mode; and Figures 6.2.11 - 6.2.15 show a combined mode involving bending and torsion. Note that there was no bending in the plane of the wing as shown in the Figures 6.2.4, 6.2.7, 6.2.10, 6.2.13, and 6.2.16.

The first mode frequency of the preliminary structural design was 0.858065 Hz. This value was extremely low. It also has insufficient stiffness in the structure to prevent flutter.

6.2.3 Revised Wing Structural Design

The revised wing structural design was developed from the preliminary model as discussed in Appendix A.5.

Natural frequencies of the each modes are shown in Figure 6.2.17 - 6.2.32. Figures 6.2.18 - 6.2.20 show the first bending mode of the wing; Figures 6.2.21 - 6.2.23 illustrate the second bending mode; Figures 6.2.24 - 6.2.26 display the first torsional mode; Figures 6.2.27 - 6.2.29 show the third bending mode; and Figures 6.2.30 - 6.2.32 display the second torsional mode. Again, note that there is no bending along longitudinal direction as shown in the Figures 6.2.20, 6.2.23, 6.2.26, 6.2.29, and 6.2.32.

Compared to the preliminary model, the additional structure gave more stiffness to the wing and resulted in higher frequency values for each of the respective modes. However, these frequencies were still quite low, indicating that the wing had excessive flexibility. To assess the adequacy of the wing structure with respect to flutter, it would be necessary to construct the power density spectrum of the in flight aerodynamic loadings and then conduct a dynamic analysis to calculate the magnitude of the structural response and associated stresses. This analysis is beyond the scope of the project, in which we sought merely to identify and investigate the wing free-vibration modes.

6.2.4 Revised Wing with External Brace

The result of the revised wing structural design showed improved eigenvalues of modal frequencies. However, it was still not satisfactory. Therefore, an additional external brace was design to hold the wing and give additional stiffness to the wing structure. Such a brace was connected from the tailplane to the mid-section of the half-wing as shown in the Figures 6.2.34 - 6.2.48.

Figures 6.2.33 - 6.2.48 show the eigenvalues for each mode. Figures 6.2.34 - 6.2.36 show the first bending mode of the wing; Figures 6.2.37 - 6.2.39 illustrated the second bending mode; Figures 6.2.40 - 6.2.42 show the first torsional mode; Figures 6.2.43 - 6.2.45 display the third bending mode; and Figures 6.2.46 - 6.2.48 show the second torsional mode.

Compared to the previous model, the natural frequency of the first mode was significantly increased from 0.9377 Hz to 1.5486 Hz. However, the brace did not adversely affect other modes because there were no significant increases in other frequencies. Figures 6.2.39 and 6.2.45 clearly show that brace caused an increased in-plane deflection of the wing, which was not apparent in previous models. The external brace did not improved the stiffness of the wing structure, therefore, the brace was not feasible for additional support.

6.2.5 Summary of Vibration Analysis

The three analyses indicated that the natural frequencies of the wing were extremely low and the values were unacceptable. This wing structural design will fail. The wing must be redesigned with more stiffness in the internal structure in order to increase the natural frequency.

7.0 Stability and Control

In order for this aircraft to fly its mission of non-piloted flight to 100,000 feet, it must be equipped with a carefully designed control system. The first step in designing a control system is to define and identify the flight characteristics. An aircraft of this nature does not need maneuverability, but it requires a high degree of reliability; its systems must be designed redundantly. The level of stability inherent in the vehicle is the basis of its flight characteristics; it must have adequate stability, yet it must also have a sufficient amount of control, especially for landing.

7.1 Static Stability Analysis

Stability may be thought of as the tendency for the aircraft to return to equilibrium after being disturbed. Disturbances may be generated by the flight computer's control actions or by atmospheric phenomena such as wind gusts, turbulence, or thermal convection. Two flight conditions are necessary for the aircraft to fly its mission successfully: it must be able to achieve equilibrium flight, and it must have the capability to maneuver effectively over a wide range of flight speeds and up to the design altitude.

In order for the aircraft to maintain steady uniform flight, the resultant force and moment about

the center of gravity (CG) must both be equal to zero. This state is known as the trim condition. If the forces and moments do not sum to zero, the airplane will be subjected to translational and rotational accelerations. To achieve static stability then, the vehicle must develop a restoring force and/or moment which tends to bring the vehicle back to equilibrium.

Figure 7.1.1 is a plot of C_m vs. α . When Airplane 1 is subjected to a disturbance which pitches the nose up, a moment develops which continues to pitch the nose up further. Clearly, Airplane 1 does not possess static longitudinal stability, for which a negative value of pitching moment derivative ($dC_m/d\alpha$) is required.

Both Airplanes 2 and 3 have negative pitching curve slopes, yet Airplane 2 cannot be trimmed at a positive angle of attack (α). Thus in addition to having static stability, the airplane must also possess trim capabilities of positive angles of attack.

A computer program was written to carry out the static stability computations. Each component's contribution to the pitching moment curves may be seen in Figure 7.1.2. It is noted that the fuselage and canard are destabilizing, while the wing and tail are stabilizing. The airplane pitching moment is stable; however, it will not trim at zero angle of attack in the absence of canard or tail deflection.

Using the data of Figure 7.1.3 and the analysis program (see Appendix A.7), the neutral point of the airplane was found to be 4.59 ft. aft of the leading edge of the wing. It was then determined that placement of the CG at 0.1 chords ahead of the neutral point would provide an acceptable level of static stability while allowing for adequate control. Thus the CG would lie 3.05 ft. aft of the wing's leading edge. Because there is no fuel carried aboard this aircraft, the CG position should remain constant during all phases of flight. Thus, at least in a preliminary design, it is not necessary to analyze the effect of center of gravity position on control.

7.1.1 Summary of Static Stability

The final task undertaken in the area of static stability analysis was that of generating pitching moment curves at different tail and canard incidences. These curves (Figures 7.1.4-7.1.9) define the limits of control of the airplane.

At high angles of attack, an upward deflection of the canard will tend to stall the canard, creating a higher overall stability and a pitching moment towards equilibrium. In the regions where the canard stalls before the tail, the total canard contribution to stability disappears. This is seen as a decrease in

the slope of the airplane pitching moment curve. If the tail stalls first, its contribution likewise disappears--decreasing overall stability. This is seen as an increase in the slope of the pitching moment curve.

The model for this analysis assumes that the lift curve slopes for the canard and tail are constant up to 8° , beyond which the section lift curve slopes become zero and the lift coefficient is constant. (See data for NACA 64208 Airfoil, Reference 01). A more rigorous analysis requires a wind tunnel model to test for these nonlinear effects.

Three types of horizontal control surface scheduling were examined; these correspond to Figures 7.1.4-7.1.9. The first shows deflections of the tail while the canard is fixed at zero incidence. The second shows deflections of the canard while the tail is fixed at zero incidence. The third shows scheduling of equal deflection between the tail and canard. Another scenario for longitudinal control scheduling might be to deflect both surfaces in such a way that each donates an equal amount to the pitching moment. More elaborate methods might include surface deflections which are a function of the stresses in the structure, or of the flight dynamics.

For the three scenarios examined, it was determined that the aircraft can trim over a range of

angle of attack from $(-7.8^{\circ}$ to $5.7^{\circ})$. This range corresponded to lift coefficients varying from $(-0.58$ to $1.02)$. Figures 7.1.4-7.1.9 demonstrate that this vehicle has adequate control regardless of the method of surface deflection scheduling, although it appears desirable to increase the maximum positive angle of attack at which the vehicle can be trimmed.

7.2 Dynamic Stability

The purpose of this analysis is to determine whether or not the aircraft will be stable at all of its flight conditions. This was done by finding its natural modes of oscillation at given altitudes and checking whether they tend to converge (stable) or diverge (unstable).

The dynamic stability analysis for our aircraft was performed for altitudes of 100,000 feet and 25,000 feet. Cruise velocities are Mach .44 and Mach .09 at the respective altitudes.

Only a longitudinal dynamic analysis was done for this aircraft, so the relevant factors were u (the dimensionless velocity change along the x axis), w (the dimensionless velocity change along the z axis), and q (the rate of change in pitch angle θ).

The manifestation of an aircraft's response to disturbance occurs in two modes. The short period is the immediate response, and the long period, or phugoid, is the "long term" response.

The first step in the analysis was the identification of the longitudinal stability derivatives. The derivatives were derived from basic equations of motion and small disturbance theory for a wing and tail (Reference 16). They were then modified to account for the aircraft's canard.

Certain assumptions were made concerning the derivatives. Compressibility effects were neglected. Direct contributions of thrust were neglected.

The stability derivatives were calculated as shown in Figure 7.2.1. They were then put into the homogenous dynamic stability equation shown below in matrix form.

(7.2.1)

$$\begin{bmatrix} \frac{du}{d\theta} \\ \frac{dw}{d\theta} \\ \frac{dq}{d\theta} \\ \frac{d\theta}{d\theta} \end{bmatrix} = \begin{bmatrix} X_u & X_w & 0 & -g \\ Z_u & Z_w & u_0 & 0 \\ M_u + M_w Z & M_w + M_w Z_w & M_q + M_w u_0 & 0 \\ 0 & 0 & 1 & 0 \end{bmatrix} \begin{bmatrix} \frac{du}{d\theta} \\ \frac{dw}{d\theta} \\ \frac{dq}{d\theta} \\ \frac{d\theta}{d\theta} \end{bmatrix} + \begin{bmatrix} X_\delta & X_{\delta T} \\ Z_\delta & Z_{\delta T} \\ M_\delta + M_w Z_\delta & M_{\delta T} + M_w Z_{\delta T} \\ 0 & 0 \end{bmatrix} \begin{bmatrix} \delta \\ \delta_T \end{bmatrix}$$

*The second matrix term is 0 since the analysis did not include control inputs

Before the exact analysis was carried out, theoretical approximations for the long and short period frequencies and damping ratios were calculated using approximation equations derived from equation 7.2.1. These theoretical values were then compared with the results of the exact analysis.

Three types of analyses were carried out. The short period was calculated using a two-degree-of-freedom system of equations while the long period motion was found by writing a second order differential equation

for the velocity perturbation u . These equations are shown below.

Short period equations:

$$\left. \begin{aligned} du &= 0 \\ dw &= (Z_w)dw + u_0 dq \\ dq &= (M_w + M_w Z_w)dw + (M_q + M_w u_0) dq \end{aligned} \right\} \quad (7.2.2)$$

Long period equation:

$$u = (X_u)u + (gZ_u/u_0)u \quad (7.2.3)$$

The exact analysis was performed by solving equation 7.2.1 using the differential equation solving computer program ASDEQ. The main block diagram used as input for ASDEQ is shown in Figure 7.2.2.

In order to find the natural modes of the aircraft, the control matrix was assumed to equal zero. This allowed the response of the aircraft to be calculated simply by changing the initial values of u , w , and q to disturb it from equilibrium. This simulates an induced perturbation in forward, vertical, and pitching motion respectively. The equations are then integrated with respect to time and the aircraft response over a chosen time period is shown graphically. The results for the airplane are given in Figures 7.2.3 - 7.2.5 and Figures 7.2.6 - 7.2.8 for the examined altitudes (100,000 feet and 25,000 feet respectively).

7.2.1 Summary of Dynamic Stability

The initial condition for the long period mode at both altitudes was $u=2$. The initial perturbation for the short period mode at both altitudes was $\alpha=1$ degree (.017 radians), as was that for the combined mode analyses.

The separate long and short period results were generally predictable. The damping at 25,000 ft was much greater than that at 100,000 ft due to the greater dynamic pressure at the lower altitude. The airplane was stable at both altitudes, but the long period mode at 100,000 ft is just barely so. The short period mode at 25,000 ft can be seen to be more than critically damped in Figure 7.2.6 (it does not have an oscillatory response), while the short period at 100,000 feet can be seen in Figure 7.2.3 to be about 4 seconds. The difference in the long periods at the two altitudes is shown in Figures 7.2.4 & 7.2.7 to be 60 seconds at 100,000 feet versus 12.5 seconds at 25,000 feet.

The results of the combined mode analysis are far more surprising. The airplane is stable at 100,000 feet, but slightly unstable at 25,000 feet (as shown in Figures 7.2.5 and 7.2.8 respectively). This is the reverse of what one would expect based on the relative dynamic pressures of the two flight conditions, as well as the opposite of what was predicted by the results of

the separate long and short period modes. Regardless, the program was functioning correctly (Appendix A.8) and the response derivatives were carefully checked, as was their precise input into the program. While an error is always a possibility, we consider it unlikely that this was the cause of the unexpected results.

A possible explanation of the discrepancy is the extreme sensitivity of the aircraft to changes in apparent velocity at low altitudes. This may overcome the aircraft's tendency to recover from a disturbance. The sensitivity may be caused by an extremely low wing loading and may occur only through coupling of the short and long period modes.

8.0 Weight and Balance

8.1 Component Sizes and Locations

The weight estimation program provided weights of the components based on statistical data. Certain components such as the wing and fuselages had their weights revised during the structural analysis. The weight of the rectenna was a function of its surface area. This weight was estimated with reasonable accuracy in the weight estimation program. Other components such as the engines and gearboxes needed a second weight estimate based on a more accurate data.

Each propeller was calculated to be $10\frac{1}{2}$ feet in diameter using momentum theory and an assumed efficiency of 85%. Using this diameter and other data, the gearbox weight was calculated at approximately 100 pounds (see Appendix A.6). The electrical motor was not designed, rather its physical dimensions were based on an existing commercial design.

After the components were weighted, they were positioned in the aircraft in order to position the aircraft's center of gravity at a predetermined location.

8.2 Mass Properties

With the components sized and positioned, the mass moments and products of inertia about the

aircraft's center of gravity were calculated by assigning geometric shapes (flat plates, cylinders and flat discs) to the components and then using corresponding equations. Figure 8.1 is a side view of the aircraft with the components located and dimensions shown. Figure 8.2 is a data table showing all the mass properties of each component in addition to the X and Y coordinates (identified as X-Bar and Y-Bar respectively) of the aircraft's center of gravity.

8.3 Summary

The vehicle components were sized and located about the aircraft so that the center of gravity was 36.71 feet behind the propellers along the roll axis of the aircraft. I_{xx} was calculated to be $5.43E+5$ slug·feet²; I_{yy} to be $4.41E+4$ slug·feet² and I_{zz} to be $517E+5$ slug·feet² by simplifying the component shapes into flat plates, cylinders and flat discs.

9.0 Performance

9.1 Objectives

The performance of an aircraft involves the method of takeoff, climb, cruise, and the path followed. The mission requirements of this aircraft require adjustment to substantial density variations resulting in a aerodynamic and structural tradeoffs. This section will analyze and discuss the intended flight conditions and parameters for the mission.

9.1.1 Power

The ground location of the power source will be fixed. Therefore, the aircraft must fly in a circular path at altitude about the power source. The power required and the availability of power at design altitude and also during the aircraft's climb to its cruising altitude must be analyzed in order to determine whether sufficient power is available to execute the desired flight path.

The aircraft will not be flying in level flight but at a small bank angle, φ , in order to turn and remain near the ground power source. The power is transmitted most efficiently if the microwave beam is perpendicular to the rectenna. Flight in a turn with a stationary power source does not allow for this. The angle between the normal to the rectenna and the beam shall be referred to as the angle of incidence, β , see

Figure 9.2.8. The availability of power will be decreased due to this angle of incidence in turning flight.

The total power which must be transmitted to the aircraft is another performance consideration. The power source beams power in a conically shaped beam in which the density of the power decreases with distance from the center of the beam, as shown in Figure 9.2.19. The amount of power and the diameter of the transmitter must also be determined for the design conditions.

9.1.2 Flight Path

The flight path to the cruising altitude will be a spiral with the bank angle, flight radius, and velocity varying during the climb. A description of the path can be determined from the chosen flight conditions at each altitude.

9.1.3 Climb

The rate of climb, dh/dt , is a function of the available and required power and the aircraft weight, W , such that :

$$dh/dt = (P_{available} - P_{required}) / W \quad (9.1)$$

The amount of excess power available determines an aircraft's capability to climb. Since this aircraft

receives microwave power most efficiently in level flight, i.e. when the beam is perpendicular to the rectenna, an analysis of the excess power and climb performance was first constructed for a wings-level flight condition.

A second analysis of the climb rate will consider flight in a turn. The corresponding bank angle, ϕ , angle of incidence, β , Mach Number, M , and flight radius, R , will be determined at each altitude after the maximum rate of climb the aircraft is capable of achieving is chosen. This will allow the optimum flight path to be described.

9.1.4 Effect of Wind Gust

The magnitude of the load factor, n , encountered due to a gust was determined in order to design the aircraft structure. A low wing loading, W/S , increases the load factor for a given gust velocity, w :

$$n = 1 + (p * a * w * V) / 2(W/S) \quad (9.2)$$

Since the design condition of the aircraft at a altitude of 100,000 feet required a low wing loading, this can not be avoided. The lower air density at higher altitudes decreases the load factor experienced at a given airspeed. Encountering a gust at the design altitude will not be a performance problem since the

structure has been designed for a load factor of 3. However at lower altitudes, expected gust velocities produce very large load factors, far in excess of the values to which the structure has been designed. Thus, a method of alleviating the effects wind gusts during the climb must be a part of the design.

9.2 Power Analysis

9.2.1 Level Flight

In order to analyze the availability of power at the design altitude and during climb a computer program was written to calculate various characteristics of the aircraft as the speed and corresponding Mach Number increase. A listing of the code can be found in the Appendix A.9. The outcome of the preliminary weight estimation were input into the program and the resulting coefficient of lift, lift, coefficient of drag, drag, thrust, propeller efficiency, power required, and power available were calculated as the Mach number and altitude varied.

The power available and required at sea level, 25,000 feet, 50,000 feet, 75,000 feet and 100,000 feet are shown in Figures 9.2.1 - 9.2.7. The results of this analysis indicate that there is sufficient power available at each altitude to maintain level flight.

9.2.2 Turning Flight

For this aircraft, flight in a turn results in a reduction of available power and an increase in required power. The wings must produce more lift since :

$$L = W / \cos\varphi \quad (9.3)$$

In level flight the lift is equivalent to the weight, as the bank angle increases the necessary lift increases. The propeller efficiency, E_p , a function of the thrust, velocity, air density, and cross-sectional propeller area, also is reduced in turning flight:

$$E_p = 2 / (1 + (1 + T / (0.5 * \rho * V^2 * A_{propeller}))^{1/2}) \quad (9.4)$$

Power Available is reduced in a turn because the microwave beam is no longer perpendicular to the rectenna surface. The angle of incidence, β , is a function of the bank angle, φ , altitude, h , and flight radius, R (see Figures 9.2.8 - 9.2.1) :

$$\beta = \varphi + \theta \quad (\tan\theta = R/h) \quad (9.5)$$

The power received by the motor is reduced by the angle

of incidence as follows :

$$\text{Preceived} = P_d * S * \cos\beta \quad (9.6)$$

The bank angle and angle of incidence which result in the maximum available excess power will be the optimal flight conditions, as long as the corresponding coefficient of lift is attainable. Since the speed and air density vary with altitude, so do the bank angle, angle of incidence, and radius of turn.

The level flight performance program was altered to account for the changes taking place in turning flight. A power analysis of turning flight at bank angles ranging from 5° to 30° at five altitudes ranging from sea level to 100,000 feet was done using the revised program. Figures 9.2.11 - 9.2.18 show the power available and required in turning flight as the bank angle varies.

The results of this analysis show that the aircraft has sufficient power to fly from sea level to 100,000 feet in turning flight, although there is very little excess power at the design altitude. Additional power could be received if the canard and tail are used as rectenna surfaces. The optimal flight speed and radius increase with altitude as shown in Equation 9.7 :

$$R = V^2 / (g * \tan\phi) \quad (9.7)$$

The coefficient of lift necessary to maintain flight also increases with altitude since it is inversely proportional to the air density :

$$C_L = L / (1/2 * \rho * S * V^2) \quad (9.8)$$

At the lower altitudes, 5 to 25 thousand feet, the optimal flight speed is very low, in the range of Mach 0.1. The necessary coefficient of lift is in the range of 0.4 to 0.5. As the flight altitude increases the necessary coefficient of lift also increases as well as the flight speed. It is difficult to design one aircraft that is capable of flight at sea level to 100,000 feet since the air density varies considerably. A configuration having variable wing area is a possible solution to this problem.

9.2.3 Total Transmitted Power

The ground power source must be sized to accomodate the power requirements. The area of the transmitter and the total power transmitted are inversely proportional and a function of the power density (P_{DENSITY}), wavelength of the microwave radiation, altitude (h), and an efficiency factor (n) (Reference 6) :

$$At Pt = (PDENSITY * wavelength^2 * h^2) / n \quad (9.9)$$

The density of the power has a parabolic power distribution in which the center has maximum power, see Figure 9.2.20. At the $\frac{1}{2}$ beam width angle, $BW_{1/2}$, there is only half of the power density. The maximum attainable power density is 700 W/m². The calculation of total power for a range of transmitter areas is presented in Figure 9.2.21.

9.3 Climb Performance

9.3.1 Climb Rate

The performance program was revised once again so that the climb rate could be calculated at the various altitudes. First the wings level climb was calculated and then turning flight, as shown in Figure 9.3.1.

The amount of excess power versus the Mach number, shown in Figures 9.3.2 - 9.3.6, was used to determine the optimal flight speeds for each altitude. It was determined that the optimal bank angle was in the range of 5° to 15° and that it varied with altitude.

The program was run once again for bank angles ranging from 3° to 13° and altitudes ranging from 5,000 feet to 100,000 feet. This information determined the climb rate and corresponding bank angle and flight

speed with the restriction of a $CL < 0.8$ at each altitude. Climb rate, bank angle, velocity, Mach number, coefficient of lift, and flight radius versus altitude are shown in Figures 9.4.2 - 9.4.7.

9.3.2 Time to Climb

The time to climb can be calculated using the inverse of the maximum rate of climb, dh/dt . This is calculated as :

$$t = \int_0^H \frac{dh}{(dh/dt)} \quad (9.10)$$

The minimum time to climb for both wings level flight and turning flight have been calculated and are given in Figures 9.3.7 and 9.3.8.

9.4 Flight Path

The aircraft must be towed to an altitude that it is capable of receiving the power from the ground power source without much of a reduction due to the angle of incidence. Twenty thousand feet is a sufficient altitude because there is an incidence angle of approximately 13° which does not result in a sizable decrease in power received by the rectenna.

The flight path to the design altitude will be

determined from the speeds and bank angles resulting in the optimal rate of climb for each altitude, see Figures 9.4.1 - 9.4.3 and 9.4.5. The aircraft's bank angle will first decrease from 7 degrees at an altitude of about 20,000 feet to 5 degrees at an altitude of 25,000 feet, stay fairly constant until an altitude of 50,000 feet, and then increase steadily to 9 degrees at 100,000 feet. The speed will be increasing during the climb from a Mach number slightly below 0.1 to a cruising Mach number close to 0.4 at 100,000 feet. The increasing speed accounts for the increasing radius, which varies from approximately 2,500 feet to 28,000 feet at the design altitude. The result is a spiral flight path to an altitude of 100,000 feet and cruising flight in a turn at a bank of 9 degrees and flight radius greater than 28,500 feet. See Figures 9.4.1 - 9.4.7 to visualize the mission flight path.

The number of turns the aircraft must make to climb to the design altitude can now be determined. The velocity at a given altitude is a function of the radial velocity and the flight radius :

$$V = \Omega * R \quad (9.11)$$

And the time to fly one turn, T , is a function of the radial velocity:

$$T = (2 * \pi) / \Omega = (2 * \pi * R) / V \quad (9.12)$$

The change in altitude, $d(\text{alt})$, for one turn is proportional to the climb rate, dh/dt , at the altitude of flight :

$$dh/dt = d(\text{alt}) / T \quad (9.13)$$

$$d(\text{alt}) = dh/dt * T \quad (9.14)$$

The aircraft will make 2 turns from 20,000 to 25,000 feet. It will then continue to 50,000 feet making 8 more turns. The climb to 75,000 feet will require almost 8 more turns. The climb rate from 75,000 to 100,000 feet is quite low, this increases the number of turns to 28. See Figure 9.4.1 to view the change in flight radius with altitude. The number of turns necessary is given in Figure 9.4.8.

9.5 V-n Diagram

A program was developed to calculate the V-n Diagram which shows the load factor of the aircraft configuration due to a vertical wind gust. At five altitudes ranging from sea level to 100,000 feet the load factor was calculated for gusts ranging from -40

ft/s to 40 ft/s as shown in Figures 9.5.1 through 9.5.5. The CL will never be greater than 1.5 or less than -1, therefore the associated load factors versus Mach Number for these CL's were calculated and plotted, as shown in Figures 9.5.6 - 9.5.10.

The aircraft was structurally designed for a load factor of 3. If it had been designed for a load much greater than 3 the structural weight would have increased significantly. At altitudes above 60,000 feet the present aircraft design is capable of encountering gusts above 40 ft/s. At lower altitudes, gusts as small as 10 ft/s result in load factors well above 3, see Figures 9.5.11 - 9.5.13. The flight speed at these altitudes is very low, yet the load factors induced by typical gusts will induce loads that exceed the design limitations of the wing.

The aircraft is structurally capable of encountering very large gusts at high altitudes. This analysis indicates that as presently designed, the aircraft would require a gust load alleviation system at altitudes below 60,000 feet. This would take the form of sensors mounted on the aircraft which would activate the flight controls in response to a gust in order to prevent the development of load factors in excess of the design value. Alternatively, a variable wing area configuration might be a possible solution.

9.6 Results

The results of this analysis showed that there is sufficient power available to climb in a spiral flight path and maintain turning flight at the design altitude.

The coefficient of lift necessary to maintain turning flight at the design altitude is approximately 0.8. The flight speeds at lower altitudes are quite low. At altitudes ranging from sea level to 50,000 feet, a coefficient of lift ranging from 0.4 to 0.5 is adequate.

The aircraft shall be towed to an altitude of 20,000 feet by another aircraft. At 20,000 feet the aircraft will begin turning flight at a flight radius of approximately 2,500 feet using microwave power on the design spiral flight path. A very sensitive gust load alleviation system will be in use as the aircraft is towed and during the climb to 60,000 feet. Once the aircraft reaches 60,000 feet the gust load alleviation system will still be available but the sensitivity can be decreased. The aircraft will climb to the cruising altitude steadily increasing the flight radius until an altitude of 100,000 feet and radius of approximately 28,500 feet is reached. This climb to 100,000 feet is estimated to take 3.75 hours.

Approximately 15 to 25 MW of microwave power must

be transmitted to the aircraft from the ground power source. This amount of power is substantial and costly.

9.7 Summary of Performance

There are critical issues in order to accomplish such a mission which our study has not yet resolved. Using the wing as a rectenna surface, the optimum wing loading is lower than would be required with some form of liquid fuel propulsion system. This low wing loading makes it difficult to design a structure which can withstand the large load factors induced by gusts at low altitude. Therefore, either a gust alleviation system or a variable wing area design should be considered.

The total power required from the transmitter is a substantial fraction of a power plant. This amount of power is quite expensive and damaging to the environment. The cost and environmental impact will be discussed in Sections 12.0 and 11.0 respectively.

10.0 Beam Tracking System

10.1 Overview

There are two major engineering tasks associated with a microwave powered high altitude aircraft: the actual aircraft itself and the system that delivers microwave energy to the aircraft. The microwave energy could be transmitted to the aircraft from several locations including the ground, an aircraft at a lower altitude or even perhaps a satellite. The most feasible approach from an engineering standpoint is transmission from the ground.

The transmitted beam of microwave power must be very narrow and accurate to maximize efficiency and minimize interference with other radio frequency sensitive objects. Since the microwave beam is very narrow, it must be kept pointing at the aircraft at all times. This is a significant engineering task when the aircraft operates at an altitude in excess of 70,000 feet.

This chapter addresses the task of tracking a simulated aircraft with a beam of energy, by using a beam of ordinary light to simulate the microwave beam. a tracking system model undergoes design, implementation and evaluation from a controls engineering perspective and for its applicability to the "real world" problem.

10.2 Background

The concept of transmitting electrical power in a "wireless" fashion using microwave energy originated with

the early work on radio waves in the late nineteenth century. Heinrich Hertz and then later Nikola Tesla showed that energy could be transmitted through the air using radio waves. The work done by Hertz and Tesla utilized low frequency radio waves and proved that efficient power transmission would require shorter wavelengths. Radio waves with wavelengths less than a meter (frequencies above 300 megahertz), known as microwaves, are required for proper beam focusing. The technology of the early 20th century did not allow generation of sufficient power levels in the microwave range for workable transmission of power. Major breakthroughs occurred during World War II when the klystron tube, and subsequently, the cavity magnetron were invented for use in radar systems. Both of these devices provided the necessary levels of power for feasible energy transmission using microwaves.

In 1959, a team led by William C. Brown at Raytheon Corporation undertook one of the first practical applications of microwave power transmission. A small helicopter with a brushless DC motor became the first airborne vehicle powered by energy from a transmitted microwave beam. The helicopter utilized an array of small dipole antennas, each one connected to a diode rectifying circuit, which collected the microwave energy and converted it to DC. This type of rectifying antenna is known as a rectenna. The original helicopter, demonstrated in 1964,

flew to a height of 60 feet guided by tethers. Raytheon also fabricated a free-flying model which they successfully demonstrated to the Air Force, however the existing technology did not allow any practical applications. The most significant result of the program was the increased knowledge of energy collection using the rectenna, as discussed in Reference 5.

The next major proposed application using microwave power transmission arose in the early seventies as a result of the energy crisis. The concept consisted of a network of satellites collecting solar energy, converting the energy into microwaves, then beaming the energy to the ground. The Solar-Powered Satellite (SPS) program, as it was called, proposed the use of satellites with collector panels the size of Manhattan Island. They would have generated up to 300 billion watts of energy at a cost well into the trillions of dollars. Although the cost of the SPS program was prohibitive, approximately ten years of research provided significant advancement in the area of microwave power transmission. An improvement in rectenna technology emerged as one of the most significant achievements of the SPS research (Reference 5).

In an effort to maximize the efficiency of a microwave transmission system, William Brown (at Raytheon) and James Triner of NASA developed a thin-film rectenna from printed circuit technology. The thin-film rectenna weighs one-tenth

of the original rectenna developed at Raytheon and provides efficiencies in excess of 80 percent. The thin-film rectenna opened the door for aerospace applications of microwave power transmission, including the most recent breakthrough, the first microwave powered airplane (Reference 6).

10.3 Microwave Powered High Altitude Aircraft

The first official flight made by an airplane powered by beamed microwave energy occurred on October 6, 1987. The airplane, called the SHARP-5 (Stationary High Altitude Relay Platform), was designed and built by the University of Toronto Institute of Aerospace Studies (UTIAS). Major funding from the project came from the Canadian Communications Research Center (CRC) because of their interest in the SHARP for communications applications (Reference 29).

The SHARP-5 aircraft has a fifteen foot wing span and carries a 3.5 foot circular disk aft of the wings for microwave reception. The entire underside of the aircraft is covered with thin-film rectenna made with diodes fabricated from silicon. The original thin-film rectenna utilizes diodes made of gallium arsenide which are more efficient for power conversion, but cost substantially more.

Power for the aircraft is generated by a battery until it reaches an altitude where it can intercept the microwave beam. The transmitted frequency of the microwave beam used is 2.45 gigahertz. There are two rectenna layers at right angles to each other to allow maximum energy collection while the airplane follows a circular path.

An aerodynamically improved model, The SHARP-6B, has also been developed by UTIAS. The SHARP-6B is intended to be the prototype for a future full-scale version with a 130 foot wing span and a 30 foot rectenna disk with 10,000 dipoles capable of flying at altitudes above 50,000 feet at speeds near 120 mph.

Future plans for autonomous aircraft include many applications. Radio and television broadcasts could be transmitted to the aircraft and then relayed down to a specific area, which would reduce the size of receiving dishes to a few feet. Possible uses in communications include telephone networking and cellular telephone service. Military reconnaissance and early warning of low flying aircraft and cruise missiles comprise other applications. Various type of airborne surveillance such as coastline monitoring could also be performed. The lower costs associated with a remotely piloted aircraft might make it an attractive alternative to satellites in certain applications (Reference 29).

10.4 Microwave Transmission System

The feasibility of a high altitude unmanned airplane powered by microwave energy depends largely on the cost of developing an effective transmission system. Current technology places the cost of a ground transmission system in the neighborhood of 30 to 50 million dollars, which is equivalent to the cost of launching a communications satellite. A microwave transmission system consists of the actual power transmitting elements and some control system that keeps the transmitting elements pointed at the target.

The most popular transmission system concept currently pursued by both NASA and CRC involves the use of several thousand individual transmitting modules powered by standard microwave oven magnetrons. The appeal of this concept exists because of the availability and low cost of oven magnetrons, and the reliability provided by a modular system. A failed transmitting module would degrade system performance only slightly and would be easily replaceable, as discussed in Reference 3.

For tracking purposes, the high altitude aircraft emits an omni-directional microwave beacon with a different frequency from the transmitting array. Interferometers on the ground detect phase changes in the signal received from the beacon. Using data from the inter-ferometers, the ground transmitting array can be pointed electronic-ally by altering the phase of each transmitting module. The system

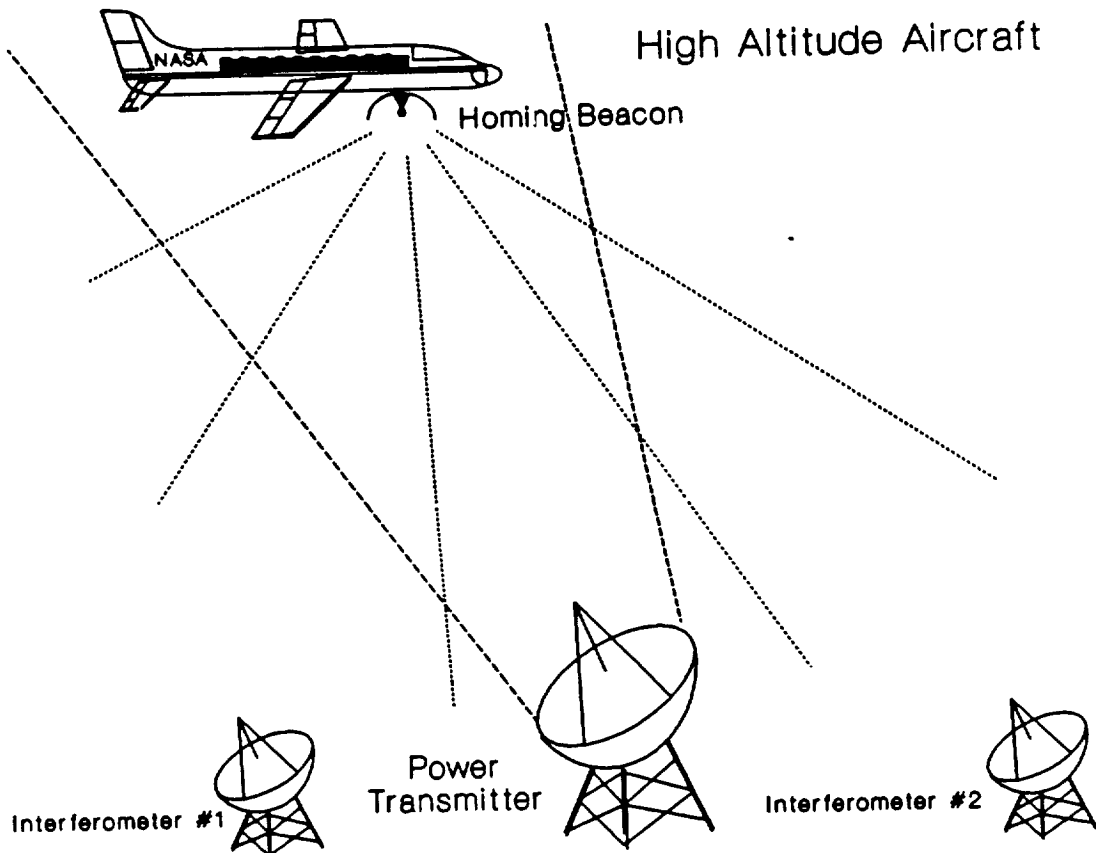


Figure 10.1 Beacon Based Tracking System

depicted in Figure 10.1 does not utilize an array, but rather one main trans-mitting antenna.

The tracking systems shown above constitutes only one of several possible tracking system methods. Another possible method employs sensing devices on the aircraft. This system is shown in Figure 10.2 on the following page. These sensors detect the power received at various points on the aircraft. Differences in received power levels are used to develop signals which indicate the status of the system, whether the microwave beam is centered on the aircraft. A

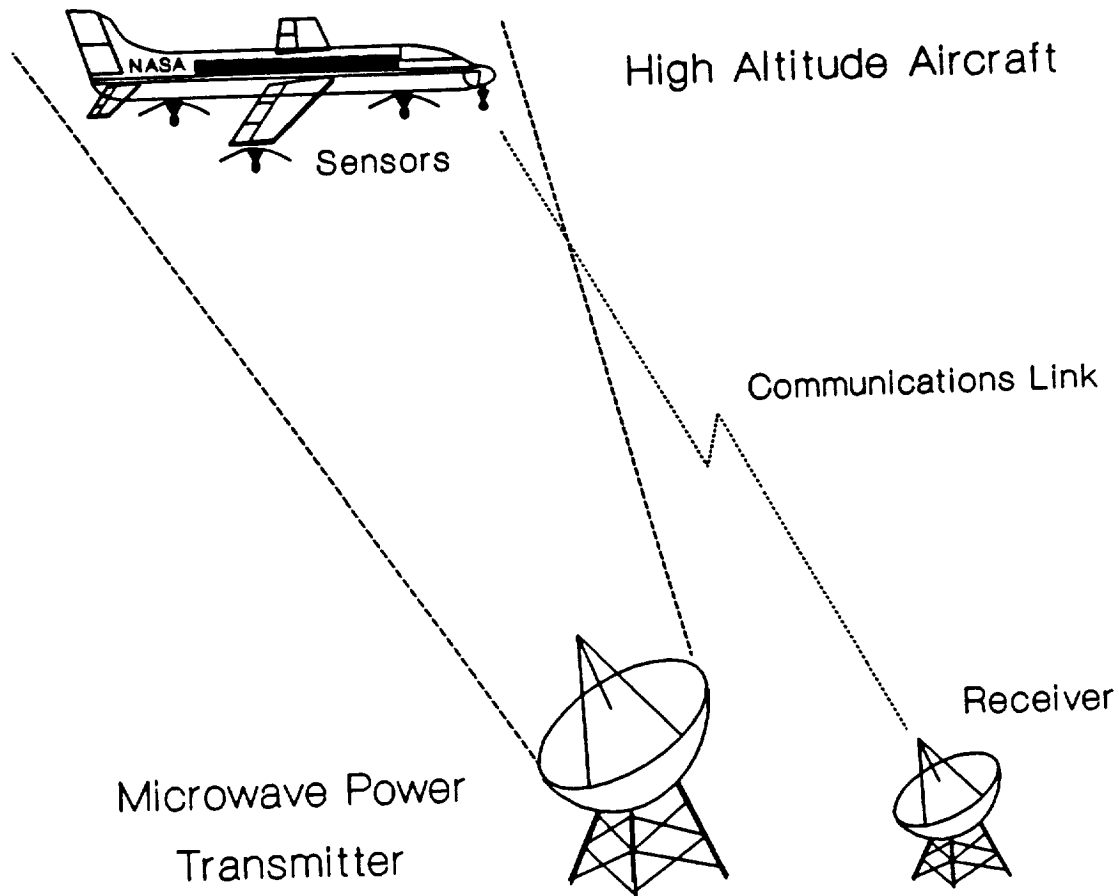


Figure 10.2 Sensor Based Tracking System

simulation of this tracking system constitutes the subject of this Major Qualifying Project.

10.5 Tracking System Model

The Tracking System Model developed in this MQP is shown in Figure 10.3 on the following page. This Model consists of several major sub-systems. The first of these is the light source which is physically mounted to a servo-

motor apparatus. The light and the motor simulate a steerable microwave beam. The Drive Circuitry block consists of amplifiers that provide the signals that control the movement of the motor. The Sensor block is made up of two sets of phototransistors mounted on a moveable model aircraft and their associated circuitry. The outputs of this stage

represent the position of the light relative to the position of the sensors.

The sensor outputs are

sent to the Signal

Processing stage where sum and difference signals are developed and sent to the next stage. These signals provide positional information regarding the airplane model with respect to the direction of the light beam.

The Radio Transmitter is a 49 megahertz transmitter that sends the sum and difference information to the Radio

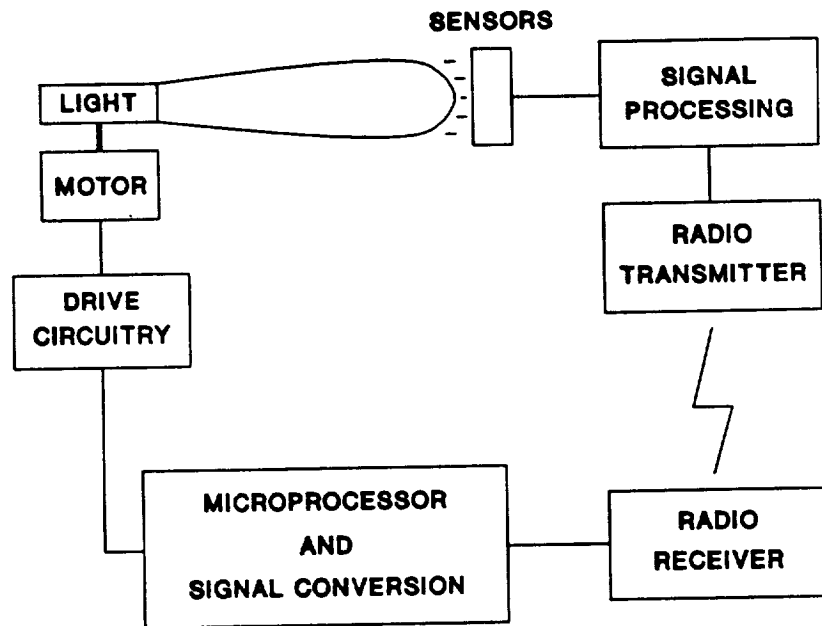


Figure 10.3 Model Block Diagram

Receiver. The Sensors, Signal Processing and Radio Transmitter blocks comprise the Aircraft Model.

The signal sent by the Radio Transmitter is demodulated by the Radio Receiver which reconstructs the sum and difference signals for use in the Microprocessor and Signal Conversion stage.

The Microprocessor block is comprised of an 8085A eight-bit microprocessor with various supporting peripherals. The Signal Conversion is performed by Analog to Digital (A/D) and Digital to Analog (D/A) converters. Control signals are then sent to the Drive Circuitry of the Motor, which completes the feedback control system.

Upon completion of the design and construction of the Tracking System Model it is thoroughly tested and a controls analysis is completed. The testing is carried out by monitoring the response of the motor as the Aircraft Model is physically moved at different speeds and at varying distances from the light source.

10.6 Summary of the Tracking System Model

The design of the tracking system simulator proved to be a challenging task requiring fundamental knowledge of several aspects of electrical engineering. Elements of electronic circuit design, computer hardware design, and signal processing are incorporated in the Tracking System Model.

An analysis of the Tracking System Model using classical control theory reveals that several parameters exist which affect the stability and response time of the system. These parameters are optimized then varied to monitor the effects each one has on the system. Although the model contains several nonlinear aspects, as does every real system, a particularly interesting nonlinearity was found in the model's radio link. This nonlinearity exactly matches the characteristics of an ideal relay with dead zone, which converts a continuous input signal into a three level output signal.

The operation of the Tracking System Model involves two modes of operation. In one of these modes, the light follows or tracks the motions of the model airplane. In the second, it performs a search pattern when the light loses contact with the sensors. These modes of operation are directly controlled by the microprocessor and can be altered by changing the programming of the microprocessor. The use of programmable memory chips makes this possible. Several different programs, each of which modifies the performance of the microprocessor in some way, are developed and implemented for both the track and search modes.

Following design and testing, the operation and performance of the model are related to the real world situation. It is found that, although the Tracking System Model operates on a much simpler scale than an actual system

would, for each obstacle to achieving reliable operation encountered in the design of the model, there would be an analogous obstacle in the real system which would have to be dealt with accordingly. Therefore, the Tracking System Model provides meaningful the actual design requirements.

11.0 Environmental Impact

The environmental effects of operating this aircraft are uncertain. There is, however, evidence of potential harm to humans from microwave ovens which use the same magnetron as the microwave power station. Several areas of potential concern need to be studied in detail. The impact could take the form of possible heating of the surrounding air, the emission of microwave radiation, and the pollution or radioactive waste associated with the electric power generation.

Some energy transmitted from the ground would end up being wasted by heating the surrounding air. There is an approximate 20% loss of all energy beamed from the transmitter (Reference 6) due to atmospheric attenuation. The exact long-term effects are uncertain, but local wildlife and human inhabitants would certainly be affected by changes in the climate.

The radiation emitted from the antenna is an obvious source of environmental concern. Any living creature that might fly through the beam, whether birds or commercial aircraft may be exposed to dangerous levels of microwave radiation. There would probably be considerable danger to any people or animals living in the vicinity of the transmission source on the ground.

Finally, there might be substantial pollution or radioactive waste associated with any power generator built for this project. While there are many existing power sources capable of the necessary electrical

output, the waste produced from the energy used would still be attributable to the aircraft. The lighting of a 120 Watt bulb for a year produces almost 900 pounds of waste products. The waste generated by this aircraft would dwarf this number.

12.0 Cost Analysis

The cost of building and operating this airplane would be tremendous. Cost of production would fall into two categories: building the power source and transmitter, and constructing the plane itself.

The power source would be required to produce approximately three megawatts of electricity. Assuming a small nuclear reactor is the chosen method of providing the power, the cost would conservatively be on the order of several hundred million dollars. The transmitter for the microwave energy would have to be the size of a football field (assuming a wavelength of 2.45 GHz), and would have to be able to be moved on two axes of rotation. Such a transmitter would cost between 30 - 50 million dollars.

The aircraft itself would have to be constructed almost entirely of composite materials which are quite expensive. Additionally, the reflecting surface and outer skin of the rectenna, and its supporting structure, would add substantially to the cost of building the plane especially if gallium-arsenide is used to increase efficiency (Reference 6). An estimate of the total airframe cost, calculated in Appendix A.10, is approximately \$40,237,700 (1990 dollars).

Additional long-term operating costs would center on the cost of continually producing the energy required for the aircraft to perform its mission.

13.0 Conclusion

This study has involved the preliminary design of a microwave-powered, ozone-sampling aircraft for operation at altitudes to 100,000 feet. A first iteration of the design has been completed, and indicates that it may not presently be technically feasible to accomplish this mission.

The aircraft has a gross weight of 6720 lbs. and is designed to carry a 1000 lb payload to an altitude of 100,000 feet at Mach number $M=0.44$. The wing planform area of 3634 ft² serves as a rectifying antenna designed to convert microwave energy to direct current at a power density of 700 W/m². The overall power required for the aircraft at the design altitude is approximately 250 hp., while the transmitted power at the ground ranges from 15 to 30 MW, depending on the transmitter area. The aircraft utilizes both a horizontal tail and canard for longitudinal stability and to enhance the structural rigidity of the twin fuselage configuration.

The wing structure is designed to withstand a gust-induced load factor $n=3$ at the cruise altitude, but the low wing loading of the aircraft makes it very sensitive to gusts at low altitudes. The wing structure was analyzed using a finite-element computational method and was found to be adequate at cruise altitude although further detailed structural design is required. Due to the low wing loading, the aircraft structure cannot withstand gusts of anticipated intensity at altitudes

under 60,000 feet, which may induce load factors in excess of $n=20$. A gust alleviation system would have sensors monitoring local wind gusts and automatically correct for these by making adjustments to the control surfaces. The design of this system has not been conducted as part of the present project.

The overall vehicle design has been accomplished using the first iteration weight and sizing estimates. However, a second weight iteration indicates an increase in gross weight, from 6720 lbs. to 15,000 lbs, and an associated increase in the power required to sustain flight. Subsequent iterations are divergent because the power available is a function of the wing area, which increases rapidly as the weight increases. This problem is unique to a microwave powered design. It appears that if the power density of 700 W/m^2 absorbed by the rectenna is increased, it would be possible to converge upon an acceptable design point.

A beam tracking system has been developed and would be capable of tracking the aircraft with sufficient accuracy to deliver the required power. However, the low wing loading inherent in the design may produce unpredictable perturbations in the flight path which may

cause difficulty in tracking.

Atmospheric absorption of the microwave radiation is on the order of 20% of the transmitted power, or 4 MW. This localized heating of the air could pose a threat to wildlife and humans in the vicinity of the transmitter. A thorough environmental study should be conducted.

This study found the cost of the airframe to be approximately \$40 million. This value reflects tooling, man hours, and materials. The cost of the transmitter and tracking system would be 30 - 50 million dollars. These expenses would be excessive for the limited scope of the proposed mission .

14.0 Bibliography

- [1] Abbott, Ira and VonDoenhoff A., Theory of Wing Sections. Dover, 1959
- [2] Boeing Advanced Systems, "Feasibility Study of a Very High Altitude Aircraft for Stratospheric Research".
- [3] Brown, William. "A Profile of Power Transmission by Microwaves," Aeronautics and Astronautics, 1979.
- [4] Brown, William, "Design Study for a Ground Microwave Power Transmission System for Use with a High Altitude Powered Platform," Raytheon Company Report PT-6052, 1982.
- [5] Brown, William, "The History of Power Transmission by Radio Waves," IEEE, 1984.
- [6] Brown, William. A Microwave Powered, Long Duration, High Altitude Platform. Baltimore, Maryland: International Microwave Symposium, 1986.
- [7] California Polytechnic Institute, NASA/USRA Project Report
- [8] Caughey, D.A., "FLO - 30M Multi-Grid/SLOR Transonic Wing-Fuselage Program". NASA Lewis Research Center.
- [9] Christian, J. "Possibilities of Ultra-Lightweight Airborne Vehicles Utilizing Millimeter Beam Power Technology."
- [10] Drela, Mark. Low-Reynolds-Number Airfoil Design for the M.I.T. Daedalus Prototype: A Case Study. Cambridge: Massachusetts Institute of Technology, 1988.
- [11] Dudley, D.W. Handbook of Practical Gear Design. New York: Mc Graw Hill, 1984.
- [12] Eppler, Richard and Somers, Dan M. Airfoil Design for Reynolds Numbers Between 50,000 and 500,000. Hampton, Virginia: NASA Langley Research Center.
- [13] Garelick, Melvin S. "DESIGN.FOR Thin Airfoil Design Code.", unpublished, 1989.
- [14] Garelick, Melvin S. "CPDIST.FOR Inviscid Incompressible Airfoil Analysis Code.", unpublished, 1990.
- [15] Garelick, Melvin S. "CPINVR.FOR Thick Airfoil Inverse Code.", unpublished, 1989.
- [16] Heyson, Harry. "Initial Feasibility Study of a

Microwave-Powered Sailplane as a High-Altitude
Observation Platform."

- [17]Holden, J.T. On the Finite Deflections of Thin Beams.
London: Pergamon Press, 1972.
- [18]Kuethe, Arnold and Chow, Chuen-Yen, Foundations of
Aerodynamics. New York: John Wiley & Sons, 1986.
- [19]Liebeck, R. and Camacho, P. Airfoil Design at Low
Reynolds Number with Constrained Pitching
Moment. Long Beach, California: Douglas Aircraft
Company.
- [20]Mead, H.R. and Melnick, R.E. "GRUMFOIL: A Computer
Code for the Viscous Transonic Flow Over Airfoils.
Grumman Aerospace Corp. Bethpage, NY, 1985.
- [21]McCormick, Barnes W., Aerodynamics, Aeronautics and
Fluid Mechanics. New York: John Wiley and Sons,
1979.
- [22]Morris, Charles E.K. Jr. "Design Study for Remotely
Piloted, High-Altitude Airplanes Powered by
Microwave Energy." New York: AIAA, 1983.
- [23]Nelson, Robert C. Flight Stability and Automatic
Control. New York: McGraw Hill, 1989.
- [24]Nicolai, L.M., Fundamentals of Aircraft Design,
San Jose: METS, 1984.
- [25]Pfenninger, W. and Vemuru, C. S. Design of Low
Reynolds Number Airfoils. Hampton, Virginia:
Analytical Services & Materials Inc.
- [26]Reifsnider, K. L., ed. Fatigue of Filamentary
Composite Materials. Philadelphia: American
Society for Testing and Materials, 1977.
- [27]Roskam, Jan. Airplane Design. Ottawa: Roskam Aviation
and Engineering Corporation, 1985.
- [28]Salkind, Michael J., ed. Applications of Composite
Materials. Philadelphia: American Society for
Testing Materials, 1973.
- [29]Schlesak, J.J. and Alden, Adrian and Ohno, Tom. "A
Microwave Powered High-Altitude Platform." Ottawa:
Communication Research Center, 1988.
- [30]Simon, W. E., Ely, W.L., Niedling, L. G., and Voda,
J.J., "Prediction of Aircraft Drag Due to Lift,"
AF Flight Dynamics Lab, AFFDL-TR-71-84, Wright
Patterson AFB, Ohio, 1971.

15.0 Figures

List of Figures

- 2.1 Mission Profile Diagram
- 3.1 Rectenna Location
- 3.2 Microwave Transmission Efficiency
- 3.3 Airborne Transmitter Configuration
- 3.4 Multi-Station Ground Transmitter Configuration
- 3.5 Single-Station Ground Transmitter Configuration
- 4.1 Wing Loading vs. Mach Number
- 4.2 Gross Weight vs. Mach Number
- 4.3 Wing Area vs. Mach Number
- 4.4 External Rectenna Area vs. Mach Number
- 4.5 Power Available vs. Mach Number
- 4.6 Wing Span vs. Mach Number
- 4.7 L/D Ratio vs. Mach Number
- 4.8 First Iteration Component Weights
- 4.9 Aircraft Design Concept #1
- 4.10 Aircraft Design Concept #2
- 4.11 Aircraft Design Concept #3
- 4.12 Landing Gear Configuration
- 4.13 Final Design Configuration
- 4.14 Planform Parameters
- 4.15 Planform Geometry
- 4.16 Second Iteration Aspect Ratios and Thicknesses
- 4.17 Second Iteration Component Weights
- 5.1.1 Transition Bubble
- 5.1.2 Sample Pressure Distribution
- 5.1.3 Span Loading
- 5.1.4 L, P & Q Target Pressure Distributions
- 5.1.5 P-Series Pressure Distribution (Designed Airfoil)
- 5.1.6 L-Series Pressure Distribution (Designed Airfoil)
- 5.1.7 Q-Series Pressure Distribution (Designed Airfoil)
- 5.1.8 L1, L2 & L3 Targets
- 5.1.9 L1 Inviscid Pressure Distribution & Geometry
- 5.1.10 L2 Inviscid Pressure Distribution & Geometry
- 5.1.11 L3 Inviscid Pressure Distribution & Geometry
- 5.1.12 L-Series c_l & c_m vs. α (Inviscid Analysis)
- 5.1.13 L-series c_l vs. α (Viscid & Compressible Analysis)
- 5.1.14 Trailing Closure
- 5.1.15 L1 Compressible & Target Pressure Distribution
- 5.1.16 L2 Compressible & Target Pressure Distribution
- 5.1.17 L3 Compressible & Target Pressure Distribution
- 5.1.18 L-Series Drag Polar
- 5.1.19 L1 vs. NACA 4415 Drag Comparison
- 5.1.20 L2 vs. NACA 4412 Drag Comparison
- 5.1.21 L3 vs. NACA 4409 Drag Comparison
- 5.1.22 L1 vs. NACA 4415 Lift Comparison
- 5.1.23 L2 vs. NACA 4412 Lift Comparison
- 5.1.24 L3 vs. NACA 4409 Lift Comparison
- 5.2.1 c_l vs. $\% \text{ Span}$
- 5.2.2 Airfoil Lift Curve Equations
- 5.2.3 Variation of Lift Curve Slope
- 5.2.4 Variation of Zero Lift Angle of Attack
- 5.2.5 Twist Distribution

- 5.2.6 First Twist Approximation
- 5.2.7 Final Twist Approximation
- 5.2.8 Main Wing Twist and Location
- 5.2.9 Main Wing Side View
- 5.2.10 C_L vs. α
- 5.2.11 Comparison of c_l vs. Span
- 5.2.12 Wing Loading vs. % Span Comparison
- 5.2.13 Untwisted Wing Pressure Distribution $\alpha = -1.0^\circ$
- 5.2.14 Untwisted Wing Pressure Distribution $\alpha = 0.375^\circ$
- 5.2.15 Untwisted Wing Pressure Distribution $\alpha = 2.0^\circ$
- 5.2.16 Untwisted Wing Pressure Distribution $\alpha = 5.0^\circ$
- 5.2.17 Twisted Wing Pressure Distribution $\alpha = -1.0^\circ$
- 5.2.18 Twisted Wing Pressure Distribution $\alpha = 0.2^\circ$
- 5.2.19 Twisted Wing Pressure Distribution $\alpha = 2.0^\circ$
- 5.2.20 Twisted Wing Pressure Distribution $\alpha = 5.0^\circ$
- 5.2.21 C_L vs. C_D
- 5.2.22 C_L vs. Lift-to-Drag Ratio
- 6.1.1 Spanwise & Chordwise Pressure Distribution
- 6.1.2 Average Chordwise Pressure Distribution
- 6.1.3 Model #1 Deflection (isometric view)
- 6.1.4 Model #1 Deflection (side view)
- 6.1.5 Model #1 Shear Stress Plot (bottom view)
- 6.1.6 Model #1 Shear Stress Plot (right I beam)
- 6.1.7 Model #1 Shear Stress Plot (left I beam)
- 6.1.8 Model #1 Shear Stress Plot (top view)
- 6.1.9 Model #1 Principle Stress (bottom view)
- 6.1.10 Model #1 Principle Stress (left I beam)
- 6.1.11 Model #1 Principle Stress (right I beam)
- 6.1.12 Model #1 Principle Stress (top view)
- 6.1.13 I-Beam Properties
- 6.1.14 Front I Beam Properties
- 6.1.15 Middle I Beam Properties
- 6.1.16 Rear I Beam Properties
- 6.1.17 Model #2 Deflection Plot Pressure & Gravity (side view)
- 6.1.18 Model #2 Shear Stress Plot Pressure & Gravity (top view)
- 6.1.19 Model #2 Shear Stress Plot II Pressure & Gravity (top view)
- 6.1.20 Model #2 Shear Stress Plot Pressure & Gravity (bottom view)
- 6.1.21 Model #2 Prin. Stress with Press. & Gravity (top view)
- 6.1.22 Model #2 Prin. Stress with Press. & Gravity (bot. view)
- 6.1.23 Model #2 Prin. Stress with Press. & Gravity (left I beam)
- 6.1.24 Model #2 Prin. Stress with Press. & Gravity (middle I beam)
- 6.1.25 Model #2 Prin. Stress with Press. & Gravity (right I beam)
- 6.1.26 Model #2 Deflection Plot with Brace (side view)
- 6.1.27 Model #2 Shear Stress Plot with Brace (top view)
- 6.1.28 Model #2 Shear Stress Plot with Brace (bottom view)
- 6.1.29 Model #2 Prin. Stress with Brace (top view)
- 6.1.30 Model #2 Prin. Stress with Brace (left I beam)
- 6.1.31 Model #2 Prin. Stress with Brace (middle I beam)
- 6.1.32 Model #2 Prin. Stress with Brace (right I beam)
- 6.1.33 Model #2 Prin. Stress with Brace (bottom view)
- 6.1.34 Pressure & Force Calculations
- 6.1.35 Model #3 Deflection Plot of Half Model (isometric view)
- 6.1.36 Model #3 Deflection Plot of Half Model (side view)
- 6.1.37 Model #3 Shear Stress Plot of Half Model (top view)
- 6.1.38 Model #3 Shear Stress Plot of Half Model (bottom view)

- 6.1.39 Model #3 Prin. Stress of Half Model (top of tail & canard)
- 6.1.40 Model #3 Prin. Stress of Half Model (top view of wing)
- 6.1.41 Model #3 Prin. Stress of Half Model (right I beams)
- 6.1.42 Model #3 Prin. Stress of Half Model (left I beams)
- 6.2.1 Eigenvalue table for preliminary design.
- 6.2.2 1st Mode for Preliminary Design (isometric view)
- 6.2.3 1st Mode for Preliminary Design (front view)
- 6.2.4 1st Mode for Preliminary Design (top view)
- 6.2.5 2nd Mode for Preliminary Design (isometric view)
- 6.2.6 2nd Mode for Preliminary Design (front view)
- 6.2.7 2nd Mode for Preliminary Design (top view)
- 6.2.8 3rd Mode for Preliminary Design (isometric view)
- 6.2.9 3rd Mode for Preliminary Design (front view)
- 6.2.10 3rd Mode for Preliminary Design (top view)
- 6.2.11 4th Mode for Preliminary Design (isometric view)
- 6.2.12 4th Mode for Preliminary Design (front view)
- 6.2.13 4th Mode for Preliminary Design (top view)
- 6.2.14 5th Mode for Preliminary Design (isometric view)
- 6.2.15 5th Mode for Preliminary Design (front view)
- 6.2.16 5th Mode for Preliminary Design (top view)
- 6.2.17 Eigenvalue table for revised design.
- 6.2.18 1st Mode for Revised Design (isometric view)
- 6.2.19 1st Mode for Revised Design (front view)
- 6.2.20 1st Mode for Revised Design (top view)
- 6.2.21 2nd Mode for Revised Design (isometric view)
- 6.2.22 2nd Mode for Revised Design (front view)
- 6.2.23 2nd Mode for Revised Design (top view)
- 6.2.24 3rd Mode for Revised Design (isometric view)
- 6.2.25 3rd Mode for Revised Design (front view)
- 6.2.26 3rd Mode for Revised Design (top view)
- 6.2.27 4th Mode for Revised Design (isometric view)
- 6.2.28 4th Mode for Revised Design (front view)
- 6.2.29 4th Mode for Revised Design (top view)
- 6.2.30 5th Mode for Revised Design (isometric view)
- 6.2.31 5th Mode for Revised Design (front view)
- 6.2.32 5th Mode for Revised Design (top view)
- 6.2.33 Eigenvalue table for revised design w/brace.
- 6.2.34 1st Mode for Design w/Brace (isometric view)
- 6.2.35 1st Mode for Design w/Brace (front view)
- 6.2.36 1st Mode for Design w/Brace (top view)
- 6.2.37 2nd Mode for Design w/Brace (isometric view)
- 6.2.38 2nd Mode for Design w/Brace (front view)
- 6.2.39 2nd Mode for Design w/Brace (top view)
- 6.2.40 3rd Mode for Design w/Brace (isometric view)
- 6.2.41 3rd Mode for Design w/Brace (front view)
- 6.2.42 3rd Mode for Design w/Brace (top view)
- 6.2.43 4th Mode for Design w/Brace (isometric view)
- 6.2.44 4th Mode for Design w/Brace (front view)
- 6.2.45 4th Mode for Design w/Brace (top view)
- 6.2.46 5th Mode for Design w/Brace (isometric view)
- 6.2.47 5th Mode for Design w/Brace (front view)
- 6.2.48 5th Mode for Design w/Brace (top view)
- 7.1.1 C_m vs. α for three arbitrary aircraft
- 7.1.2 Component Contributions to Static Stability
- 7.1.3 Static Stability Analysis Data

- 7.1.4 C_m vs. α ($\delta_c = 0$)
- 7.1.5 C_m vs. α ($\delta_t = 0$)
- 7.1.6 C_m vs. α ($\delta_c = \delta_t$)
- 7.1.7 C_m vs. C_L ($\delta_c = 0$)
- 7.1.8 C_m vs. C_L ($\delta_t = 0$)
- 7.1.9 C_m vs. C_L ($\delta_c = \delta_t$)
- 7.2.1 Response Derivatives
- 7.2.2 Combined Mode Block Diagram
- 7.2.3 Short Period Response at 100,000 feet
- 7.2.4 Long Period Response at 100,000 feet
- 7.2.5 Combined Period Response at 100,000 feet
- 7.2.6 Short Period Response at 25,000 feet
- 7.2.7 Long Period Response at 25,000 feet
- 7.2.8 Combined Period Response at 25,000 feet
- 8.1 Mass Location Diagram
- 8.2 Mass Properties Spreadsheet
- 9.2.1 Net Power Available
- 9.2.2 Power Required
- 9.2.3 Power Available and Required - sea level
- 9.2.4 Power Available and Required - 25,000 feet
- 9.2.5 Power Available and Required - 50,000 feet
- 9.2.6 Power Available and Required - 75,000 feet
- 9.2.7 Power Available and Required - 100,000 feet
- 9.2.8 Angle of Incidence
- 9.2.9 Angle of Incidence - As Flight Radius Increases
- 9.2.10 Angle of Incidence - As Flight Radius Decreases
- 9.2.11 Net Power Available - 25,000 feet
- 9.2.12 Power Required - 25,000 feet
- 9.2.13 Net Power Available - 50,000 feet
- 9.2.14 Power Required - 50,000 feet
- 9.2.15 Net Power Available - 75,000 feet
- 9.2.16 Power Required - 75,000 feet
- 9.2.17 Net Power Available - 100,000 feet
- 9.2.18 Power Required - 100,000 feet
- 9.2.19 Transmitted Power Distribution
- 9.2.20 Parabolic Power Density Distribution
- 9.2.21 Total Transmitted Power Calculation
- 9.3.1 Rate of Climb vs Altitude - wings level flight
- 9.3.2 Rate of Climb vs Mach Number - sea level (level flight)
- 9.3.3 Rate of Climb vs Mach Number - 25,000 feet
- 9.3.4 Rate of Climb vs Mach Number - 50,000 feet
- 9.3.5 Rate of Climb vs Mach Number - 75,000 feet
- 9.3.6 Rate of Climb vs Mach Number - 100,000 feet
- 9.3.7 Time to Climb - wings level flight
- 9.3.8 Time to Climb - turning flight
- 9.4.1 Altitude vs Flight Radius
- 9.4.2 Mach Number vs Altitude
- 9.4.3 Velocity vs Altitude
- 9.4.4 Coefficient of Lift vs Altitude
- 9.4.5 Bank Angle vs Altitude
- 9.4.6 Flight Radius vs Altitude
- 9.4.7 Climb Rate vs Altitude
- 9.4.8 Altitude vs Flight Radius - number of turns
- 9.5.1 Effect of Wind Gust - sea level
- 9.5.2 Effect of Wind Gust - 25,000 feet

- 9.5.3 Effect of Wind Gust - 50,000 feet
- 9.5.4 Effect of Wind Gust - 75,000 feet
- 9.5.5 Effect of Wind Gust - 100,000 feet
- 9.5.6 Load Factor at Maximum and Minimum CL - sea level
- 9.5.7 Load Factor at Maximum and Minimum CL - 25,000 feet
- 9.5.8 Load Factor at Maximum and Minimum CL - 50,000 feet
- 9.5.9 Load Factor at Maximum and Minimum CL - 75,000 feet
- 9.5.10 Load Factor at Maximum and Minimum CL - 100,000 feet
- 9.5.11 Wind Gust Effect (increased load factor range at sea level)
- 9.5.12 Wind Gust Effect (increased load factor range at 25,000 ft)
- 9.5.13 Wind Gust Effect (increased load factor range at 50,000 ft)
- 10.1 Beacon Based Tracking System
- 10.2 Sensor Based Tracking System
- 10.3 Model Block Diagram

Figure 2.1 Flight Path

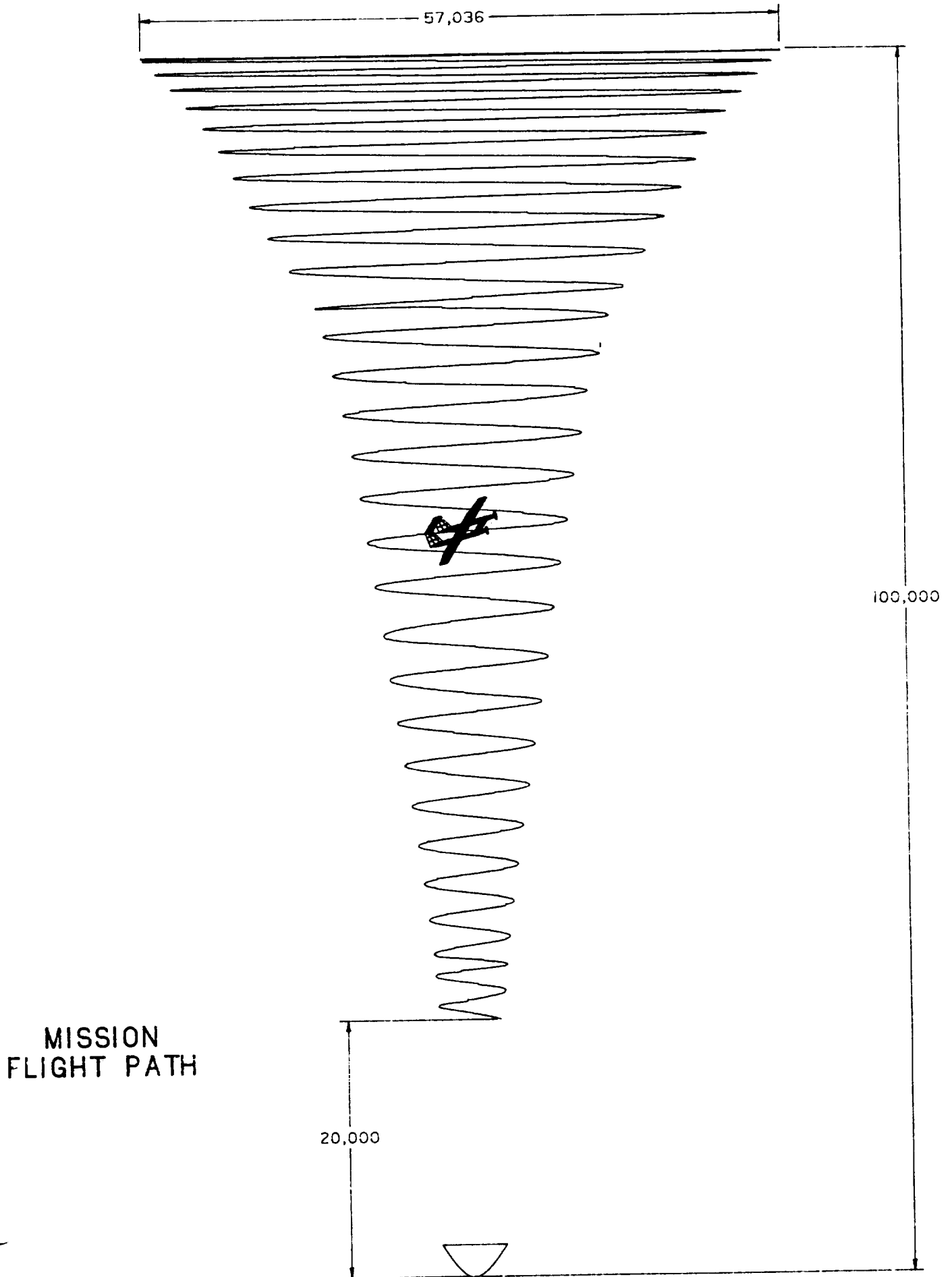
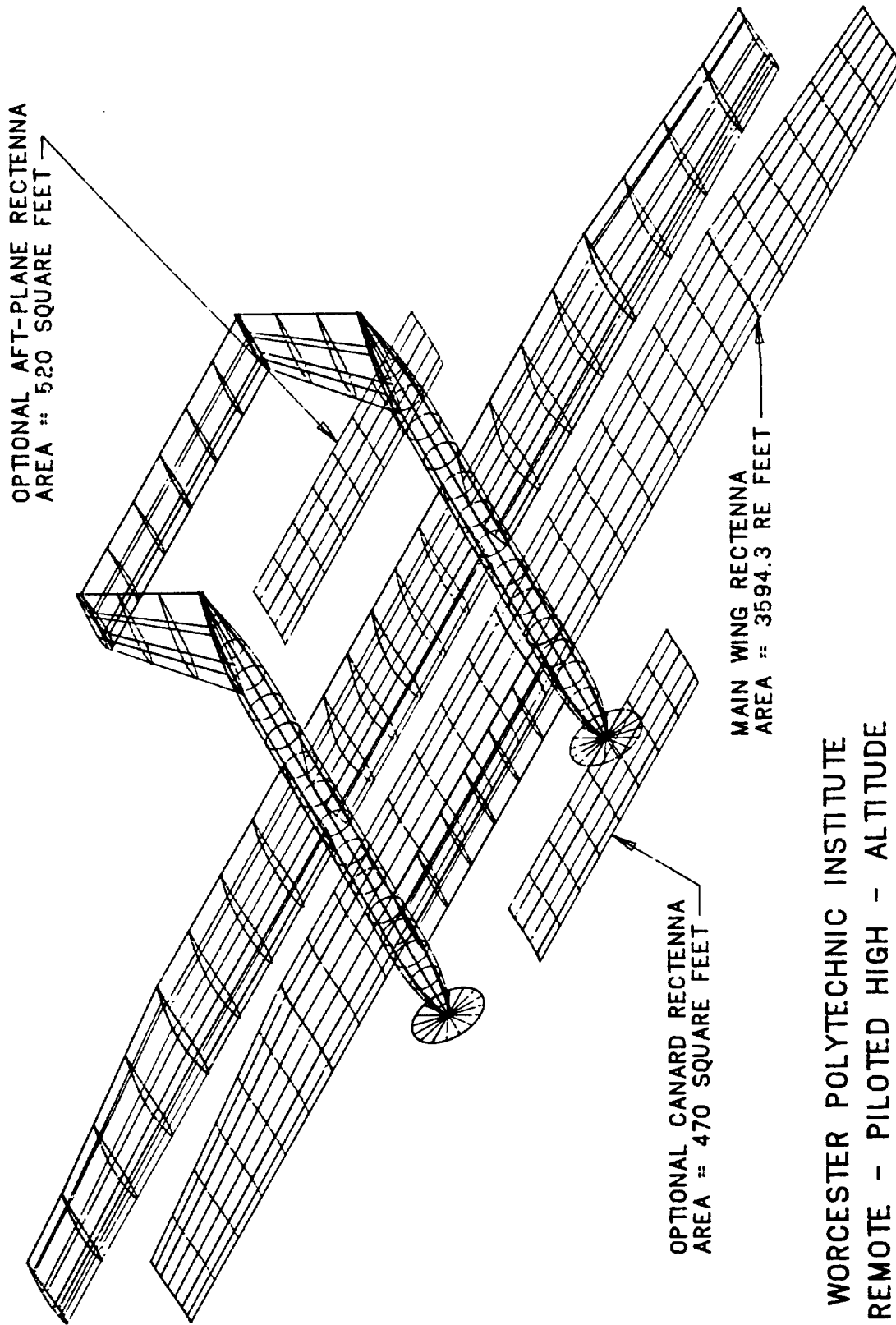


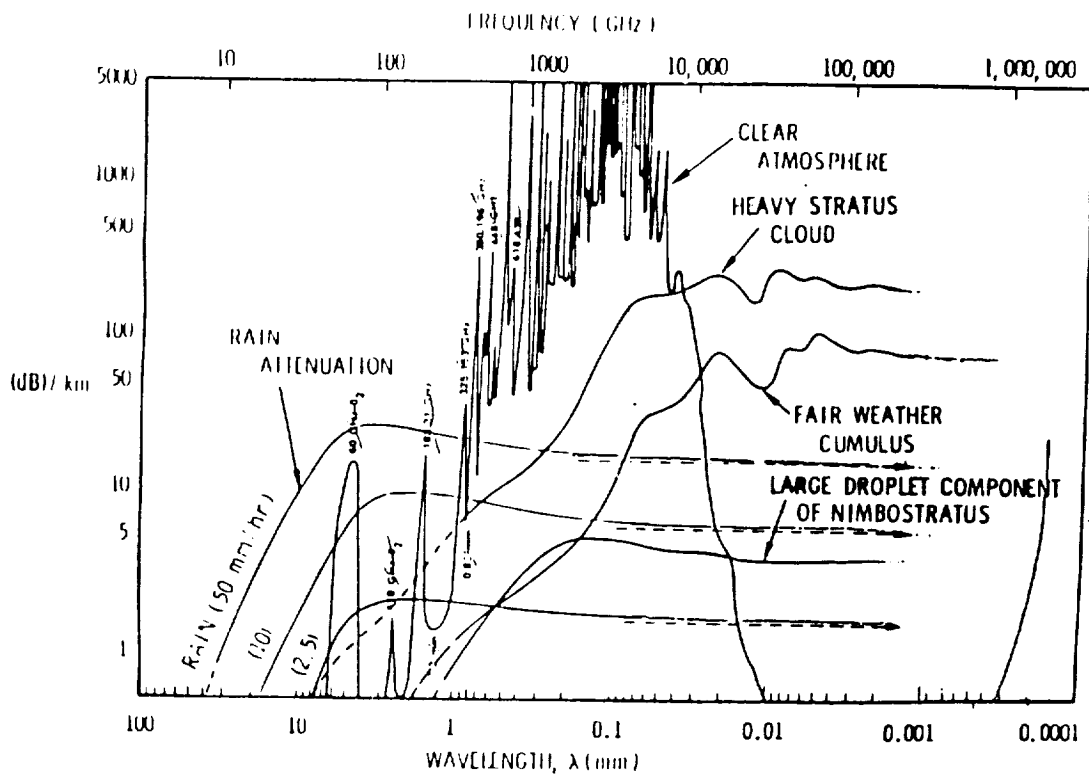
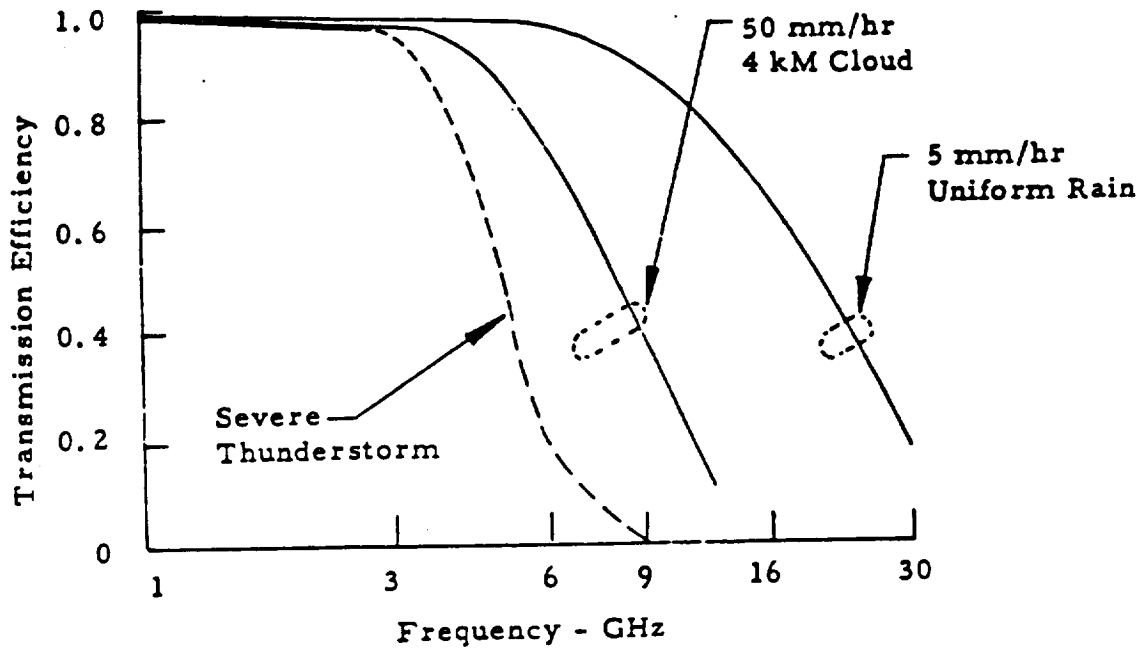
Figure 3.1



WORCESTER POLYTECHNIC INSTITUTE
REMOTE - PILOTED HIGH - ALTITUDE
MICROWAVE - POWERED OZONE SAMPLER AIRCRAFT

WPI CAD LABORATORY	TITLE: FINAL DRAFT - ISO VIEW	NO: 1
SCALE: 004	DATE: 4/29/90	DRAWN BY: TOM JUTRAS
		SHEET: 1

Figure 3.2
Microwave Transmission Efficiency



Summary of sea-level atmospheric attenuation

ORIGINAL PAGE IS
OF POOR QUALITY

Figure 3.3
Airborne Transmitter Configuration

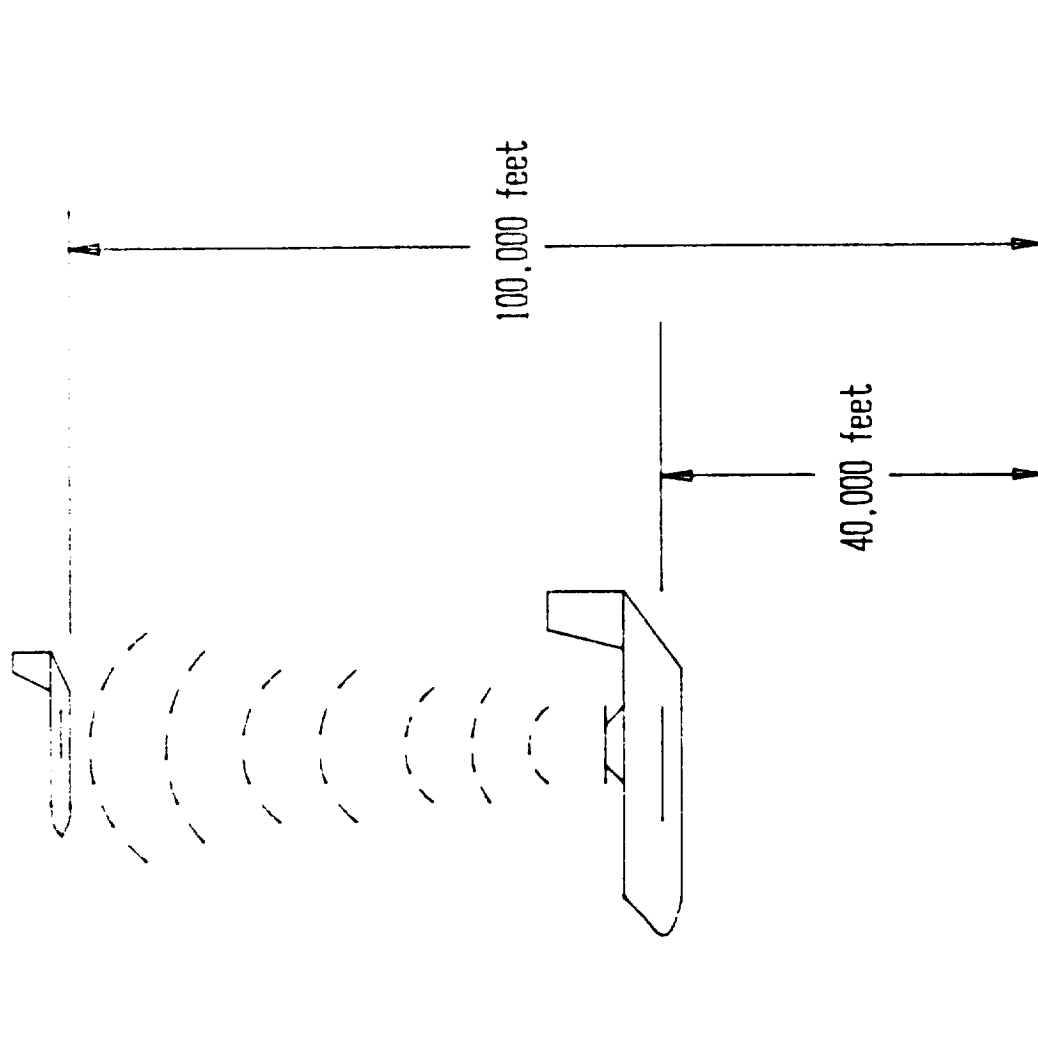


Figure 3.4
Multi-Station Configuration

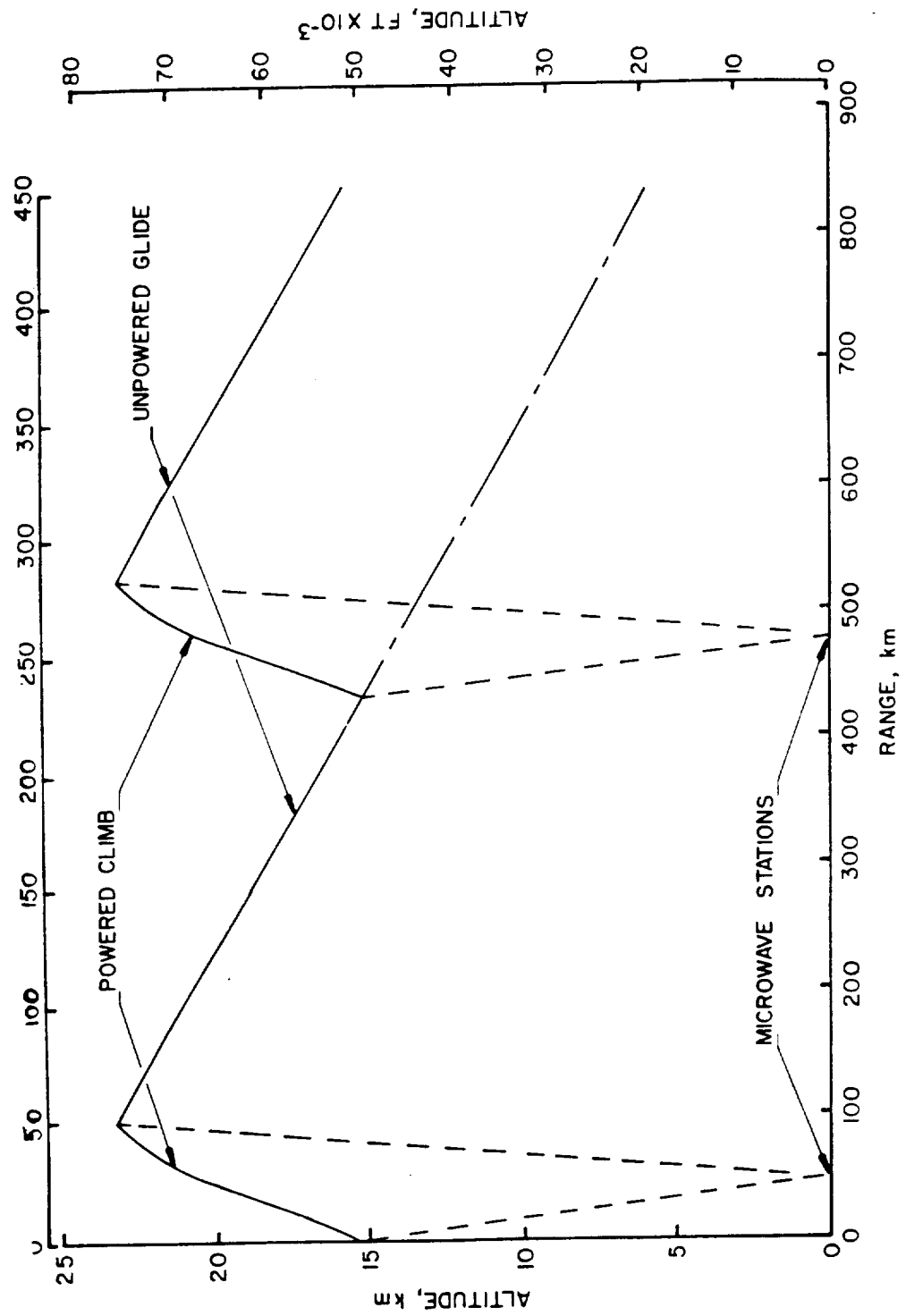
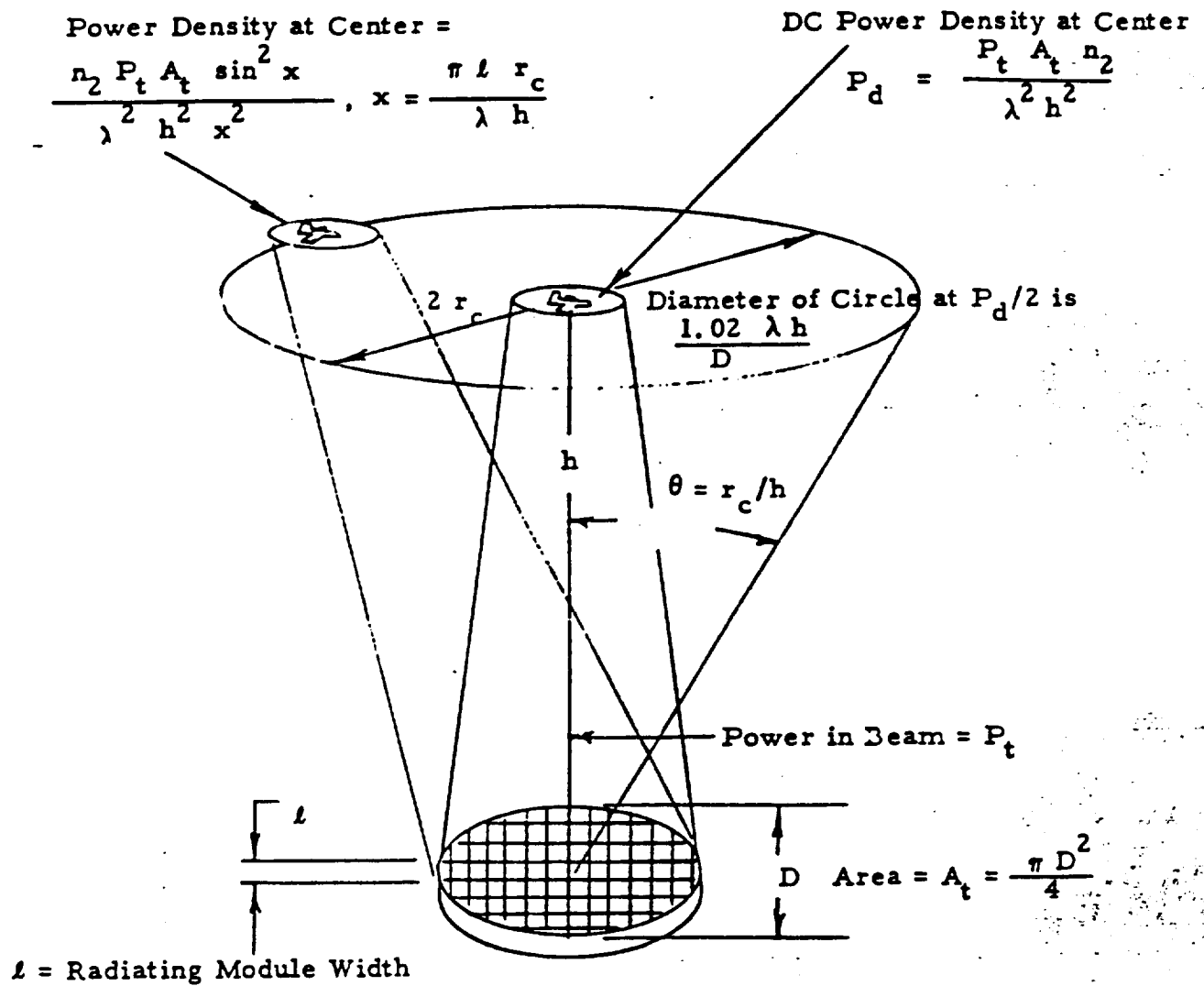


Figure 3.5
Single-Station Configuration



Wing Loading vs. Mach Number

altitude = 100,000 feet

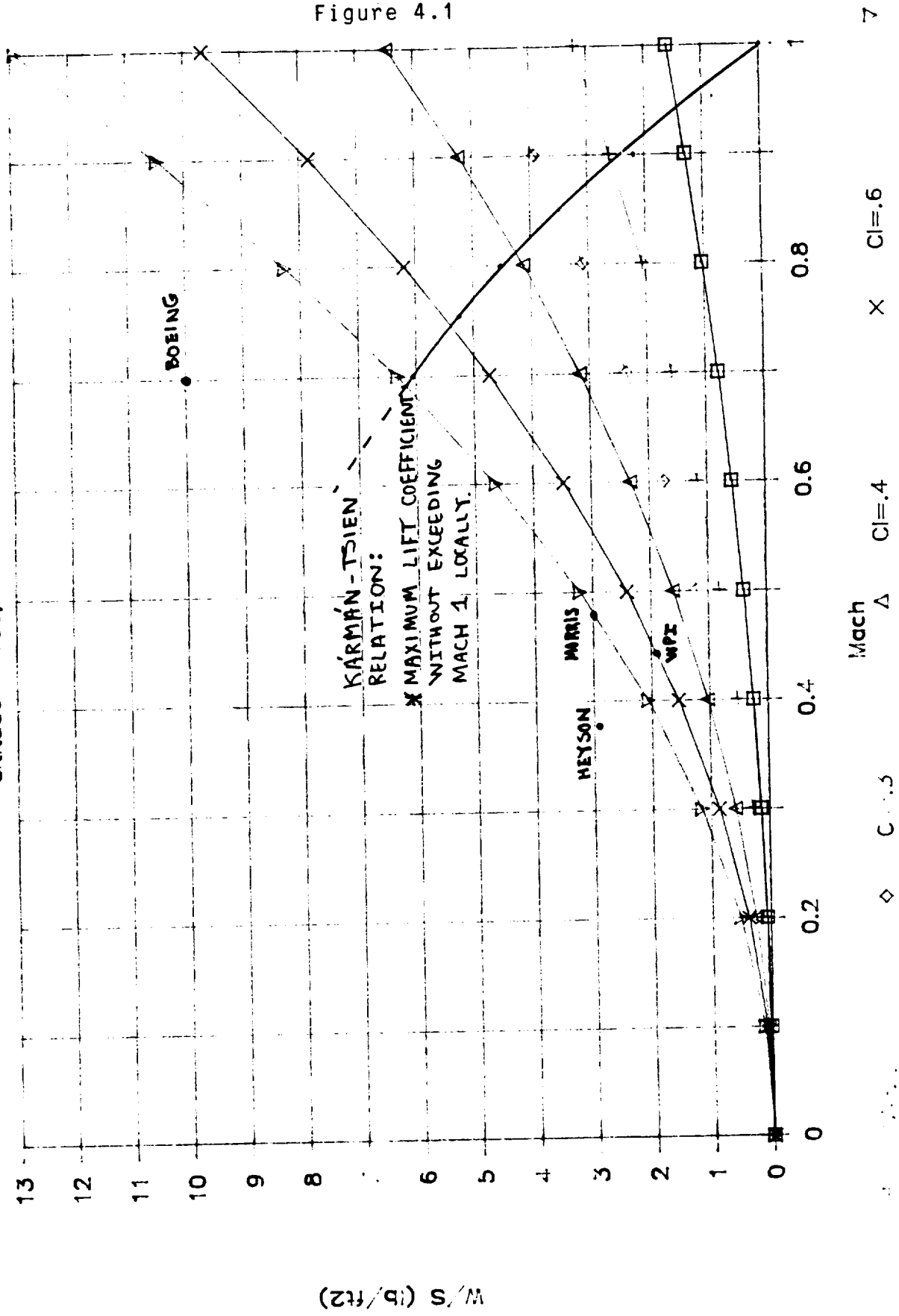
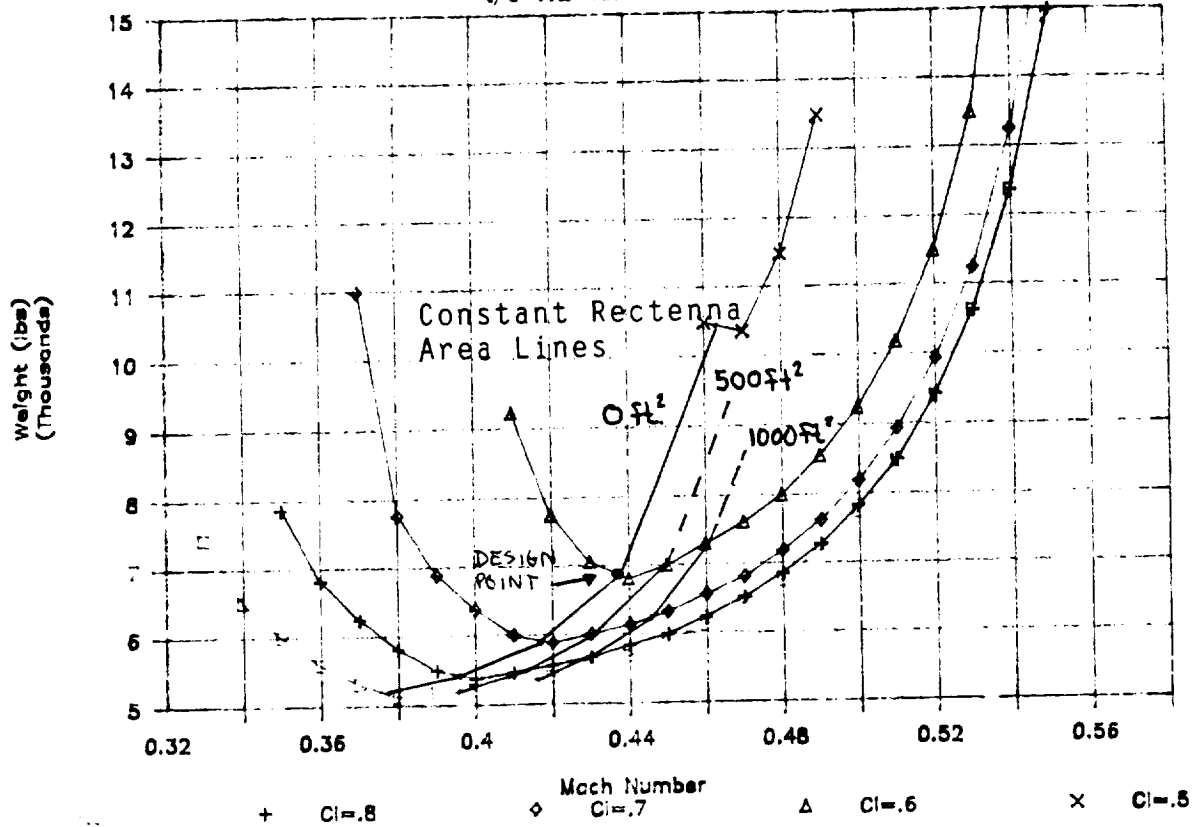


Figure 4.1

Gross Weight Vs. Mach Number

$t/c=.12$ $AR=15$ $Nult=3$

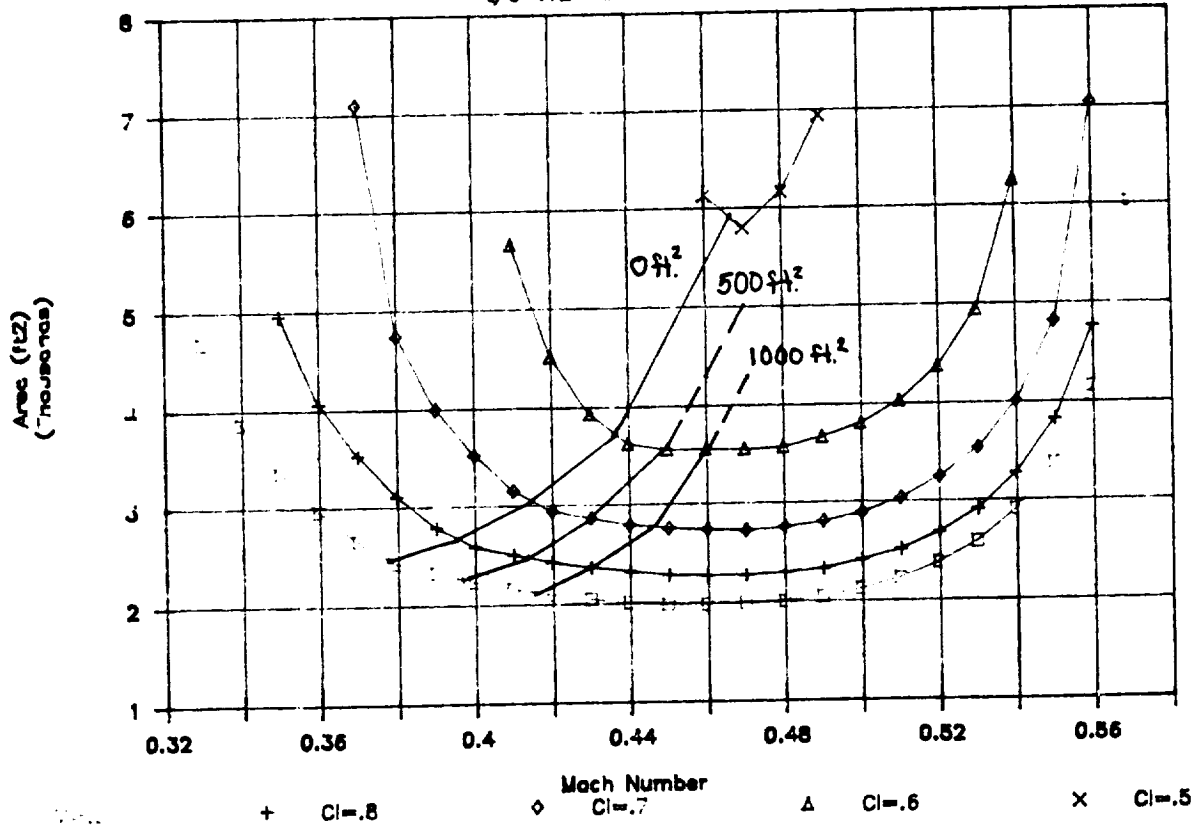
Figure 4.2



Wing Area Vs. Mach Number

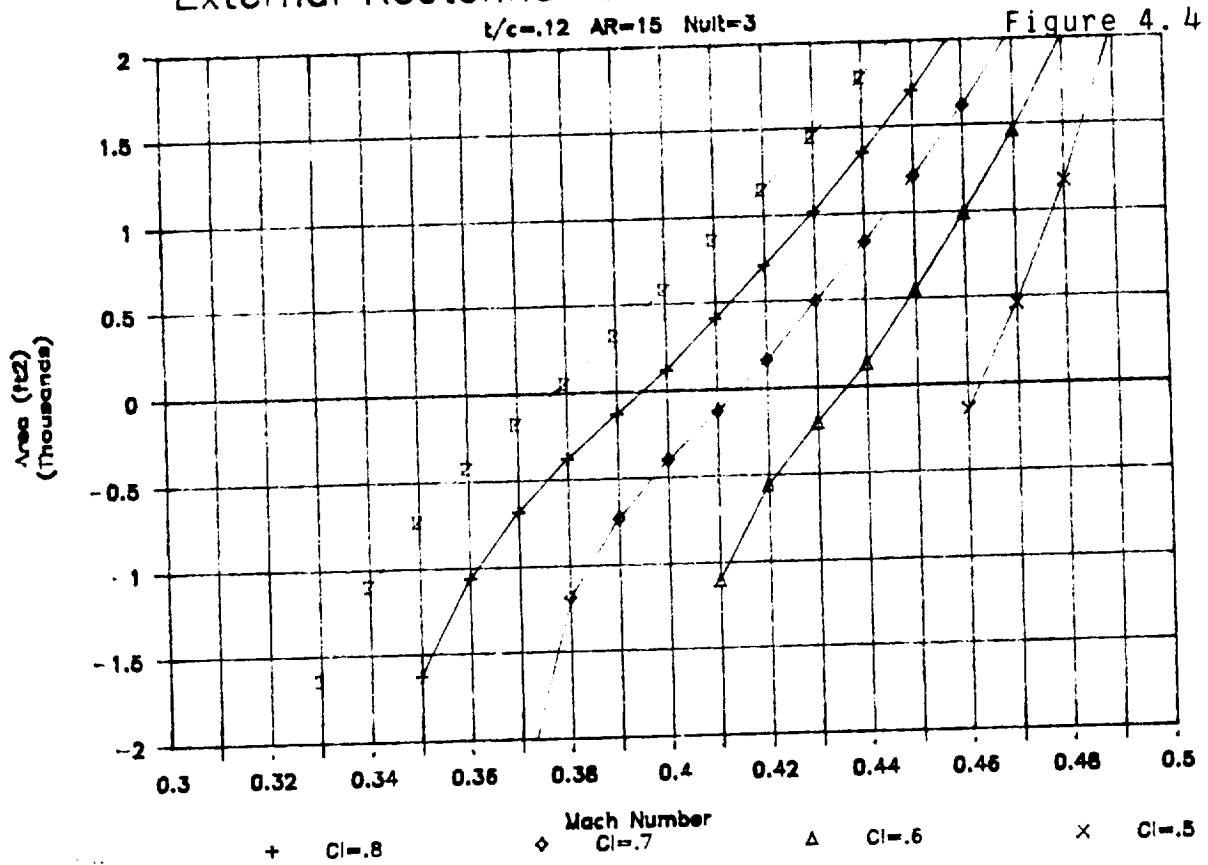
$t/c=.12$ $AR=15$ $Nult=3$

Figure 4.3

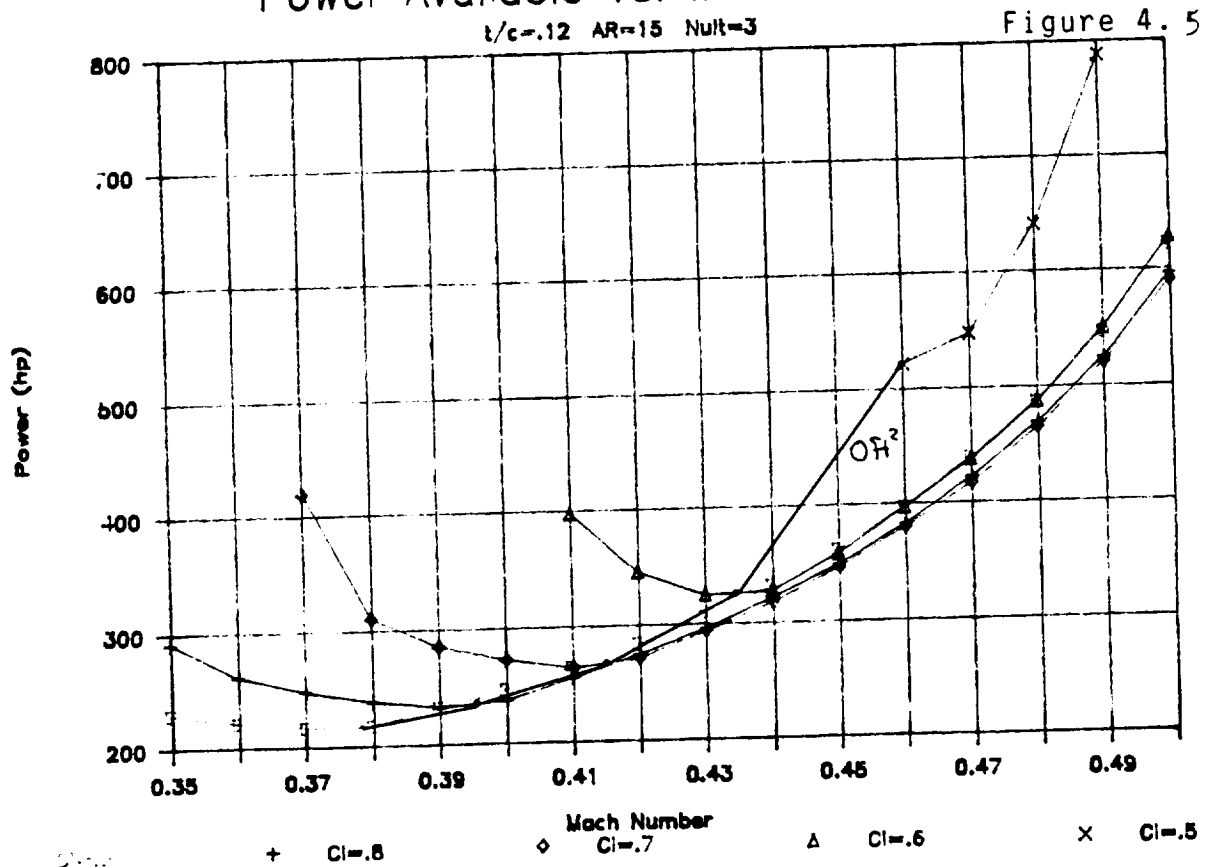


ORIGINAL PAGE IS
OF POOR QUALITY

External Rectenna Area Vs. Mach Number



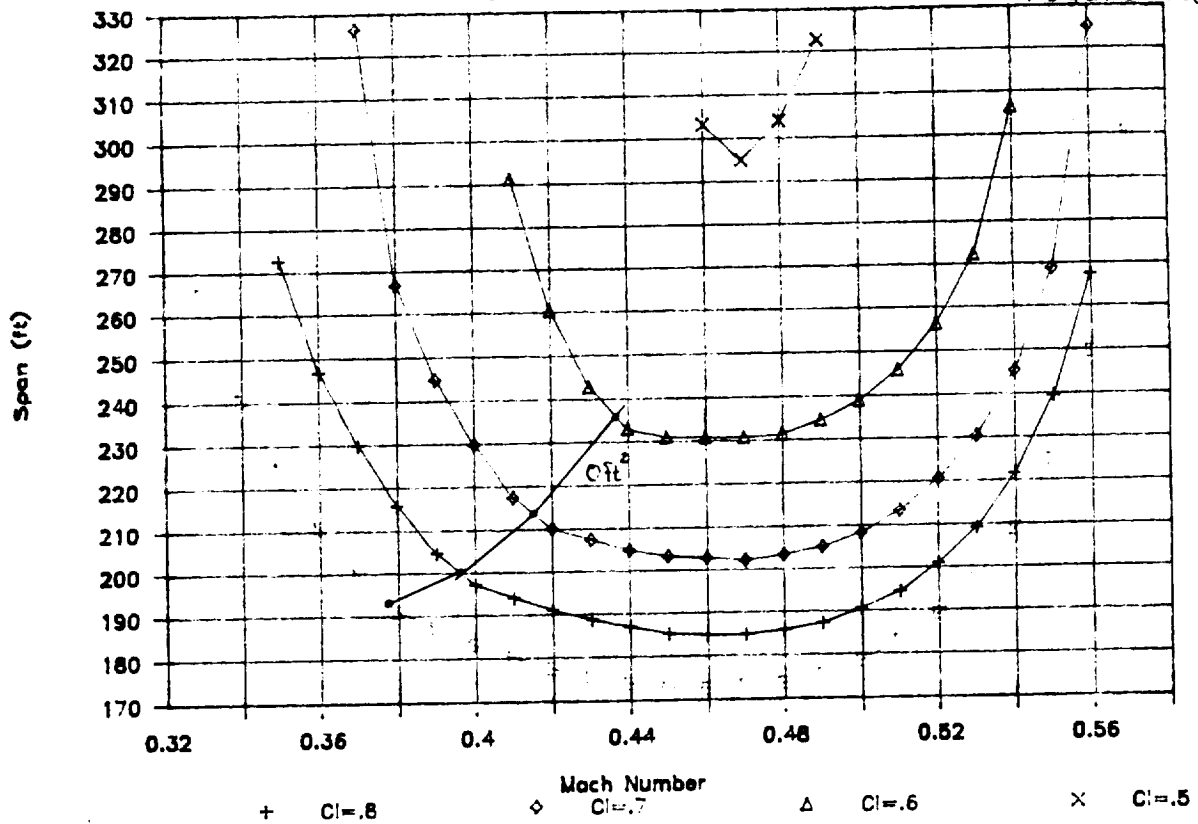
Power Available Vs. Mach Number



Span Vs. Mach Number

$t/c=.12$ $AR=15$ $Nutt=3$

Figure 4.6



L/D Ratio Vs. Mach Number

$t/c=.12$ $AR=15$ $Nutt=3$

Figure 4.7

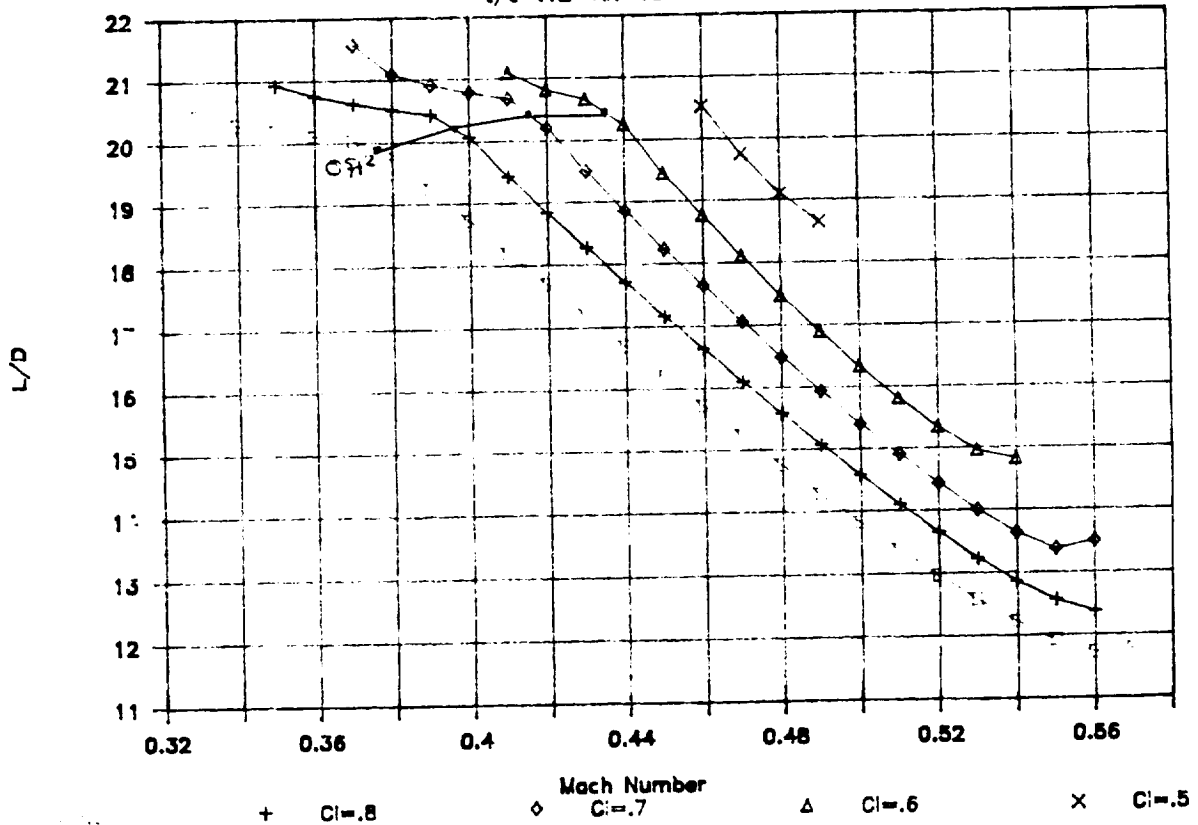


Figure 4.8
First Iteration Component Weights

Component:	Weight(Lbs):	Percent of Gross:
Wing	2705	40.3
Rectenna	276	4.1
Horizontal Tail	335	4.9
Vertical Tail	161	2.4
Controls	516	7.7
Fuselage	263	3.9
Landing Gear	202	3.0
Hydraulics	40	.6
Electronics	355	5.3
Motor(Inst. Air Induction)	550	8.2
Gearbox	79	1.2
Propellers	238	3.5
Payload	1000	14.9
Gross Weight	6720	100%

Aspect Ratio: 15 Wing Area : 3634 ft²
 C_l : .6 Wing Loading : 1.85 lb/ft²
 t/c : 12% L/D Ratio : 20.6
 Power Req. : 317hp Span : 234 ft
 Ultimate Load Factor : 3

Component Weight Breakdown

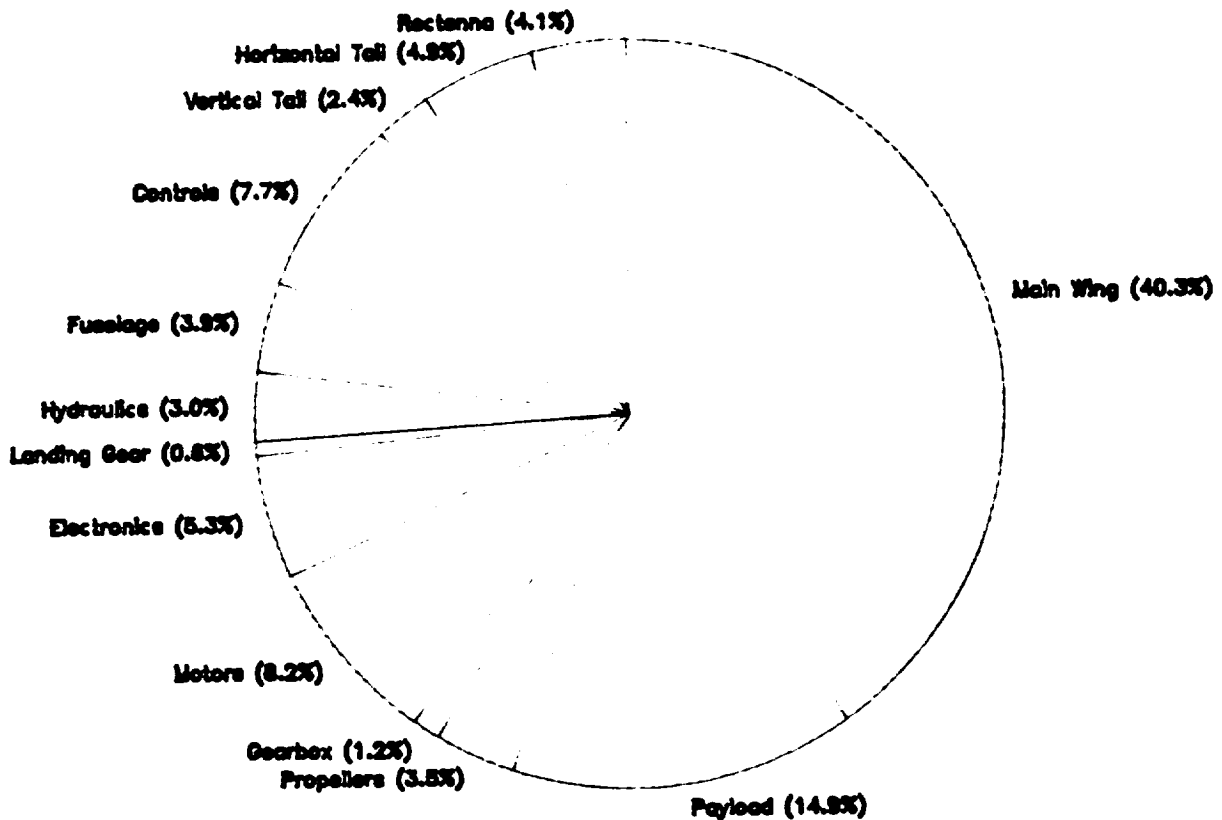


Figure 4.9 : Design Concept No.1

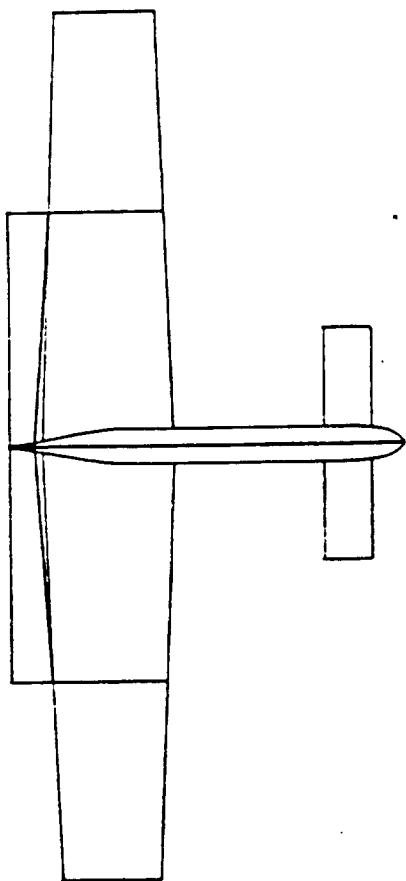
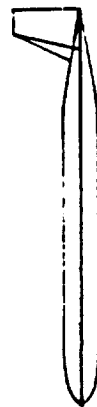
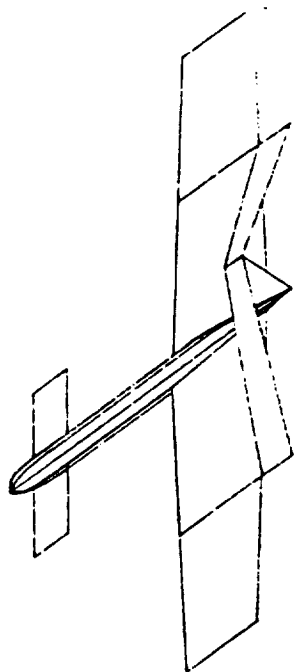


Figure 4.10 : Design Concept No.2

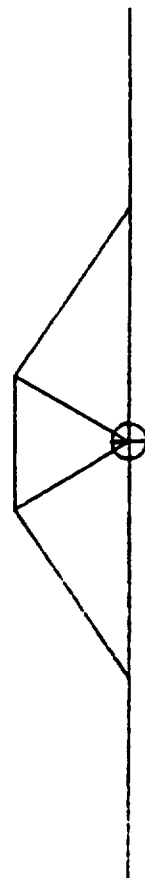
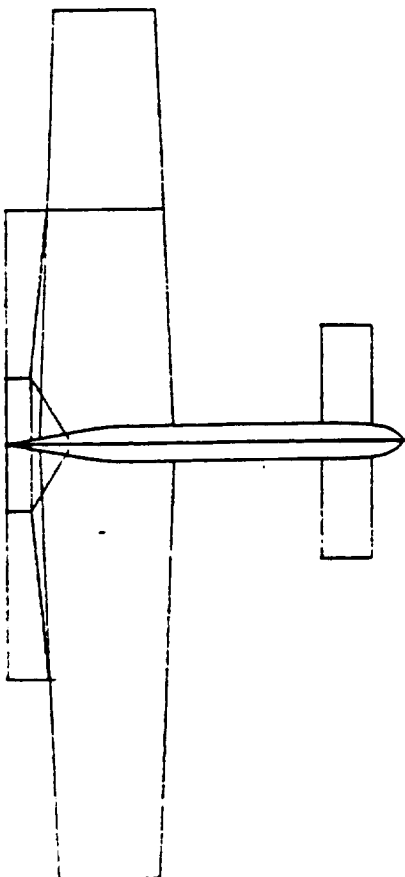
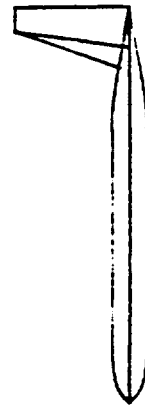
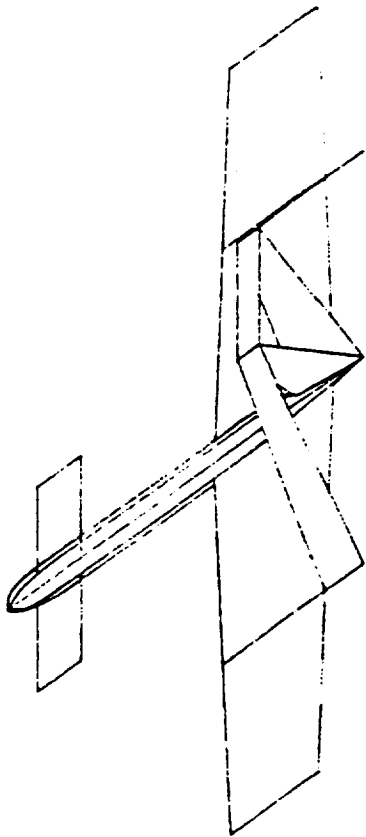


Figure 4.11 : Design Concept No.3

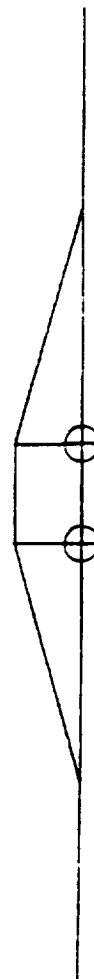
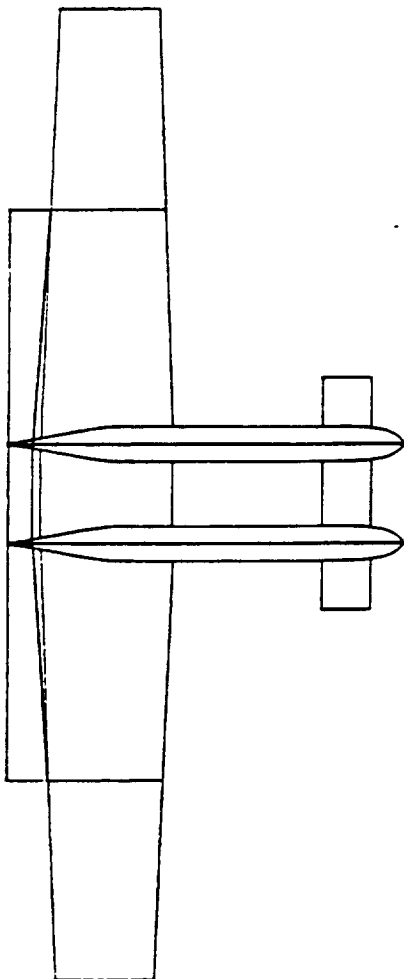
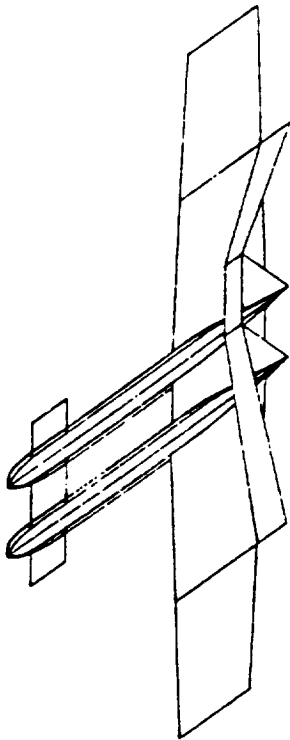
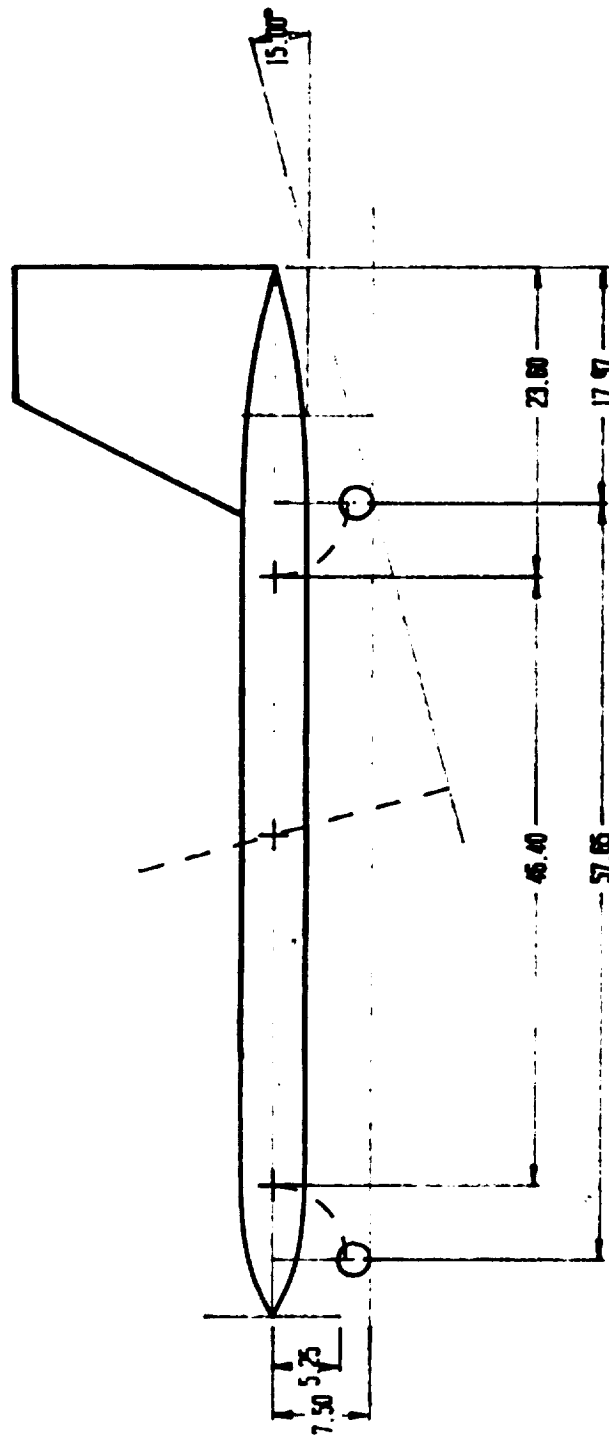
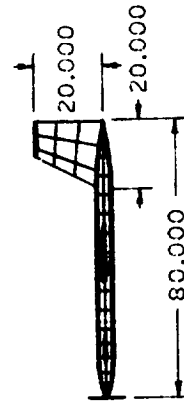
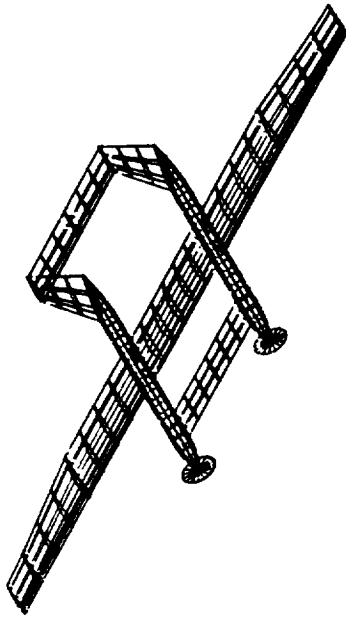
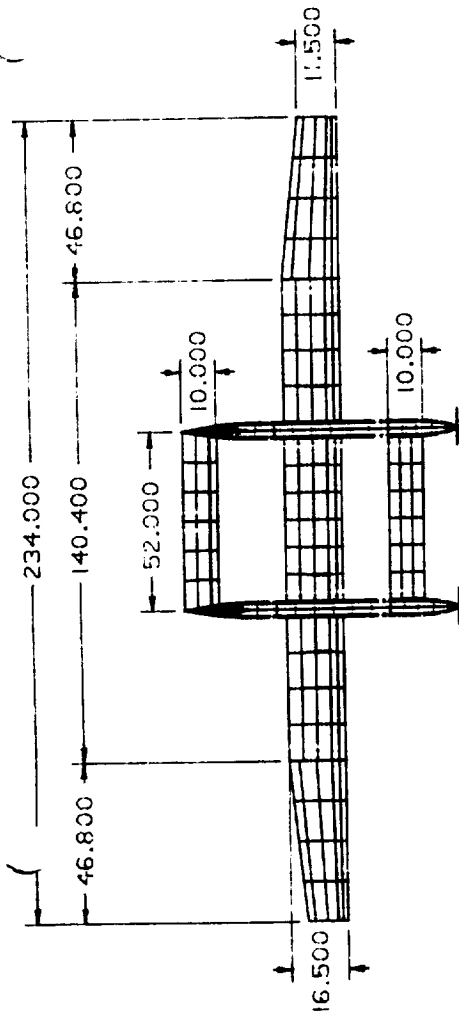


Figure 4.12
Landing Gear Configuration



ORIGINAL PAGE IS
OF POOR QUALITY

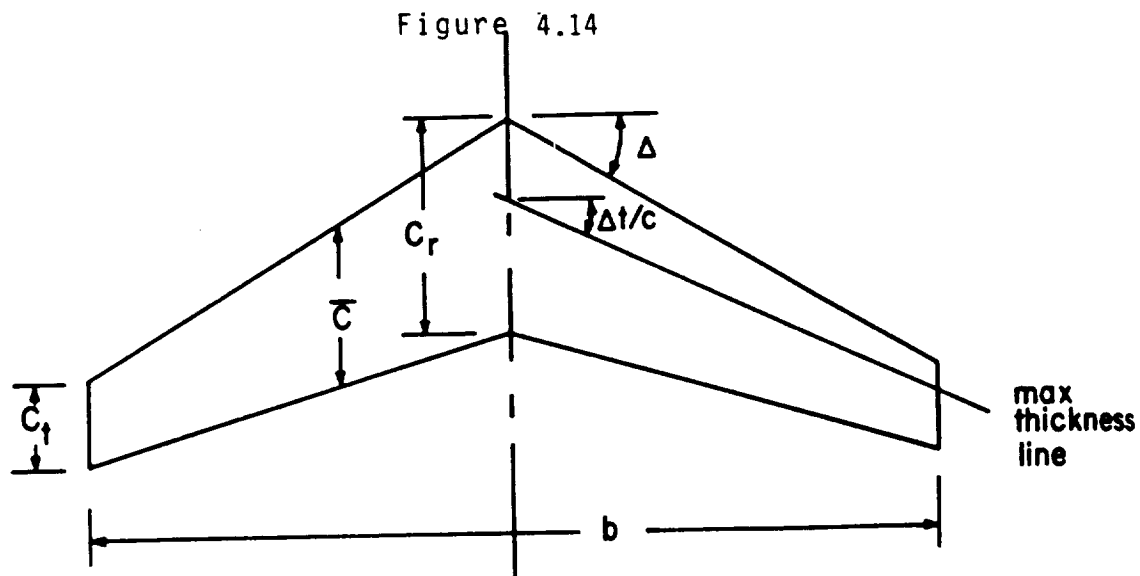
Figure 4.13



WPI CAD LABORATORY
TITLE: FINAL DRAFT
DRAWN BY: TOM JUTRAS
SCALE: 003 DATE: 4/2/90
NO: 1 SHEET: 1

Planform Parameters

Figure 4.14



$$A = \text{Aspect ratio} = \frac{b}{C_{\text{ave}}} = \frac{b^2}{S} = \frac{2b}{C_r(1 + \lambda)}$$

S = Wing area

λ = Taper ratio = C_t/C_r

\bar{C} = Mean aerodynamic chord (MAC)
 $= \frac{2}{3} C_r \left(\frac{1 + \lambda + \lambda^2}{1 + \lambda} \right)$

Planform Geometry

Figure 4.15

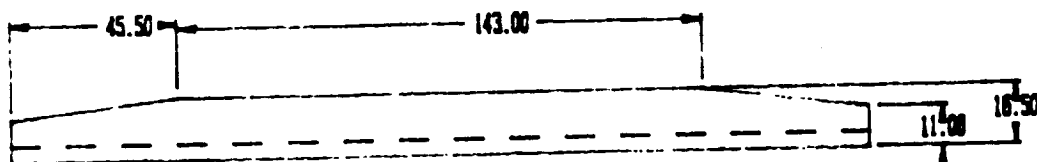


Figure 4.16

Second Iteration Aspect Ratios and Thicknesses

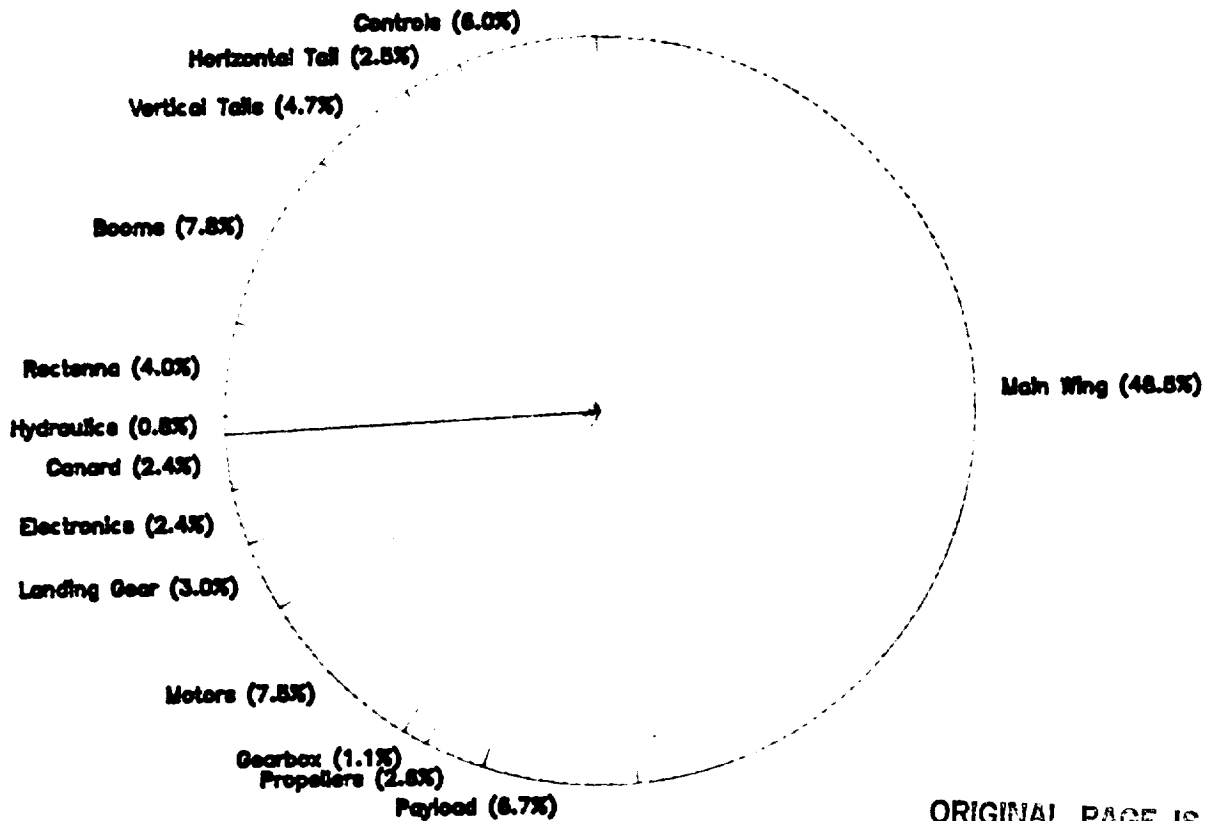
Component	AR	t/c
WING	15	12% Av
CANARD	4.7	8%
VERTICAL TAIL	1.33	10%
HORIZONTAL TAIL	5.2	8%

Figure 4.17
Second Iteration Component Weights

Component:	Weight(Lbs):	Percent of Gross:
Wing	7281	48.5
Rectenna	599	4.0
Horizontal Tail	371	2.5
Vertical Tails	712	4.7
Canard	362	2.4
Controls	905	6.0
Booms	1170	7.8
Landing Gear	450	3.0
Hydraulics	111	.8
Electronics	355	2.4
Motor(Inst. Induction)	1123	7.5
Gearbox	172	1.1
Propellers	393	2.6
Payload	1000	6.7
Gross Weight	15004	100%

Aspect Ratio: 15 Wing Area : 7920 ft²
 C_l : .6 Wing Loading : 1.89 lb/ft²
 t/c : 12% L/D Ratio : 21.4
 Power Req. : 688hp Span : 345 ft
 Ultimate Load Factor : 3

Component Weight Breakdown



ORIGINAL PAGE IS
OF POOR QUALITY

Figure 5.1.1 Transition bubble

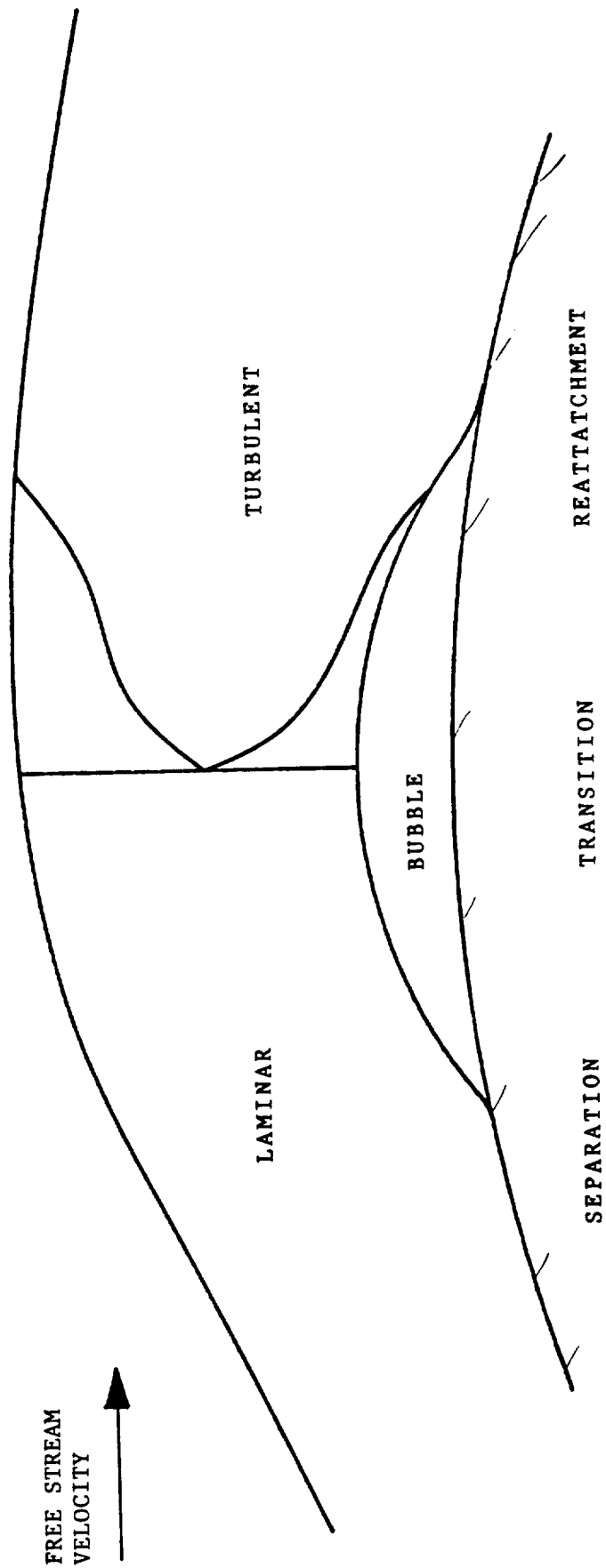


Figure 5.1.2 Sample Pressure Distribution

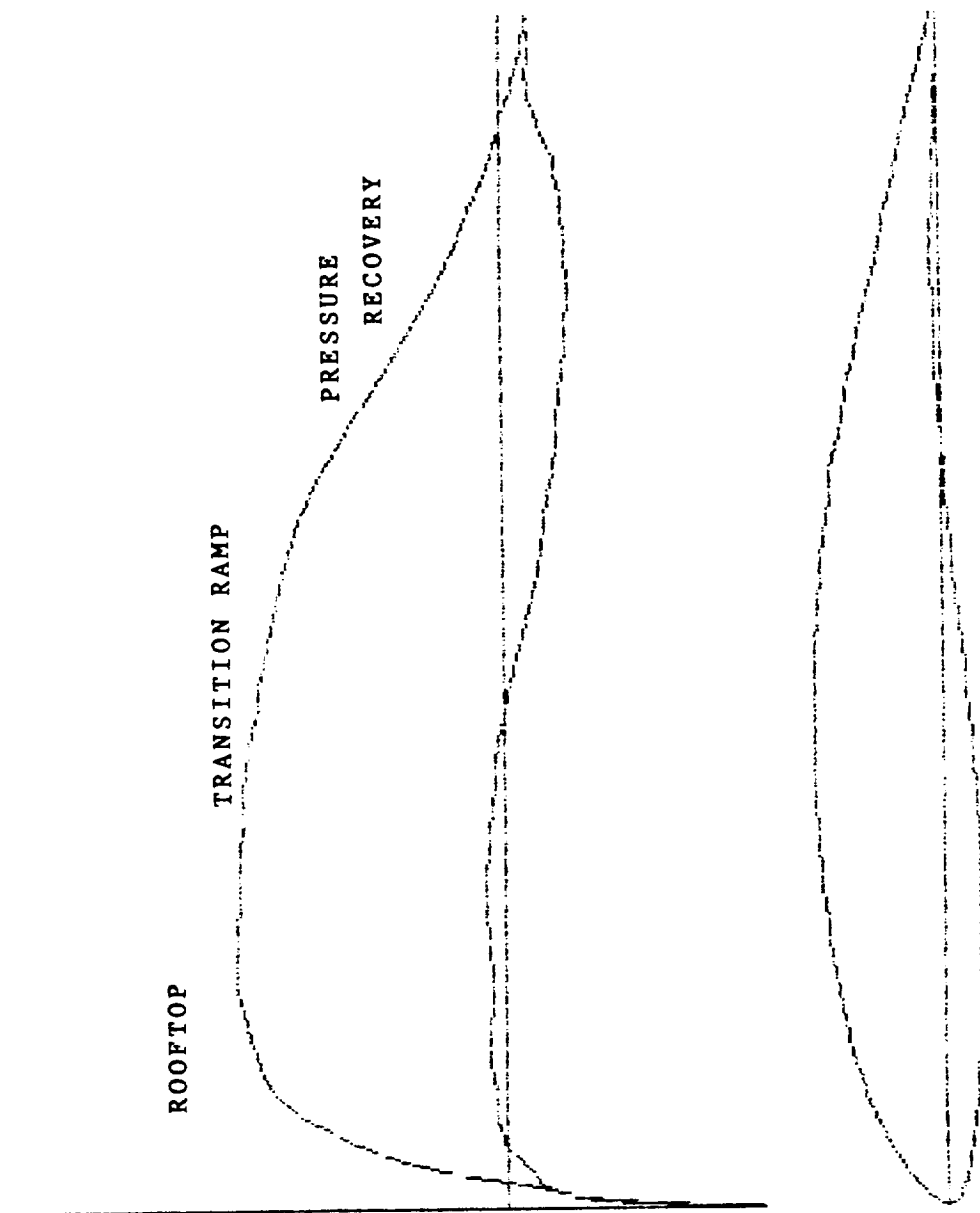


Figure 5.1.3 Span Loading

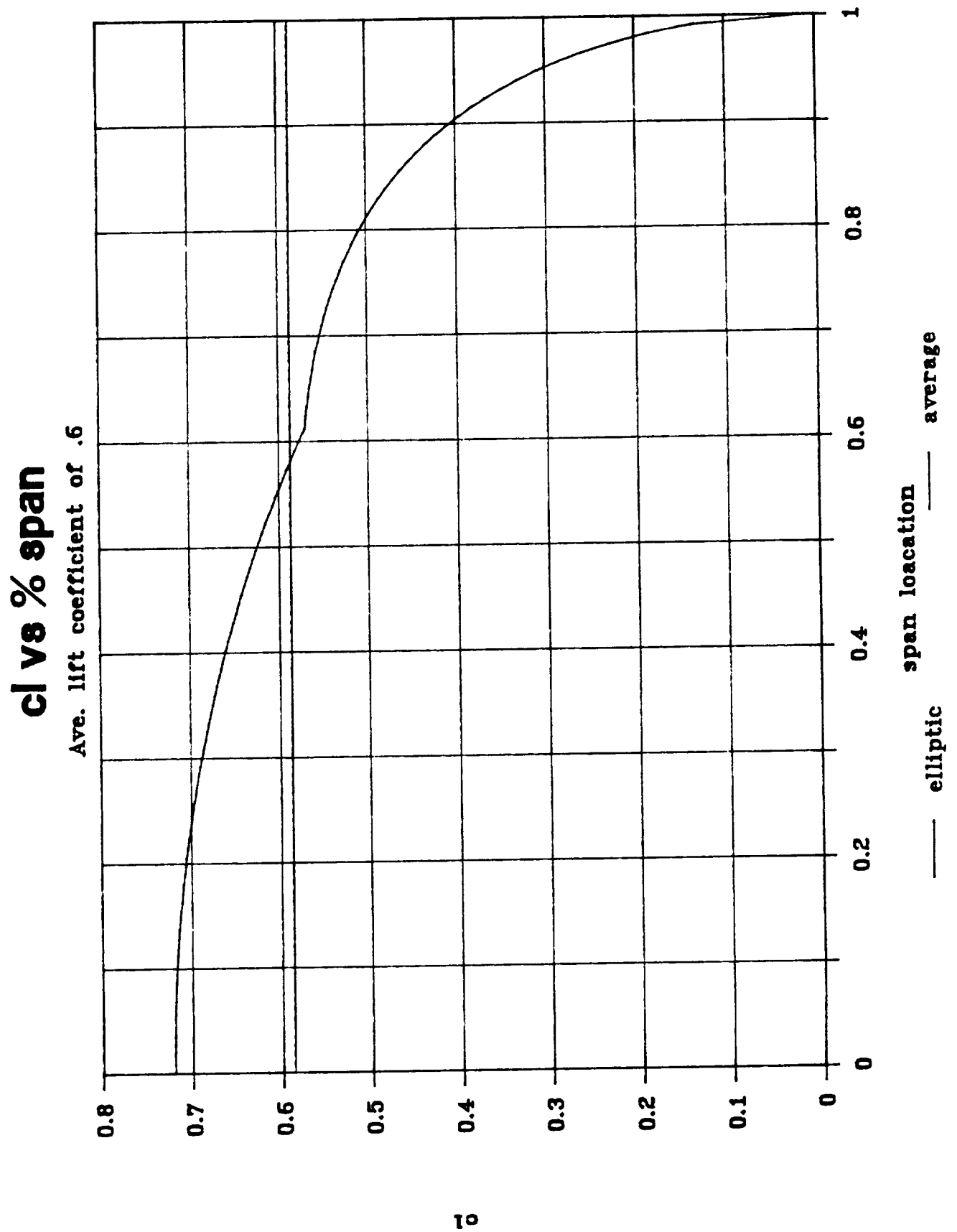


Figure 5.1.4 L, P, Q Target Pressure Distributions

Target Pressure Distributions

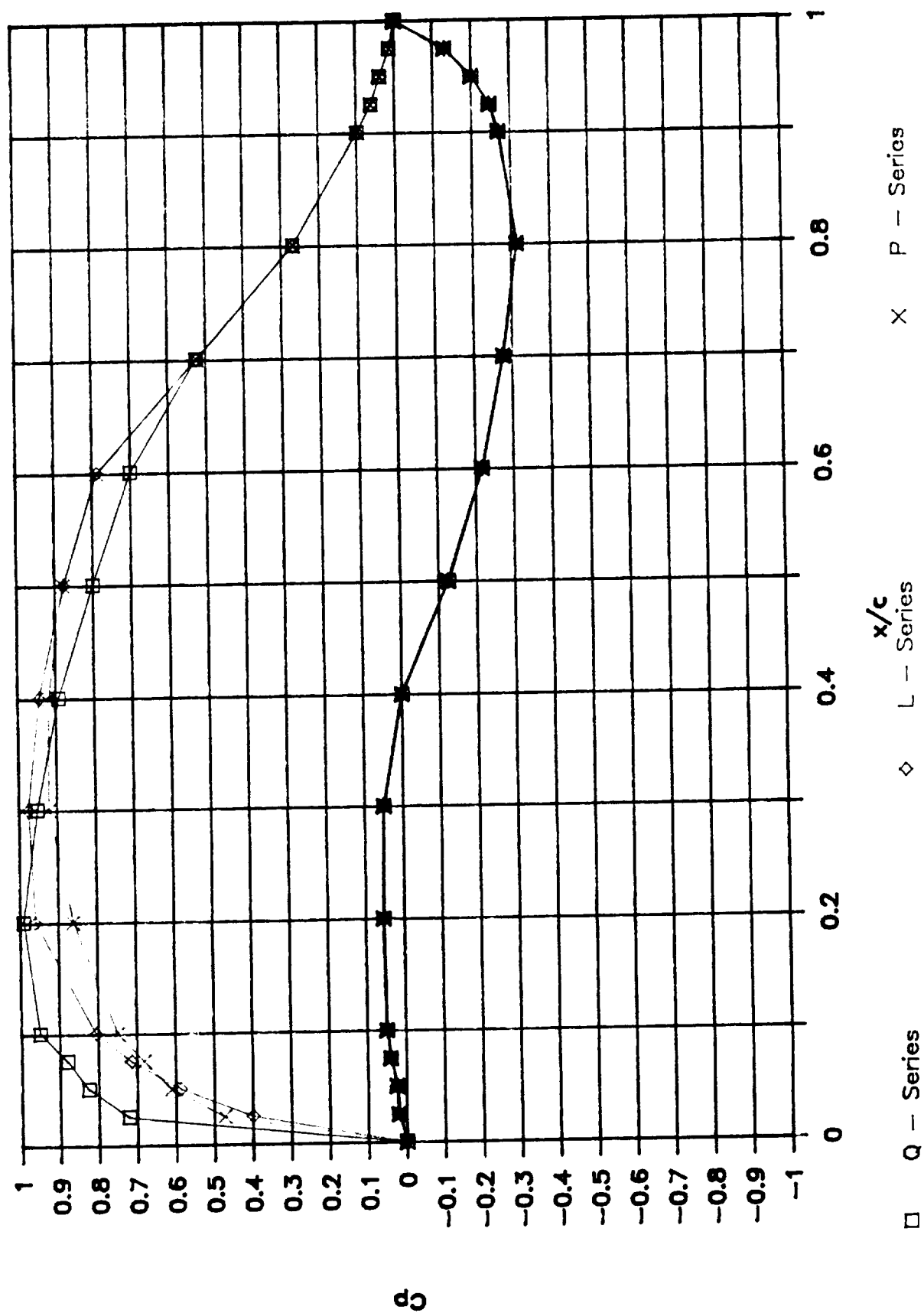


Figure 5.1.5 P-Series Pressure Distribution (inviscid analysis)

Airfoil P1
design point
 $c_l = 0.7238$
 $\alpha = 0.514^\circ$

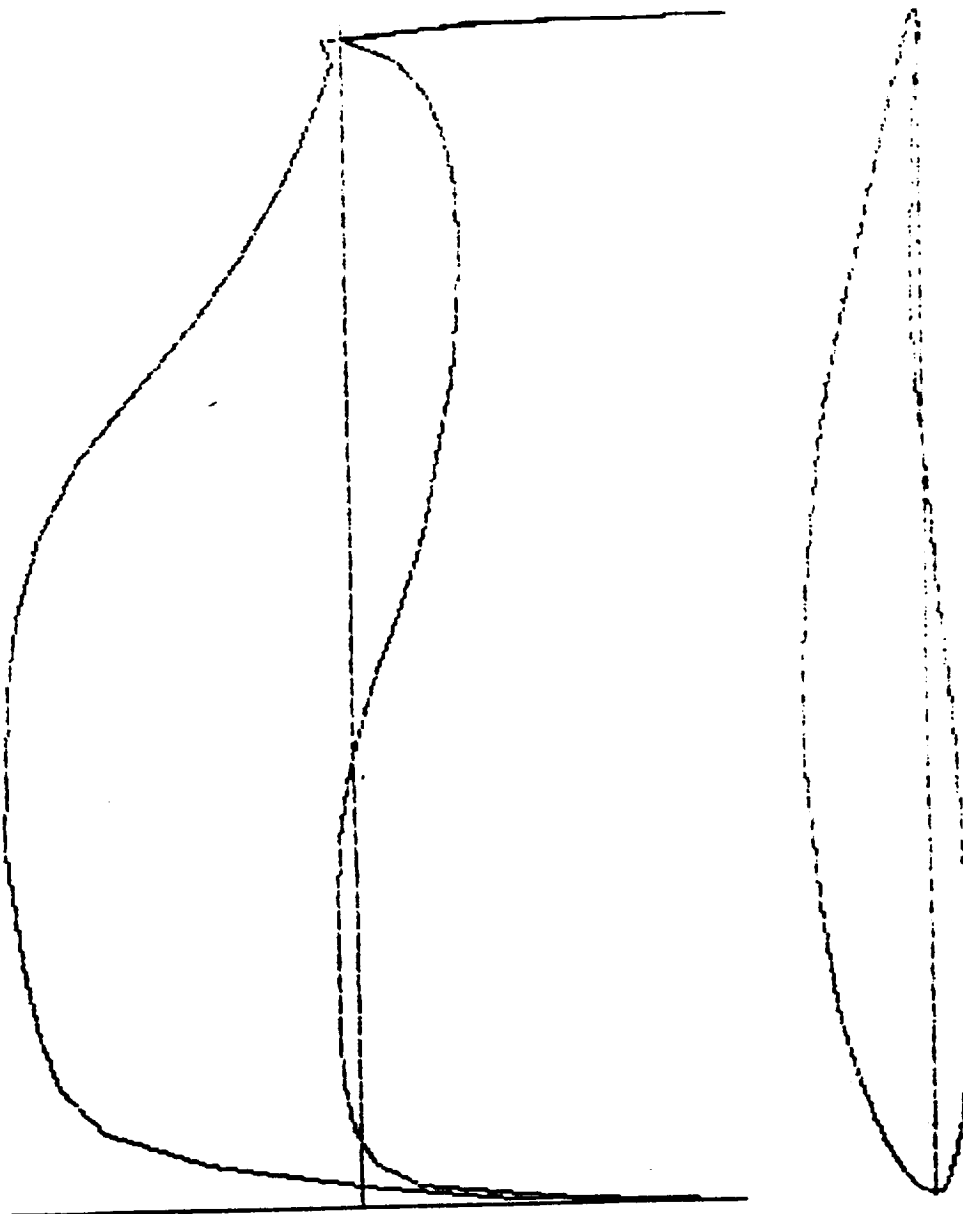


Figure 5.1.6 L-Series Pressure Distribution (inviscid analysis)

Airfoil L1
design point
 $c_l = 0.740$
 $\alpha = 0.57^\circ$

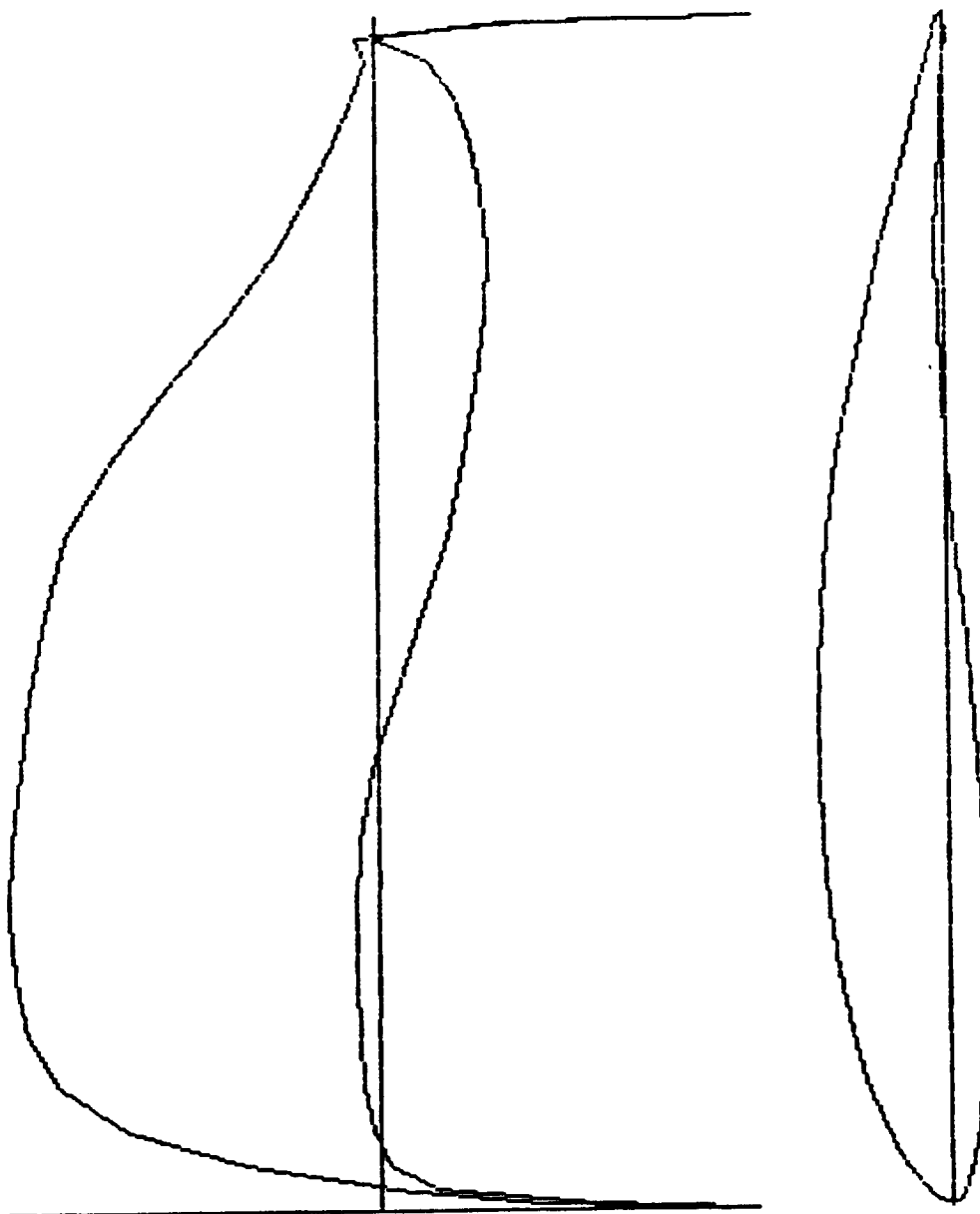


Figure 5.1.7 Q-Series Pressure Distribution (inviscid analysis)

Airfoil Q1
design point
 $c_l = 0.740$

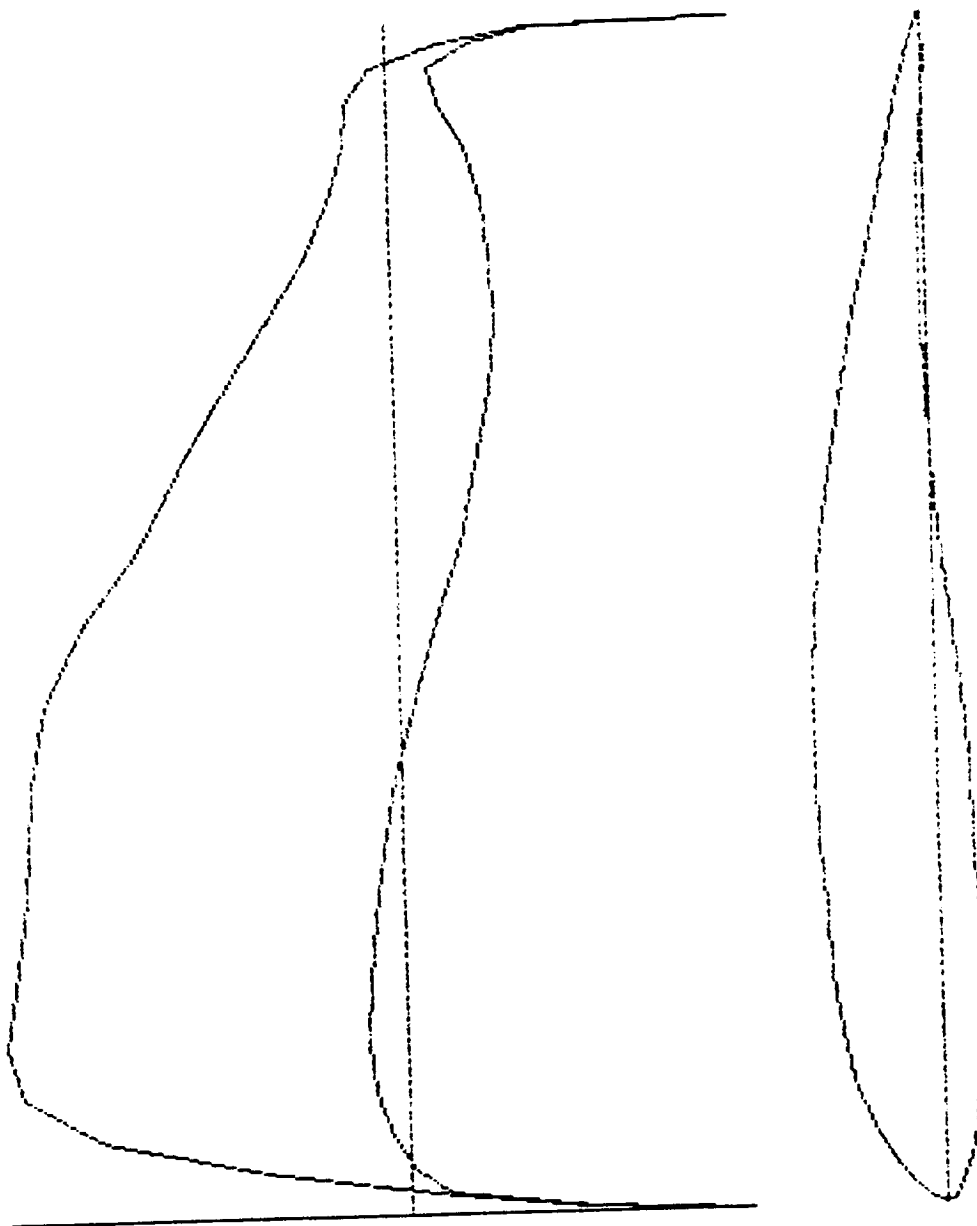


Figure 5.1.8 L1, L2, L3 Targets

Target Pressure Distributions

L-Series Airfoils

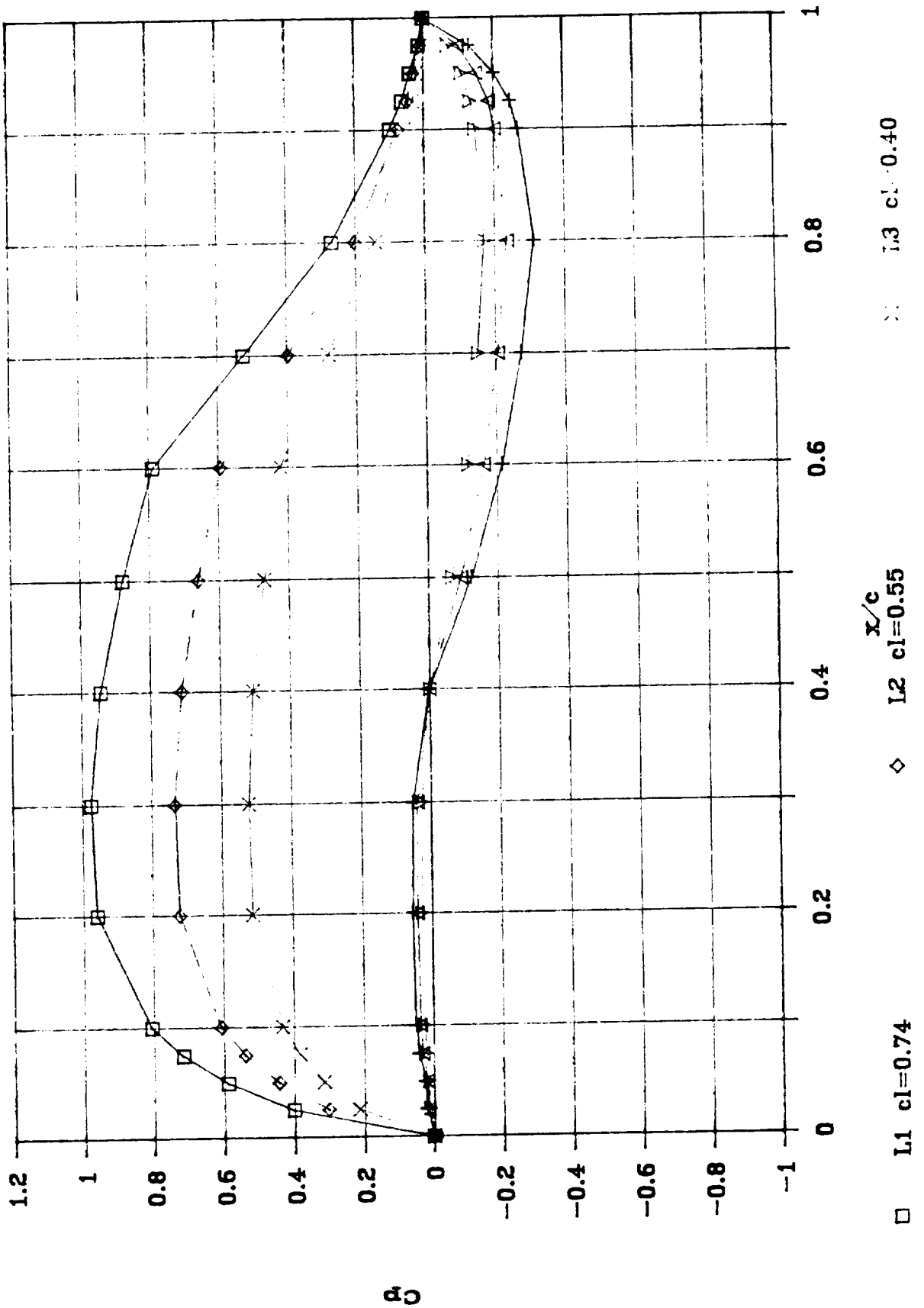


Figure 5.1.9 L1 Inviscid Pressure Distribution, Geometry

Airfoil L1
design point
 $c_l = 0.740$
 $\alpha = 0.57^\circ$

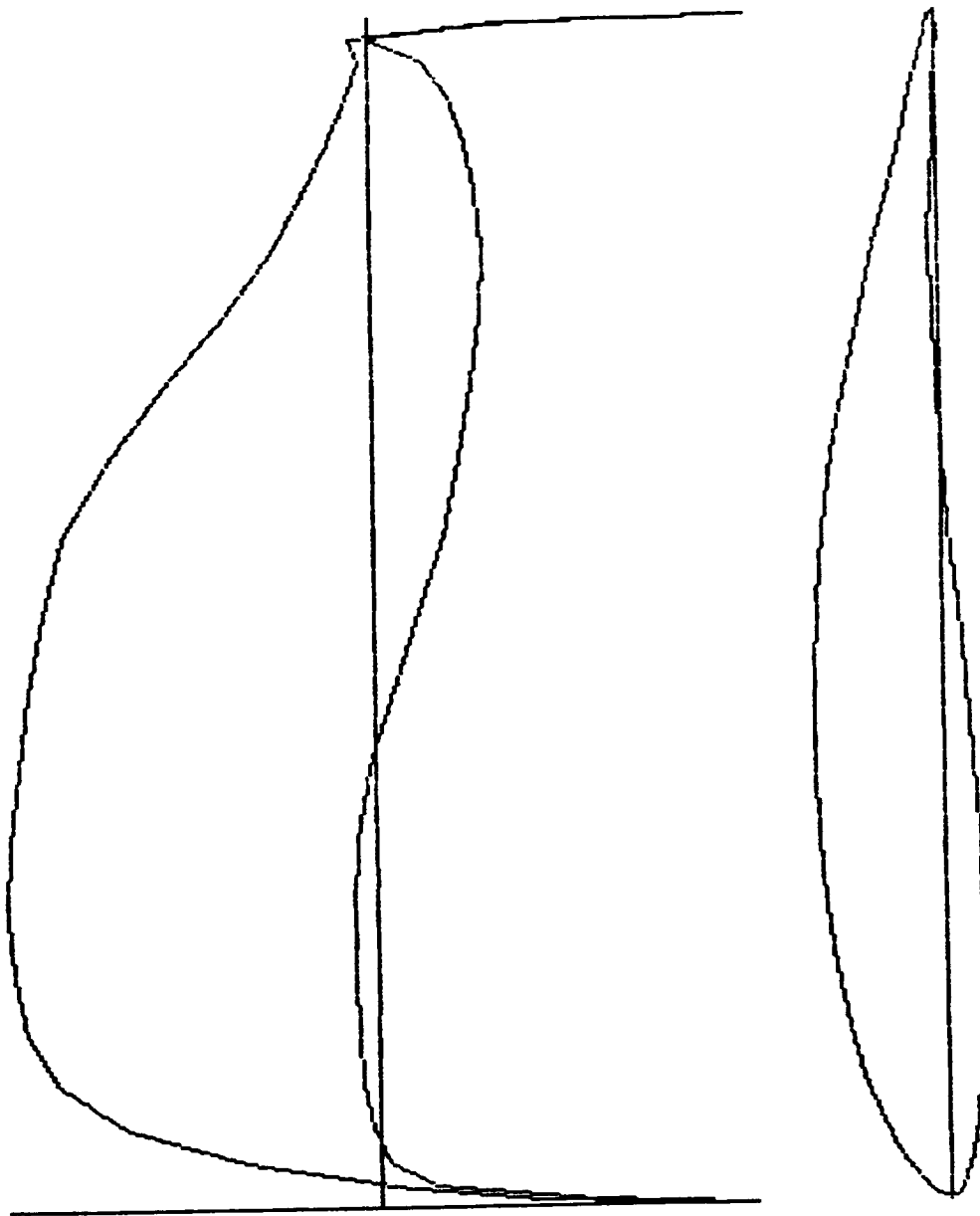


Figure 5.1.10 L2 Inviscid Pressure Distribution, Geometry

Airfoil L2
design point
 $c_l = 0.559$
 $\alpha = 0.464^\circ$

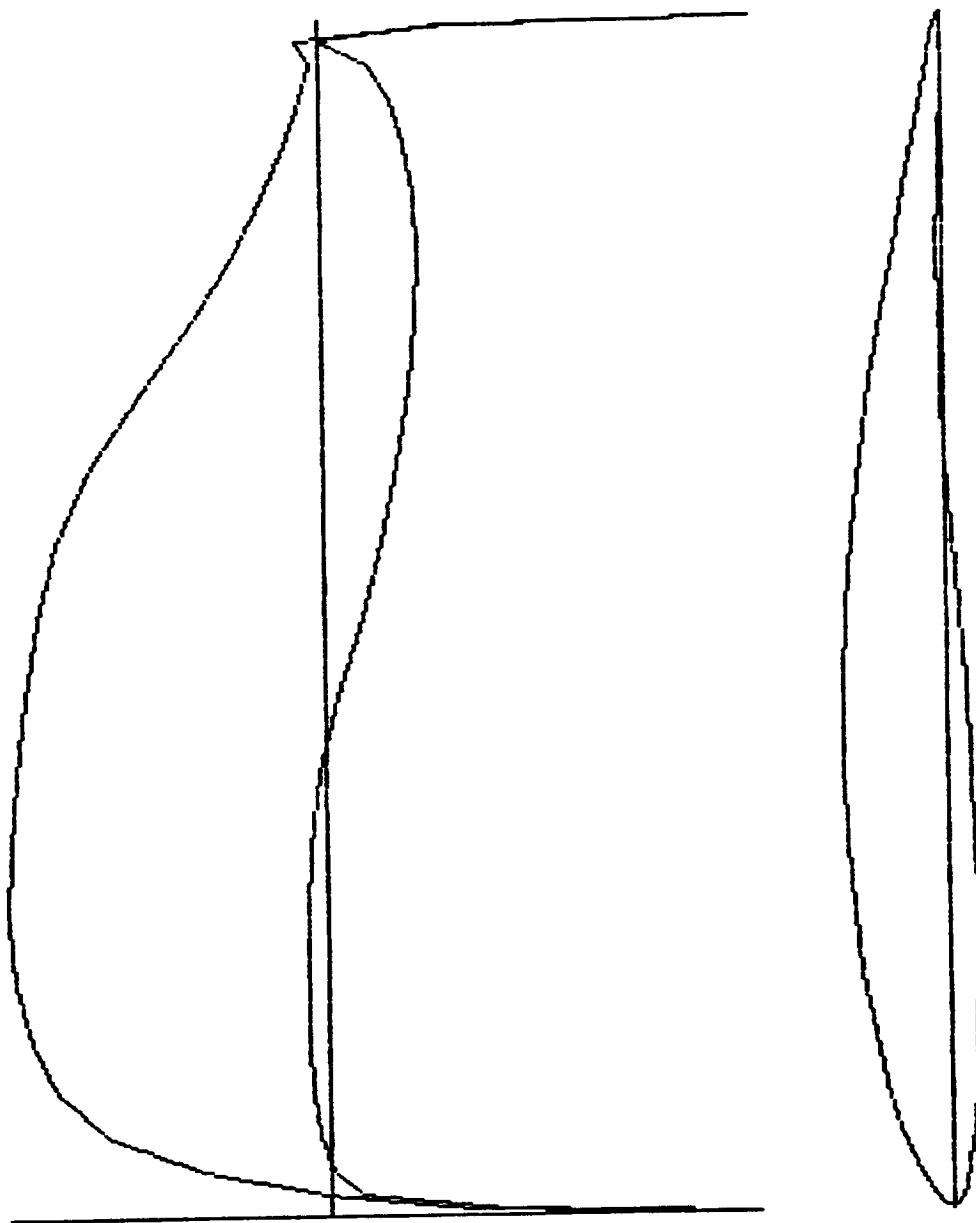


Figure 5.1.11 L3 Inviscid Pressure Distribution, Geometry

Airfoil L3
design point
 $c_l = 0.399$
 $\alpha = 0.35^\circ$

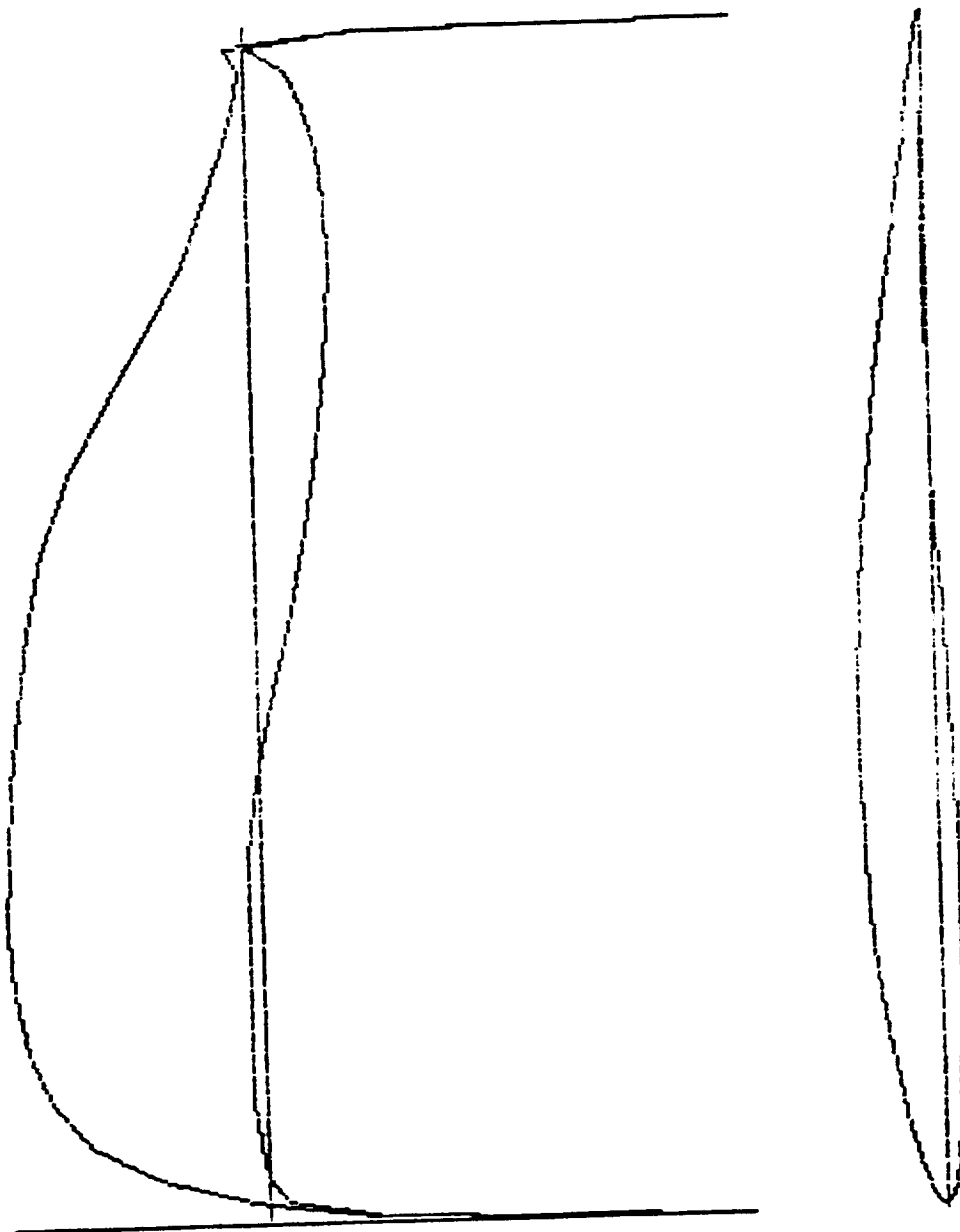
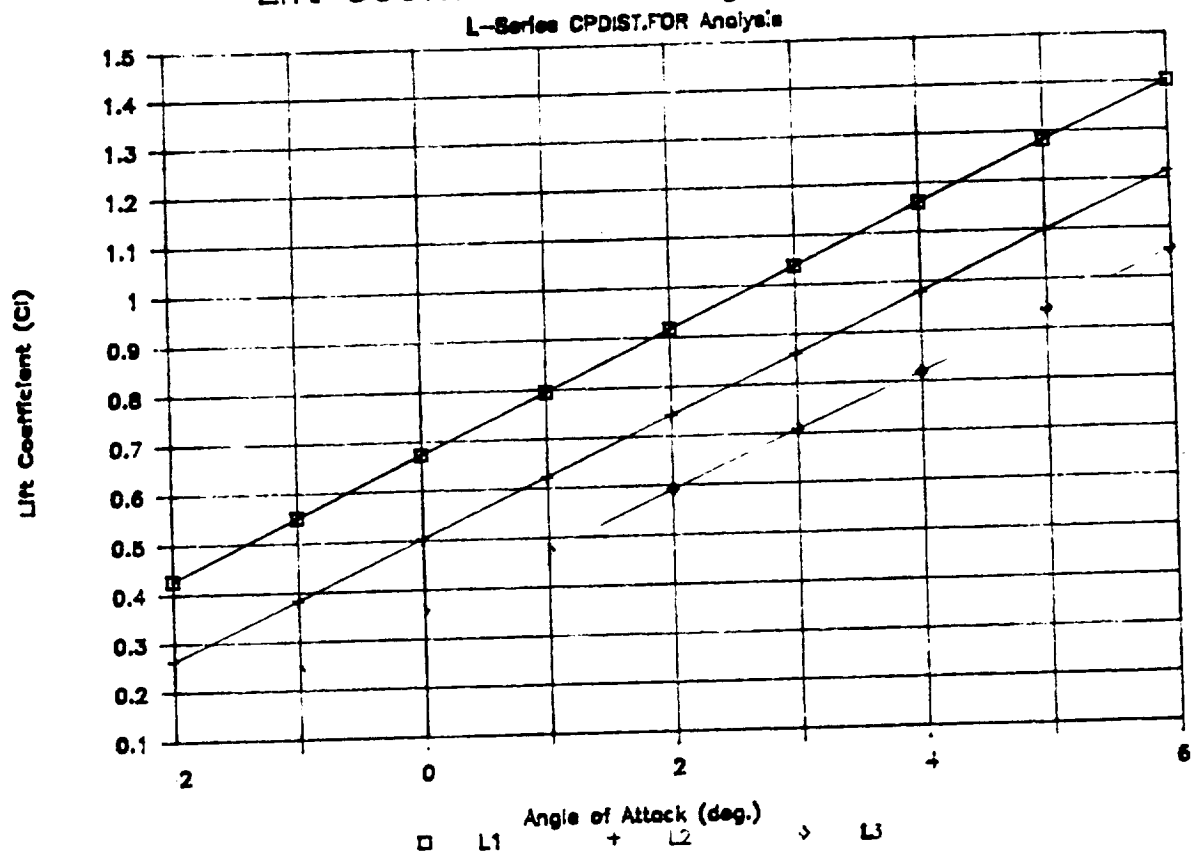
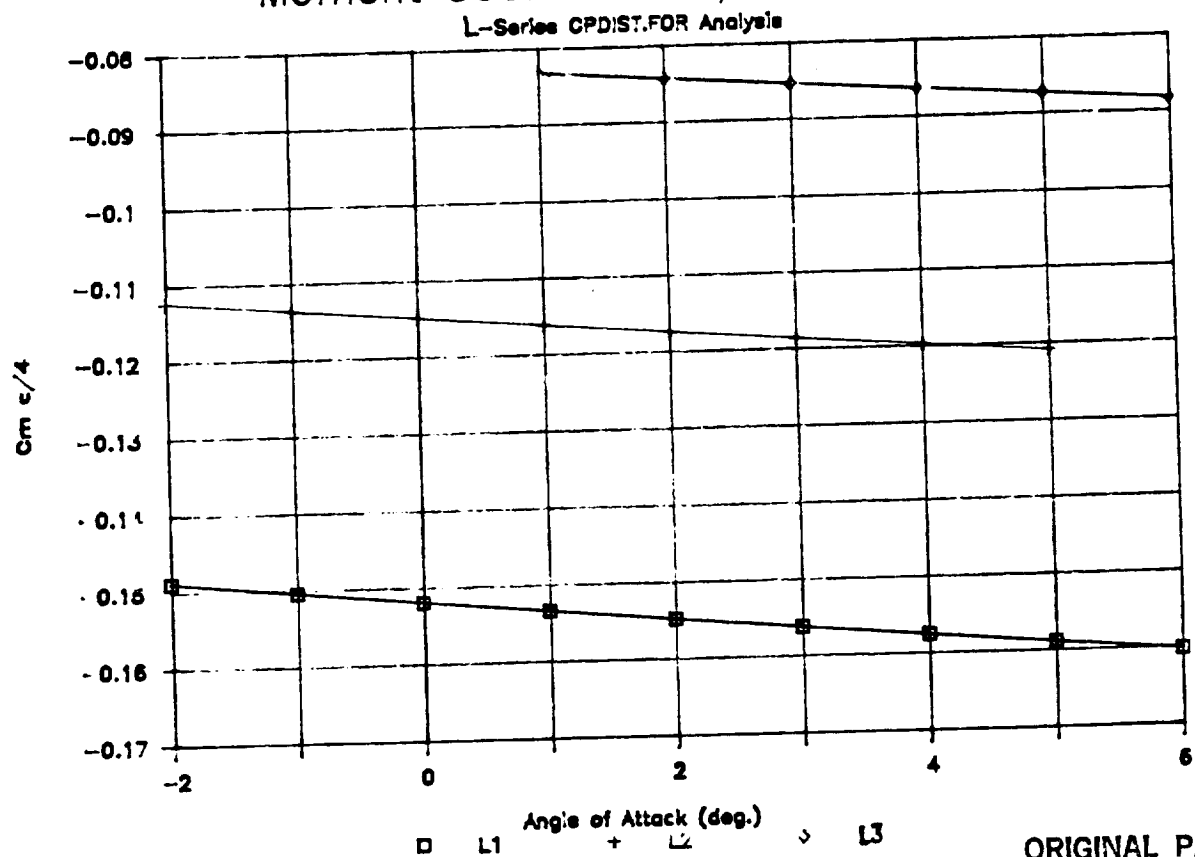


Figure 5.1.12 L-Series C_l , c_m vs. α (inviscid analysis)

Lift Coefficient vs. Angle of Attack



Moment Coefficient $C_{m/4}$ vs. Alpha



ORIGINAL PAGE IS
OF POOR QUALITY

Figure 5.1.13 L-Series C_l vs. α (compressible analysis)

Section c_l versus Angle of Attack

Grumfoil Analysis

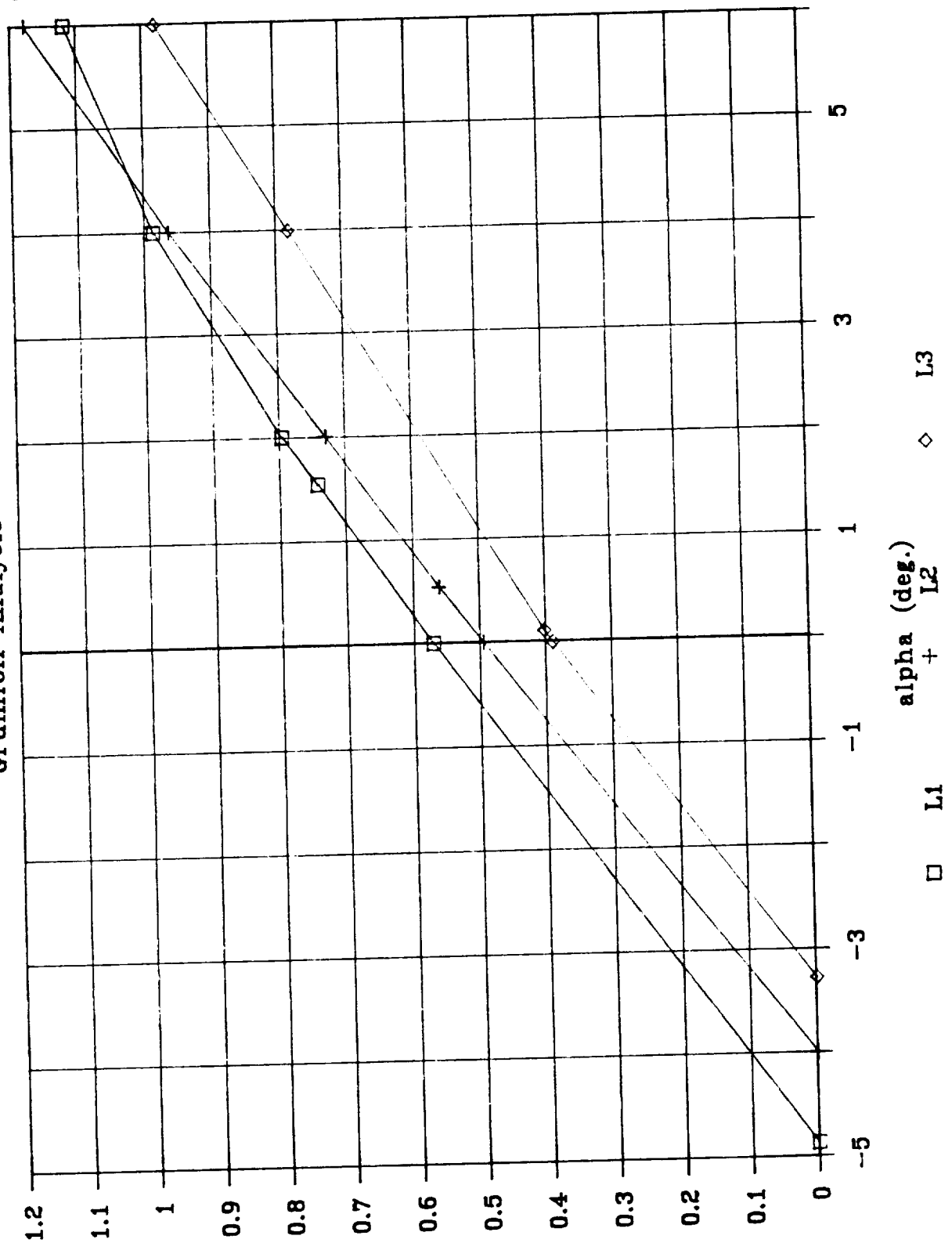
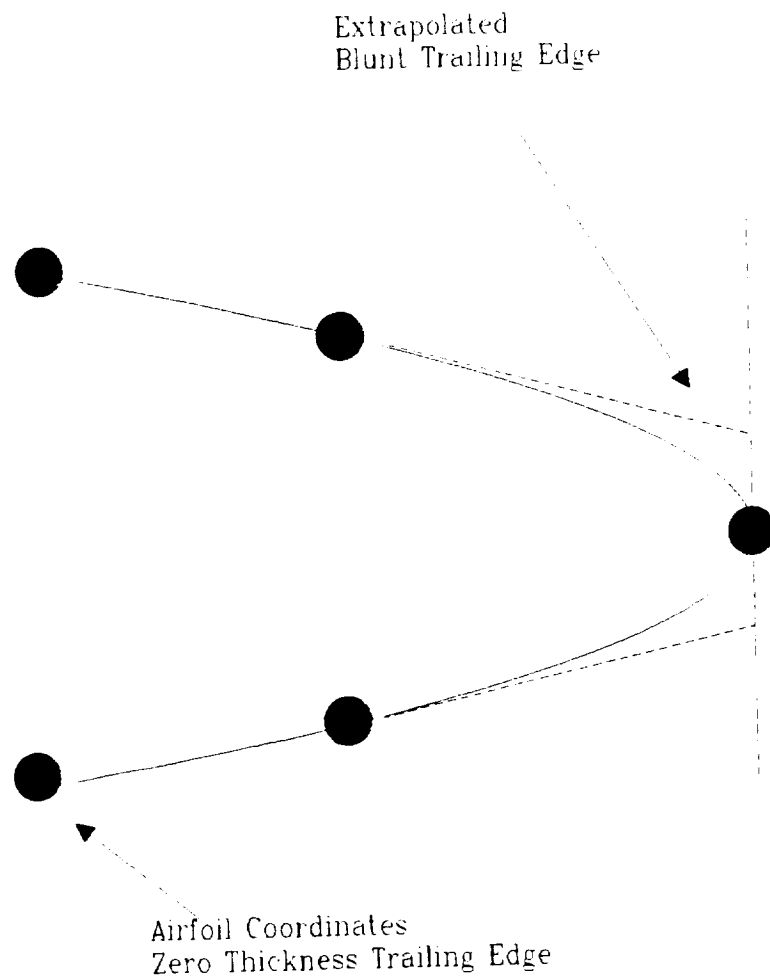


Figure 5.1.14
CPIXVRS.FOR
Trailing Edge Closure



ORIGINAL PAGE IS
OF POOR QUALITY

Figure 5.1.15 L1 Compressible and Target Pres. Distributions

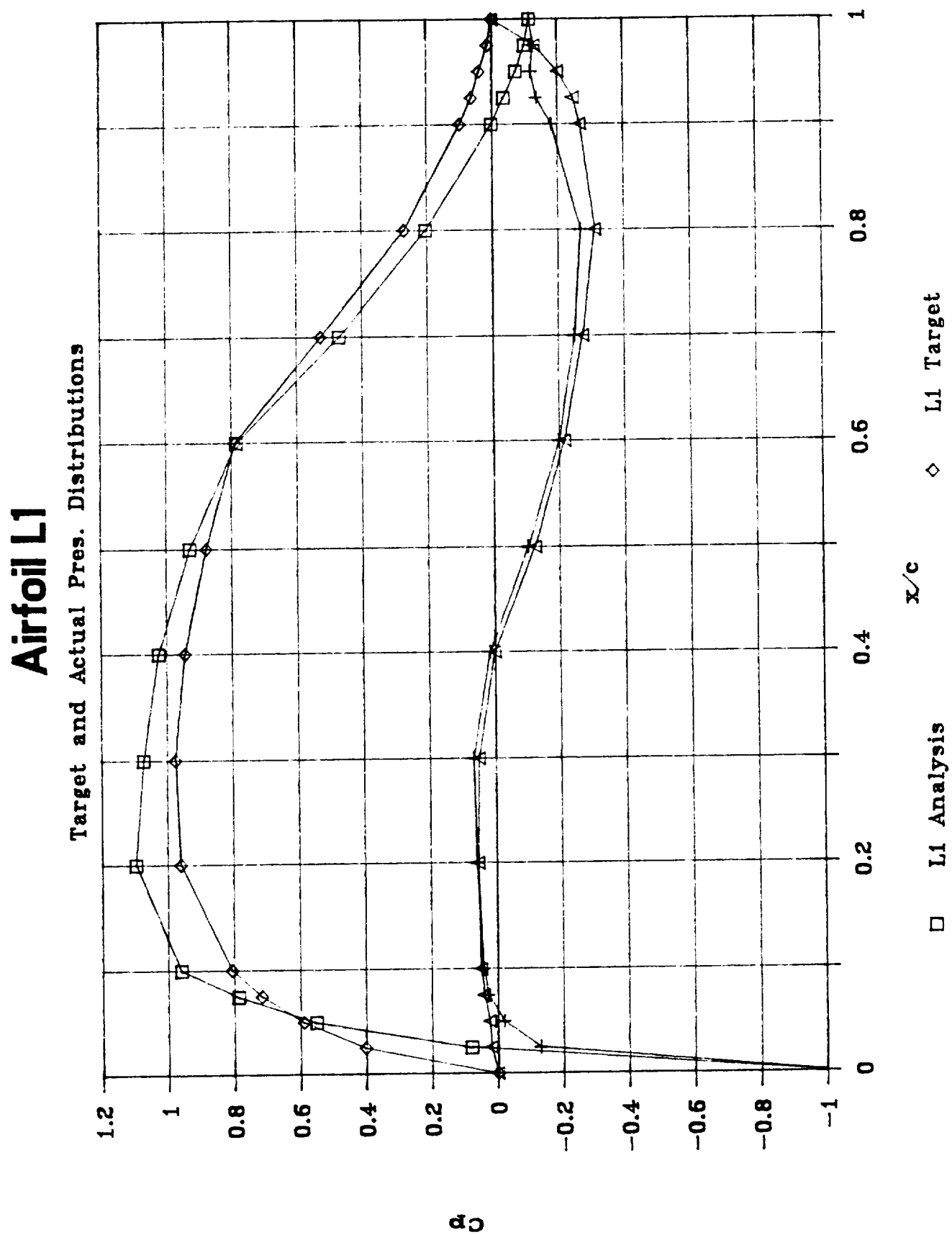


Figure 5.1.16 L2 Compressible and Target Pres. Distributions

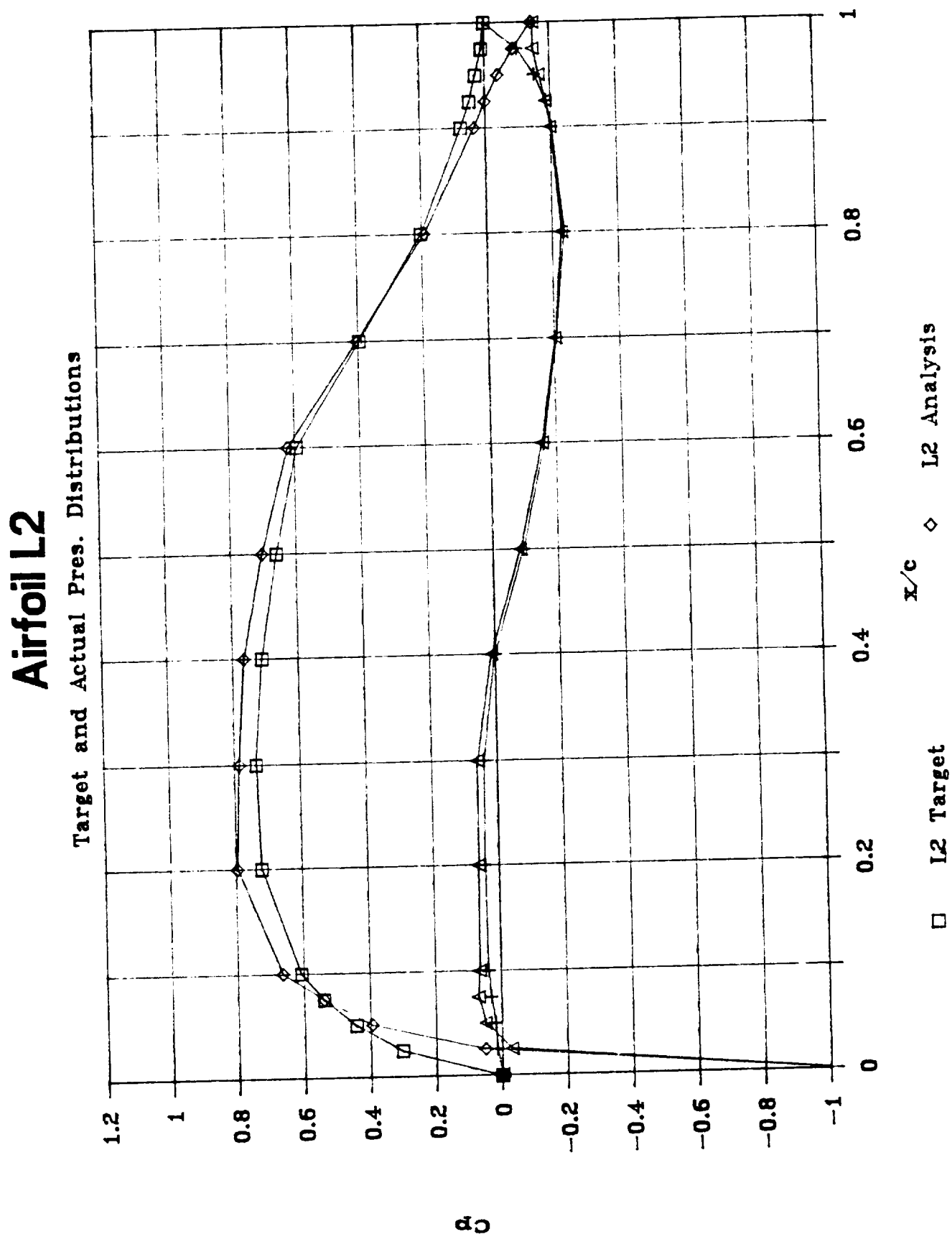


Figure 5.1.17 L3 Compressible and Target Pres. Distributions

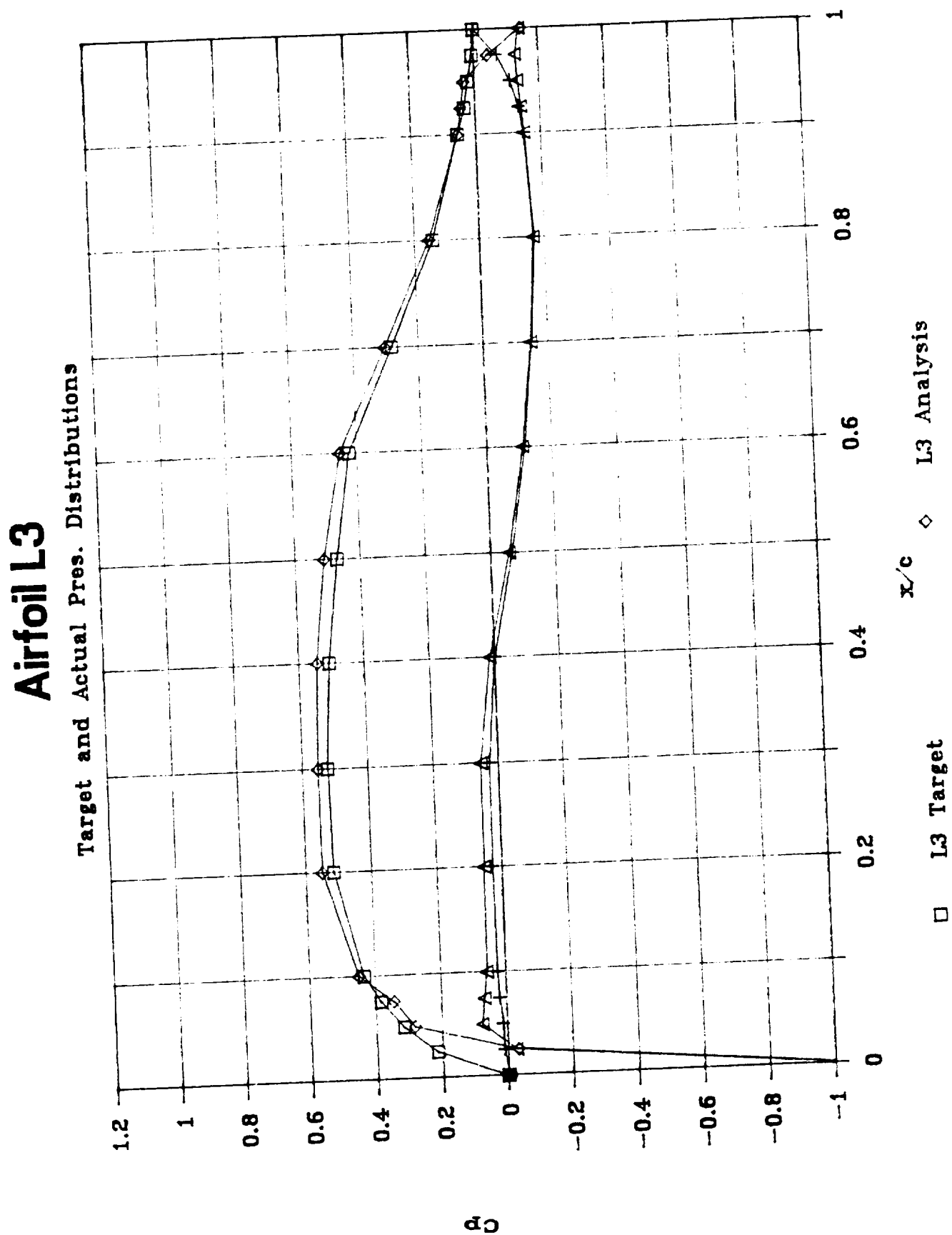


Figure 5.1.18 L-Series Drag Polar

c_d versus c_l

Grumfoil Analysis

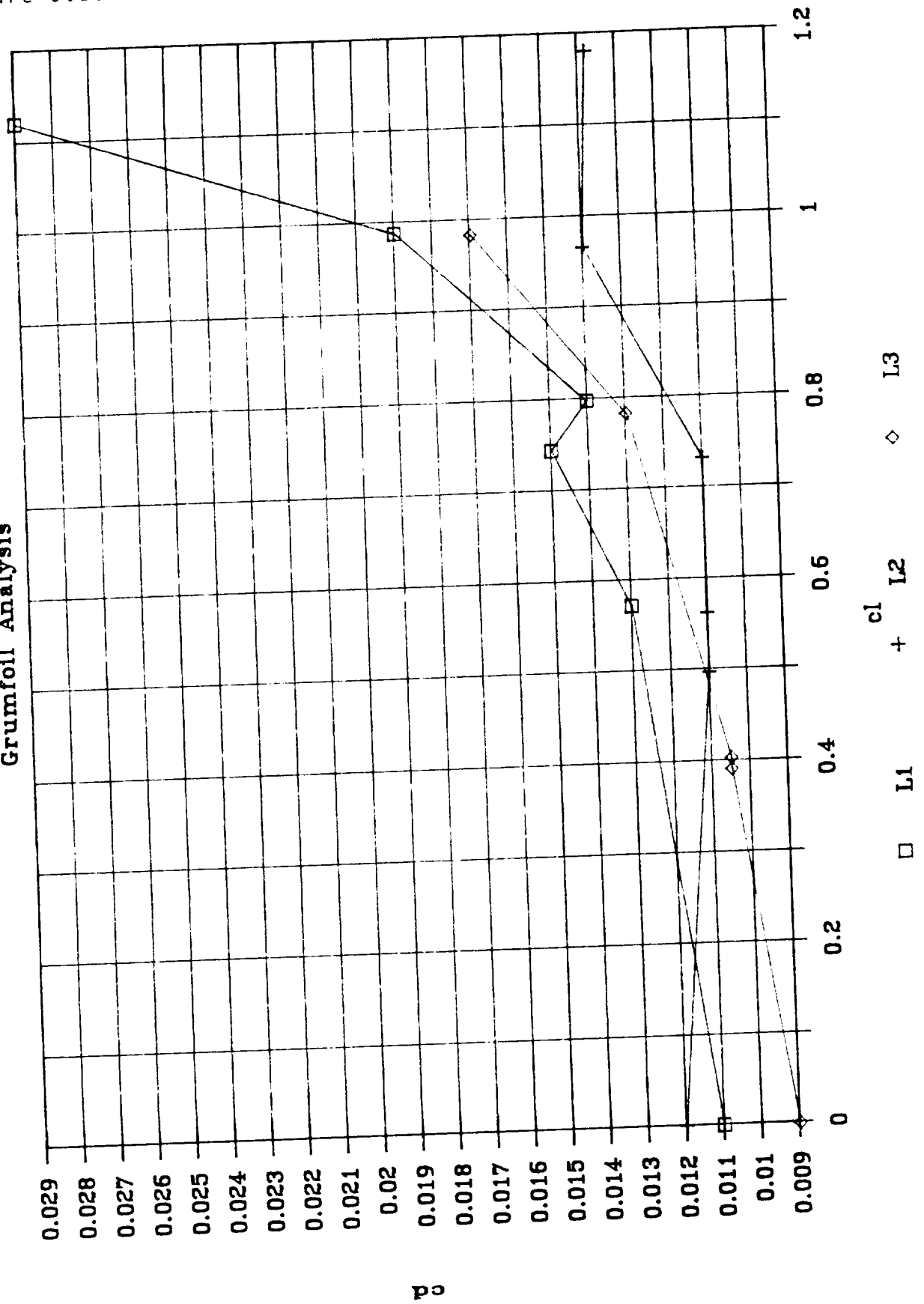


Figure 5.1.19 L1, NACA 4415 Drag Comparison

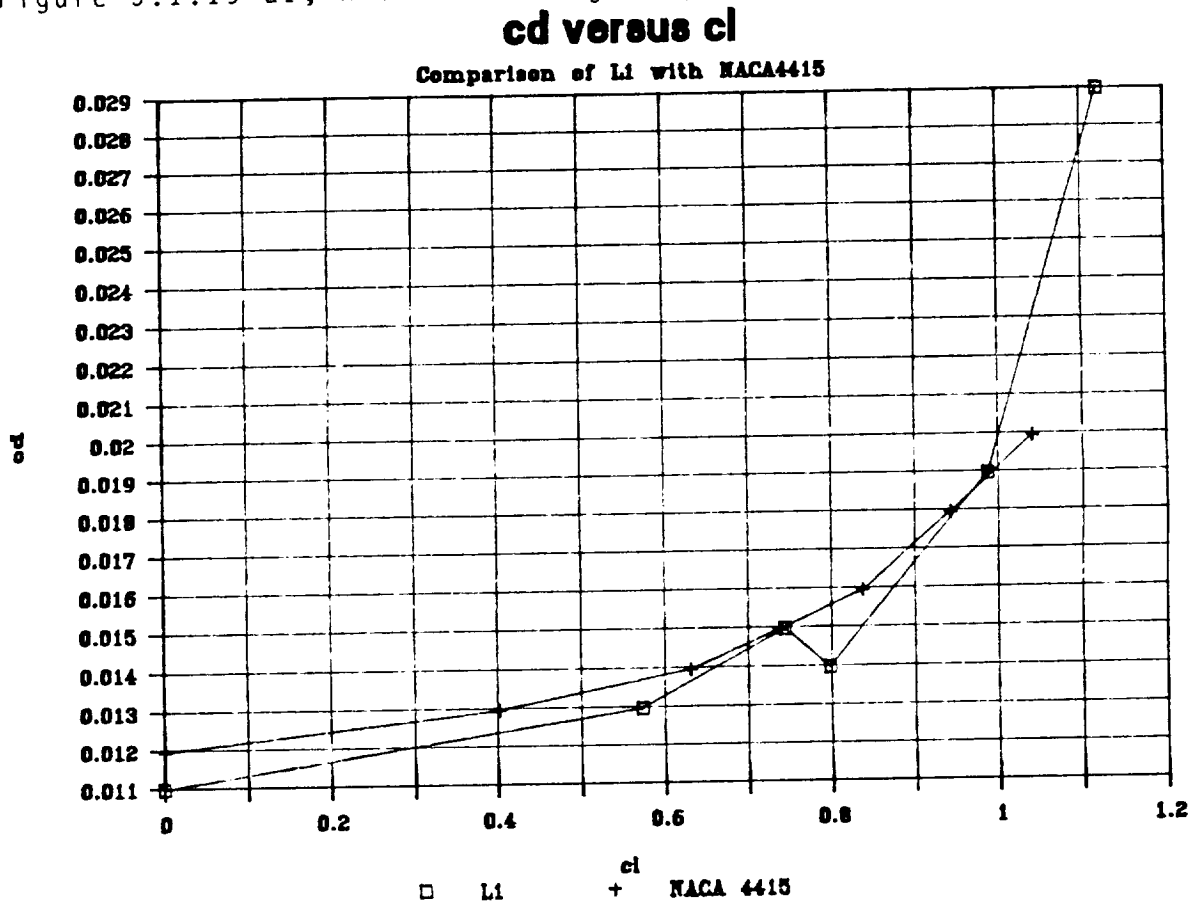


Figure 5.1.20 L2, NACA 4412 Drag Comparison

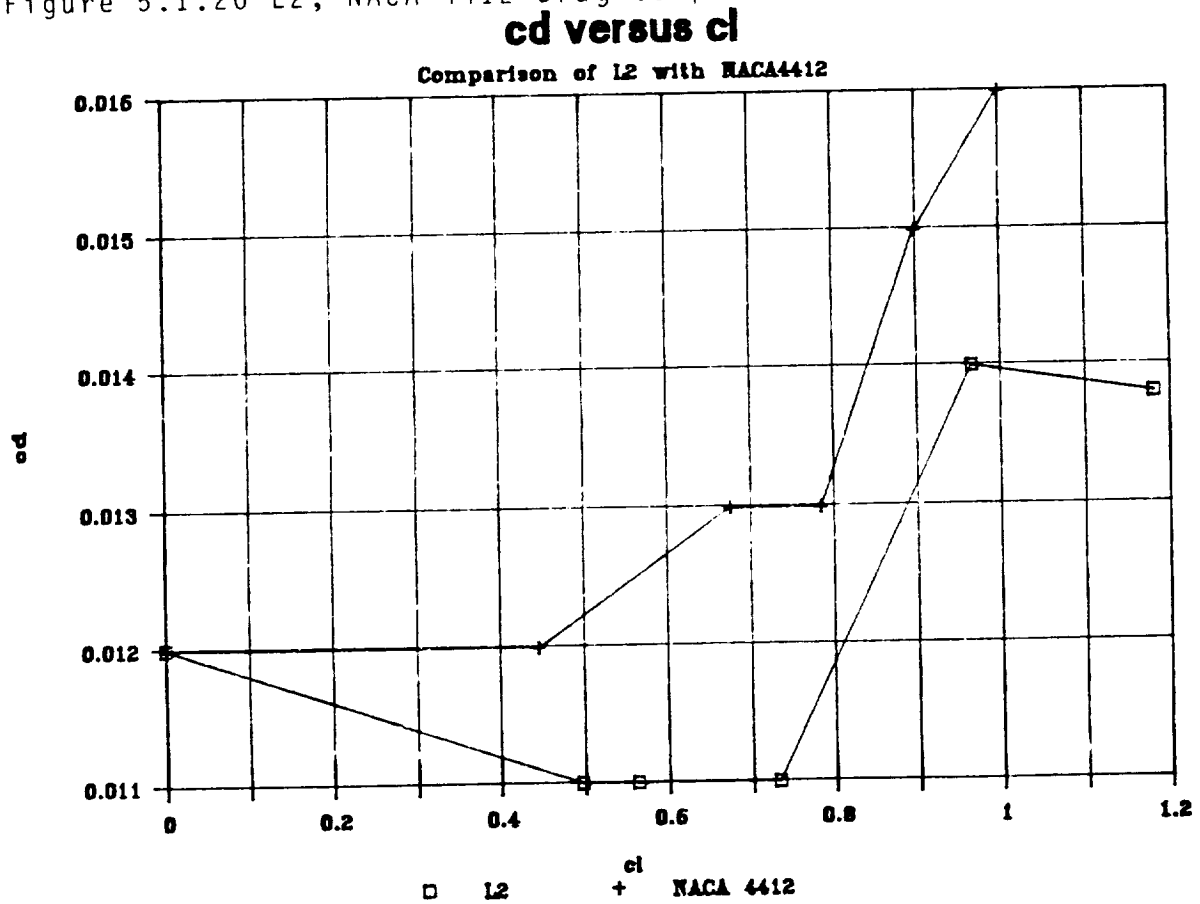


Figure 5.1.21 L3, NACA 4409 Drag Comparison

cd versus cl

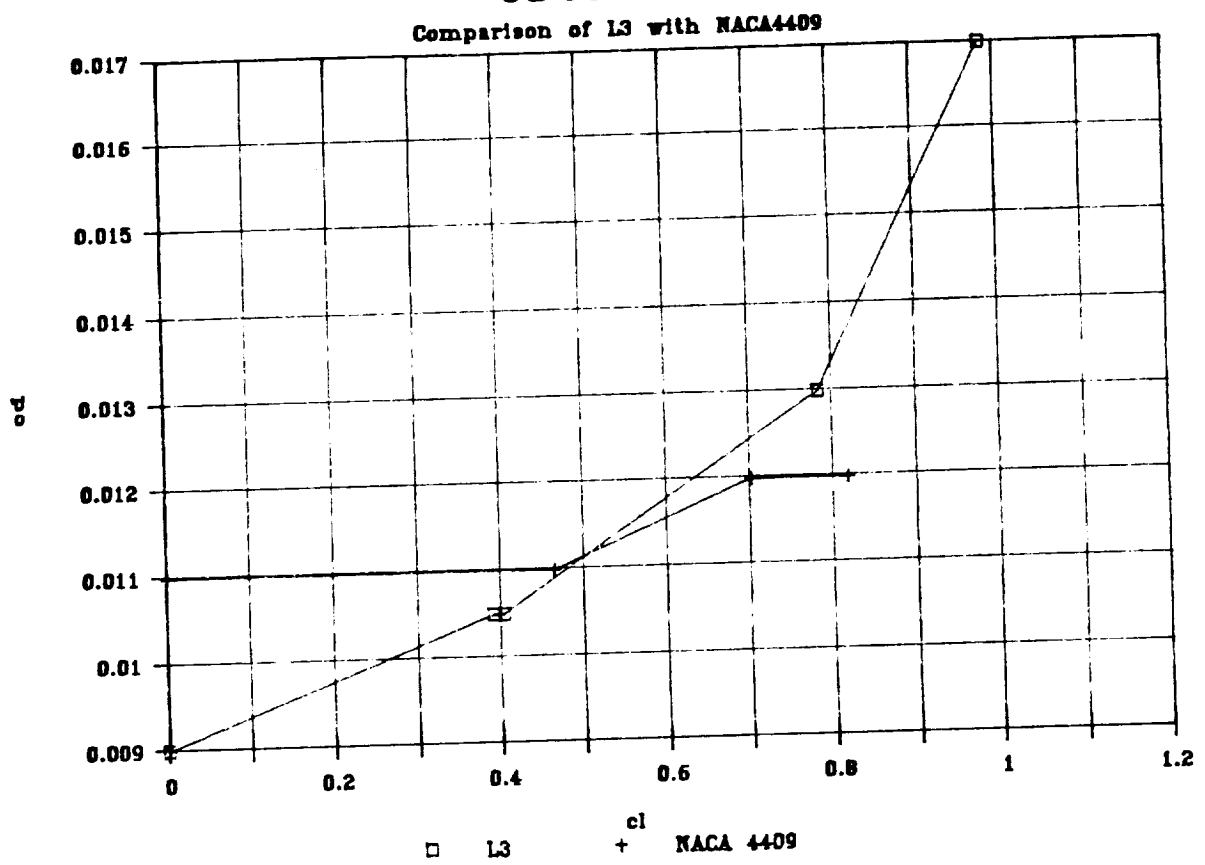


Figure 5.1.22 L1, NACA 4415 Lift Comparison

Section c_l versus Angle of Attack

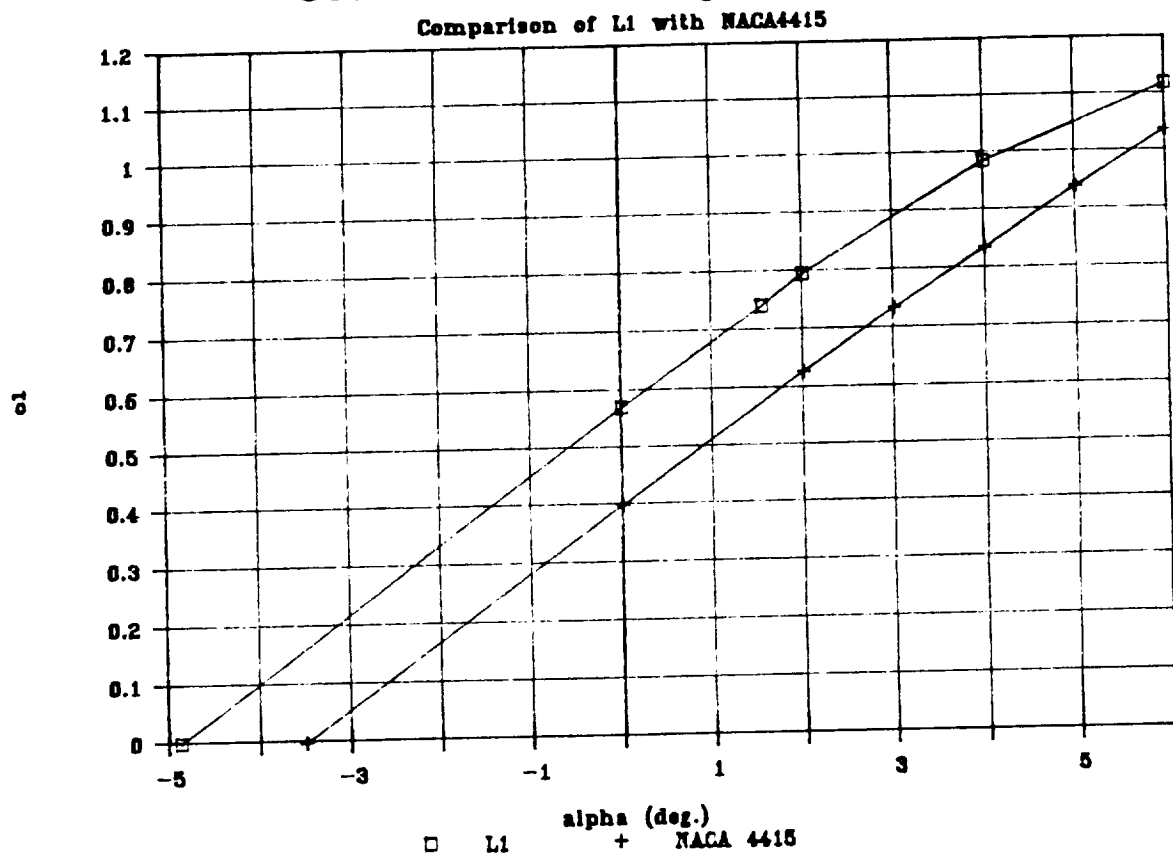


Figure 5.1.23 L2, NACA4412 Lift Comparison

Section c_l versus Angle of Attack

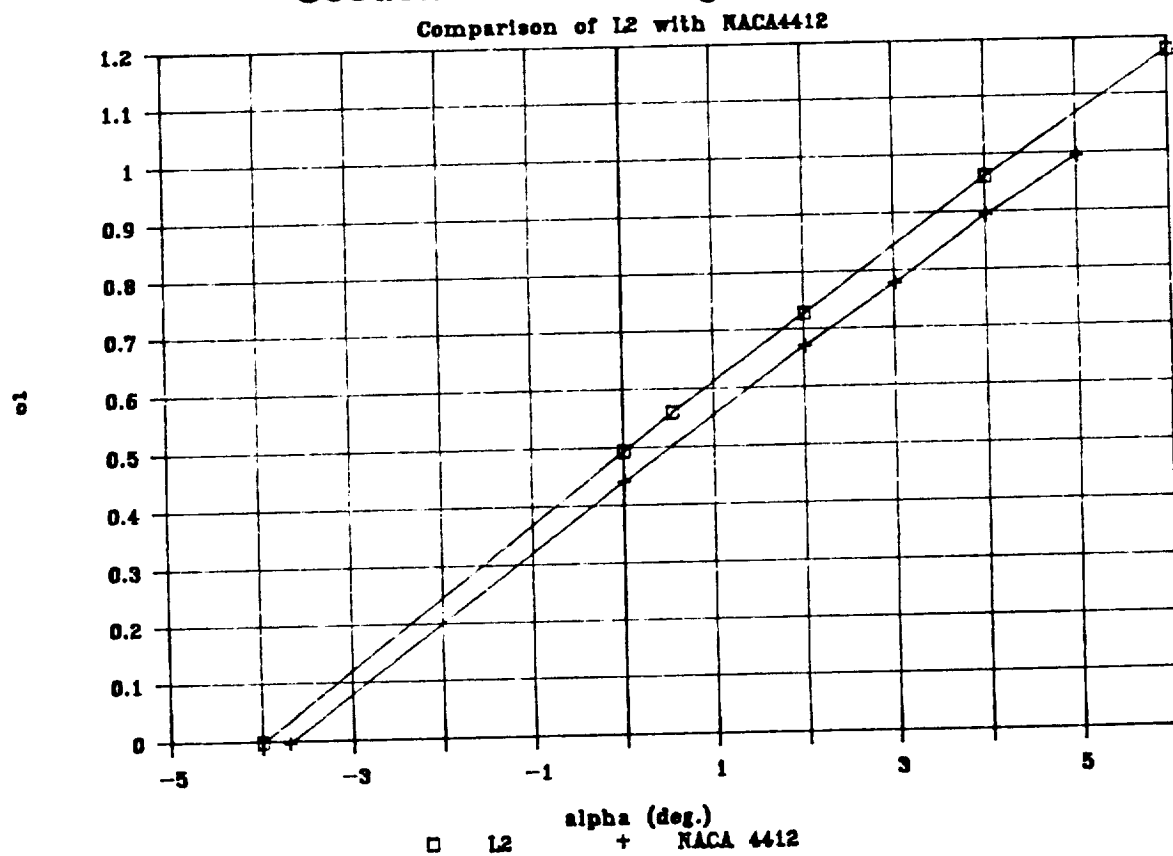


Figure 5.1.24 L3, NACA 4409 Lift Comparison

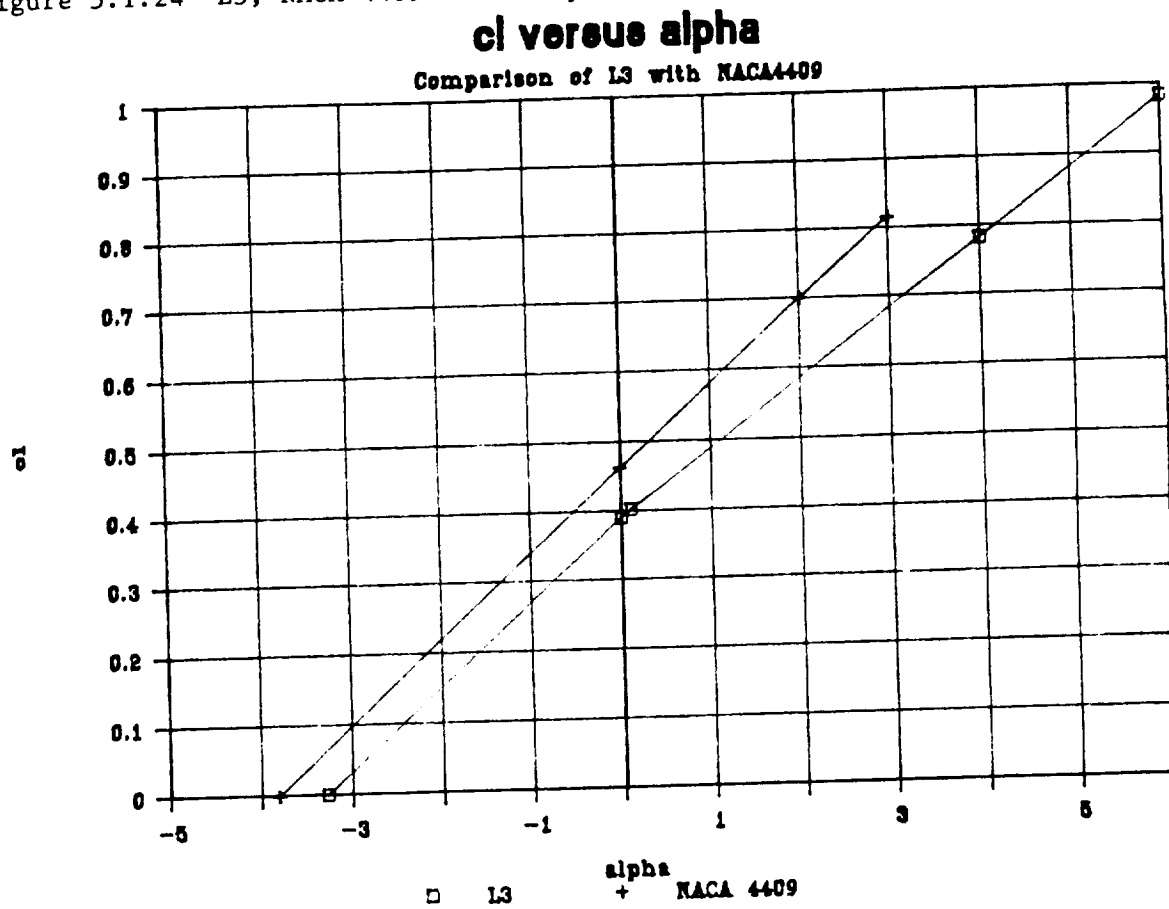


Figure 5.2.1

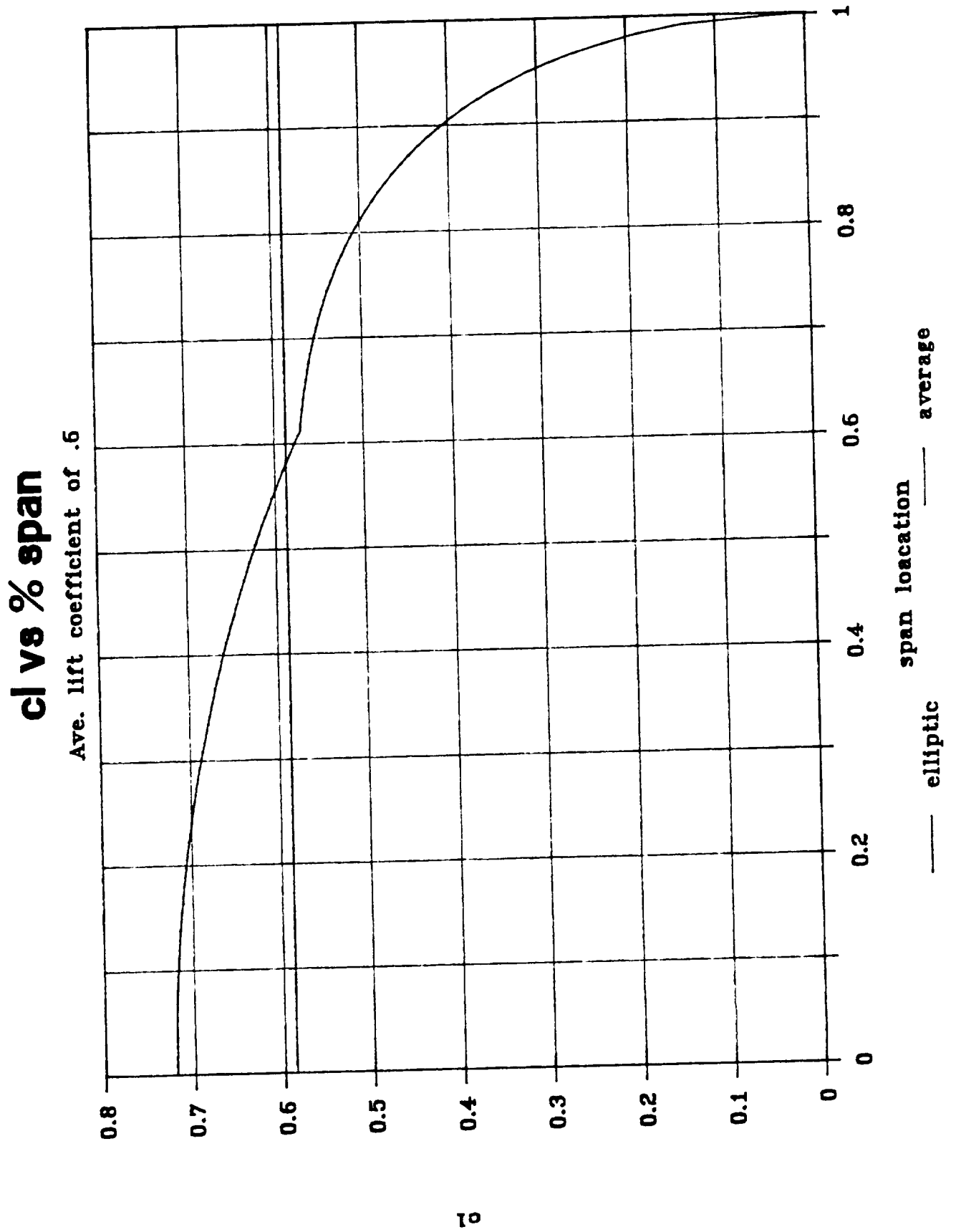


Figure 5.2.2

Airfoil Lift Curve Equations

Airfoil L1:	$c_l = 7.02 \alpha + .673$
Airfoil L2:	$c_l = 6.80 \alpha + .504$
Airfoil L3:	$c_l = 6.70 \alpha + .359$

Figure 5.2.3

Variation of Lift Curve Slope

lift curve slope:	
$0 < b < .6$	$m = -.3667b + 7.02$
$.6 < b < .9$	$m = -.3333b + 6.99$
$.9 < b < 1$	$m = \text{constant} = 6.69 \text{ per radian}$

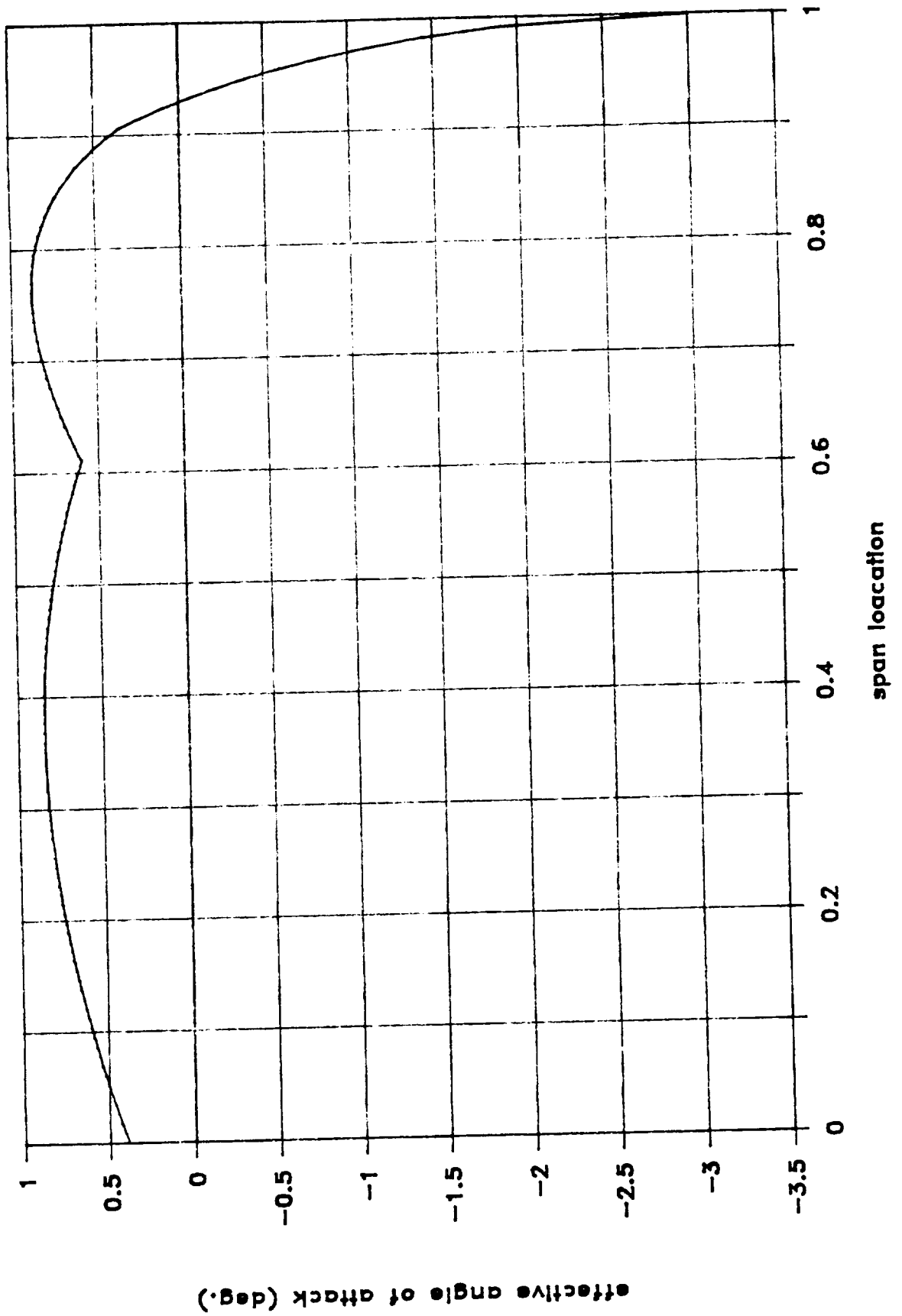
Figure 5.2.4

Variation of Zero Lift Angle of Attack

zero angle lift coefficient:	
$0 < b < .6$	$c_{l_{\alpha=0}} = -.2813b + .673$
$.6 < b < .9$	$c_{l_{\alpha=0}} = -.4852b + .7953$
$.9 < b < 1$	$c_{l_{\alpha=0}} = \text{constant} = .3586$

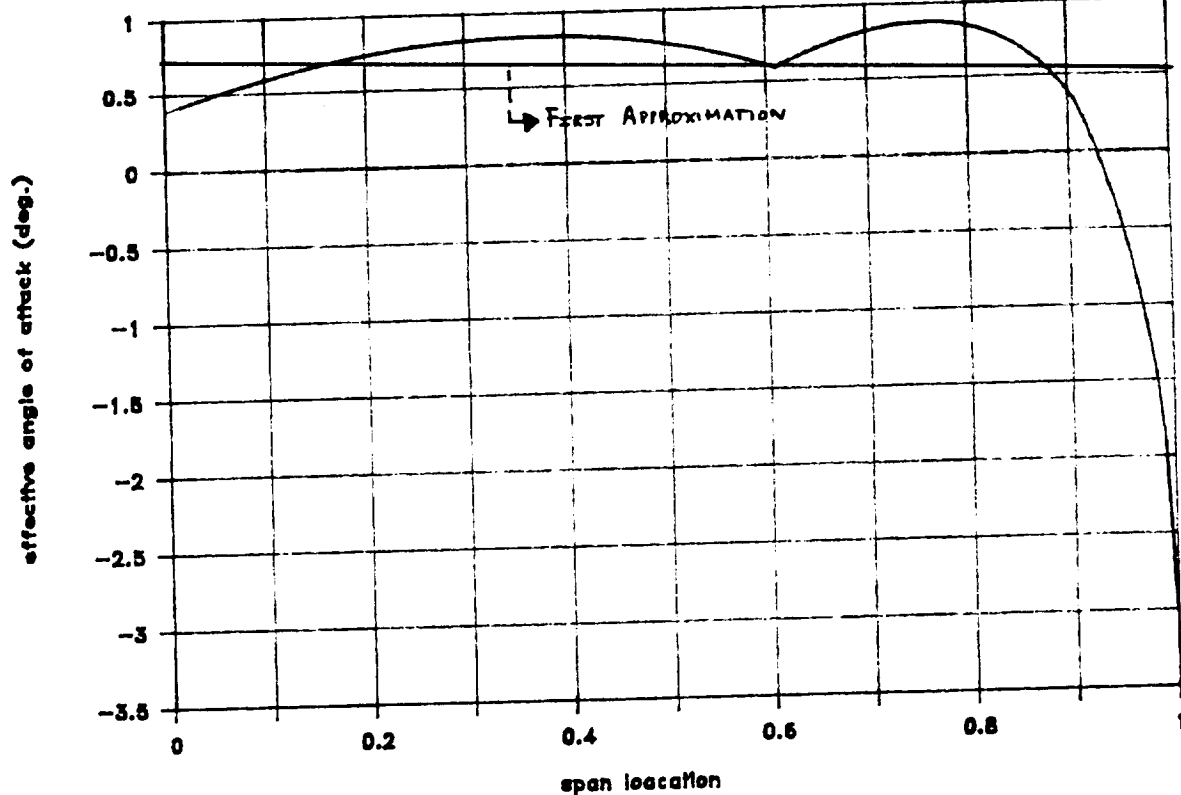
Figure 5.2.5

Twist Distribution



Twist Distribution

Figure 5.2.6



Twist Distribution

Figure 5.2.7

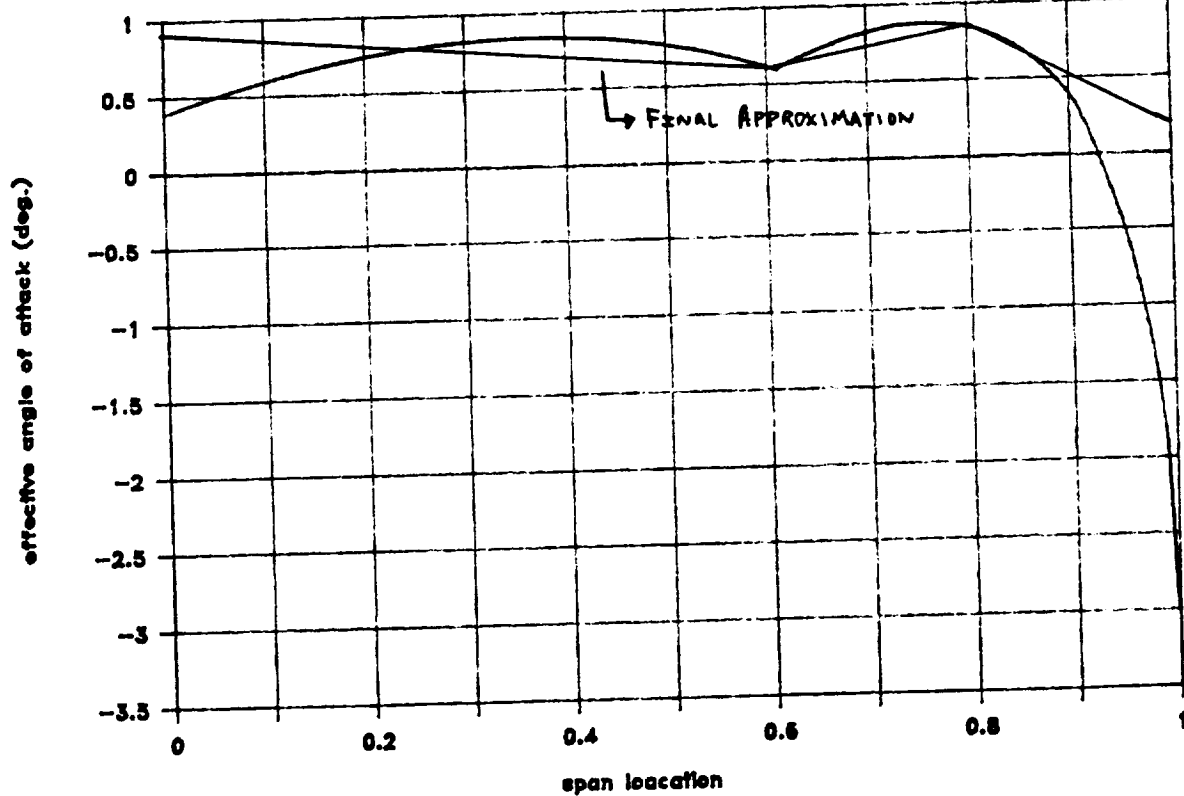











Figure 5.2.8

BL 0 TWIST 0.8 DEG. CHORD 16.5'		
BL 180 TWIST 0.75 DEG. CHORD 16.5'		
BL 360 TWIST 0.70 DEG. CHORD 16.5'		
BL 540 TWIST 0.65 DEG. CHORD 16.5'		
BL 720 TWIST 0.60 DEG. CHORD 16.5'		
BL 900 TWIST 0.61 DEG. CHORD 15.97'		
BL 1080 TWIST 0.79 DEG. CHORD 14.32'		
BL 1260 TWIST 0.20 DEG. CHORD 12.67'		
BL 1404 TWIST 3.00 DEG. CHORD 11.5'		
TITLE: MAIN WING-TWIST & LOCATION		NO: 1
DRAWN BY: TOM JUTRAS		SHEET: 1
DATE: 4/8/90		
WPI CAD LABORATORY		
SCALE: 1:1000		

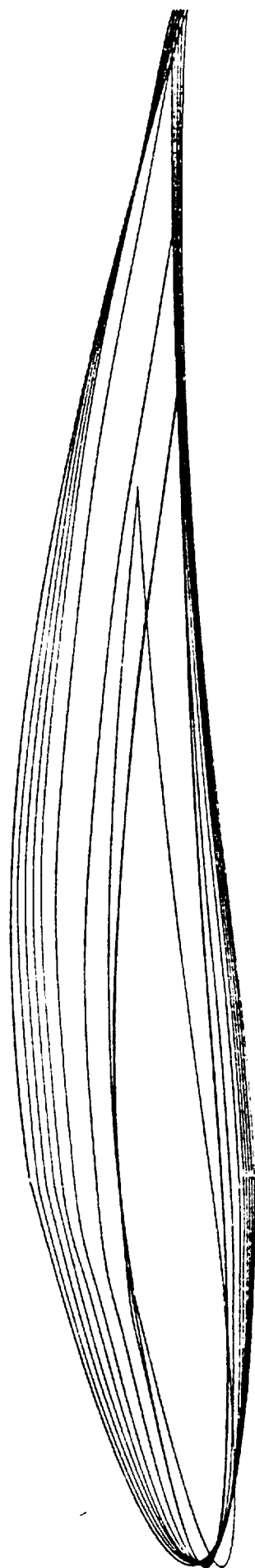
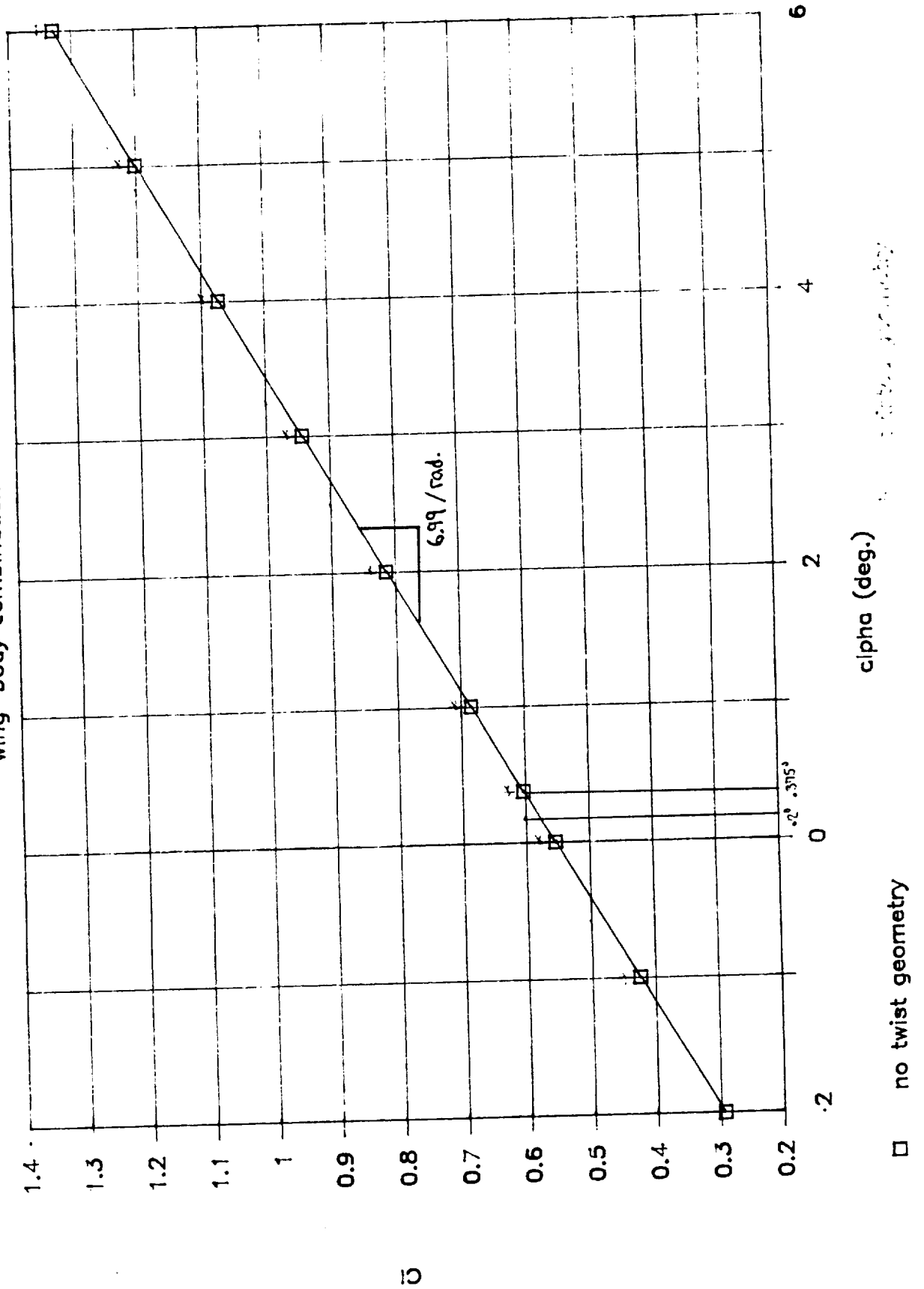


Figure 5.2.9

WPI CAD LABORATORY	TITLE: MAIN WING - SIDE VIEW	NO: 1
SCALE: .05	DRAWN BY: TOM JUTRAS	SHEET: 1
DATE: 4/8/90		

Figure 5.2.10

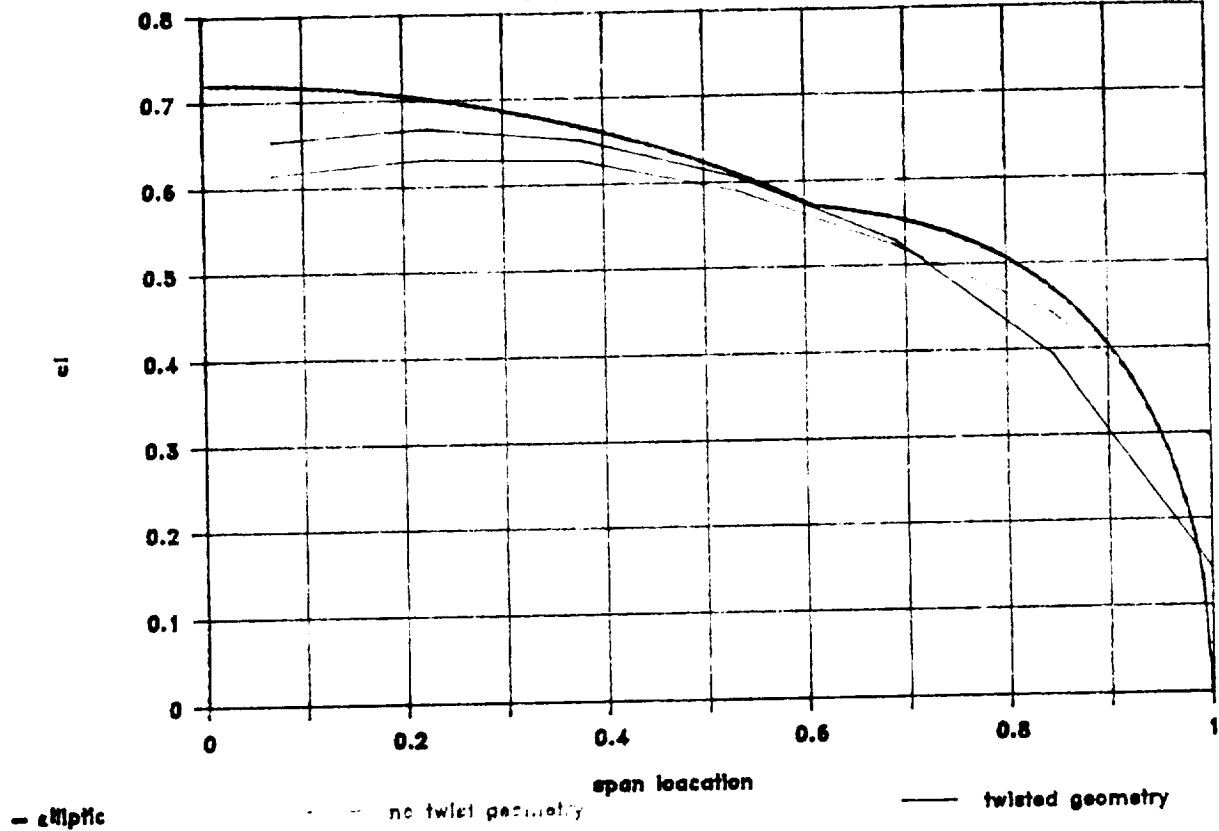
Cl vs Alpha wing-body combination



Section c_l vs Span

Ave. lift coefficient of .6

Figure 5.2.11



L' vs. %Span

Ave. lift coefficient of .6

Figure 5.2.12

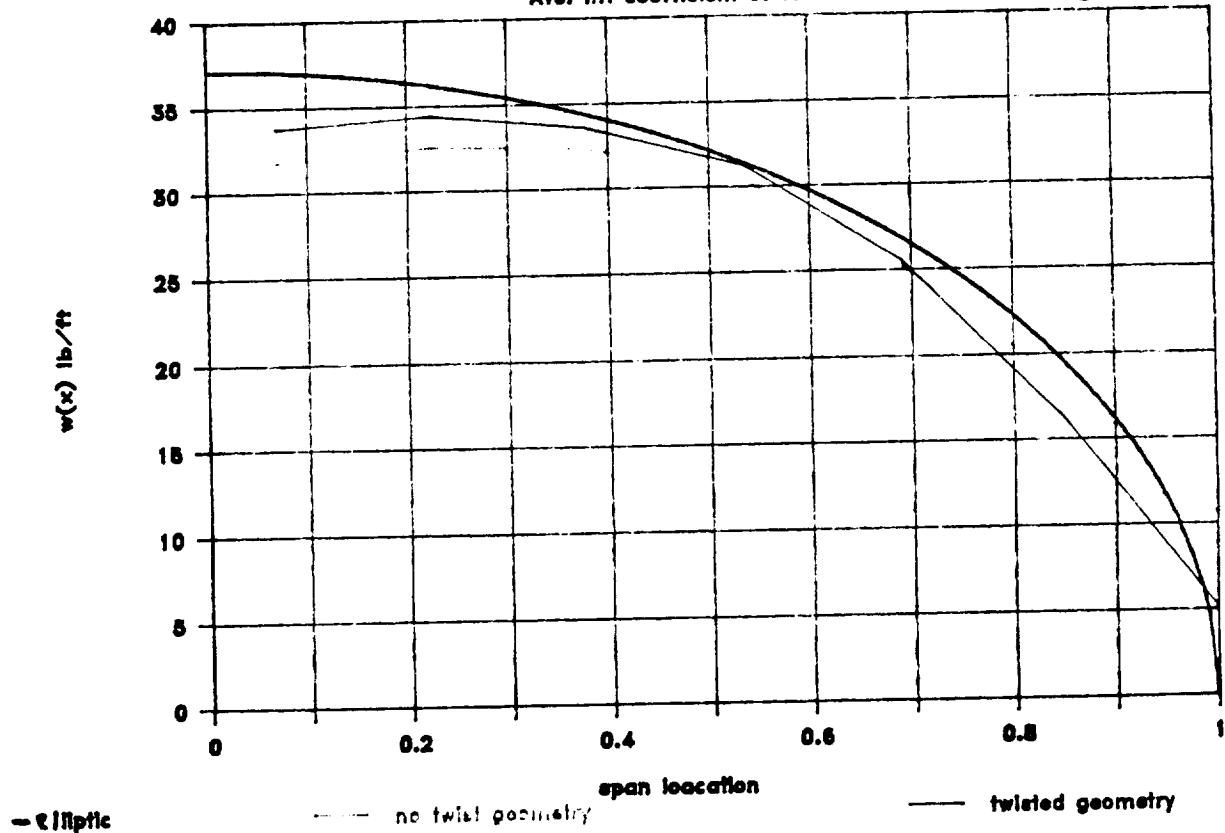


Figure 5.2.13

Untwisted Planform

$C_L = 0.4237$

$\alpha = -1.0^\circ$

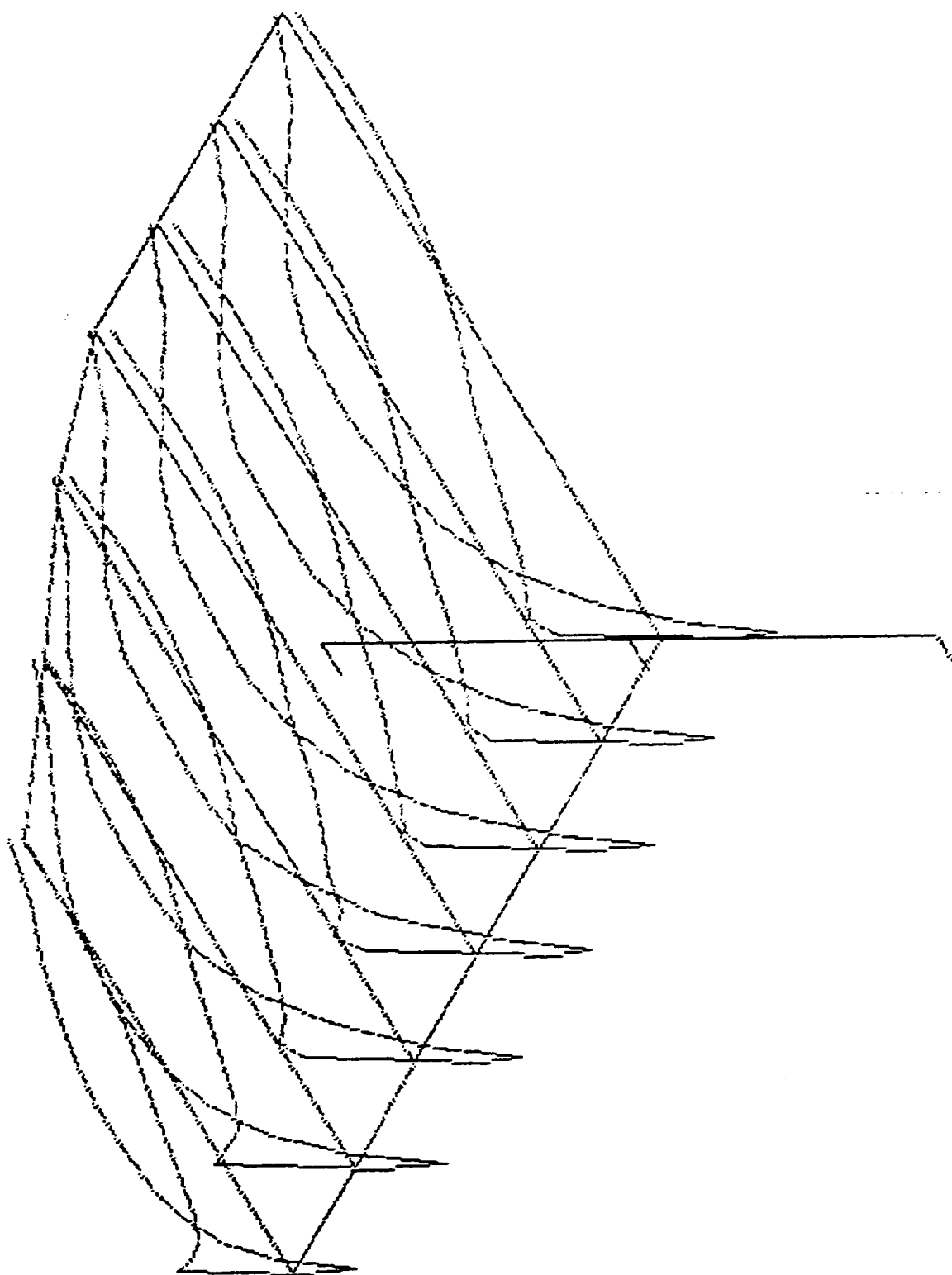


Figure 5.2.14

Untwisted Planform
 $C = 0.600$
 $\alpha = 0.375^\circ$
Design Point

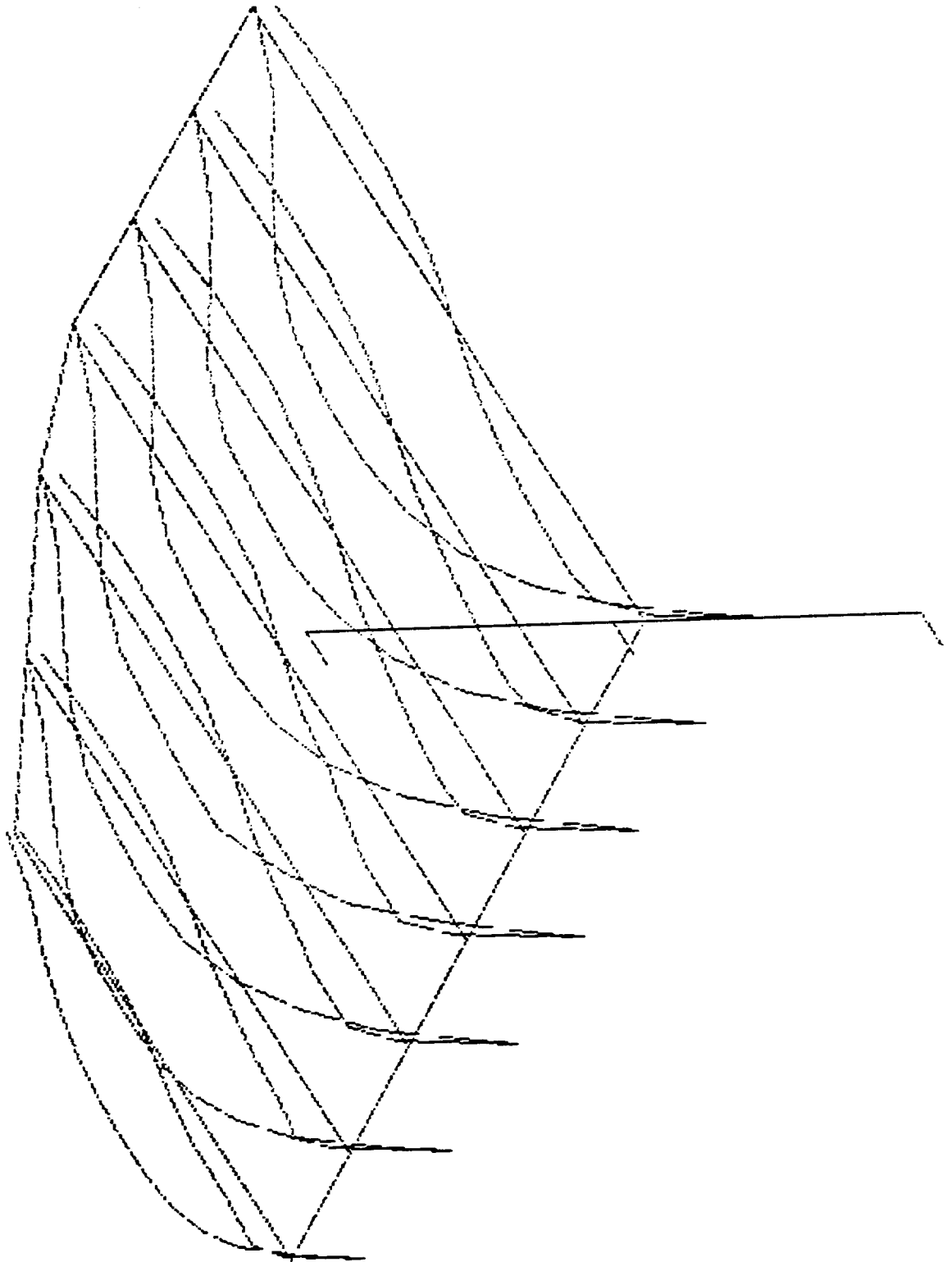


Figure 5.2.15

Untwisted Planform

$C_L = 0.814$

$\alpha = 2.0^\circ$

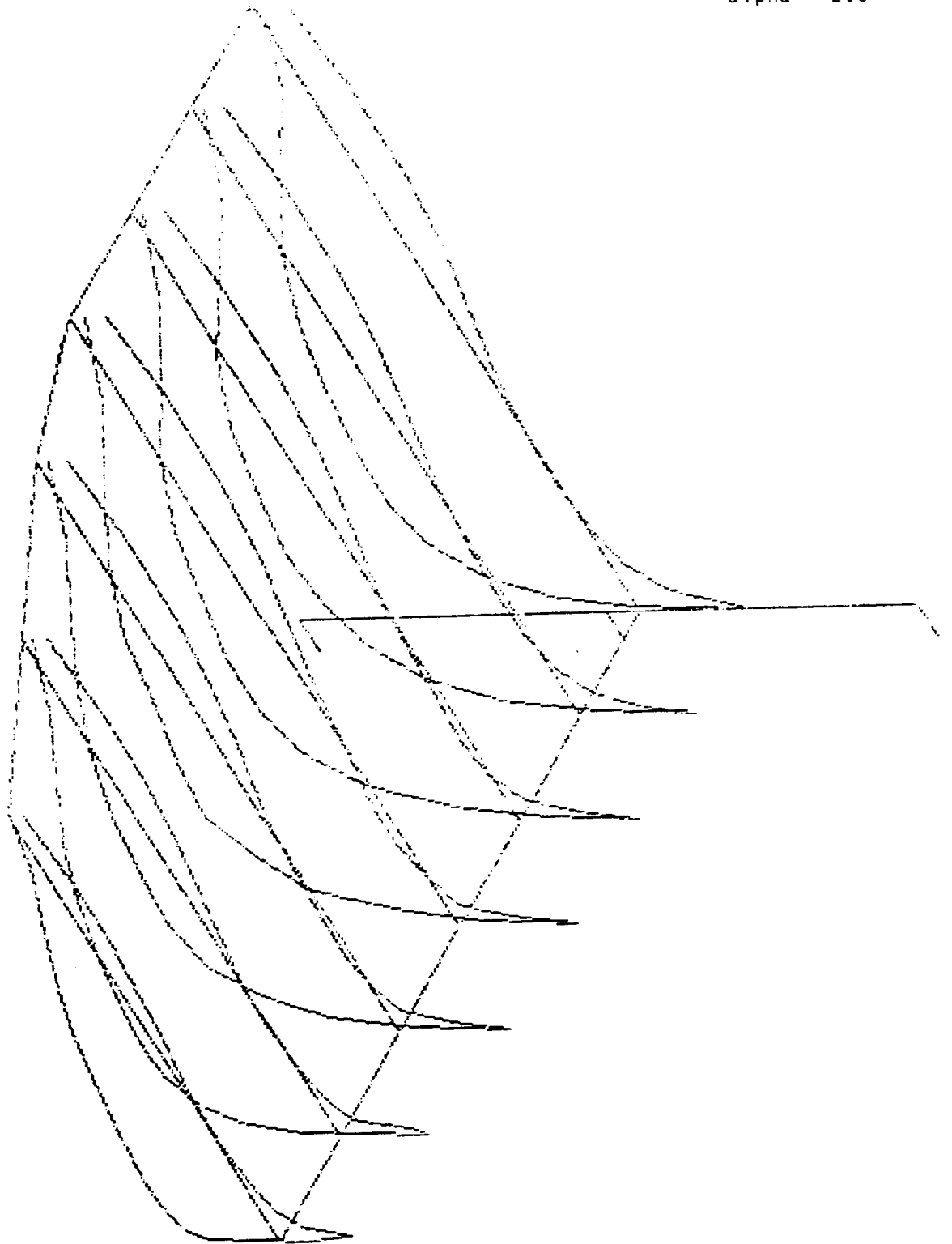


Figure 5.2.16

Untwisted Planform
 $C_l = 1.2$
 $\alpha = 5.0^\circ$

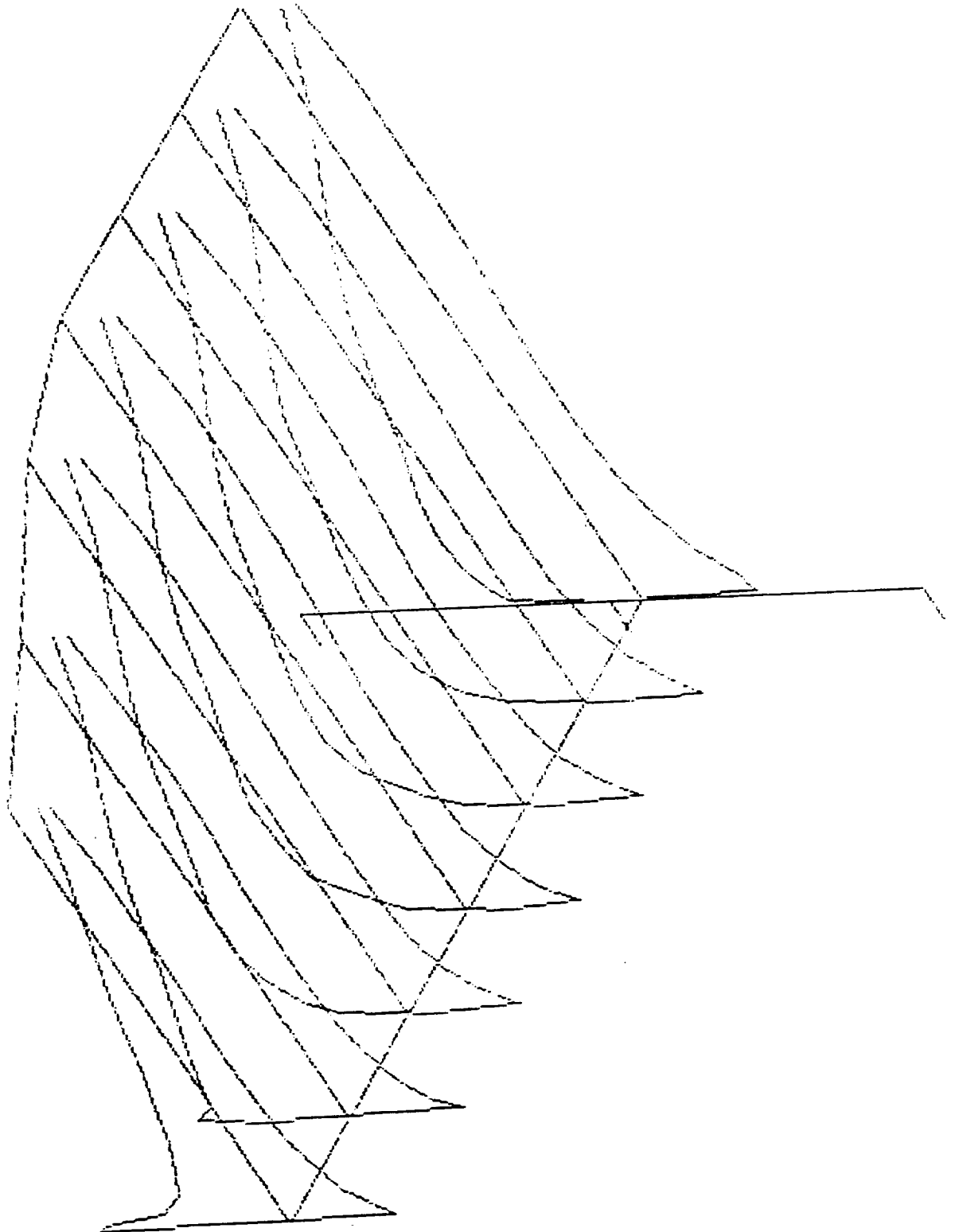


Figure 5.2.17

Twisted Planform

$C_L = .4485$

$\alpha = -1.0^\circ$

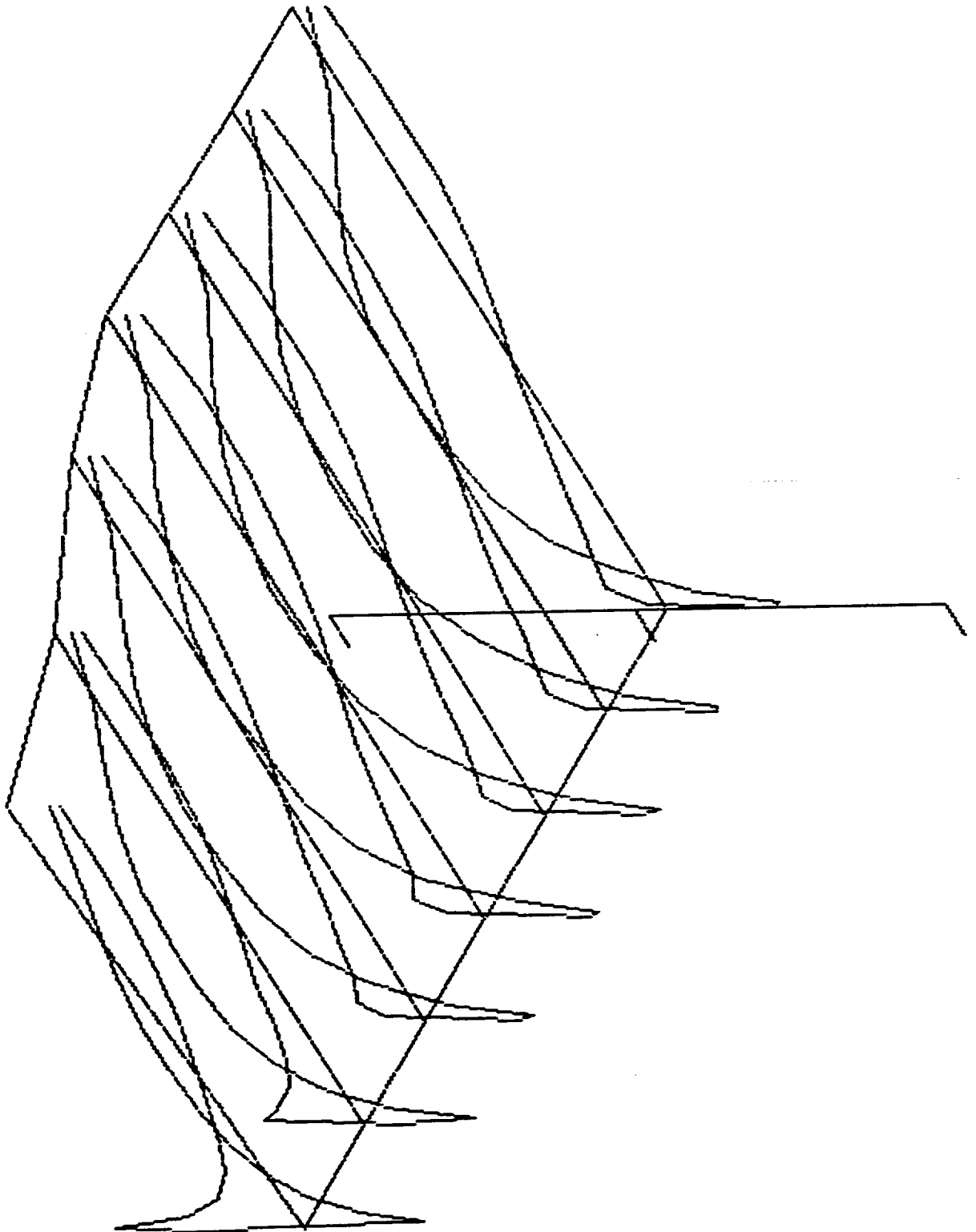


Figure 5.2.18

$C_l = 0.6$

$\alpha = 0.2^\circ$

Twisted Planform

Design Point

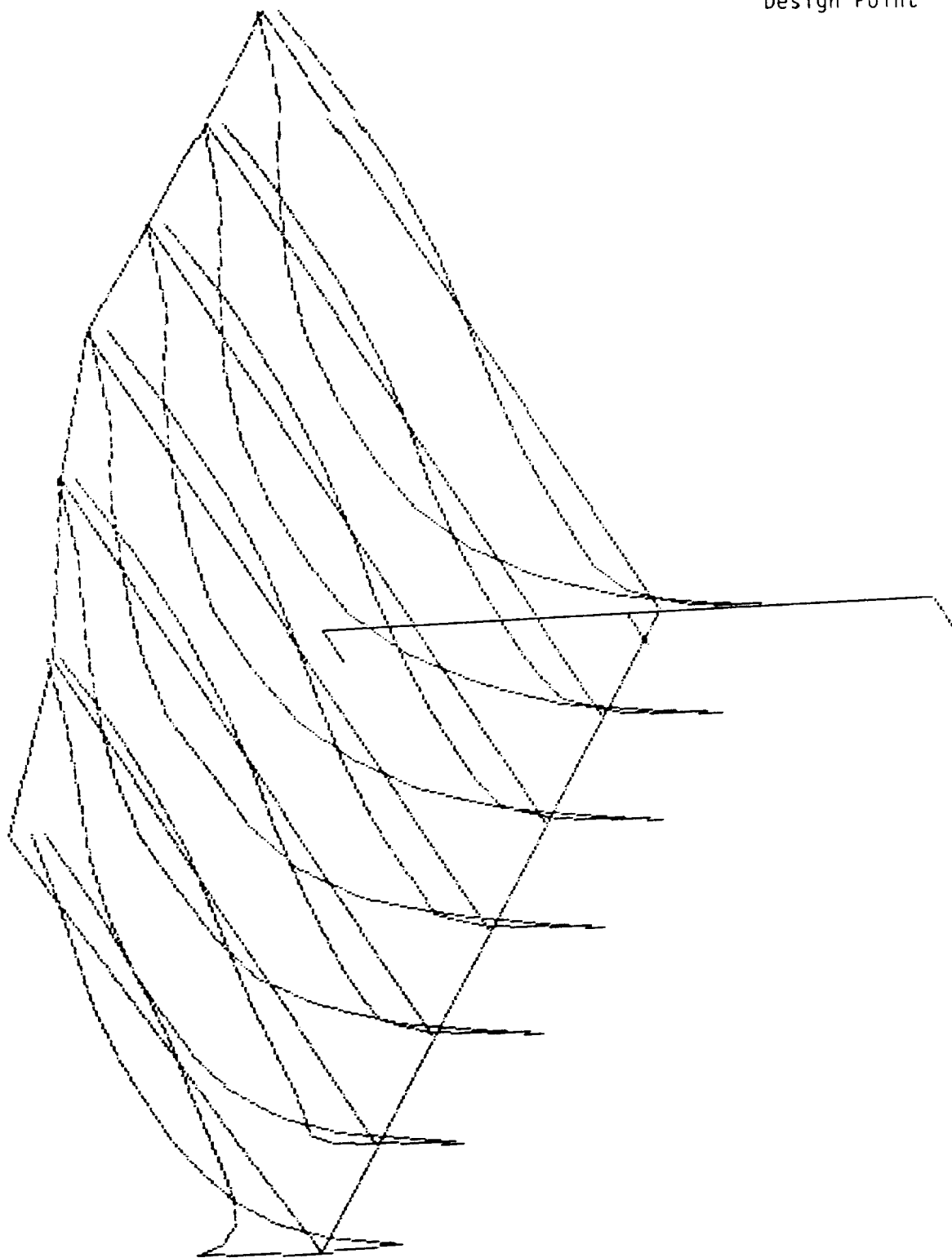


Figure 5.2.19

Twisted Planform

$C_L = 0.838$

$\alpha = 2.0^\circ$

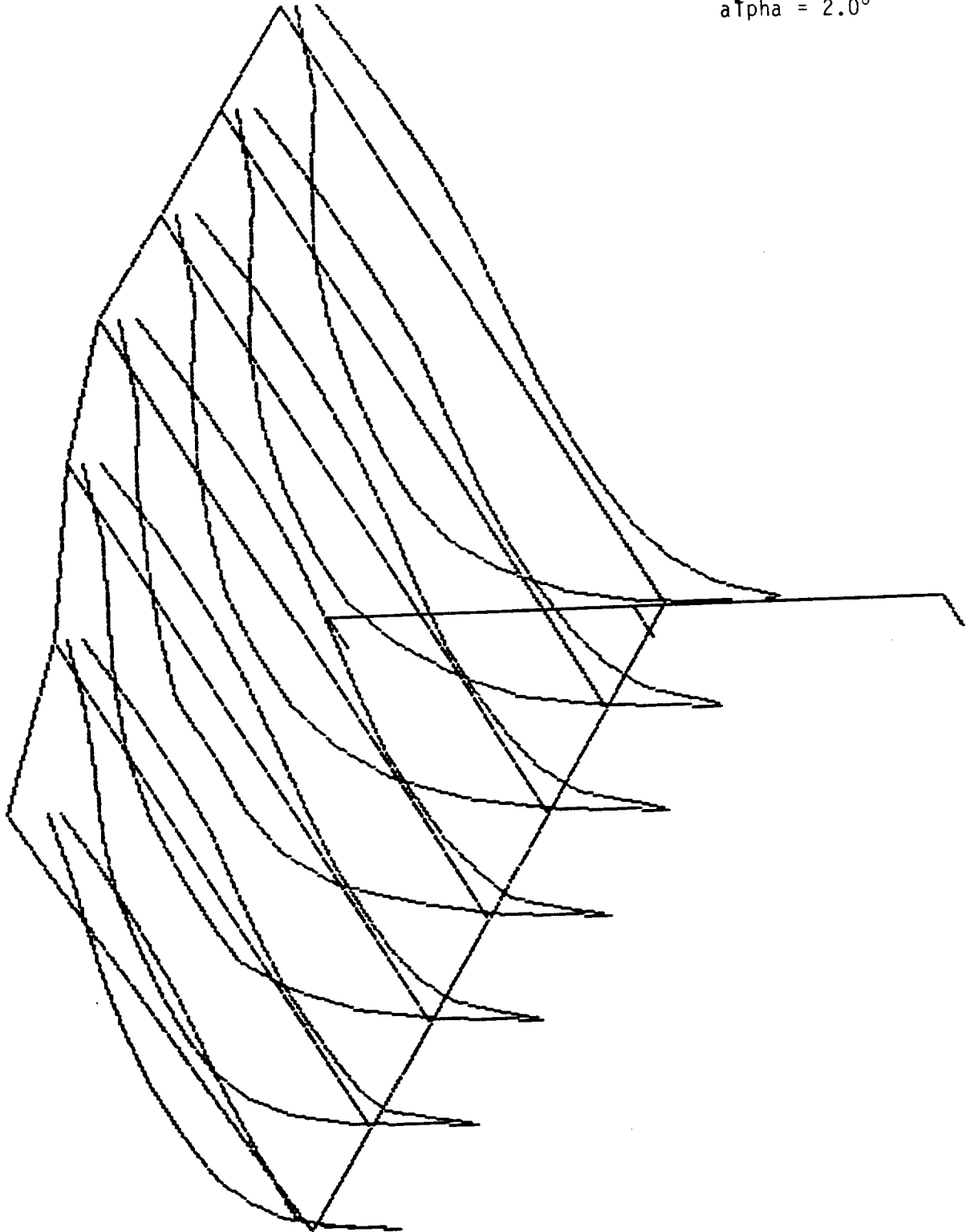


Figure 5.2.20

Twisted Planform

$C_l = 1.23$

$\alpha = 5.0^\circ$

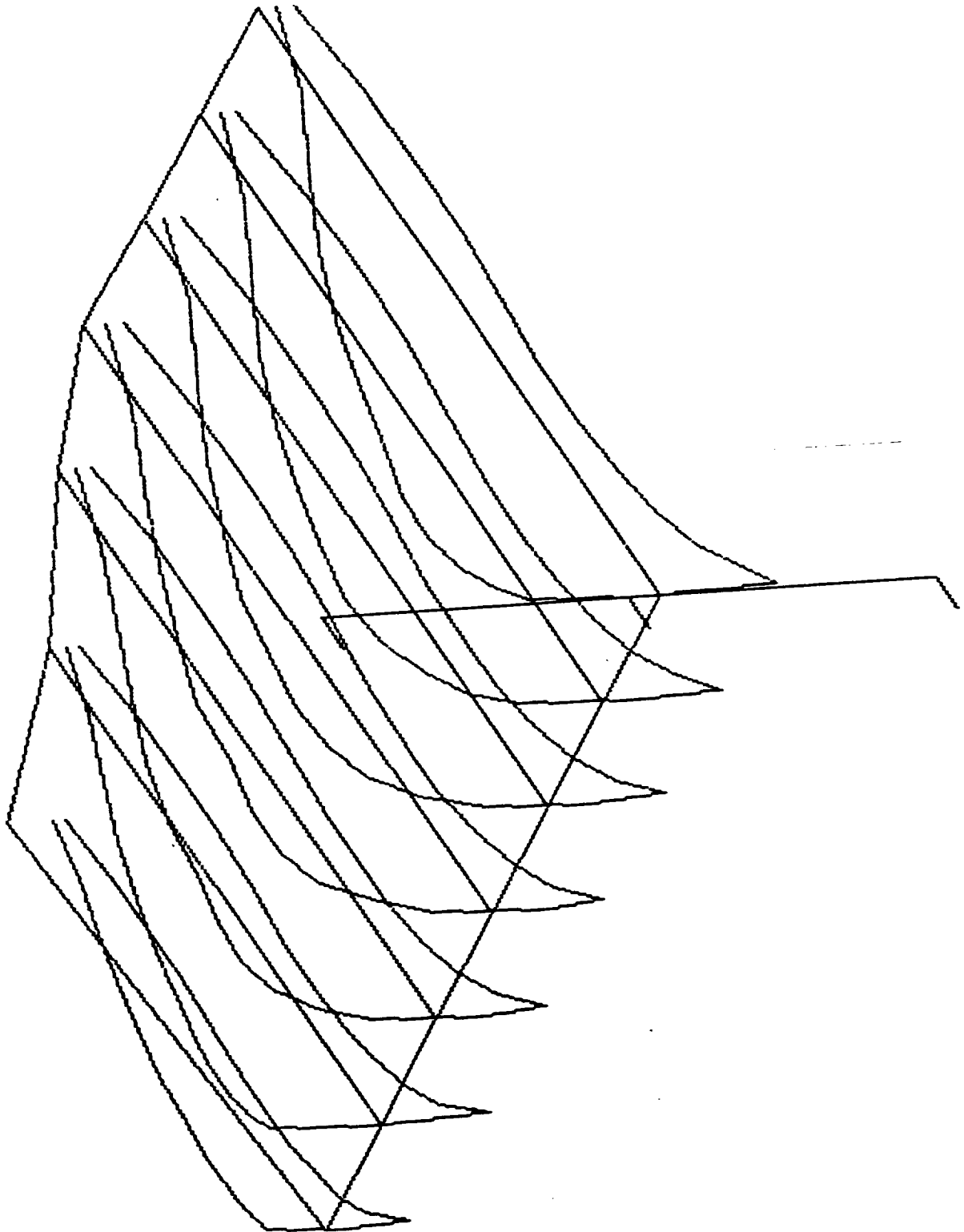


Figure 5.2.21

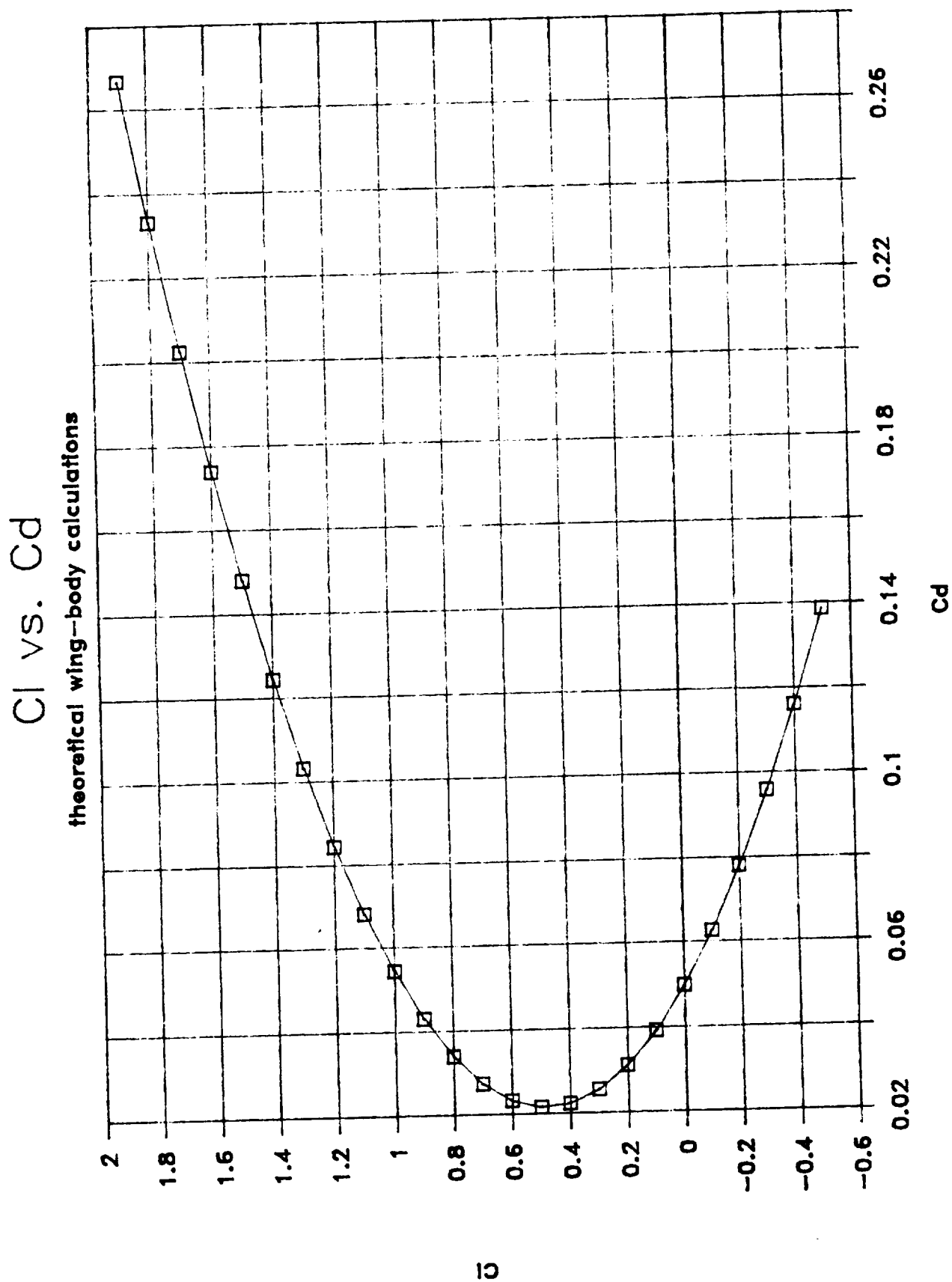
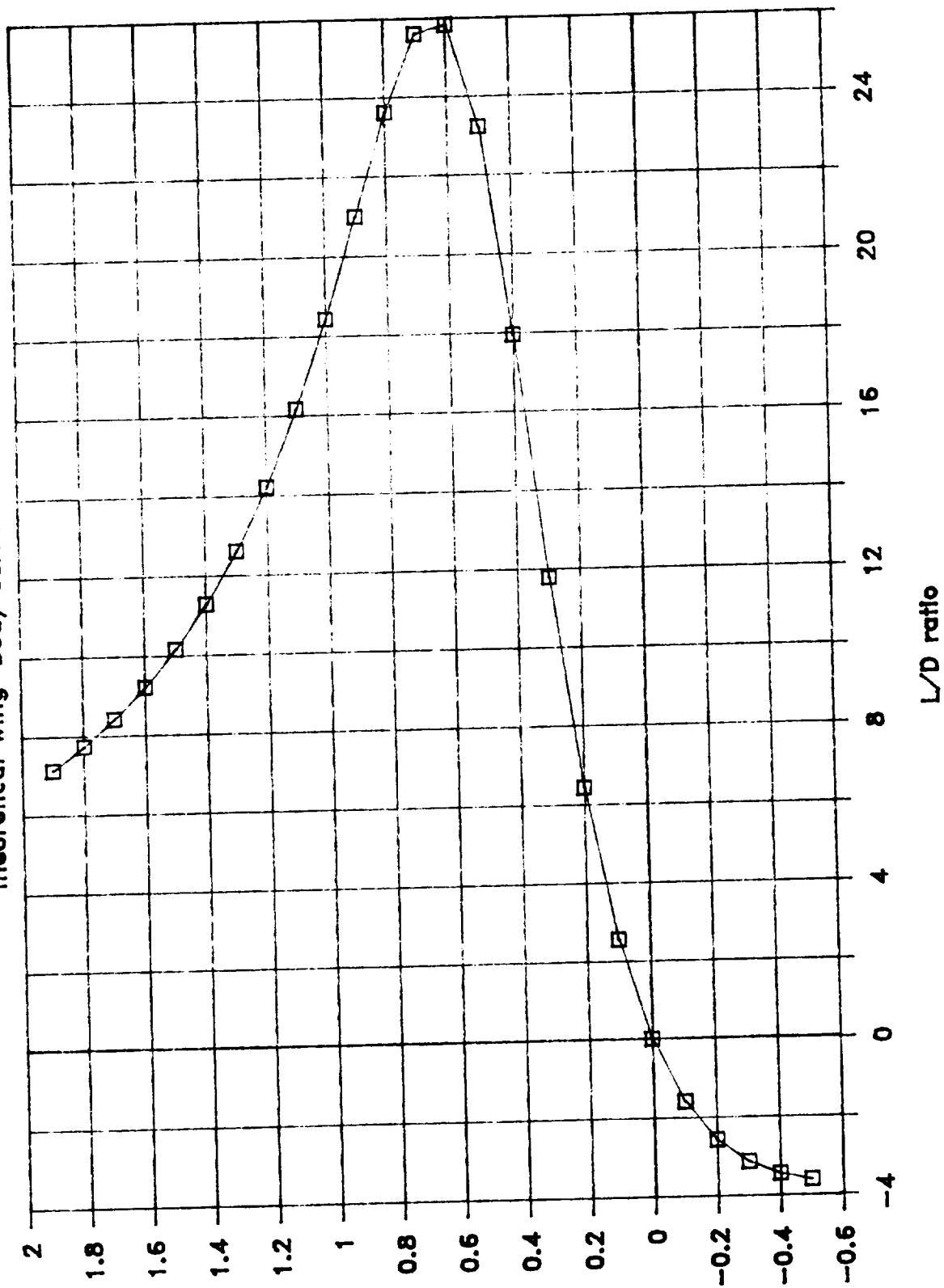


Figure 5.2.22

CI vs. L/D Ratio
theoretical wing-body calculations



ANSYS 4.3A2
FEB 18 1990
16: 41: 31
ELEMENTS

XV -1
YV -1
ZV -1
DIST=600
XF -90
YF -10.8
ZF -690

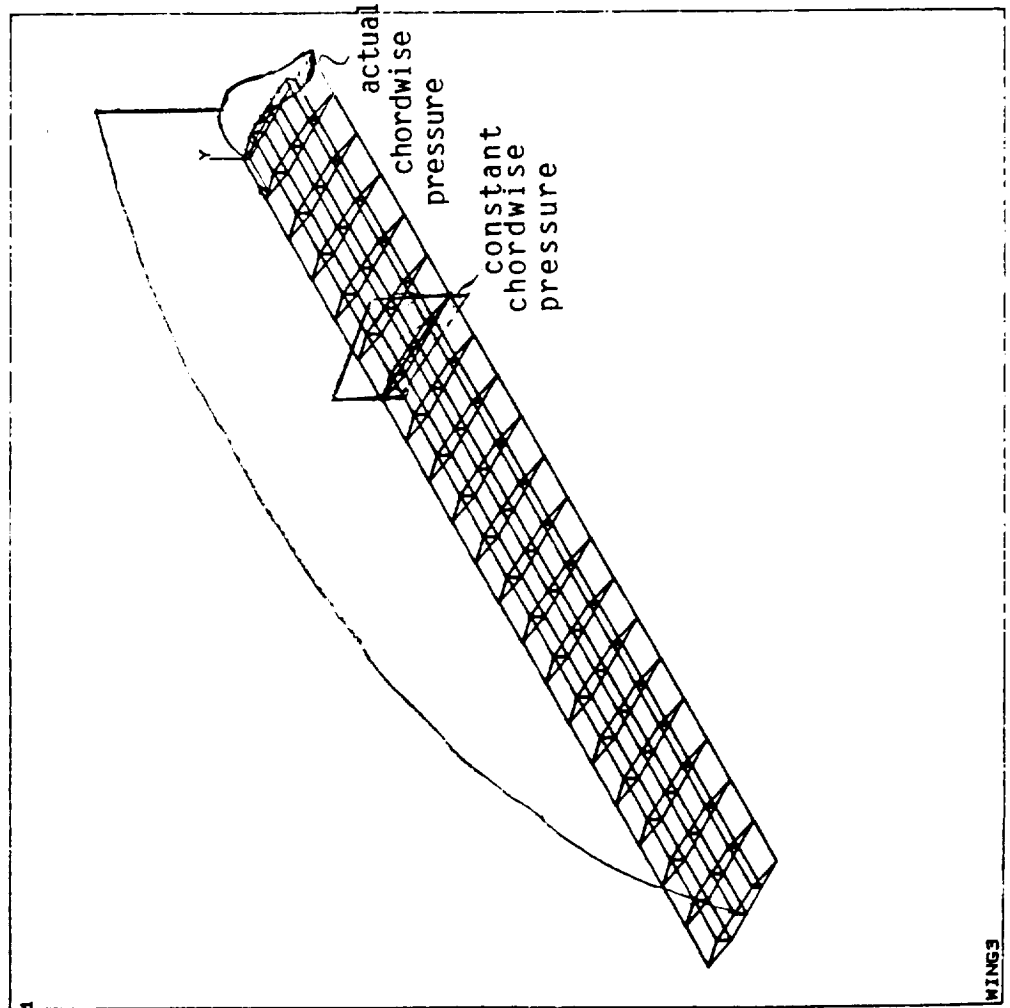


FIGURE 6.1.1
Spanwise & Chordwise
Pressure Distribution

Root Pressure Distribution

Figure 6.1.2
Average Chordwise Pressure Distribution

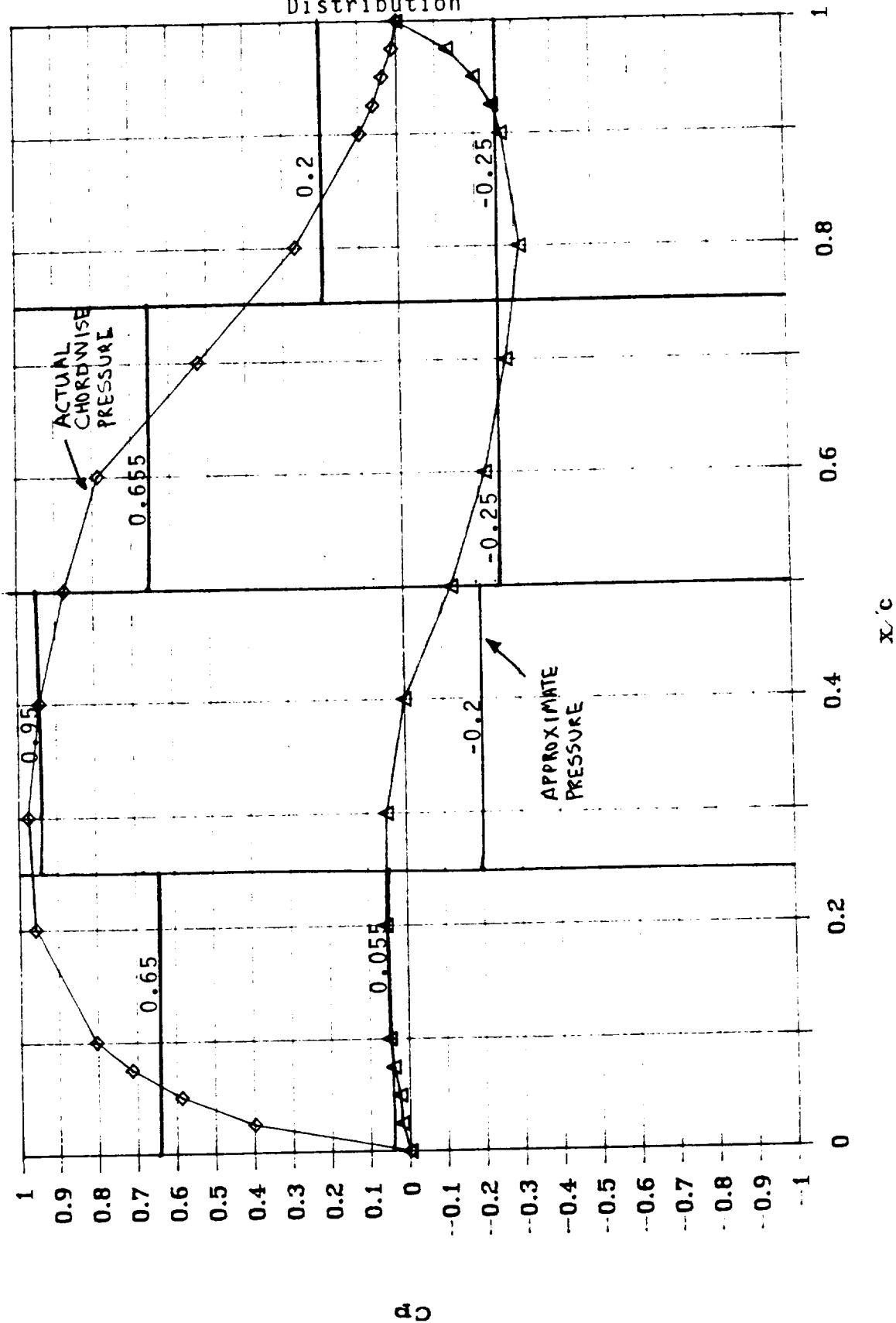
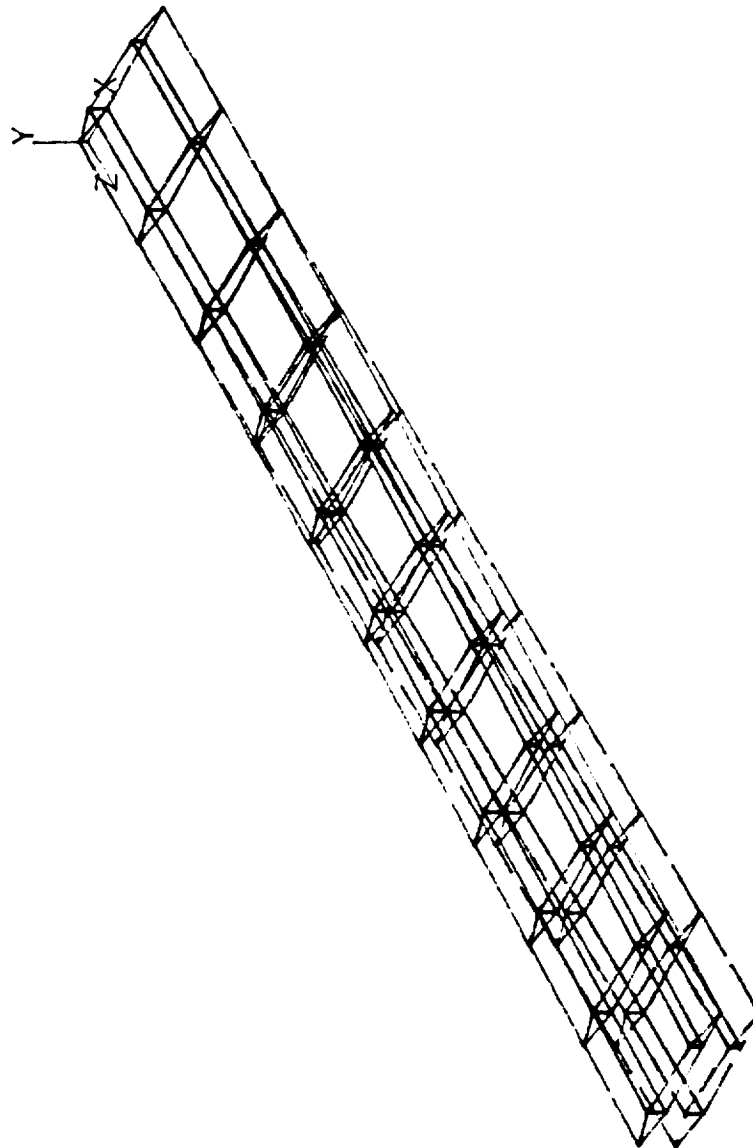


Figure 6.1.3
Model #1

DISPL:
STEP=1
ITER=1
XV = 1
YV = 1
ZV = 1
DIST=650
XF = 90
YF = 10.8
ZF = 690



DMX = 198 Weight = 2050 BAR

Figure 6.1.4
Model #1

DISPL.
STEP=1
ITER=1

XV = 1
DIST=800
XF = 90
YF = 10.8
ZF = 690

ORIGINAL PAGE IS
OF POOR QUALITY



DMX = 198 Weight = 2050 BAR

Figure 6.1.5
Model #1

ORIGINAL PAGE IS
OF POOR QUALITY

STRESS
STEP=1
ITER=1
SXY (AVG)
MIDDLE
ELEM CS
SMN = -1010
SMX = 2184

YV = 1
DIST=800
XF = 90
YF = 10.8
ZF = 690
XRT0=7<-
PRECISE HIDDEN

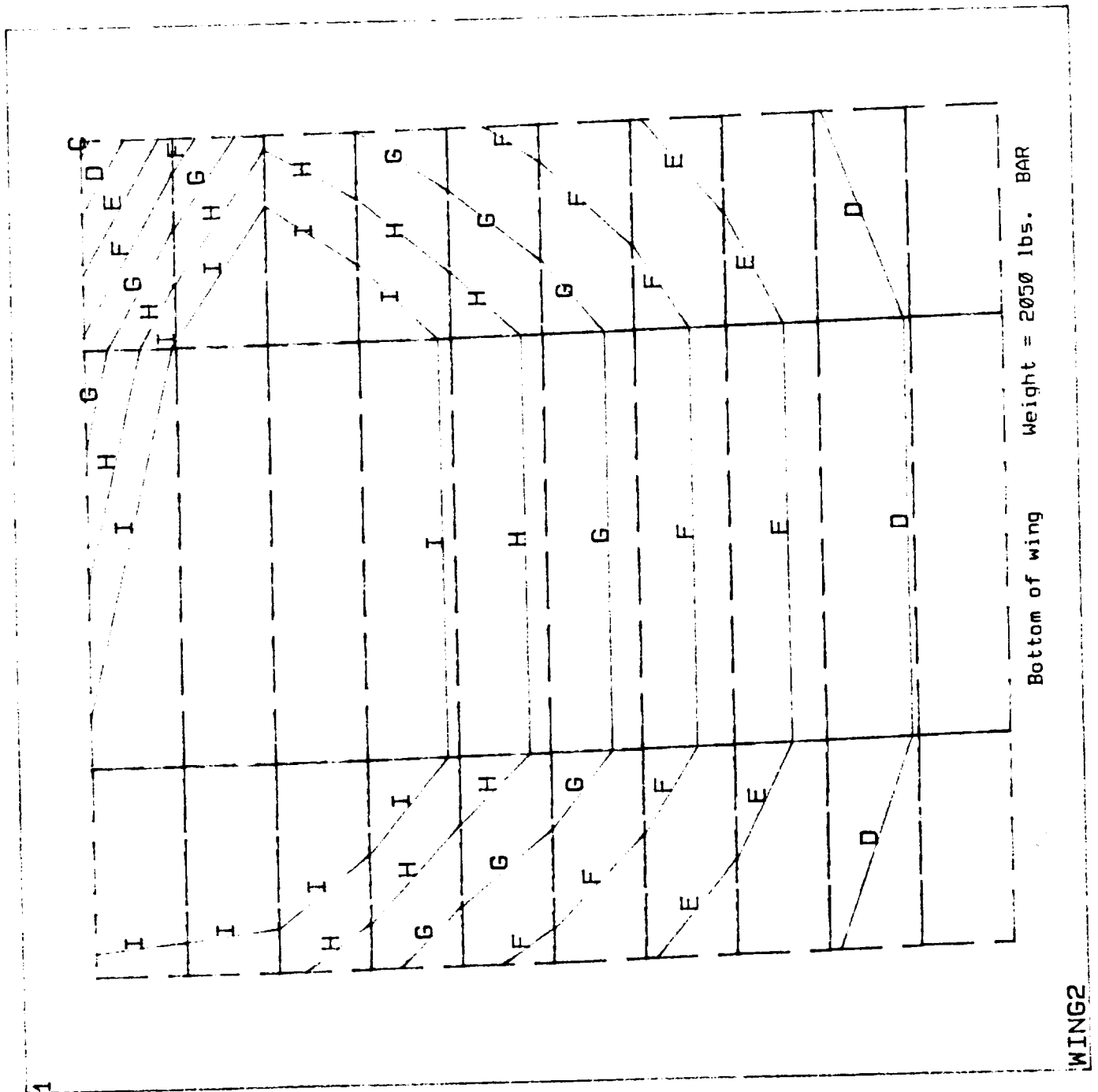
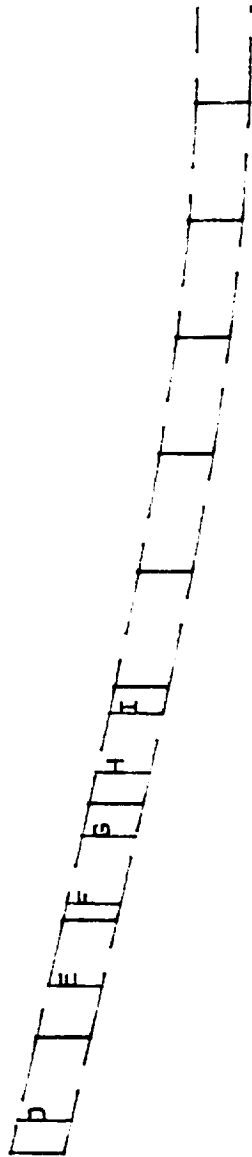


Figure 6.1.6
Model #1

ORIGINAL PAGE IS
OF POOR QUALITY

ANSYS 4.3A2
DEC 12 1989
18:50:14
STRESS
STEP=1
ITER=1
SXY (AVG)
MIDDLE
ELEM CS
SMN =-1010
SMX =2184

XV =1
DIST=800
XF =90
YF =10.8
ZF =690
YRTO=3 <-
PRECISE HIDDEN
A =-832.252
B =-477.347
C =-122.441
D =232.464
E =587.37
F =942.275
G =1297
H =1652
I =2007



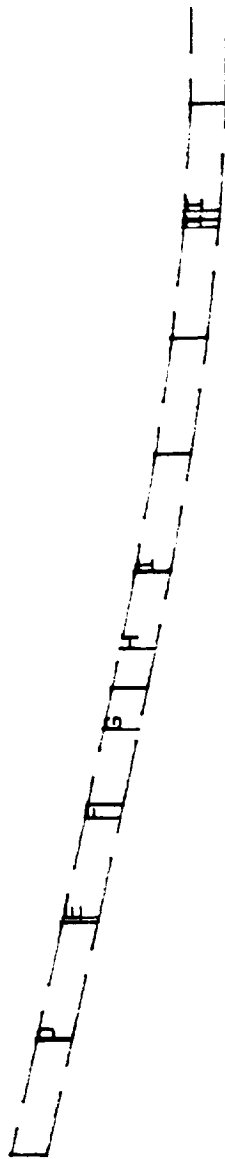
WING2

Right I beam Weight = 2050 lbs. BAR

Figure 6.1.7
Model #1

ORIGINAL PAGE IS
OF POOR QUALITY

ANSYS 4.3A2
DEC 12 1989
18: 47: 24
STRESS
STEP=1
ITER=1
SXY (AVG)
MIDDLE
ELEM CS
SMN --1010
SMX --2184
XV -1
DIST=800
XF -90
YF -10.8
ZF -690
YRTO=3 <-
PRECISE HIDDEN
A --832.252
B --477.347
C --122.441
D --232.464
E --587.37
F --942.275
G --1297
H --1652
I --2007



WING2

Left I beam

Weight = 2050 lbs. BAR

Figure 6.1.8
Model #1

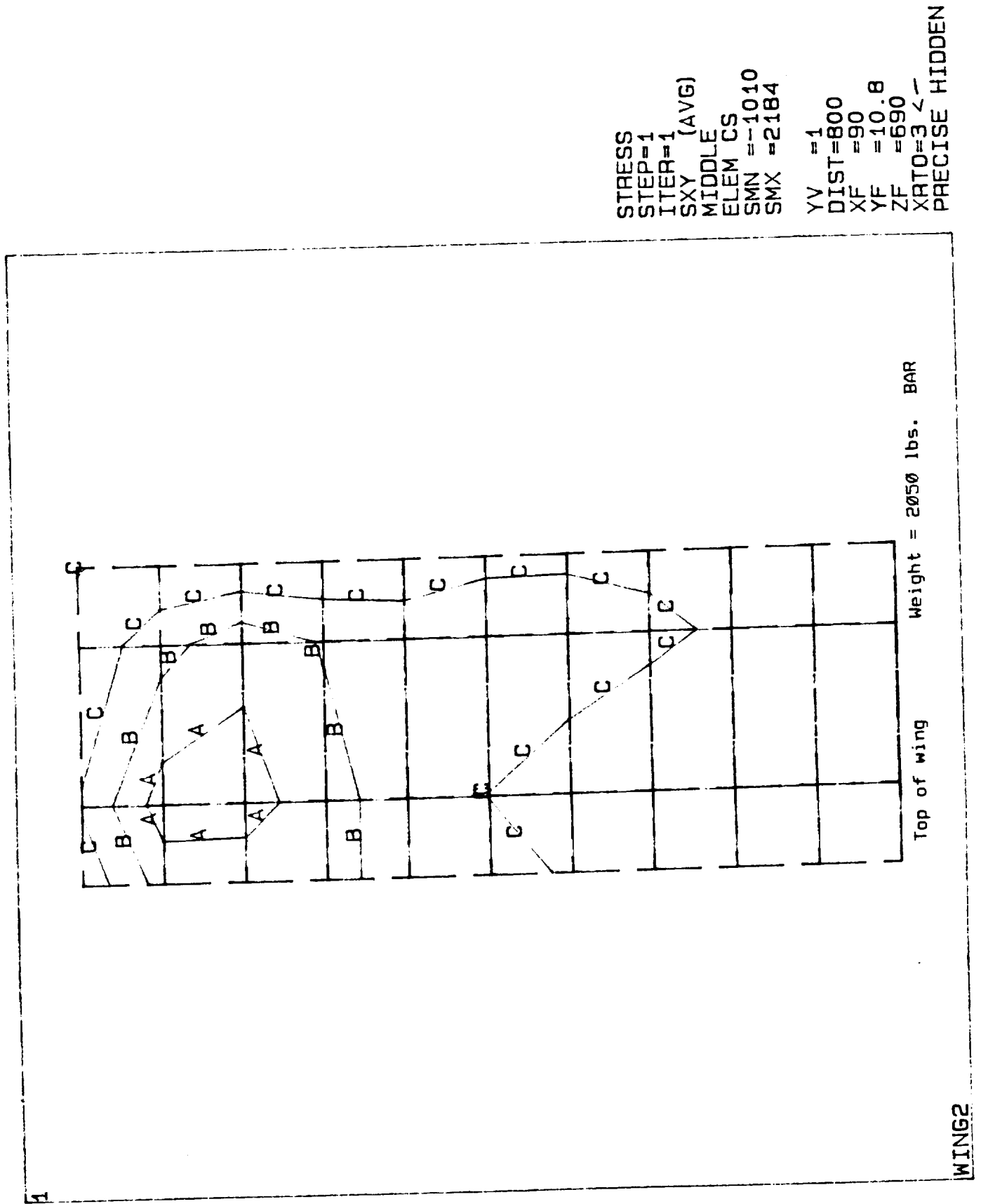
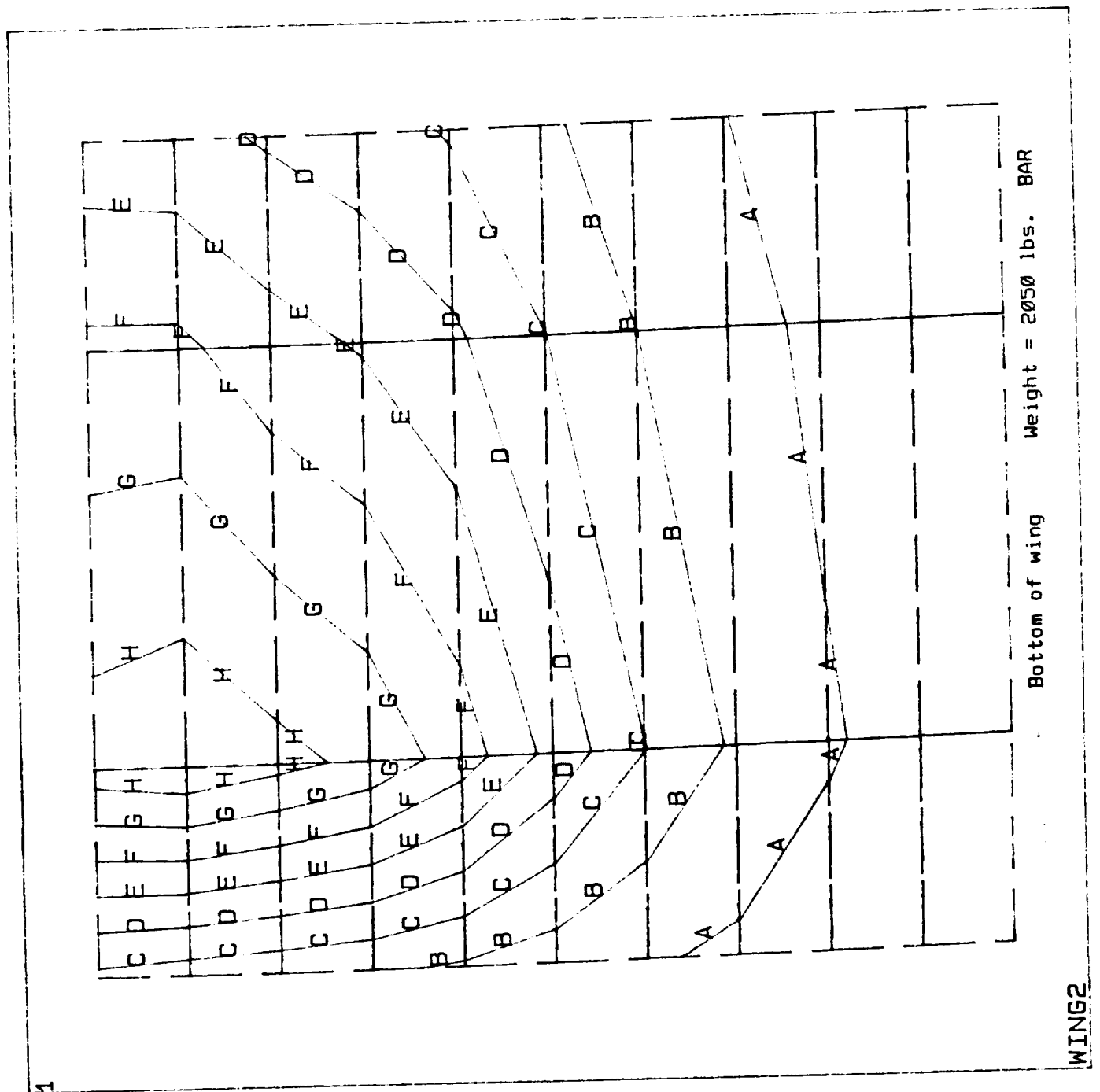


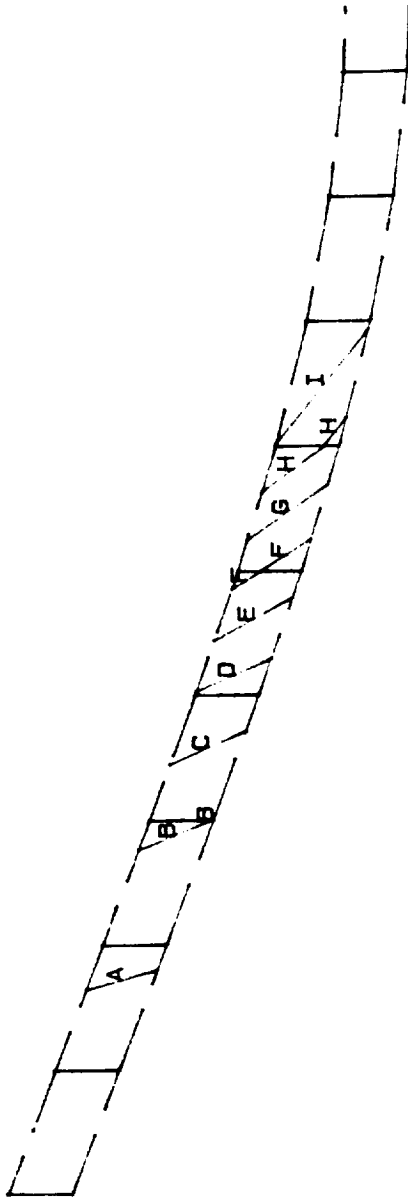
Figure 6.1.9
Model #1



STRESS
STEP=1
ITER=1
SIGE (AVG)
MIDDLE
SMN =88.713
SMX =33153
YV =1
DIST=800
XF =90
YF =10.8
ZF =690
XRTO=7
PRECISE HIDDEN
A =1926
B =5599

Figure 6.1.10
Model #1

ANSYS 4.3A2
DEC 12 1989
18: 4: 4
STRESS
STEP=1
ITER=1
SIGE (AVG)
MIDDLE
SMN -88.713
SMX -33153
XV -1
DIST=750
XF -90
YF -10.8
ZF -690
YATO=5 <-
PRECISE HIDDEN
A -1926
B -5599
C -9273
D -12947
E -16621
F -20295
G -23969
H -27643
I -31315



WING2

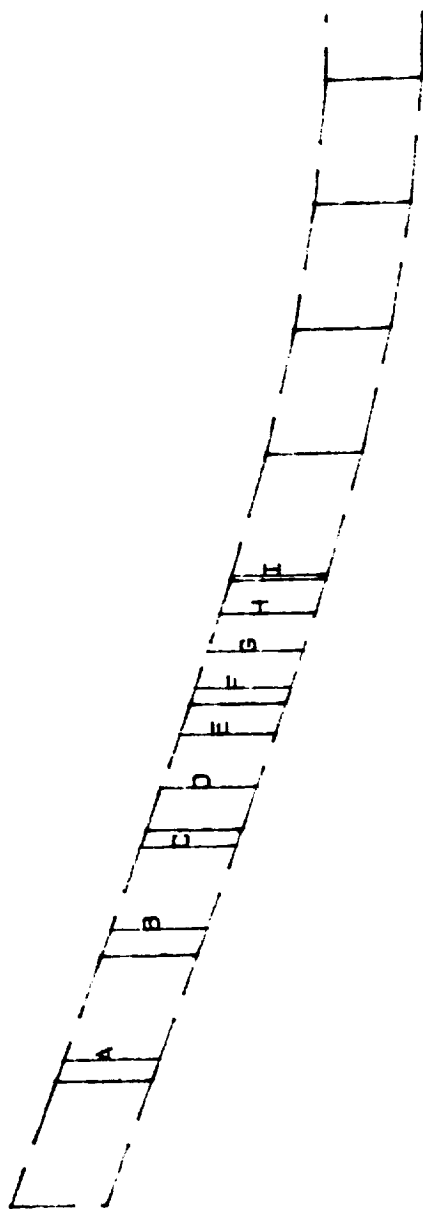
Left I beam Weight = 2050 lbs. BAR

ANSYS 4.3A2
 DEC 12 1989
 18: 0:20
 STRESS
 STEP=1
 ITER=1
 SIGE (AVG)
 MIDDLE
 SMN =88.713
 SMX =33153

XV =1
 DIST=750
 XF =90
 YF =10.8
 ZF =690
 YRTO=5 <-
 PRECISE HIDDEN
 A =1926
 B =5599
 C =9273
 D =12947
 E =16621
 F =20295
 G =23969
 H =27643
 I =31316

Figure 6.1.11
 Model #1

ORIGINAL PAGE IS
 OF POOR QUALITY



WING2

Right I beam Weight = 2050 lbs. BAR

Figure 6.1.12
Model #1

STRESS
STEP=1
ITER=1
SIGE (AVG)
MIDDLE
SMN =88.713
SMX =33153
YV =1
DIST=800
XF =90
YF =10.8
ZF =690
XRT0=6<-
PRECISE HIDDEN
A =1926

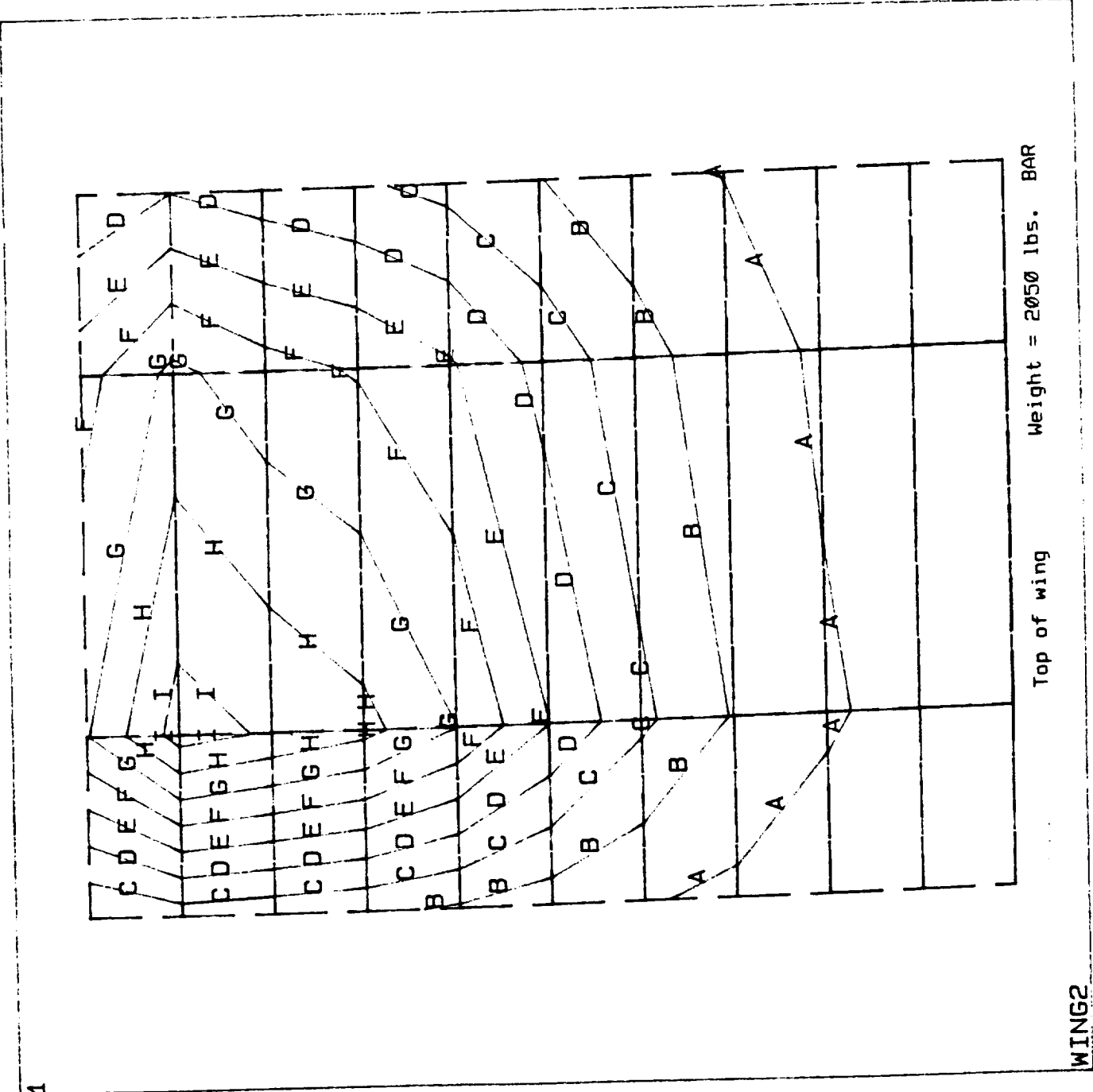


Figure 6.1.13
I Beam Properties

Section	Thick Front I Beam	Thick Middle I Beam	Thick Rear I Beam
1	0.1	0.11	0.105
2	0.09	0.098	0.094
3	0.08	0.087	0.083
4	0.07	0.079	0.075
5	0.06	0.07	0.065
6	0.053	0.058	0.055
7	0.045	0.047	0.046
8	0.0425	0.043	0.042
9	0.04	0.04	0.04
10	0.04	0.04	0.04
20	0.04	0.04	0.04

Figure 6.1.14

TABLE 6.1.6

SECTION	AREA FRONT I BEAM	THICK FRONT I BEAM	BASE FRONT I BEAM	Ixx	Iyy
1	2.16	0.5	4.32	0.045	3.36
2	1.94	0.45	4.32	0.0328	3.02
3	1.728	0.4	4.32	0.023	2.69
4	1.52	0.35	4.32	0.015	2.35
5	1.32	0.3	4.32	0.00972	2.02
6	1.14	0.26	4.32	0.00633	1.75
7	0.972	0.225	4.32	0.0041	1.51
8	0.918	0.21	4.32	0.00333	1.41
9	0.864	0.2	4.32	0.00288	1.34
10	0.864	0.2	4.32	0.00288	1.34
20	0.864	0.2	4.32	0.00288	1.34

Figure 6.1.15

TABLE 6.1.7

SECTION	AREA MIDDLE I BEAM	THICK MIDDLE I BEAM	BASE MIDDLE I BEAM	Ixx	Iyy
1	1.872	0.5	3.74	0.039	2.18
2	1.68	0.45	3.74	0.028	1.96
3	1.49	0.4	3.74	0.02	1.74
4	1.327	0.355	3.74	0.014	1.55
5	1.164	0.31	3.74	0.00928	1.35
6	0.995	0.27	3.74	0.00613	1.18
7	0.825	0.22	3.74	0.00332	0.96
8	0.7725	0.207	3.74	0.00276	0.9
9	0.72	0.19	3.74	0.00214	0.83
10	0.72	0.19	3.74	0.00214	0.83
20	0.72	0.19	3.74	0.00214	0.83

Figure 6.1.16

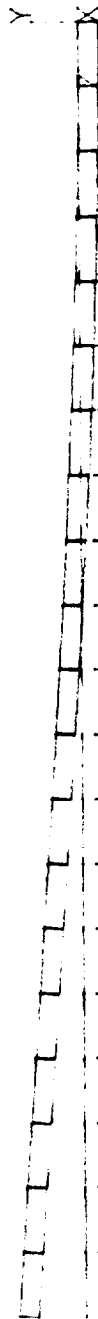
TABLE 6.1.8

SECTION	AREA REAR I BEAM	THICK REAR I BEAM	BASE REAR I BEAM	Ixx	Iyy
1	1.584	0.5	3.17	0.033	1.33
2	1.418	0.45	3.17	0.024	1.195
3	1.253	0.4	3.17	0.017	1.06
4	1.131	0.357	3.17	0.012	0.948
5	1.01	0.319	3.17	0.00858	0.847
6	0.844	0.266	3.17	0.00497	0.706
7	0.677	0.214	3.17	0.00259	0.568
8	0.626	0.197	3.17	0.00202	0.523
9	0.576	0.182	3.17	0.00159	0.483
10	0.576	0.182	3.17	0.00159	0.483
20	0.576	0.182	3.17	0.00159	0.483

Figure 6.1.17
Model #2

ORIGINAL PAGE IS
OF POOR QUALITY

DISPL.
STEP=1
ITER=1
XV =1
DIST=720
XZ =40
YF =20.8
ZF =690

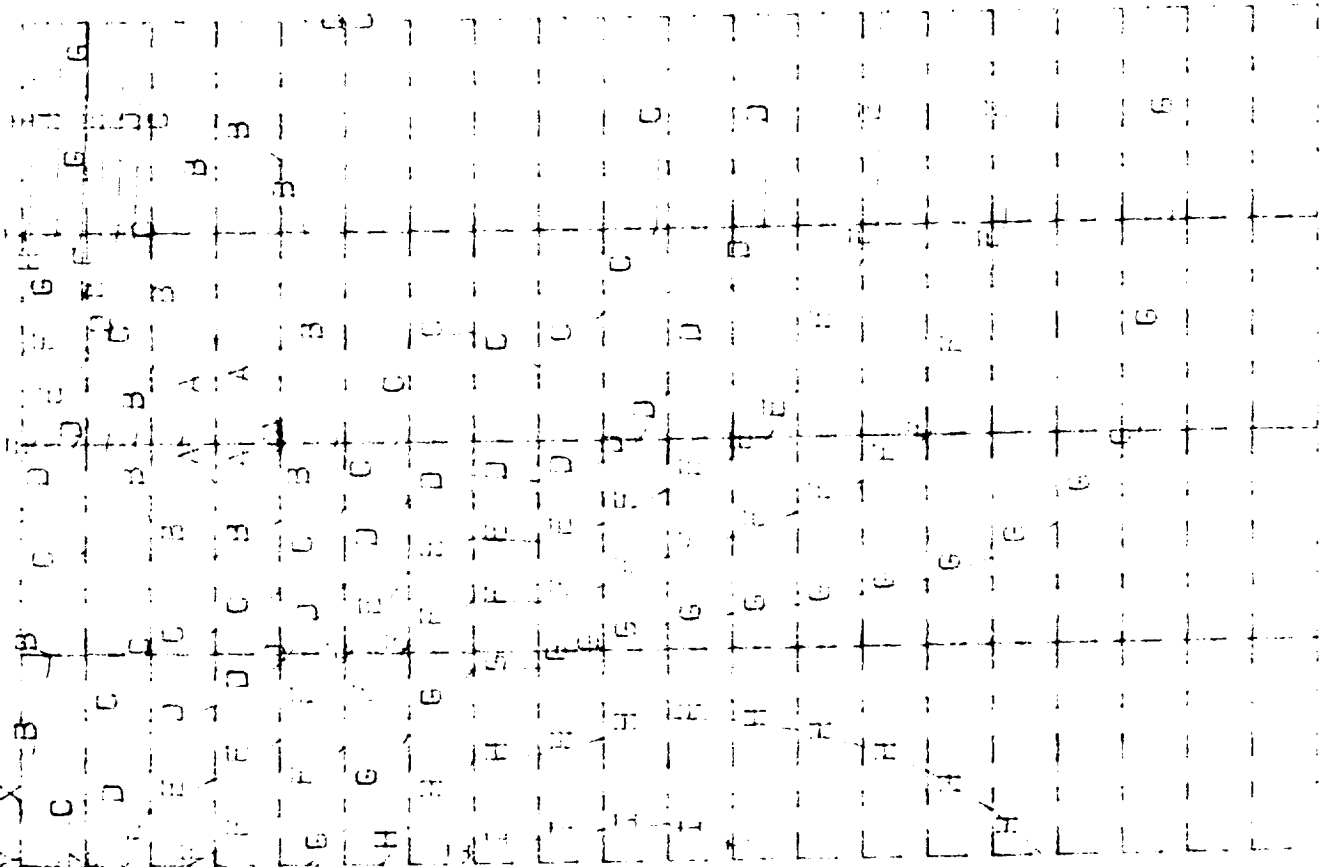


DMX = 113.27 inches Pressure & gravity Weight = 2410 lbs.

Figure 6.1.18
Model #2

ORIGINAL PAGE IS
OF POOR QUALITY

Top view
Pressure & gravity
Weight = 2319 lbs.



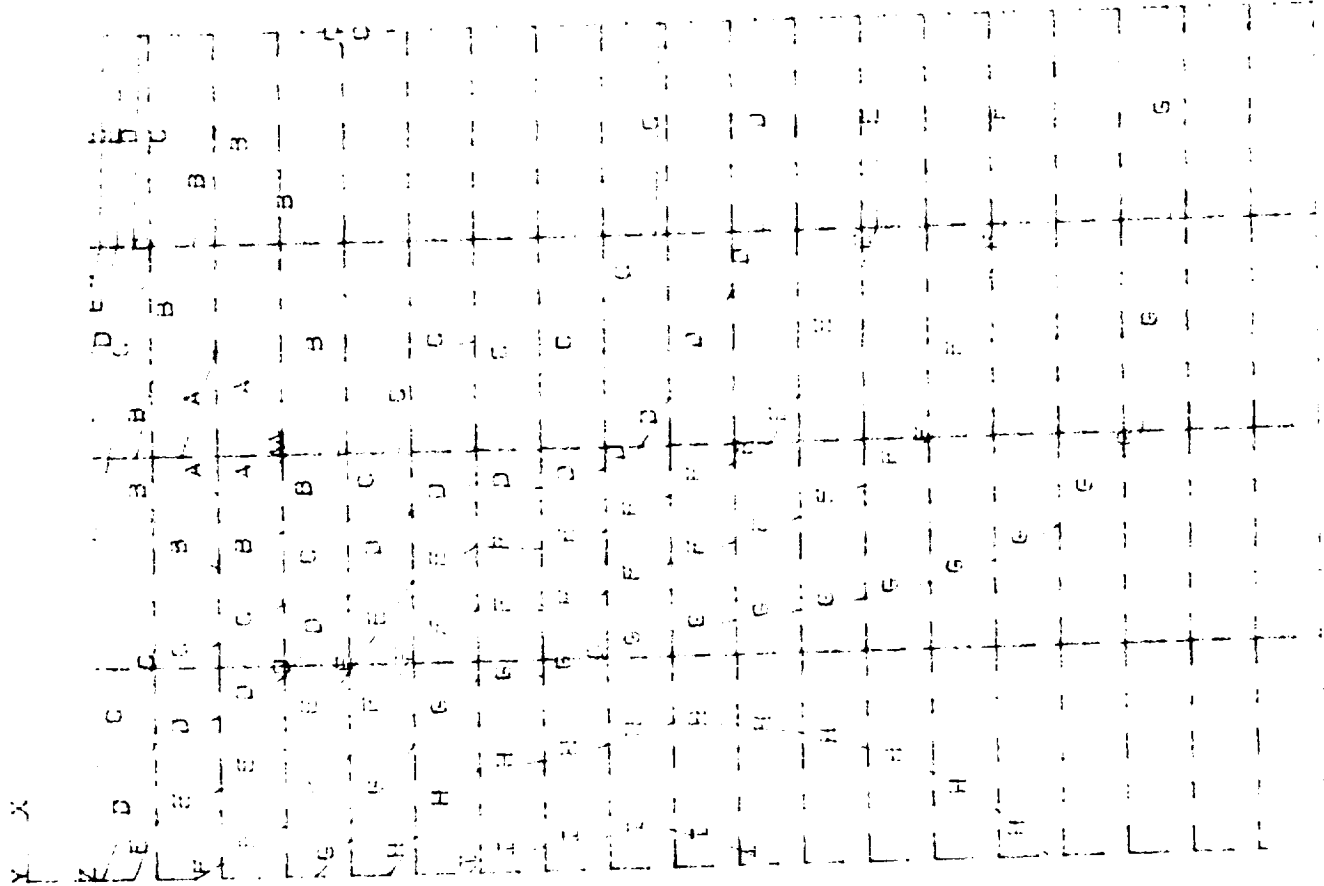
STRESS
STRESS
THERM
SXX (AVG)
MIDDLE
BURN CS
SMN = 1783
SMX = 515.204

STRESS
STRESS
THERM
SXX (AVG)
MIDDLE
BURN CS
SMN = 1783
SMX = 515.204

ANSYS 4.3A2
 FEB 25 1990
 18: 15: 49
 STRESS
 STEP=1
 IITER=1
 SXY (AVG)
 MIDDLE
 PLEN 05
 SWI 0.170
 SWI 0.515,004

Figure 6.1.19
 Model #2

ORIGINAL PAGE IS
 OF POOR QUALITY



Top view Pressure & gravity Weight = 2317 lbs.

W1854

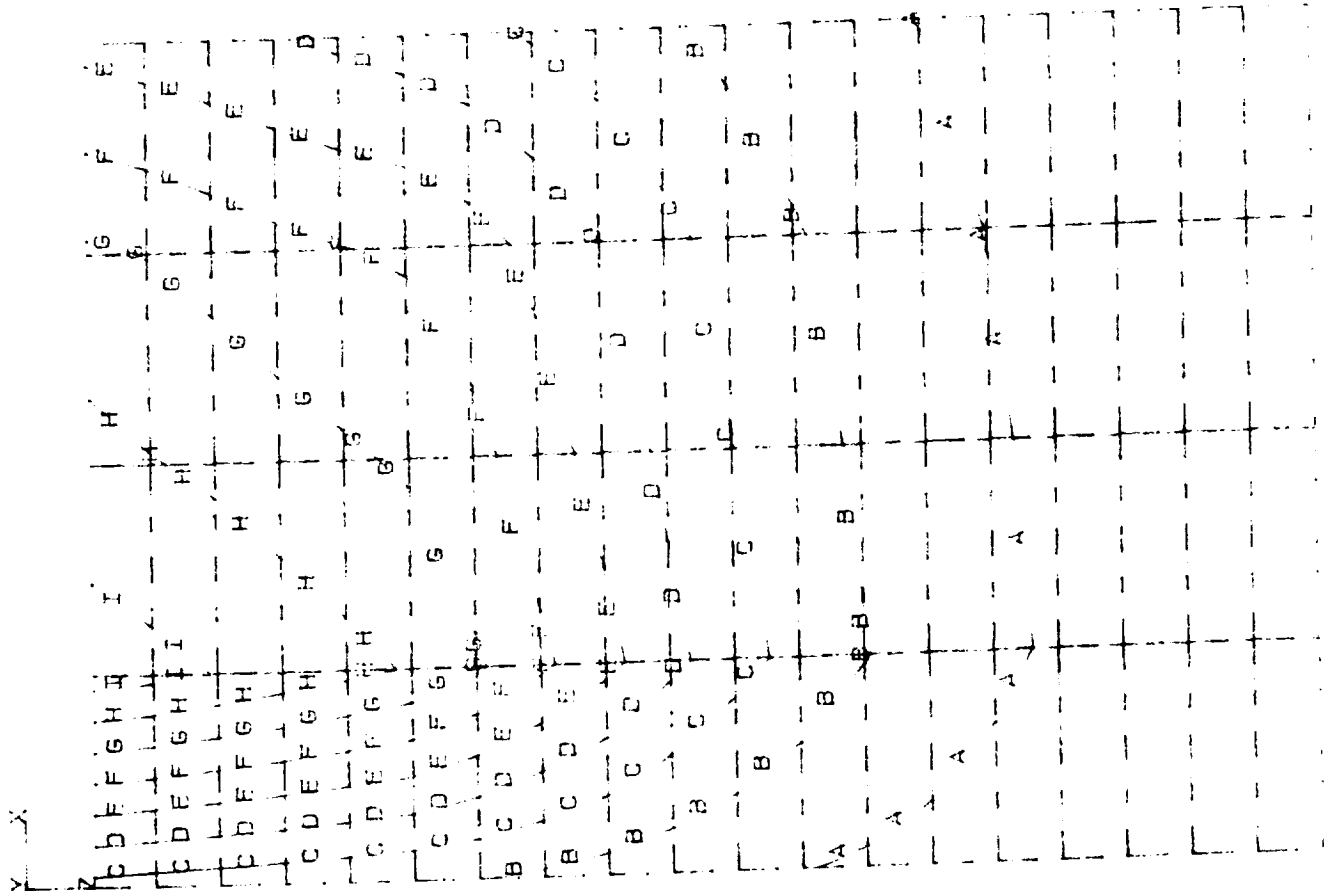
ANSYS 4.3A2
FEB 25 1990
17:44:38

STRESS
STEP=1
ITER=1
SIZE (AVG)
MIDDLE
SMN 18.942
SMX 35955

IV 11
DISP720
XF .30
YF 10.8
ZF .590
XROT=5
A =2061
B =6167
C =10272
D =14377
E =18482
F =22587
G =26592
H =30797
I =34902

Figure 6.1.21
Model #2

ORIGINAL PAGE IS
OF POOR QUALITY

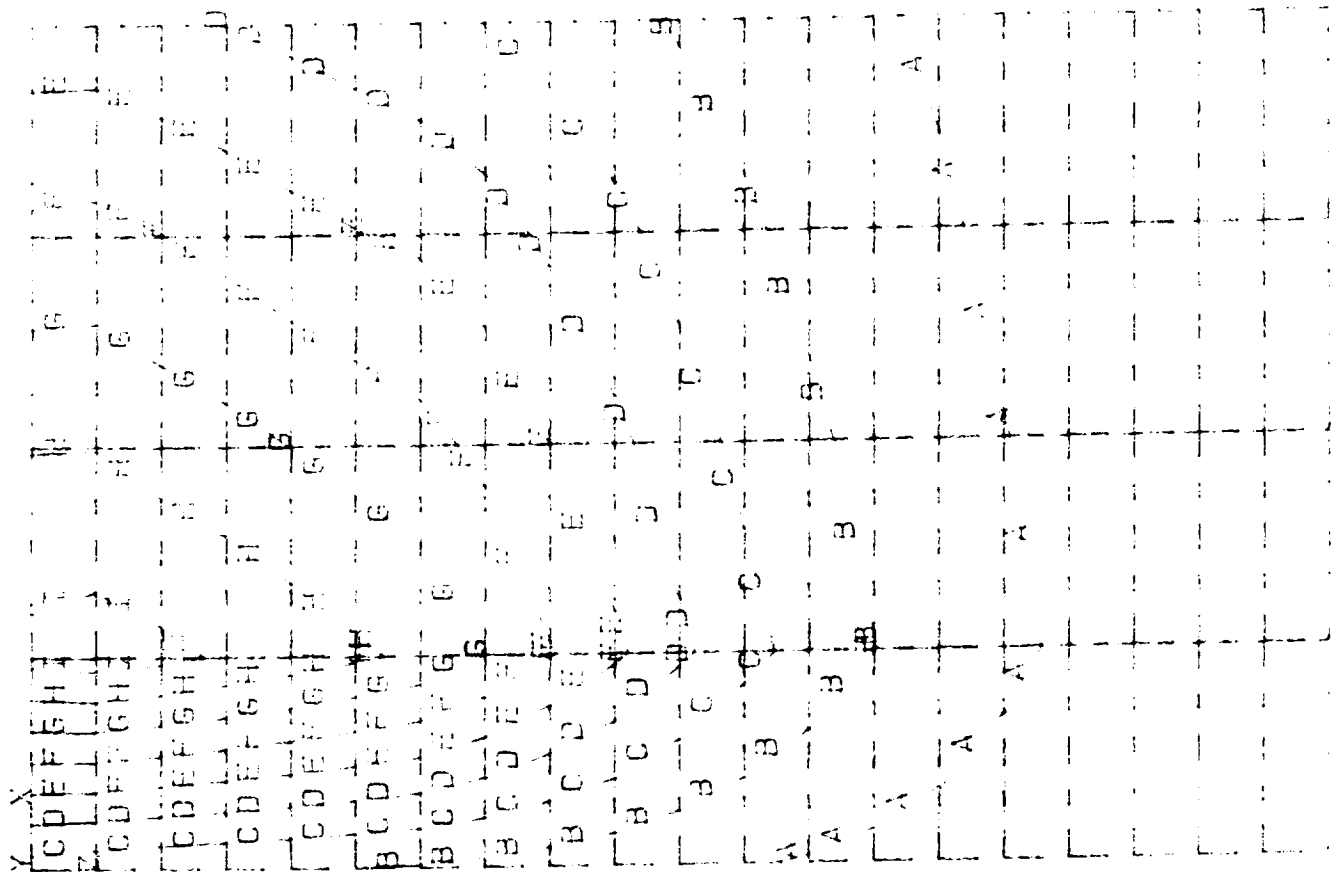


Top view Pressure & gravity Weight = 2319 lbs.

Figure 6.1.22
Model #2

ORIGINAL PAGE IS
OF POOR QUALITY

Bottom view
Pressure & gravity
Weight = 2319 lbs.

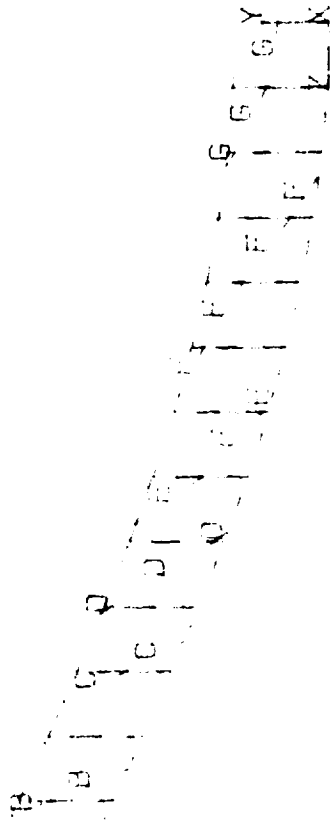


STRESS
STEP=1
ITER=1
STGE (AVG)
MIDDLE
SMN = 8.941
SMX = 96955
VY = 1.0
DIST=7.20
XZ = 1.0
YZ = 1.0
VZ = 1.0
PRD=1.0
A = 1.0
B = 1.0
C = 1.0
D = 1.0
E = 1.0
F = 1.0
G = 1.0
H = 1.0

Figure 6.1.23
Model #2

ORIGINAL PAGE IS
OF POOR QUALITY

STRESS
STEP=1
ITER=1
SIGE (AVG)
MODUL
SMI = 8.941
SMX = 36955
X1 = 1
DIST=20
X2 = 90
X3 = 10.8
ZF = 690
YHFO=7
A = 2051
B = 5157
C = 10272
D = 14377
E = 18482
F = 22587
G = 26692
H = 30797
I = 34902

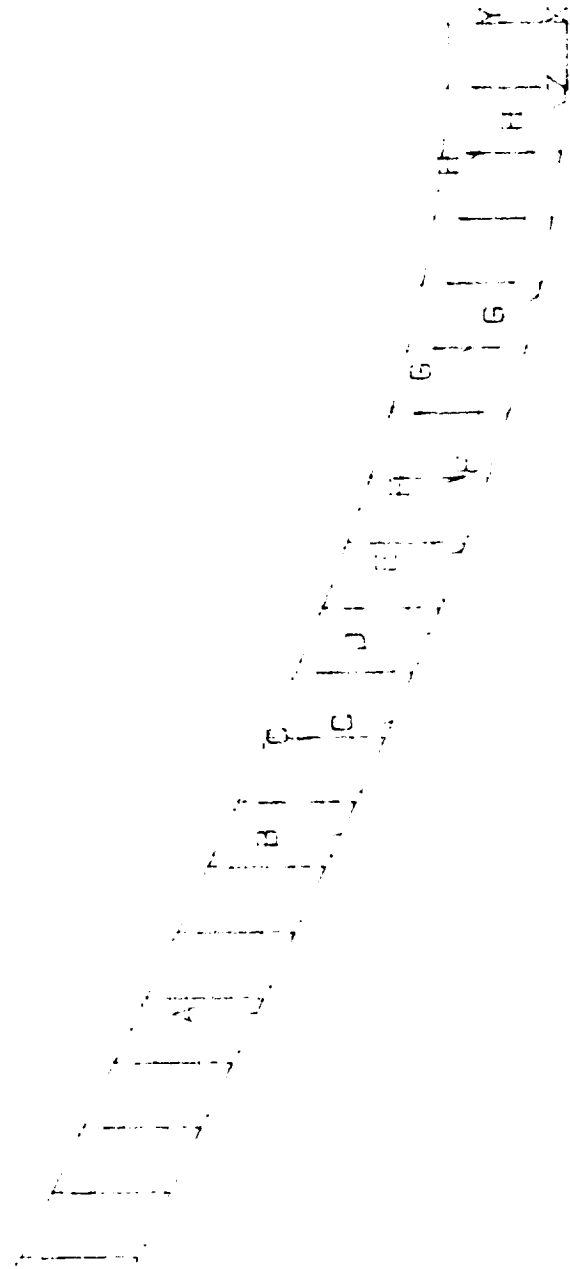


Left I beam Pressure & gravity Weight = 2319 lbs.

Figure 6.1.24
Model #2

ORIGINAL PAGE IS
OF POOR QUALITY

STRESS
STEP=1
ITER=1
SIGE (AVG)
MIDDLE
SMX = 8.941
SMY = -35995
VW = 11
DIST = 220
XF = 390
YF = 10.8
ZF = 590
PRIO=7
A = 2061
B = 16167
C = 110272
D = 114377



Middle I beam Pressure & gravity Weight = 2319 lbs.

ORIGINAL PAGE IS
OF POOR QUALITY

Figure 6.1.25
Model #2

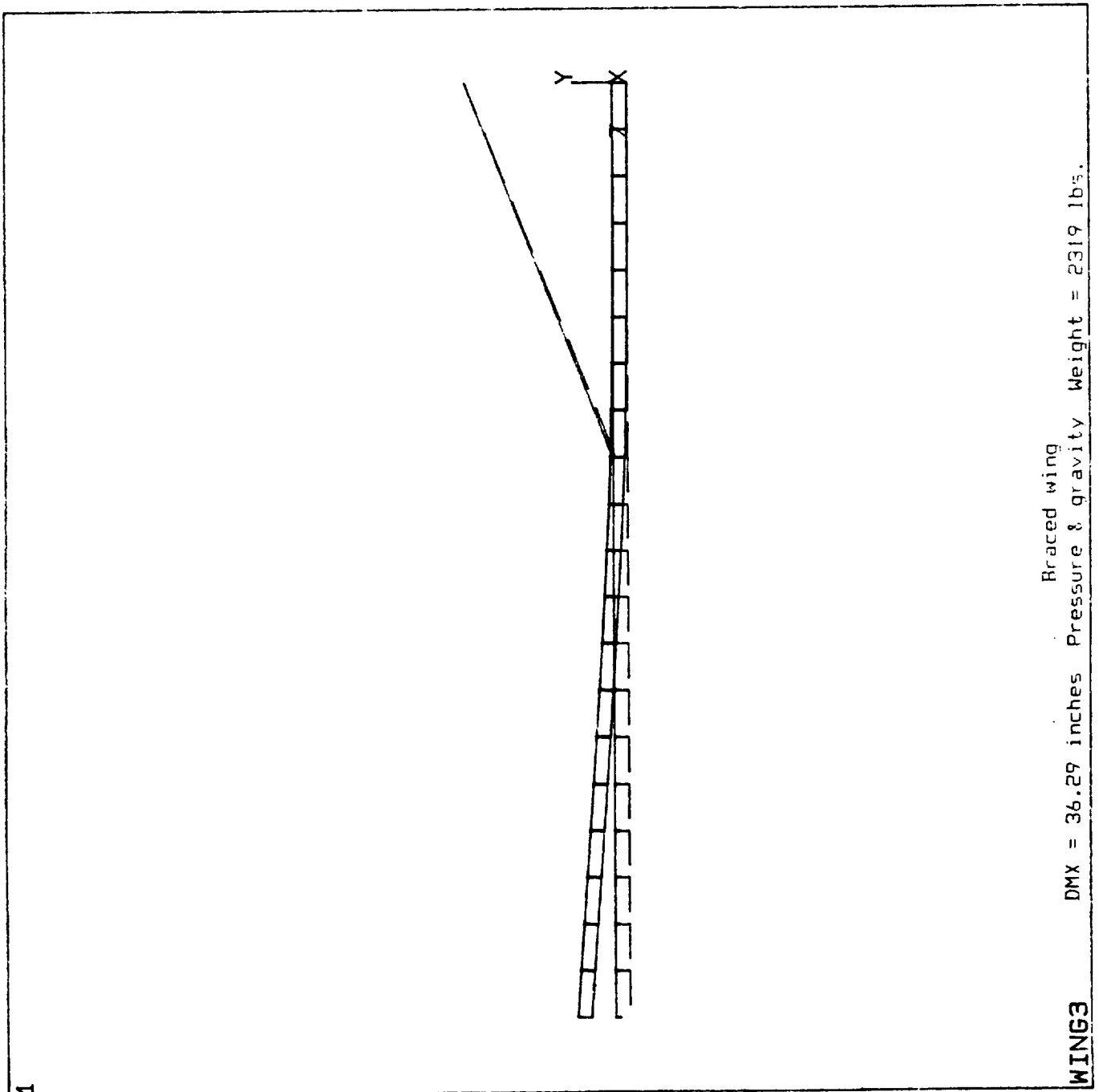
STRESS
STEP=1
ITER=1
SIGE (AVG)
MIDDLE
SMN =8.941
SMX =35955
AV =1
DIST=720
XC =90
YE =19.8
ZC =590
YHIC=7
A =2061
B =5167
C =10272
D =14377

Right I beam Pressure & gravity Weight = 2319 lbs.

Figure 6.1.26
Model #2

ORIGINAL PAGE IS
OF POOR QUALITY

DISPL:
STEP=1
ITER=1
XV =1
DIST=800
XF =255
YF =120
ZF =690



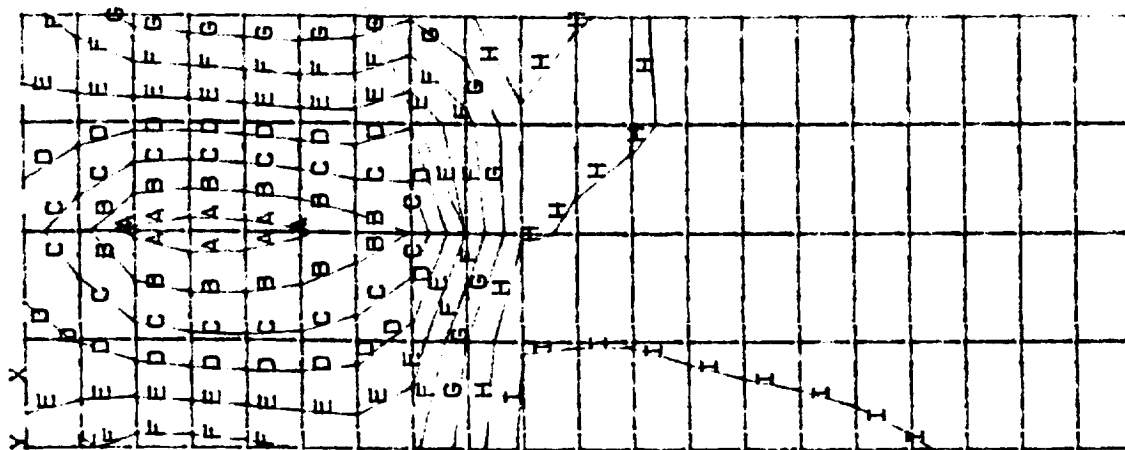
ANSYS 4.3A2
FEB 25 1990
21: 23: 50

STRESS
STEP=1
ITER=1
SXY (AVG)
MIDDLE
ELEM CS
DMX =36.286
SMN =-8866
SMX =532.006

YV =1
DIST=841.5
XF =255
YF =120
ZF =590
XRTD=3 < -
A =-8339
B =-7283
C =-6228
D =-5172
E =-4117
F =-3062
G =-2006
H =-951.026
I =-104.329

Figure 6.1.27
Model #2

ORIGINAL PAGE IS
OF POOR QUALITY



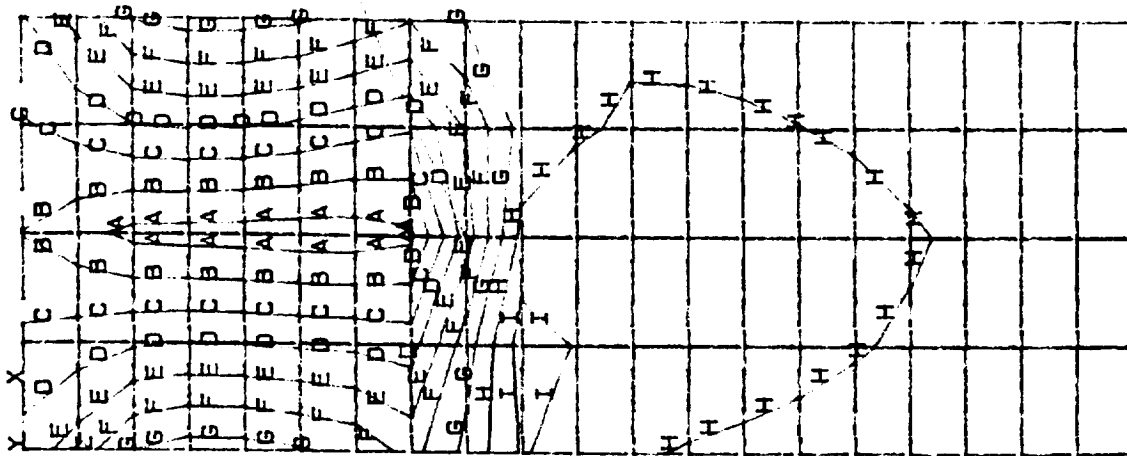
WING3

Top view Pressure & gravity Weight = 2319 lbs.

Figure 6.1.28
Model #2

ORIGINAL PAGE IS
OF POOR QUALITY

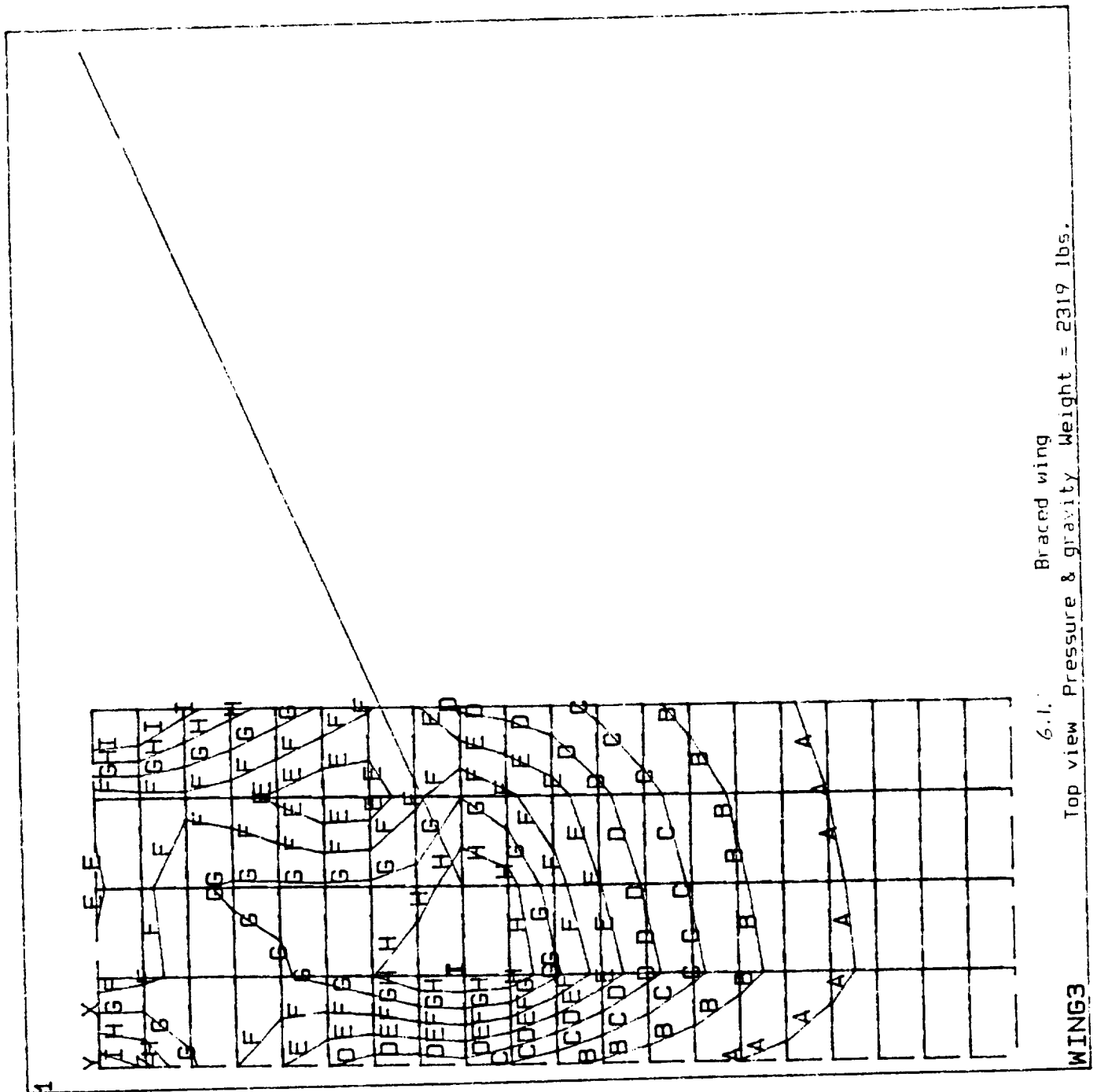
ANSYS 4.3A2
FEB 25 1990
21:29: 8
STRESS
STEP=1
ITER=1
SXY (AVG)
MIDDLE
ELEM CS
DMX =36.285
SMN =-5636
SMX =1395
YV =1
DIST=841.5
XF =255
YF =120
ZF =690
XRT0=3
A =-5245
B =-4464
C =-3683
D =-2902
E =-2121
F =-1339
G =-558.304
H =-222.837
I =-1004



WING3

6.1. Braced wing
Bottom view Pressure & gravity Weight = 2319 lbs.

Figure 6.1.29
Model #2



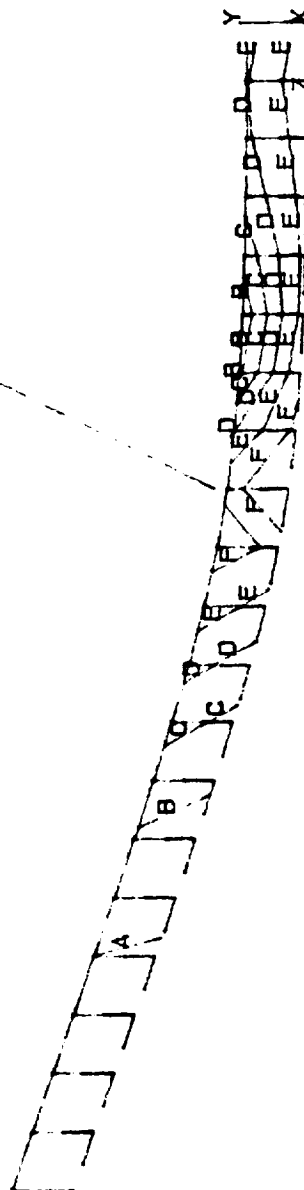
STRESS
STEP=1
ITER=1
SIGE (AVG)
MIDDLE
SMN =8.945
SMX =27039
YV =1
DIST=800
XF =255
YF =120
ZF =690
XRTD=3 <-
A =1176
B =3501
C =5825
D =8150
E =10474
F =12799
G =15123

ANSYS 4.3A2
 FEB 25 1990
 21: 10: 40
 STRESS
 STEP=1
 ITER=1
 SIGE (AVG)
 MIDDLE
 SMN =8.945
 SMX =27039

XV =1
 DIST=800
 XF =255
 YF =120
 ZF =690
 YRTO=5 /-
 A =-1176
 B =-3501
 C =-5825
 D =-8150
 E =-10474
 F =-12799
 G =-15123
 H =-17448
 I =-19772

Figure 6.1.30
 Model #2

ORIGINAL PAGE IS
 OF POOR QUALITY

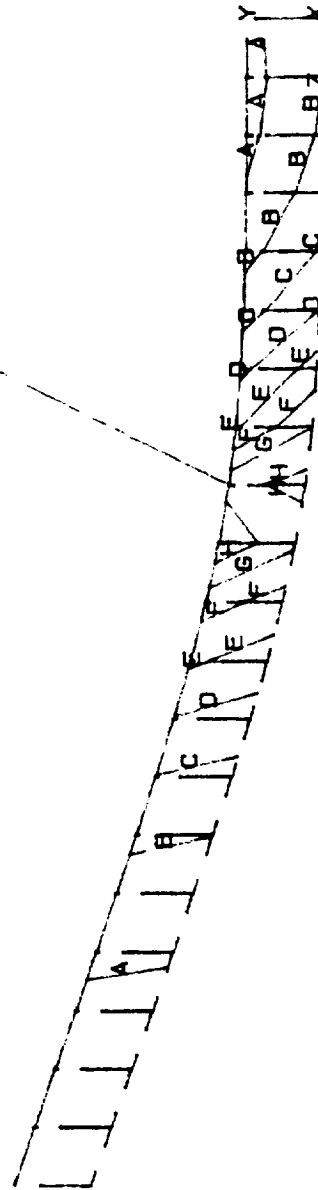


left 1 beam Braced wing Pressure & quality Weight = 2319 lbs.

Figure 6.1.31
Model #2

ORIGINAL PAGE IS
OF POOR QUALITY

ANSYS 4.3A2
FEB 25 1990
21: 8: 14
STRESS
STEP=1
ITER=1
SIGE (AVG)
MIDDLE
SMN =8.945
SMX =27039
XV =1
DIST=800
XF =255
YF =120
ZF =690
YRT0=5 <-
A =1176
B =3501
C =5825
D =8150
E =10474
F =12799
G =15123
H =17448
I =19772



WING3

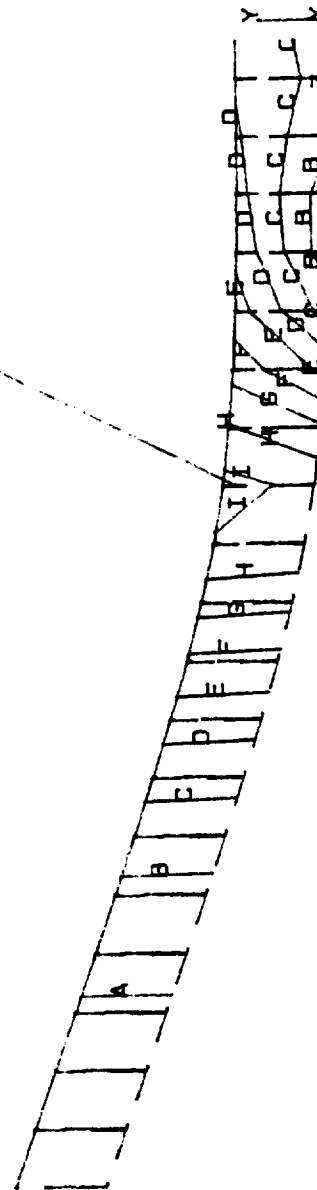
6.1. Braced wing
Middle I beam Pressure & gravity Weight = 2319 lbs.

ANSYS 4.3A2
 FEB 25 1990
 21: 5:37
 STRESS
 STEP=1
 ITER=1
 SIGE (AVG)
 MIDDLE
 SMN =8.945
 SMX =27039

XV =1
 DIST=800
 XF =255
 YF =120
 ZF =690
 YATO=5 < -
 A =1176
 B =3501
 C =5825
 D =8150
 E =10474
 F =12799
 G =15123
 H =17448
 I =19772

Figure 6.1.32
 Model #2

ORIGINAL PAGE IS
 OF POOR QUALITY

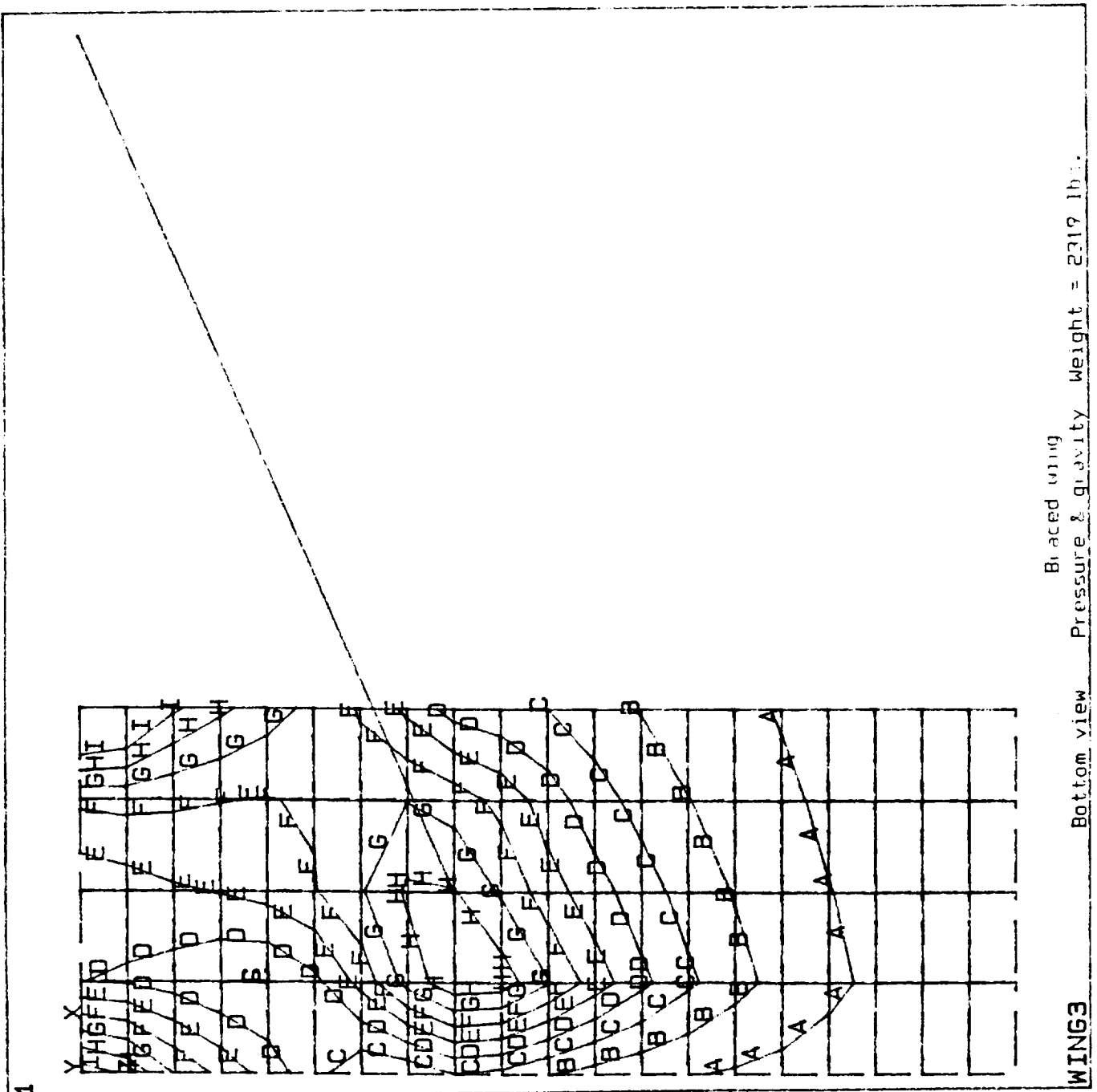


WING3
 6.1. Braced wing
 Right I beam Pressure & gravity Weight = 2319 lbs.

Figure 6.1.33
Model #2

ORIGINAL PAGE IS
OF POOR QUALITY

STRESS
STEP=1
ITER=1
SIGE (AVG)
MIDDLE
SMN =8.945
SMX =27039
YV =1
DIST=800
XF =255
YF =120
ZF =690
XRT0=3
A =1176
B =3501
C =5825
D =8150



ORIGINAL PAGE IS
OF POOR QUALITY

Figure 6.1.34

Pressure & Force Calculations

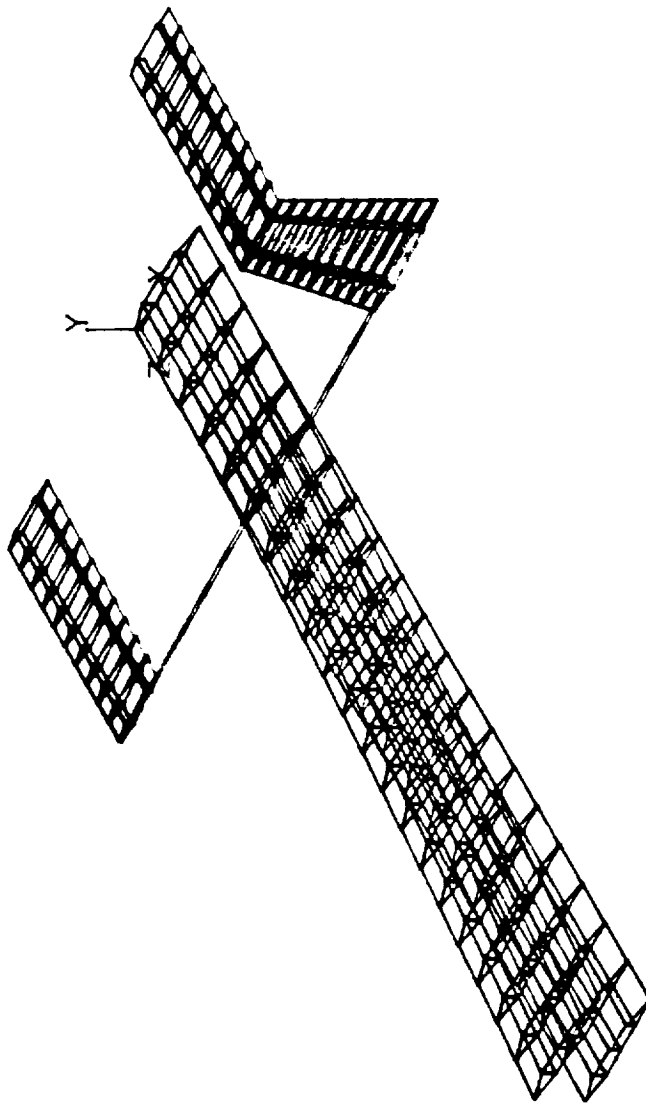
SECTION	WIX	SPAC	DIFF COEF	CL=1	CL=2	REQUIRED	DESIGN	REQ/DESIGN	OPPER	OPPER	OPPER	LOWER	LOWER	LOWER
		MID				DIFF COEF	DIFF COEF		Cp(1)	Cp(2)	Cp(3)	Cp(4)	Cp(5)	Cp(6)
1	35.71026	1.0	1.074100			1.071648	0.743913	1.709424	1.111112	1.371796	0.341880	0.427351	0.247863	-0.034208
2	39.11015	3.6	1.061470			1.058835	0.743913	1.652180	1.099517	1.357974	0.338436	0.423045	0.245366	-0.033844
3	38.49745	6.5	1.031190			1.022800	0.743913	1.657196	1.077177	1.329900	0.331439	0.414296	0.240253	-0.033114
4	37.10415	9.1	1.016205			1.007007	0.743913	1.603285	1.042138	1.286639	0.320657	0.400222	0.232476	-0.03206
5	35.50681	11.7	1.005421			1.000040	0.743913	1.528458	0.993498	1.226188	0.305691	0.382114	0.227626	-0.03056
6	33.10604	14.3	1.005590			1.002365	0.743913	1.429421	0.929124	1.147111	0.285884	0.357351	0.207266	-0.02858
7	30.20458	16.5	0.969605			0.967379	0.743913	1.300661	0.845430	1.043780	0.260132	0.325165	0.188595	-0.02601
8	26.19876	19.5	0.841933			0.842169	0.743913	1.132080	0.735852	0.908464	0.226436	0.283020	0.164151	-0.02264
9	20.94481	22.0	0.670103			0.670701	0.743913	0.901612	0.586047	0.723443	0.180322	0.235403	0.130733	-0.01803
10	10.41691	24.7	0.593400			0.597565	0.743913	0.534429	0.347379	0.428879	0.106885	0.133607	0.077492	-0.01068

1.005546

PRESSURE								
	TOP	TOP	TOP	BOTTOM	BOTTOM	BOTTOM	Total	
SECTION	FRONT 1	MID 1	REAR 3	REAR 4	MID 5	FRONT 6	Pressure	
1	0.001417	0.029788	0.007423	0.009019	0.005382	-0.00074	0.027607	
2	0.003884	0.029486	0.007349	0.009186	0.005328	-0.00073	0.027325	
3	0.003390	0.02818	0.007037	0.008699	0.005107	-0.00071	0.026764	
4	0.002805	0.027659	0.006980	0.008703	0.005048	-0.00069	0.026583	
5	0.002167	0.026639	0.006638	0.008237	0.004872	-0.00066	0.026085	
6	0.002070	0.026409	0.006407	0.007959	0.004800	-0.00062	0.023085	
7	0.001818	0.022463	0.005648	0.007060	0.004059	-0.00056	0.021306	
8	0.001397	0.019707	0.004916	0.006045	0.003164	-0.00049	0.018281	
9	0.001013	0.015711	0.003518	0.004494	0.002638	-0.00035	0.014561	
10	0.000784	0.009111	0.002101	0.002901	0.001680	-0.00023	0.008631	
FORCE								
	TOP	TOP	TOP	BOTTOM	BOTTOM			
SECTION	FRONT 1	MID 1	REAR 3	REAR 4	MID 5	FRONT 6	CALCULATED FORCE	EXPECTED FORCE
1	101.59101	51.74358	8.948733	8.895117	10.07566	-0.69487	103.3624	103.3528
2	111.22183	11.20172	8.878719	8.981999	9.674143	-0.66187	101.3225	102.3115
3	111.00000	4.706245	7.70508	8.420631	9.767937	-0.47365	100.2055	100.1963
4	111.08147	50.30194	6.527376	8.046720	9.450199	-0.65173	96.94596	96.93701
5	111.05006	49.98004	6.000000	7.706486	9.009104	-0.60101	92.42118	92.41265
6	108.88448	46.63016	5.870604	7.004235	8.425376	-0.58104	86.43274	86.42476
7	111.06337	40.42971	5.007190	6.907891	7.996430	-0.52871	78.64700	78.63974
8	104.94401	36.93101	4.821001	6.782049	6.671771	-0.46013	68.44343	68.44711
9	111.91143	29.41038	3.666186	4.581001	5.014330	-0.36650	54.51772	54.51268
10	111.86450	10.42058	2.170458	2.711073	3.132005	-0.21724	32.31552	32.31233
							615.6223	615.5469

Figure 6.1.35
Model #3

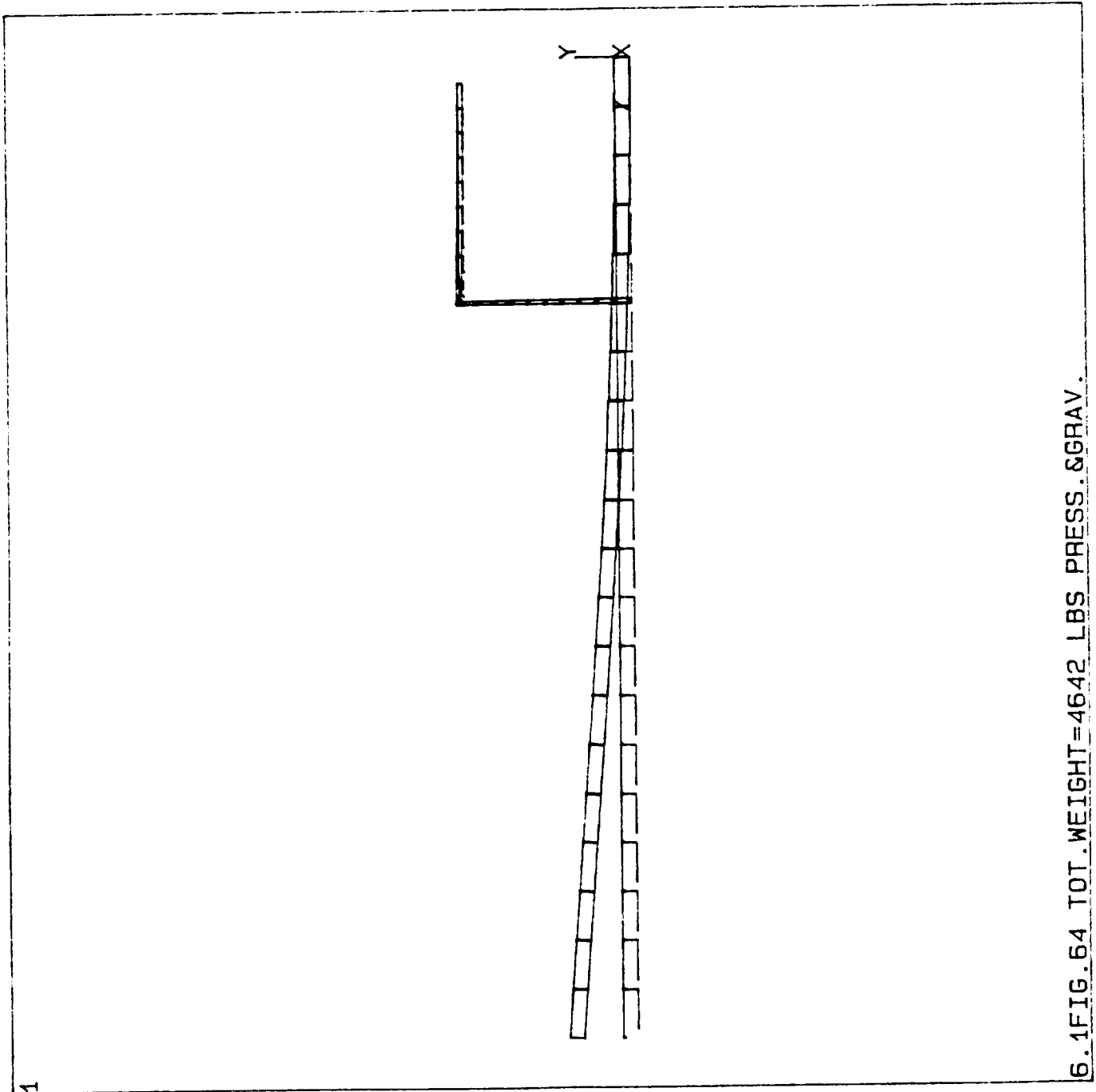
DISPL:
STEP=1
ITER=1
XV =1
YV =1
ZV =1
DIST=850
XF =90
YF =123
ZF =690



6.1FIG. 57 DMX=103 PRESSURE & GRAVITY WEIGHT = 4642 lbf.

Figure 6.1.36
Model #3

DISPL.
STEP=1
ITER=1
DMX =103.281
XV =1
DIST=759
XF =90
YF =123
ZF =690



6.1FIG.64 TOT.WEIGHT=4642 LBS PRESS.&GRAV.

Figure 6.1.37
Model #3

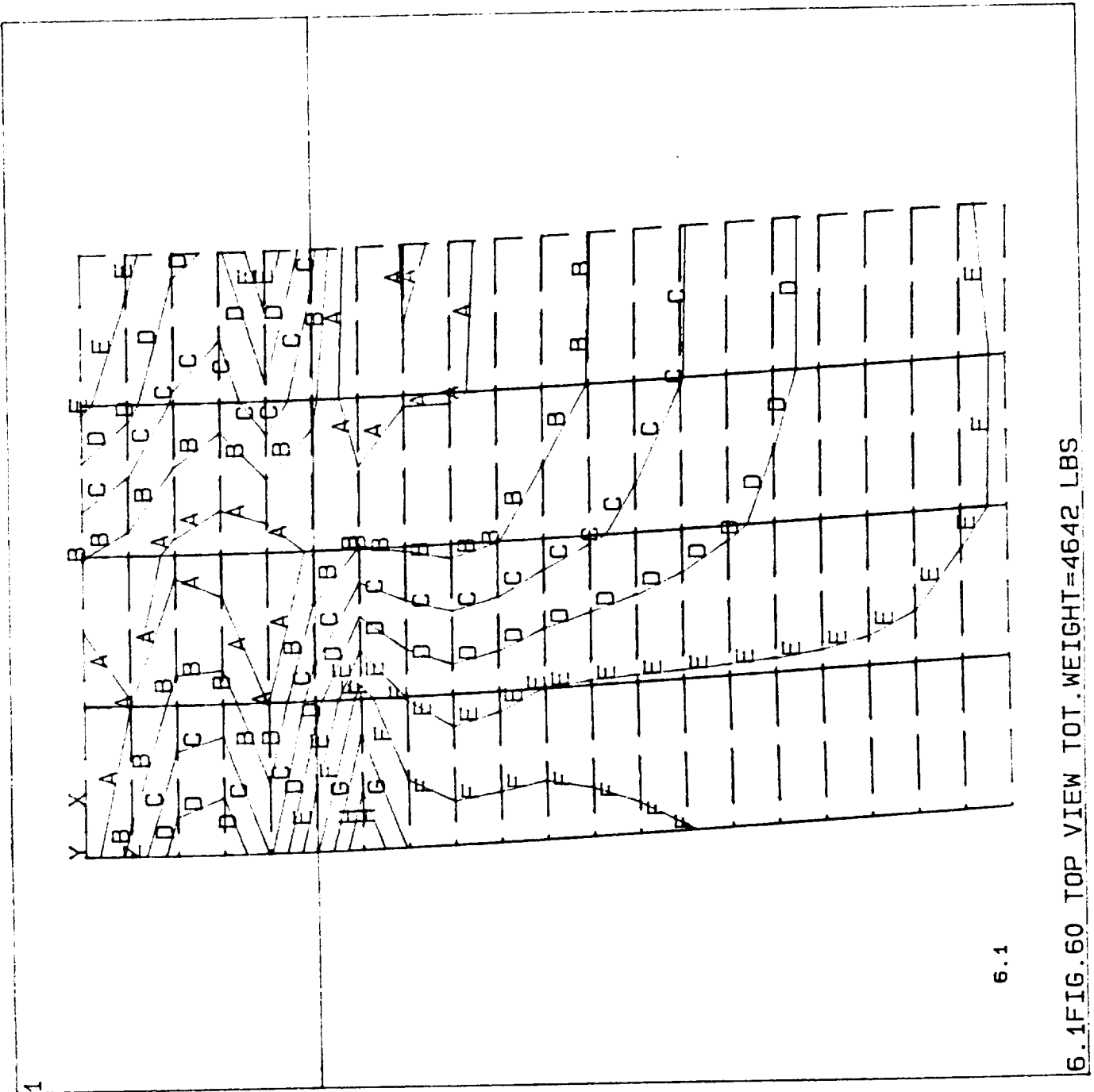
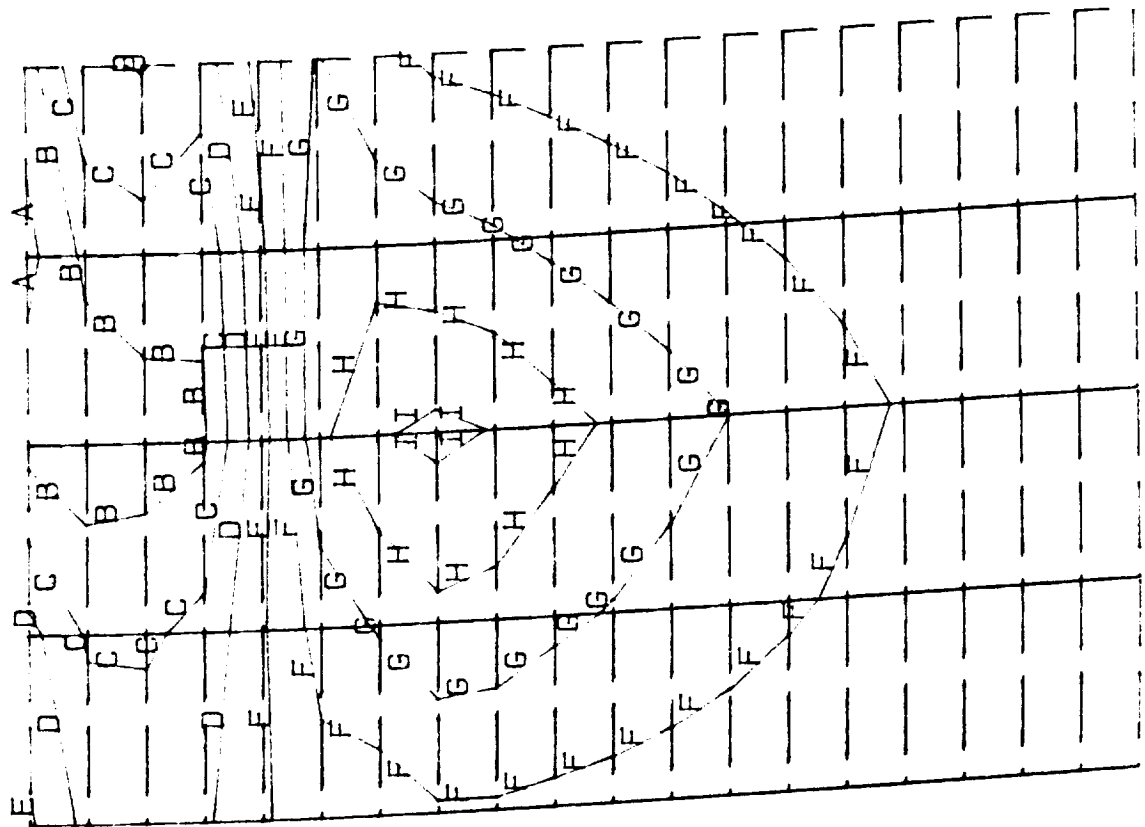


Figure 6.1.38
Model #3

SXY (AVG)

YV = 1
DIST = 800
XF = 90
YF = 123
ZF = 690
XRT0 = 5
A = -1276
B = -954.888
C = -653.566
D = -342.244
E = -30.922
F = 280.4
G = 591.721
H = 903.043
I = 1214



6.1FIG. 61 BOTTOM VIEW PRESS. & GRAV.

Figure 6.1.39
Model #3

STRESS
STEP=1
ITER=1
SIGE (AVG)
MIDDLE
SMN =8.914
SMX =32609
YV =1
DIST=600
XF =1
A =1820
B =5442
C =9064
D =12687
E =16309
F =19931
G =23553
H =27175
I =30797

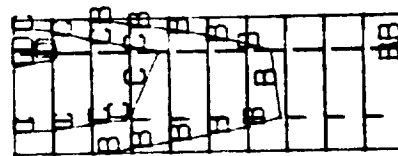
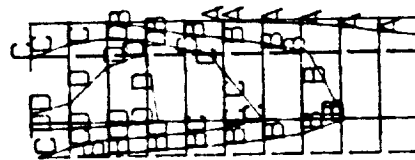
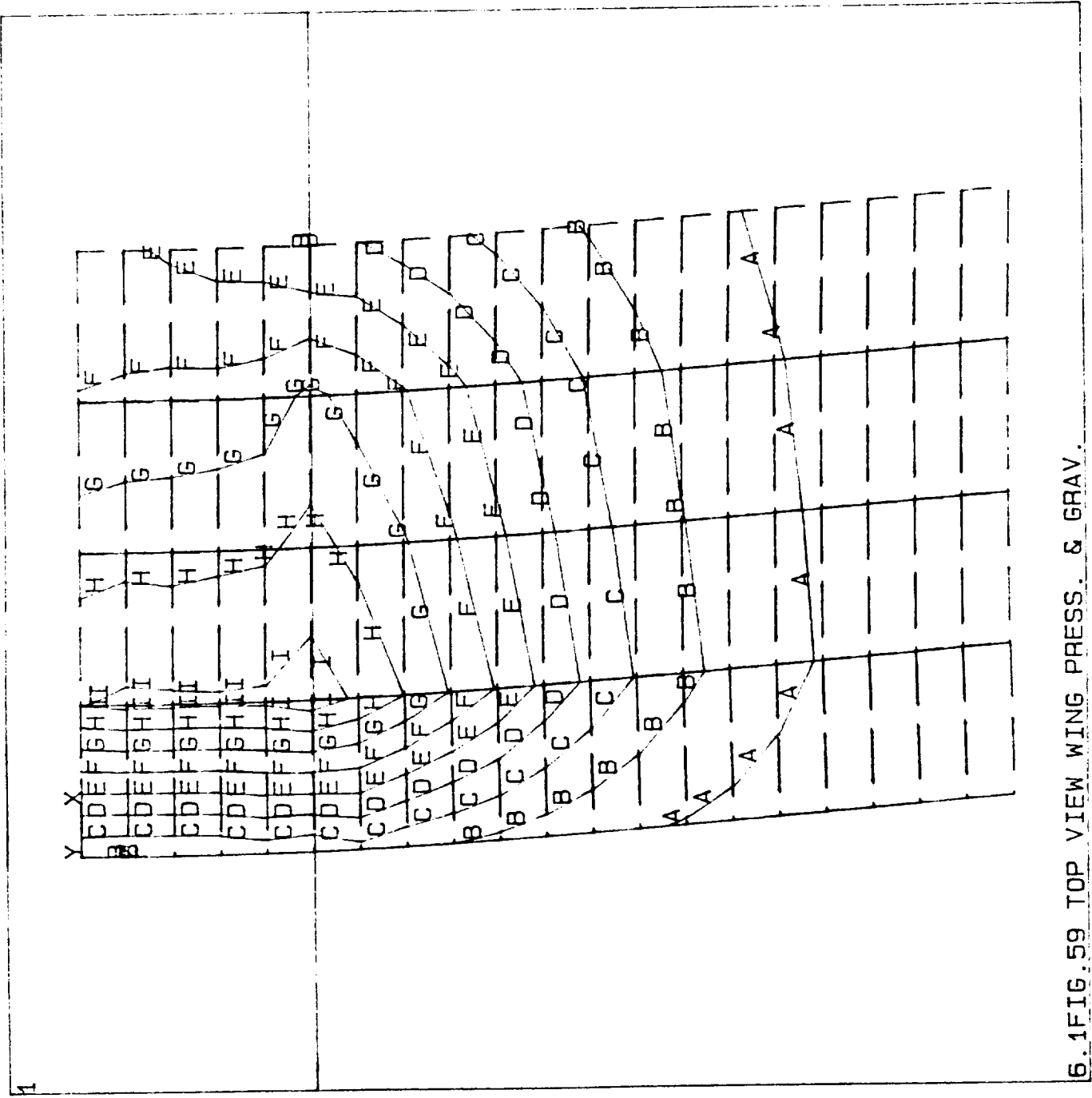


Figure 6.1.40
Model #3



STRESS
STEP=1
ITER=1
SIGE (AVG)
MIDDLE
SMN =8.914
SMX =32609
YV =1
DIST=800
XF =90
YF =123
ZF =690
XRT0=5
A =1820
B =5442
C =9064
D =12687

6.1FIG.59 TOP VIEW WING PRESS. & GRAV.

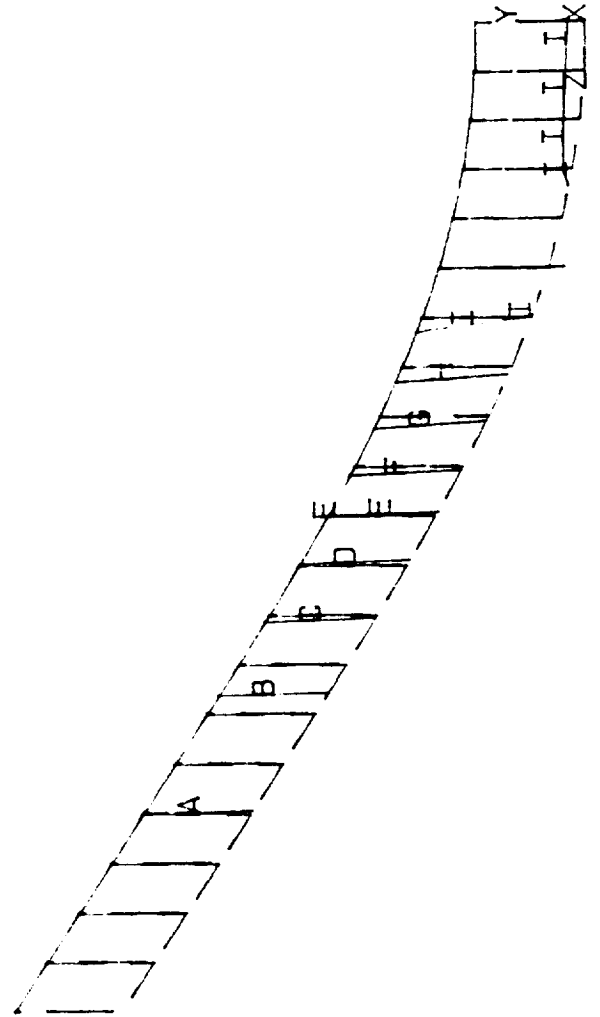
Figure 6.1.41
Model #3

IST=947.1
XF =90
YF =123
ZF =690
YRTO=7
A =1816
B =5364
C =8913
D =12461
E =16009
F =19558
G =23106
H =26654
I =30203

STRESS
STEP=1
ITER=1
SIGE (AVG)
MIDDLE
DMX =102.773
SMN =41.96
SMX =31977

XV =1
DIST=947.1
XF =90
YF =123
ZF =690
YRTO=7
A =1816
B =5364

6.1FIG.62 WING & TAIL RIGHT I BEAM



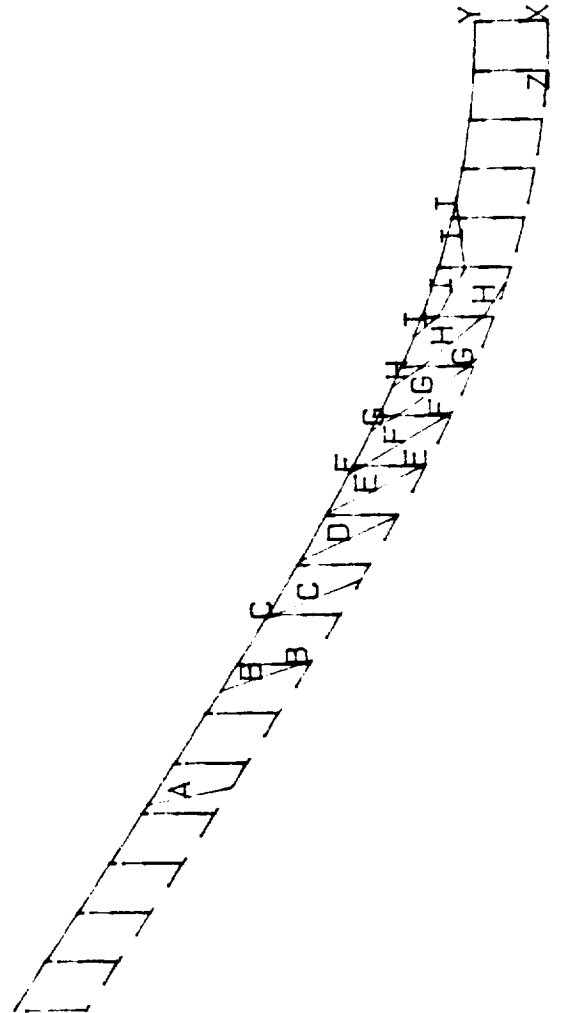
6.1FIG.62 WING & TAIL RIGHT I BEAM

Figure 6.1.42
Model #3

A B C D E

.1
XF =90
YF =123
ZF =690
YRTO=7
A =1305
B =3898
C =6491
D =9083
E =11676
F =14268
G =16861
H =19453
I =22046

STRESS
STEP=1
ITER=1
SIGE (AVG)
MIDDLE
DMX =103.111
SMN =9.153
SMX =23342
XV =1
DIST=947.1
XF =90
YF =123
ZF =690
YRTO=7
A =1305
B =3898



6.1FIG.63 WING & TAIL LEFT I BEAMS PRESS.&GRAV.

Figure 6.2.1

The frequency value in each mode for preliminary wing structural design is shown below:

EIGENVALUE (NATURAL FREQUENCY)

MODE	FREQUENCY (CYCLE/SEC)
1	0.858065
2	4.048
3	4.843
4	11.931
5	13.368

FIGURE 6.2.2

Mode 1 Preliminary Design
1st Bending

ANSYS 4.3A2
FEB 23 1990
14: 48: 80
DISPL.
STEP=1
ITER=1
FREQ=0.858065
XV -1
YV -1
ZV -1
DIST=600
XF -90
YF -10.8
ZF -690

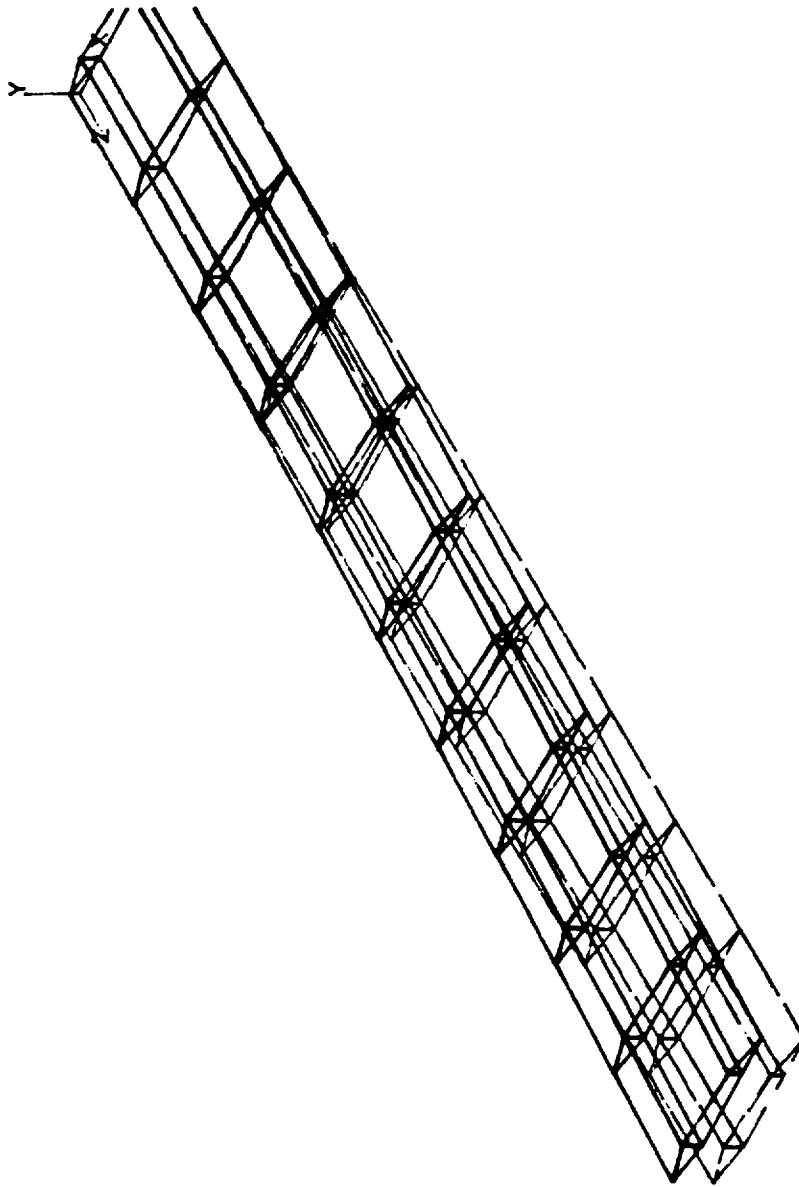


FIGURE 6.2.3
Mode 1 Preliminary Design
1st Bending

ANSYS 4.3A2
FEB 23 1990
15:43:32
DISPL.
STEP=1
ITER=1
FREQ=0.858065
DMX =1.255

XV =1
DIST=759
XF =90
YF =10.8
ZF =690



WING2

FIGURE 6.2.4
 Mode 1 Preliminary Design
 1st Bending

ANSYS 4.3A2
 FEB 23 1990
 15:38:54
 DISPL.
 STEP=1
 ITER=1
 FREQ=0.858065
 DMX =1.255
 YV =1
 DIST=759
 XF =90
 YF =10.8
 ZF =690

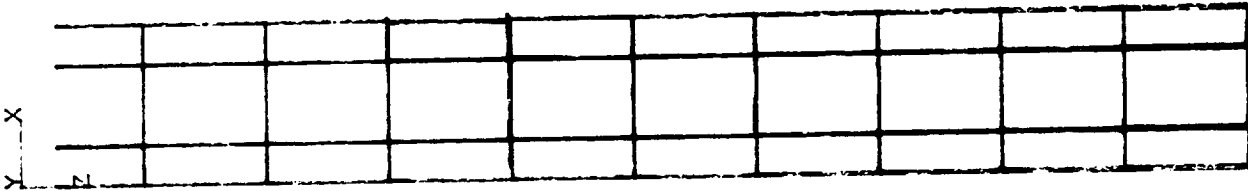


FIGURE 6.2.5

Mode 2 Preliminary Design
1st Torsion

ANSYS 4.3A2
FEB 23 1990
14: 52: 29

DISPL.

STEP=1

ITER=2

FREQ=4.048

XV =1

YV =1

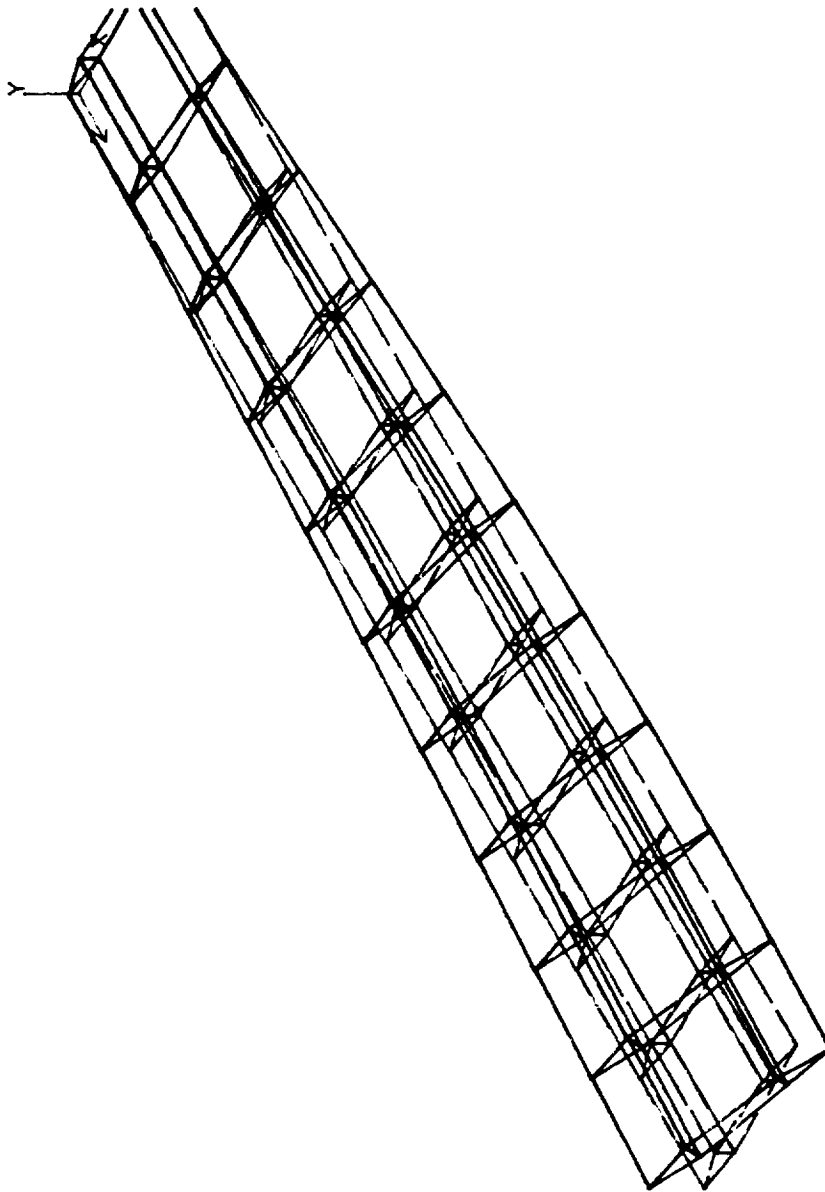
ZV =1

DIST=600

XF =90

YF =10.8

ZF =690



WING2

FIGURE 6.2.6
Mode 2 Preliminary Design
1st Torsion

ANSYS 4.3A2
FEB 23 1990
15:47:16
DISPL.
STEP=1
ITER=2
FREQ=4.048
DMX =1.581

XV =1
DIST=759
XF =90
YF =10.8
ZF =690



WING2

FIGURE 6.2.7

Mode 2 Preliminary Design
1st Torsion

ANSYS 4.3A2
FEB 23 1990
15:34:58
DISPL.
STEP=1
ITER=2
FREQ=4.048
DMX =1.581
YV =1
DIST=759
XF =90
YF =10.8
ZF =690

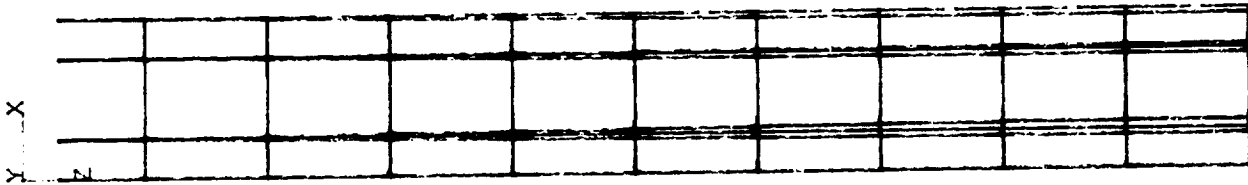


FIGURE 6.2.8
Mode 3 Preliminary Design
2nd Bending

ANSYS 4.3A2
FEB 23 1990
14:56:50
DISPL.
STEP=1
ITER=3
FREQ=4.843

XV -1
YV -1
ZV -1
DIST=600
XF -90
YF -10.8
ZF -690

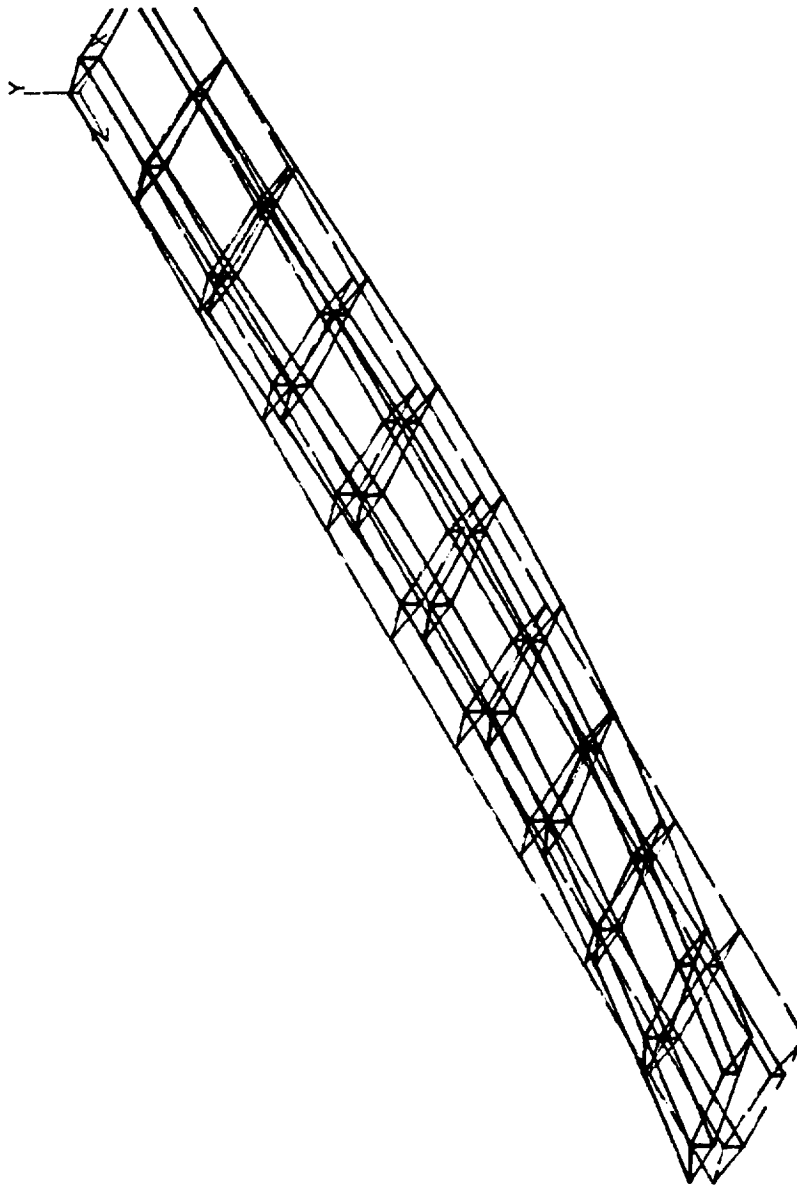


FIGURE 6.2.9
Mode 3 Preliminary Design
2nd Bending

ANSYS 4.3A2
FEB 23 1990
15: 54: 37
DISPL.
STEP=1
ITER=3
FREQ=4.843
DMX =1.602

XV =1
DIST=759
XF =90
YF =10.8
ZF =690



WING2

FIGURE 6.2.10
Mode 3 Preliminary Design
2nd Bending

ANSYS 4.3A2
FEB 23 1990
15:30:57
DISPL.
STEP=1
ITER=3
FREQ=4.843
DMX =1.602
YV =1
DIST=759
XF =90
YF =10.8
ZF =690

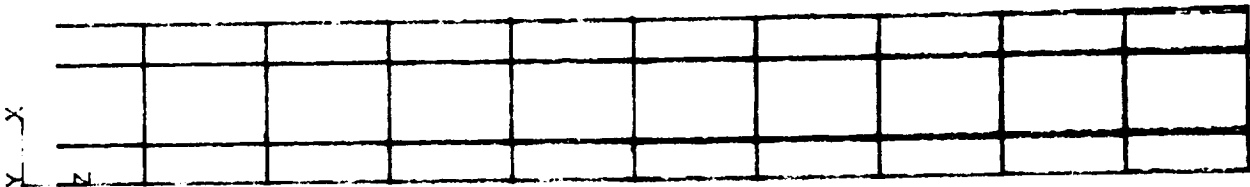
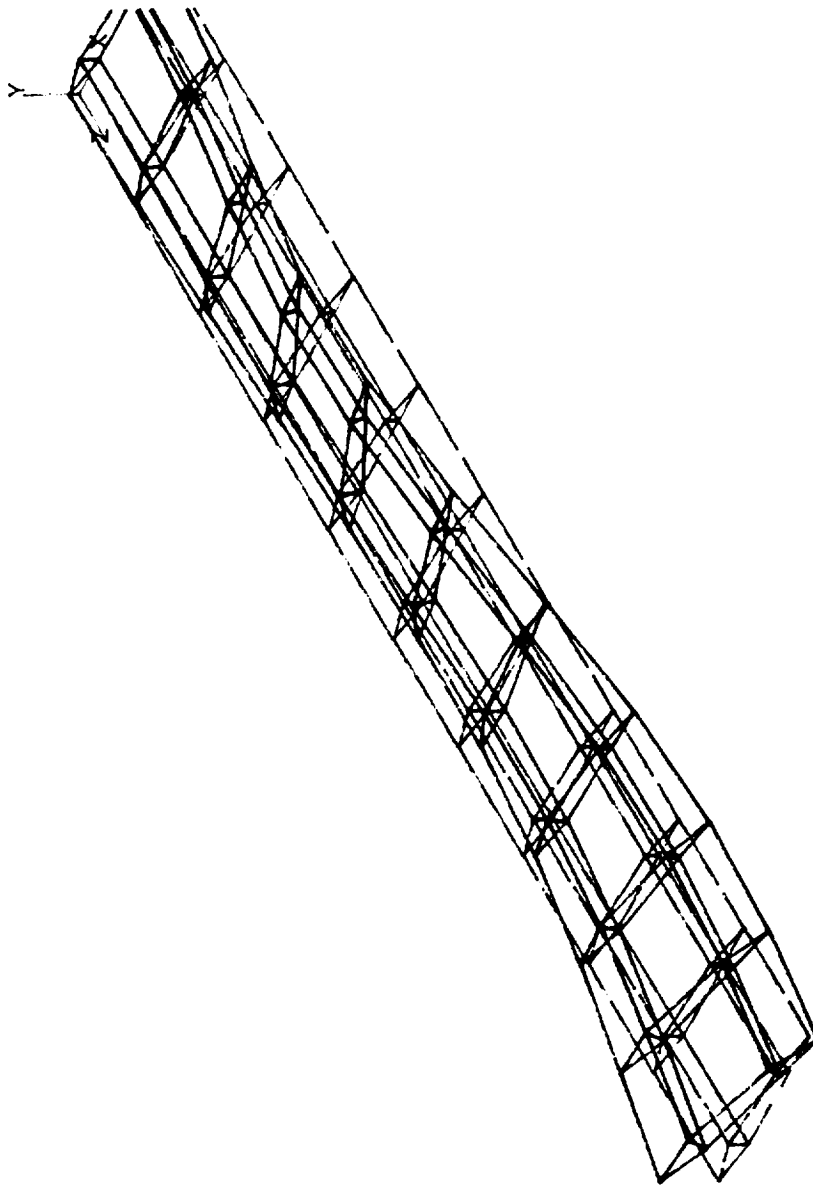


FIGURE 6.2.11
Mode 4 Preliminary Design
Combined mode

ANSYS 4.3A2
FEB 23 1990
15: 1:18
DISPL.
STEP=1
ITER=4
FREQ=11.931

XV =1
YV =1
ZV =1
DIST=600
XF =90
YF =10.8
ZF =690



WING2

FIGURE 6.2.12
Mode 4 Preliminary Design
Combined mode

ANSYS 4.3A2
FEB 23 1990
15:58:14
DISPL.
STEP=1
ITER=4
FREQ=11.931
DMX=-1.726
XV=-1
DIST=759
XF=-90
YF=-10.8
ZF=-690



WING2

FIGURE 6.2.13

Mode 4 Preliminary Design

Combined mode

ANSYS 4.3A2
FEB 23 1990
15:22:40
DISPL.
STEP=1
ITER=4
FREQ=11.931
DMX =1.726
YV =1
DIST=759
XF =90
YF =10.8
ZF =690

ORIGINAL PAGE IS
OF POOR QUALITY

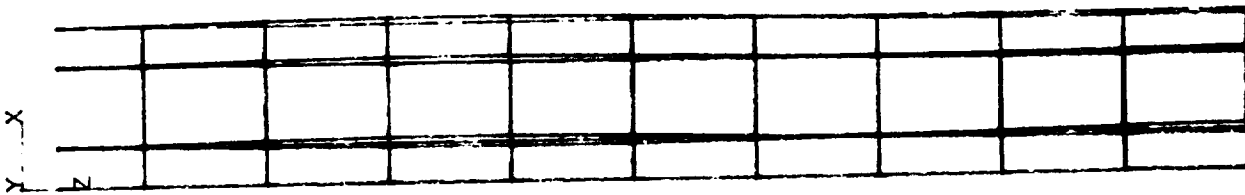


FIGURE 6.2.14
Mode 5 Preliminary Design
Combined mode

ANSYS 4.3A2
FEB 23 1990
15: 5: 38
DISPL.
STEP=1
ITER=5
FREQ=13.368

XV =1
YV =1
ZV =1
DIST=600
XF =90
YF =10.8
ZF =690

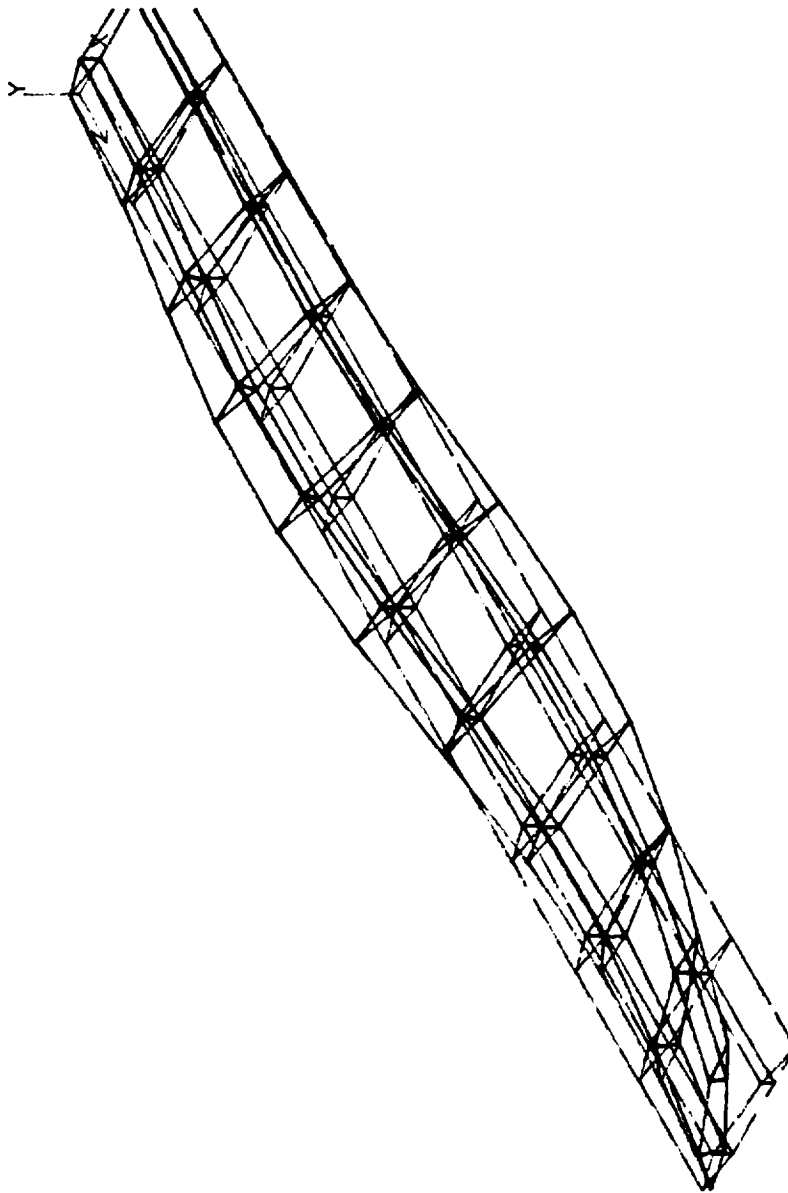


FIGURE 6.2.15
Mode 5 Preliminary Design
Combined mode

ANSYS 4.3A2
FEB 23 1990
16: 1: 54
DISPL.
STEP=1
ITER=5
FREQ=13.368
DMX =2.046

XV =1
DIST=759
XF =90
YF =10.8
ZF =690



WING2

FIGURE 6.2.16
 Mode 5 Preliminary Design
 Combined mode

ANSYS 4.3A2
 FEB 23 1990
 15: 11: 58
 DISPL.
 STEP=1
 ITER=5
 FREQ=13.368
 DMX =2.045
 YV =1
 DIST=759
 XF =90
 YF =10.8
 ZF =690

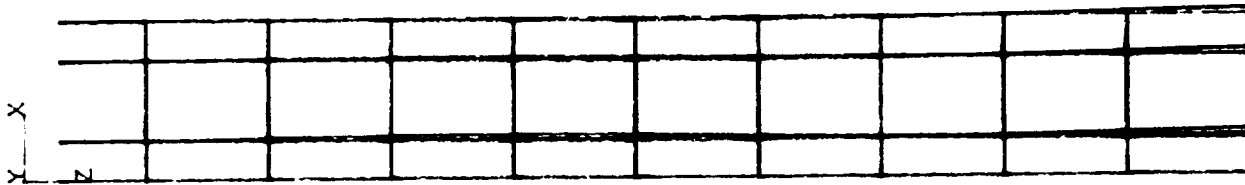


Figure 6.2.17

The frequency value in each mode for the revised wing:

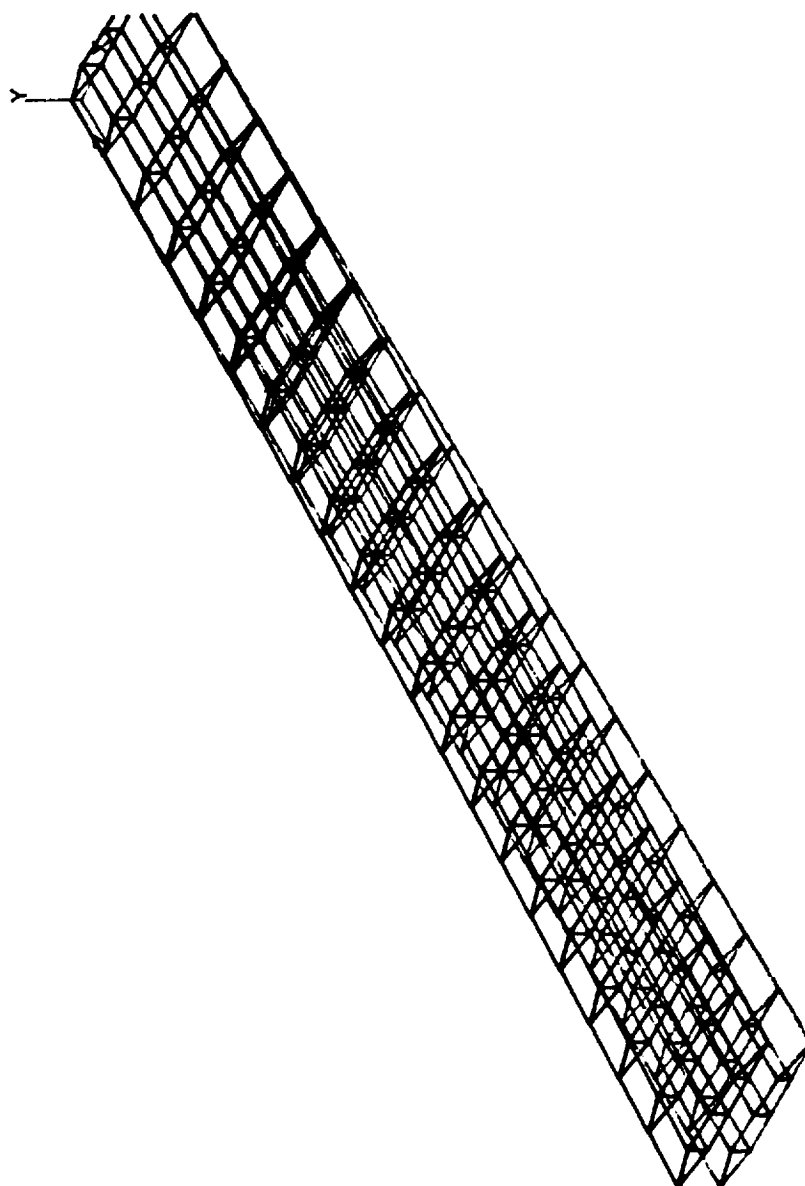
EIGENVALUE (NATURAL FREQUENCY)

MODE	FREQUENCY (CYCLE/SEC)
1	0.937703
2	5.27937
3	7.20949
4	14.0685
5	21.3167
6	26.8827
7	35.9328
8	43.5590
9	52.0220
10	63.4687

FIGURE 6.2.18
Mode 1 Revised Design
1st Bending

ANSYS 4.3A2
FEB 28 1990
14: 5: 8
DISPL.
STEP=1
ITER=1
FREQ=0.937703

XV =1
YV =1
ZV =1
DIST=600
XF =90
YF =10.8
ZF =690



WING3

FIGURE 6.2.19

Mode 1 Revised Design
1st Bending

ANSYS 4.3A2
FEB 28 1990
14:45:46
DISPL.
STEP=1
ITER=1
FREQ=0.937703
DMX =1.28

XV =1
DIST=759
XF =90
YF =10.8
ZF =690



FIGURE 6.2.20
Mode 1 Revised Design
1st Bending

ANSYS 4.3A2
FEB 28 1990
15:22:48
DISPL.
STEP=1
ITER=1
FREQ=0.937703
DMX =1.28
YV =1
DIST=759
XF =90
YF =10.8
ZF =690

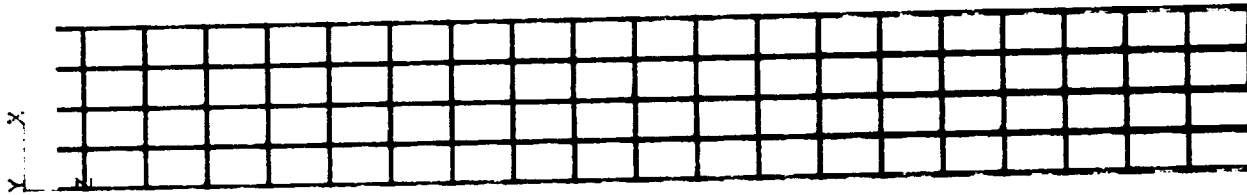


FIGURE 6.2.21

Mode 2 Revised Design

2nd Bending

ANSYS 4.3A2
FEB 28 1990

14: 13: 46

DISPL.

STEP=1

ITER=2

FREQ=5.279

XV =1

YV =1

ZV =1

DIST=600

XF =90

YF =10.8

ZF =890

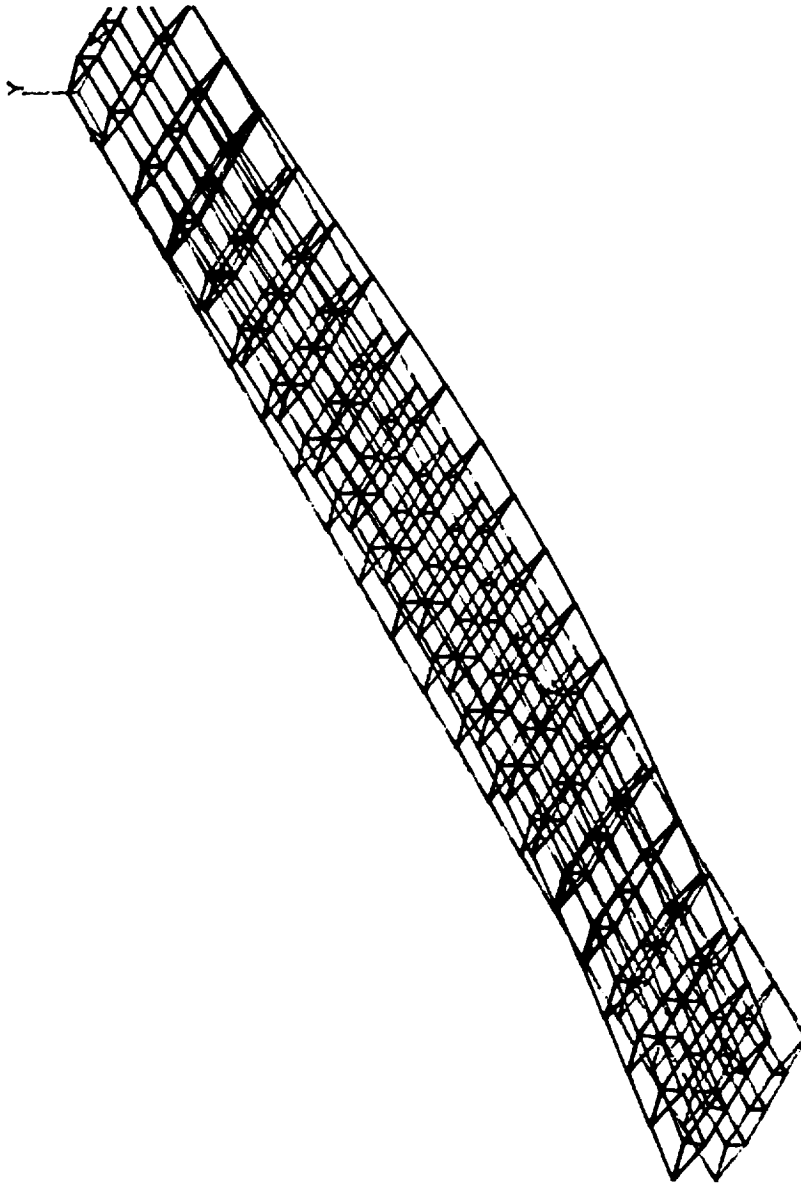


FIGURE 6.2.22
Mode 2 Revised Design
2nd Bending

ANSYS 4.3A2
FEB 28 1990
14:52: 9
DISPL.
STEP=1
ITER=2
FREQ=5.279
DMX =1.289

XV =1
DIST=759
XF =90
YF =10.8
ZF =690



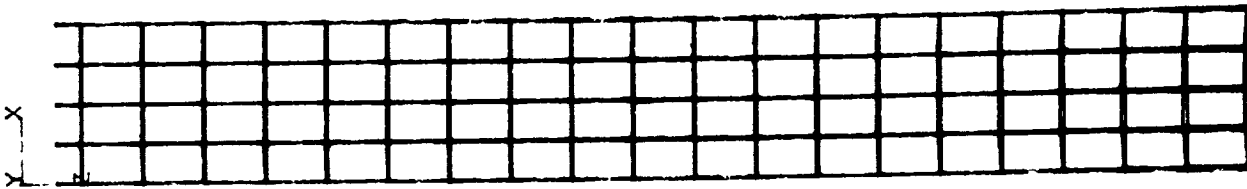
WING

FIGURE 6.2.23

Mode 2 Revised Design

2nd Bending

ANSYS 4.3A2
FEB 28 1990
15:29:51
DISPL.
STEP=1
ITER=2
FREQ=5.279
DMX =1.289
YV =-1
DIST=759
XF =90
YF =10.8
ZF =690

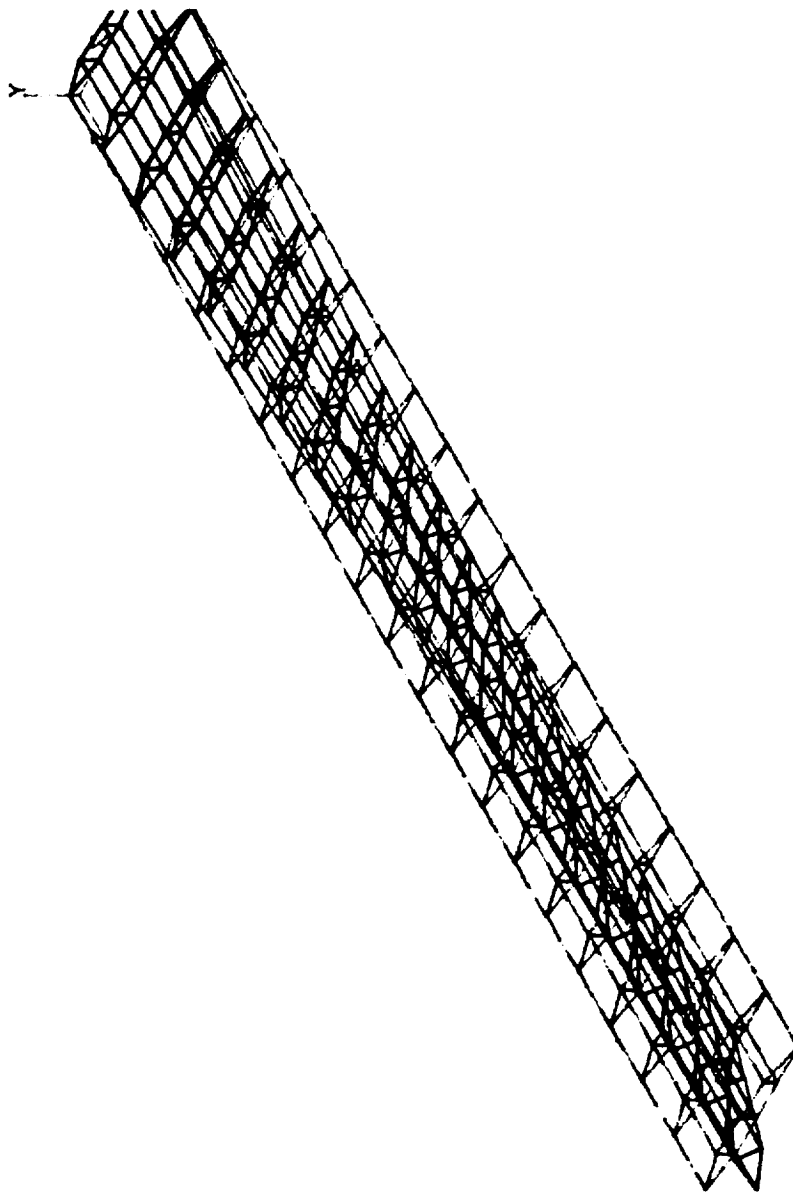


WING3

FIGURE 6.2.24
Mode 3 Revised Design
1st Torsion

ANSYS 4.3A2
FEB 28 1990
14: 24: 10
DISPL.
STEP=1
ITER=3
FREQ=7.209

XV =1
YV =1
ZV =1
DIST=600
XF =90
YF =10.8
ZF =690

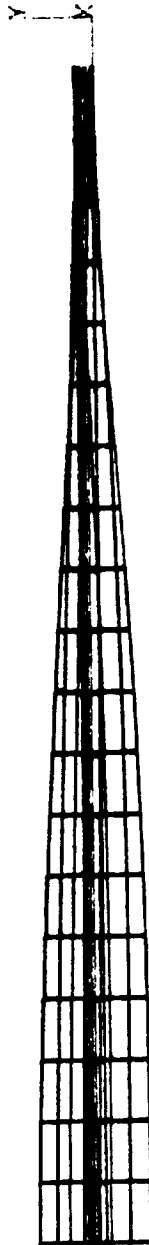


WING3

FIGURE 6.2.25
Mode 3 Revised Design
1st Torsion

ANSYS 4.3A2
FEB 28 1990
14:58:25
DISPL.
STEP=1
ITER=3
FREQ=7.209
DMX =1.954

XV =-1
DIST=759
XF =-90
YF =-10.8
ZF =-690



WING3

FIGURE 6.2.26

Mode 3 Revised Design

1st Torsion

ANSYS 4.3A2
FEB 28 1990
15:43: 5
DISPL.
STEP=1
ITER=3
FREQ=7.209
DMX =1.954
YV =1
DIST=759
XF =90
YF =10.8
ZF =690

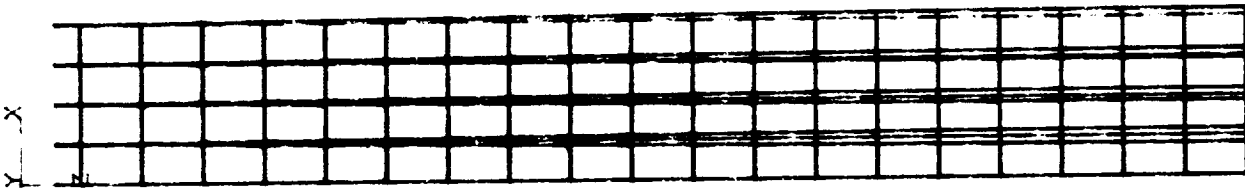
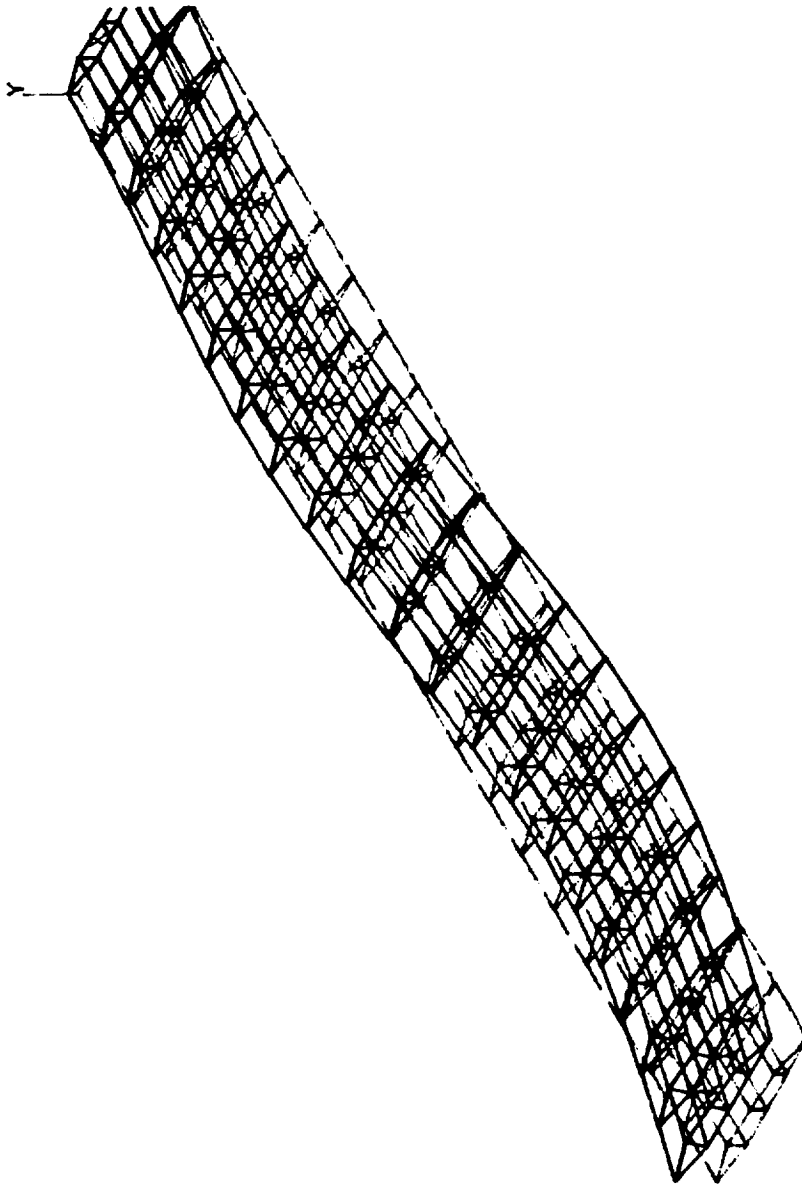


FIGURE 6.2.27
Mode 4 Revised Design
3rd Bending

ANSYS 4.3A2
FEB 28 1990
14:28:37
DISPL.
STEP=1
ITER=4
FREQ=14.068

XV =1
YV =1
ZV =1
DIST=600
XF =90
YF =10.8
ZF =690



WING3

FIGURE 6.2.28

Mode 4 Revised Design
3rd Bending

ANSYS 4.3A2
FEB 28 1990
15: 4: 50
DISPL.
STEP=1
ITER=4
FREQ=14.058
DMX =1.247

XV =1
DIST=759
XF =90
YF =10.8
ZF =690



FIGURE 6.2.29

Mode 4 Revised Design
3rd Bending

ANSYS 4.3A2
FEB 28 1990
15:50:20
DISPL.
STEP=1
ITER=4
FREQ=14.068
DMX =1.247
YV =1
DIST=759
XF =90
YF =10.8
ZF =690

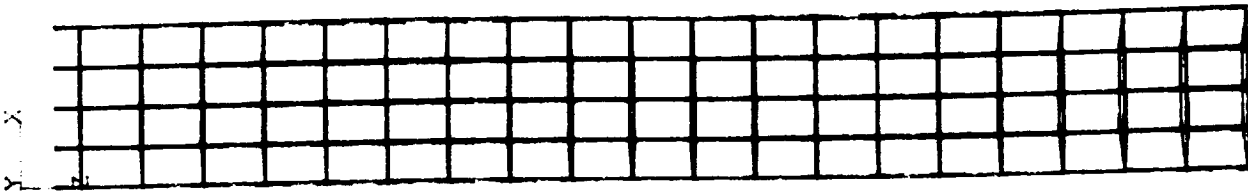
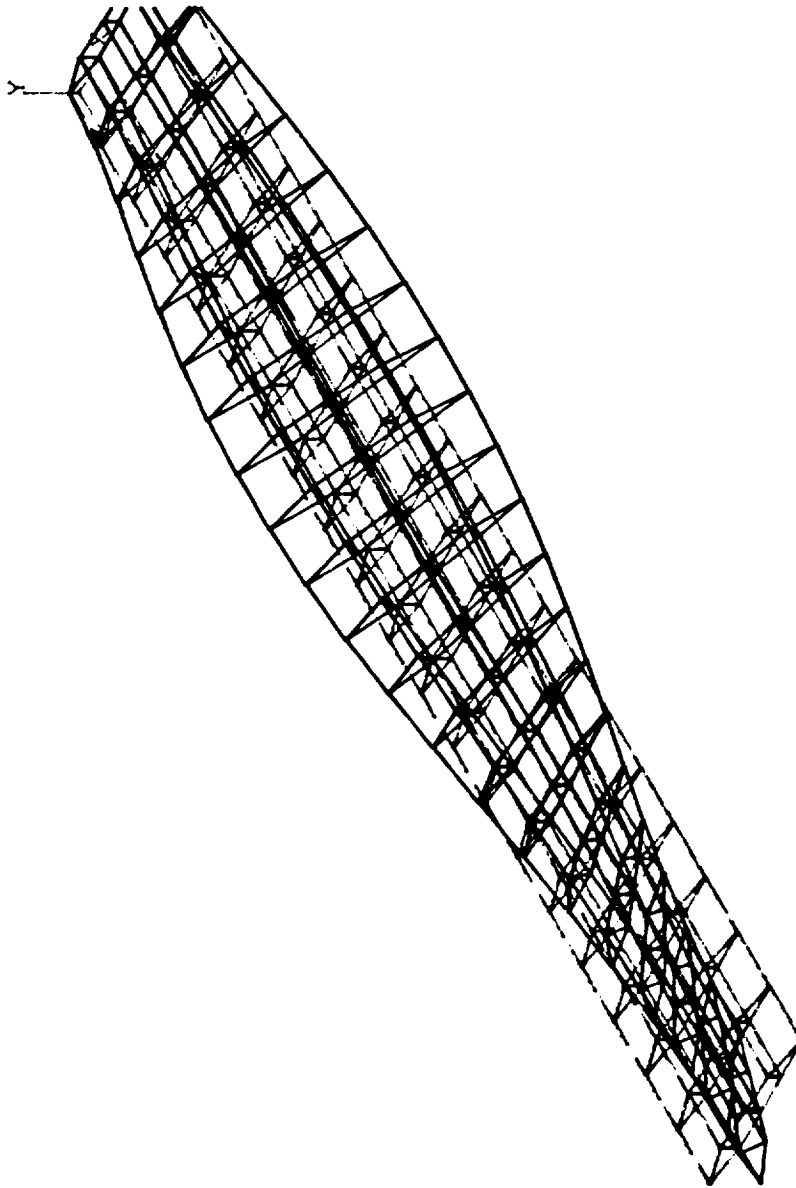


FIGURE 5.2.30
Mode 5 Revised Design
2nd Torsion

ANSYS 4.3A2
FEB 28 1990
14:36: 2
DISPL.
STEP=1
ITER=5
FREQ=21.317

XV =1
YV =1
ZV =1
DIST=600
XF =90
YF =10.8
ZF =690



WING3

FIGURE 6.2.31
Mode 5 Revised Design
2nd Torsion

ANSYS 4.3A2
FEB 28 1990
15:11: 6
DISPL.
STEP=1
ITER=5
FREQ=21.317
DMX =1.958
XV =1
DIST=759
XF =90
YF =10.8
ZF =690



FIGURE 6.2.32

Mode 5 Revised Design
2nd Torsion

ORIGINAL PAGE IS
OF POOR QUALITY

ANALYSIS 4.342
FEB 28 1990
15:57:29
DISPL.
STEP=1
ITER=5
FREQ=21.317
DMZ=1.958
YV -1
DIST=759
XF -90
YF -10.8
ZF -690

Y X

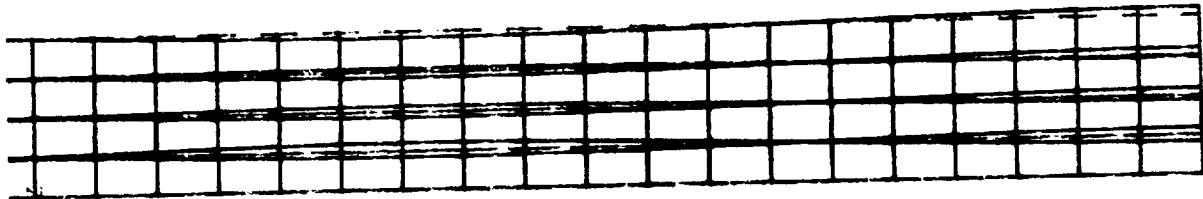


Figure 6.2.33

The frequency value in each mode for the revised wing:

EIGENVALUE (NATURAL FREQUENCY)

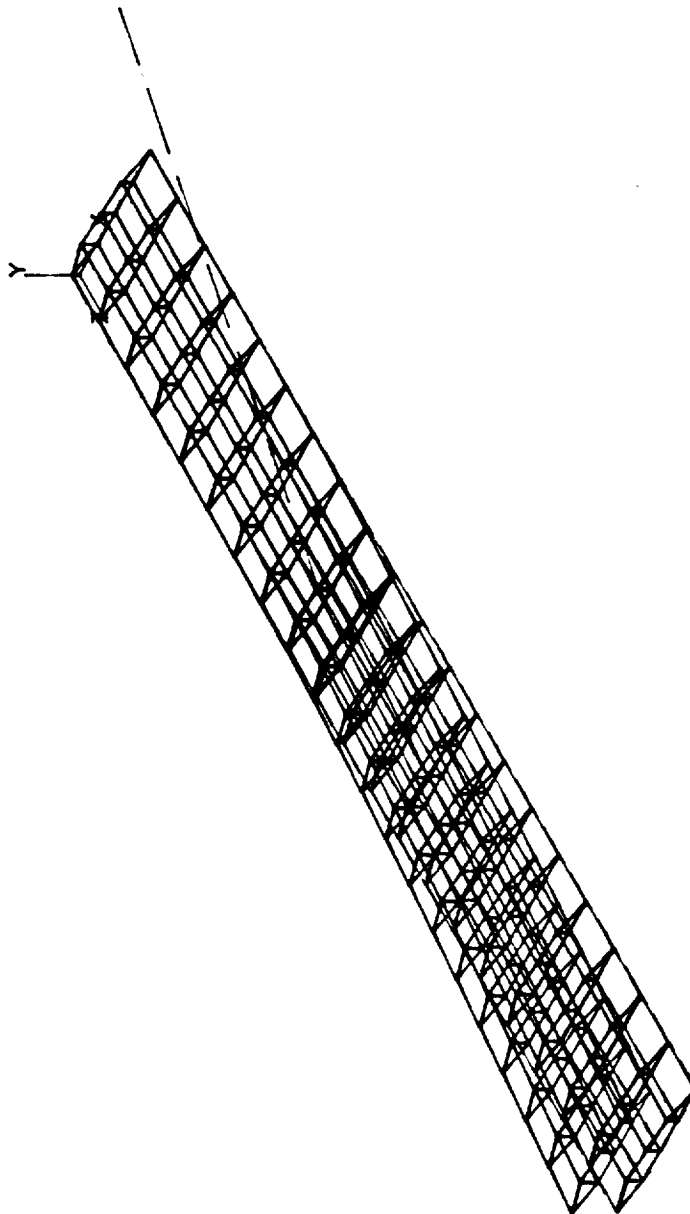
MODE	FREQUENCY (CYCLE/SEC)
1	1.54863
2	5.88586
3	7.17381
4	12.6177
5	20.9103
6	25.4295
7	35.9099
8	37.5427
9	47.5733
10	56.8922

FIGURE 6.2.34

Mode 1 Revised Design w/Brace
1st Bending

ANSYS 4.3A2
MAR 29 1990
16:32:33
DISPL.
STEP=1
ITER=1
FREQ=1.549

XV -1
YV -1
ZV -1
DIST=700
XF -255
YF -120
ZF -690



WING3

FIGURE 6.2.35

Mode 1 Revised Design w/Brace
1st Bending

ANSYS 4.3A2
MAR 29 1990
18:24:39

DISPL.

STEP=1

ITER=1

FREQ=1.549

DMX =1.464

XV =1

DIST=759

XF =255

YF =120

ZF =690

ORIGINAL PAGE IS
OF POOR QUALITY



FIGURE 6.2.36
Mode 1 Revised Design w/Brace
1st Bending

ANSYS 4.3A2
MAR 29 1990
17:13:45
DISPL.
STEP=1
ITER=1
FREQ=1.549
DMX =1.464
YV =1
DIST=759
XF =255
YF =120
ZF =690

ORIGINAL PAGE IS
OF POOR QUALITY

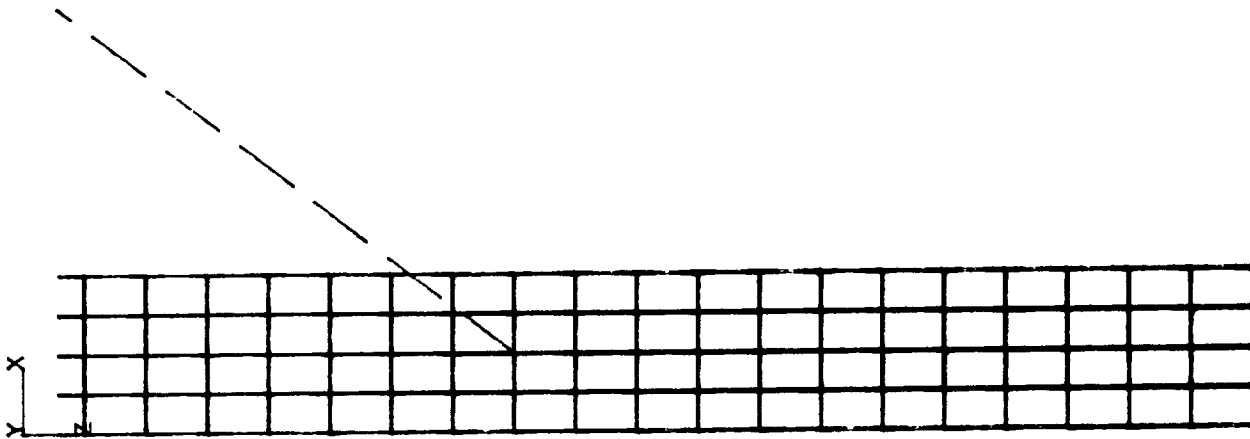


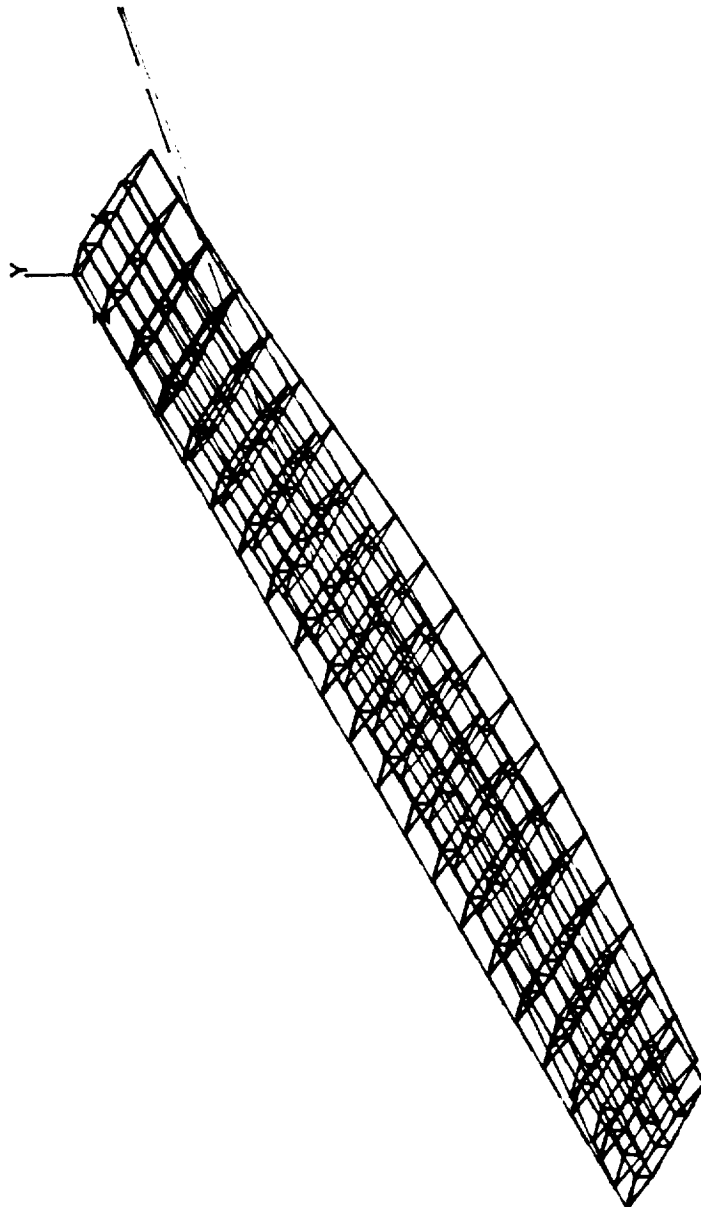
FIGURE 6.2.37

Mode 2 Revised Design w/Brace

2nd Bending

ANSYS 4.3A2
MAR 29 1990
16:39:49
DISPL.
STEP=1
ITER=2
FREQ=5.886

XV -1
YV -1
ZV -1
DIST=700
XF -255
YF -120
ZF -690



WING3

FIGURE 6.2.38
Mode 2 Revised Design w/Brace
2nd Bending

ANSYS 4.3A2
MAR 29 1990
18:14:46
DISPL.
STEP=1
ITER=2
FREQ=5.886
DMX =1.193

XV =1
DIST=759
XF =255
YF =120
ZF =690

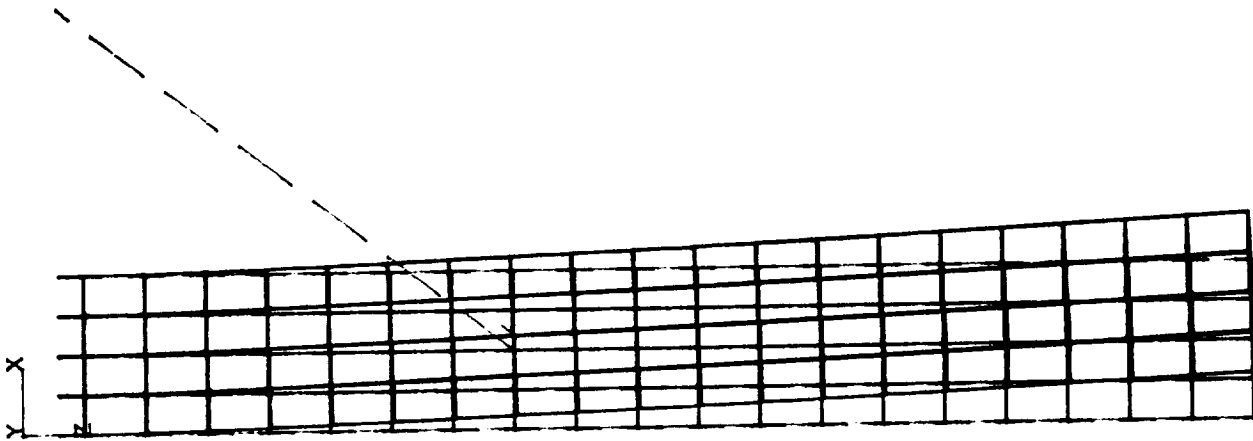


FIGURE 6.2.39

Mode 2 Revised Design w/Brace

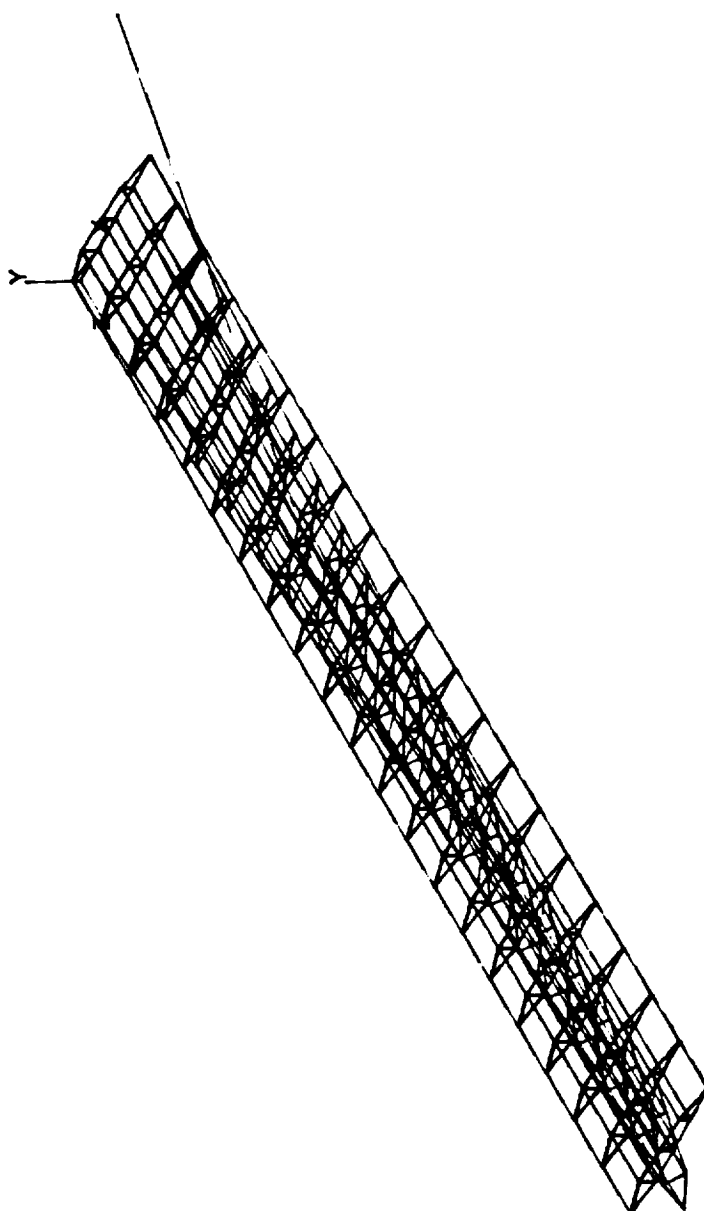
2nd Bending

ANSYS 4.3A2
MAR 29 1990
17:20:58
DISPL.
STEP=1
ITER=2
FREQ=5.886
DMX =1.193
YV =1
DIST=759
XF =255
YF =120
ZF =690



ANSYS 4.3A2
MAR 29 1990
16: 46: 57
DISPL.
STEP=1
ITER=3
FREQ=7.174

XV =1
YV =1
ZV =1
DIST=700
XF =255
YF =120
ZF =690



WING3

FIGURE 6.2.40
Mode 3 Revised Design w/Brace
1st Torsion

FIGURE 6.2.41

Mode 3 Revised Design w/Brace
1st Torsion

ORIGINAL PAGE IS
OF POOR QUALITY

ANSYS 4.3A2
MAR 29 1990
18: 8:14
DISPL.
STEP=1
ITER=3
FREQ=7.174
DMX =1.838

XV =1
DIST=759
XF =255
YF =120
ZF =690

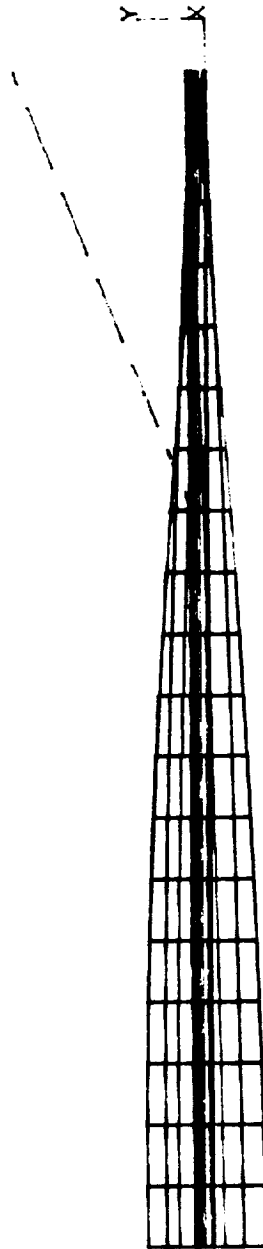
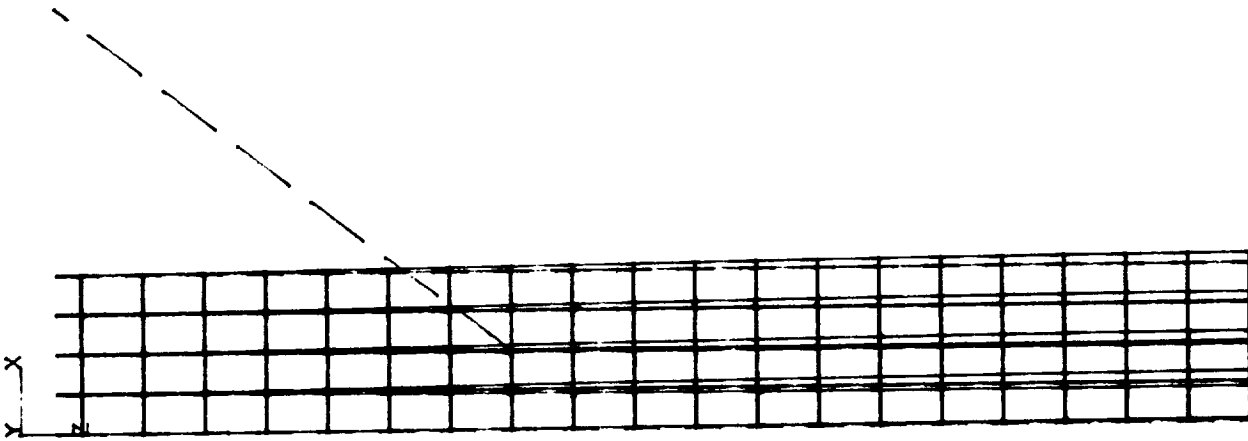


FIGURE 6.2.42
Mode 3 Revised Design w/Brace
1st Torsion

ANSYS 4.3A2
MAR 29 1990
17:28:41
DISPL.
STEP=1
ITER=3
FREQ=7.174
DMX =1.838
YV =1
DIST=759
XF =255
YF =120
ZF =690



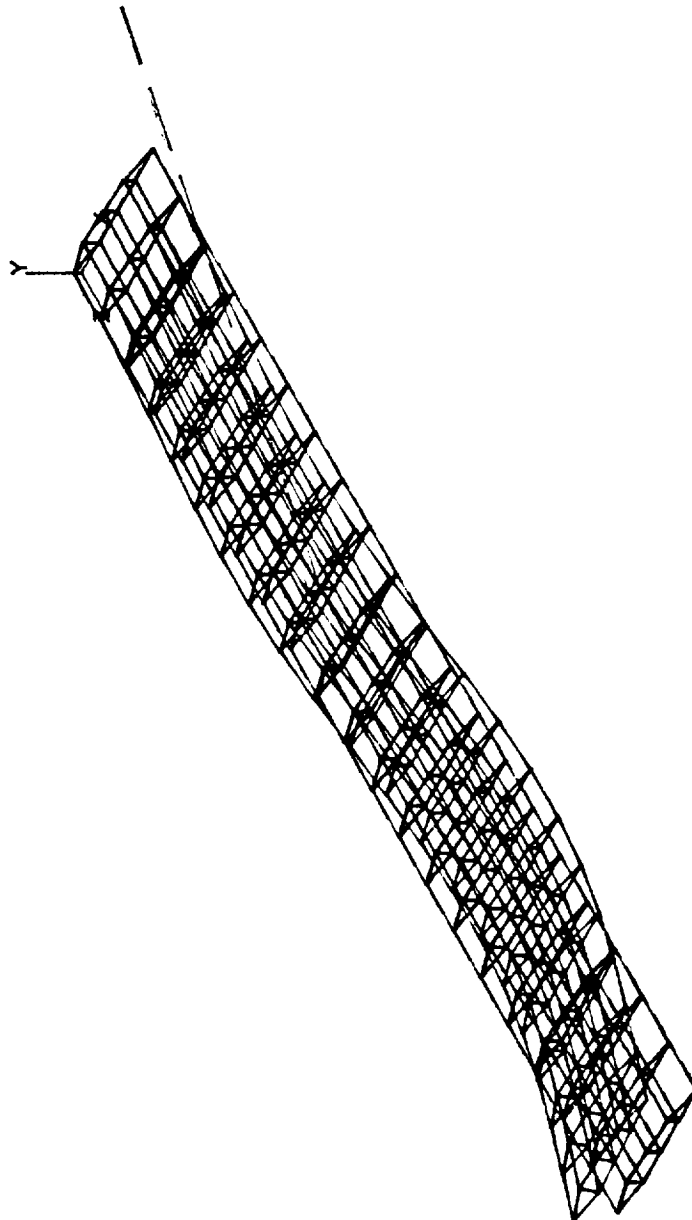
WING3

FIGURE 6.2.43

Mode 4 Revised Design w/Brace
3rd Bending

ANSYS 4.3A2
MAR 29 1990
16: 53: 53
DISPL.
STEP=1
ITER=4
FREQ=12.618

XV =1
YV =1
ZV =1
DIST=700
XF =255
YF =120
ZF =690



WING3

ANSYS 4.3A2
MAR 29 1990
18: 1:51
DISPL.
STEP=1
ITER=4
FREQ=12.618
DMX =1.525

XV =1
DIST=759
XF =255
YF =120
ZF =690

FIGURE 6.2.44
Mode 4 Revised Design w/Brace
3rd Bending



FIGURE 6.2.45

Mode 4 Revised Design w/Brace
3rd Bending

ANSYS 4.3A2
MAR 29 1990
17:35:50
DISPL.
STEP=1
ITER=4
FREQ=12.618
DMX =1.525
YV -1
DIST=759
XF -255
YF -120
ZF -690

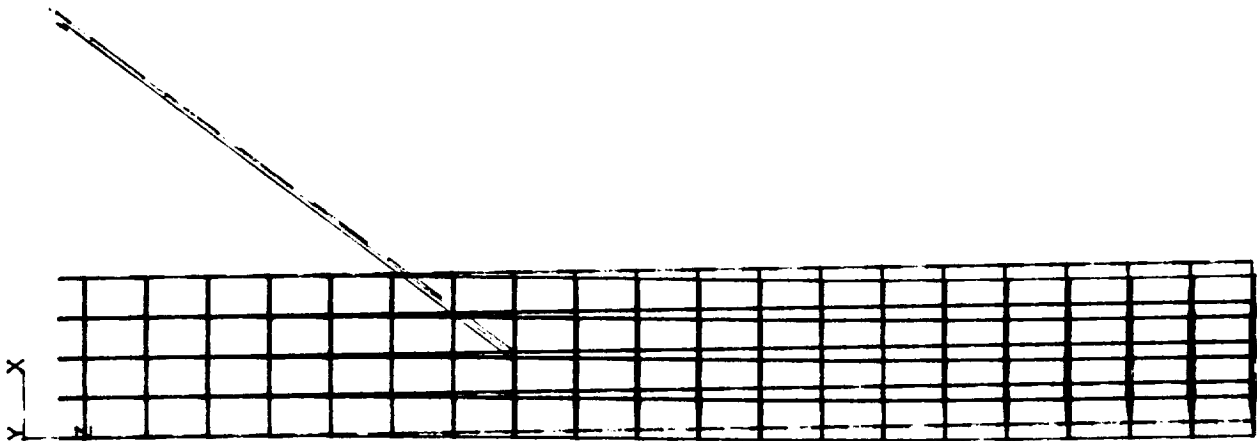
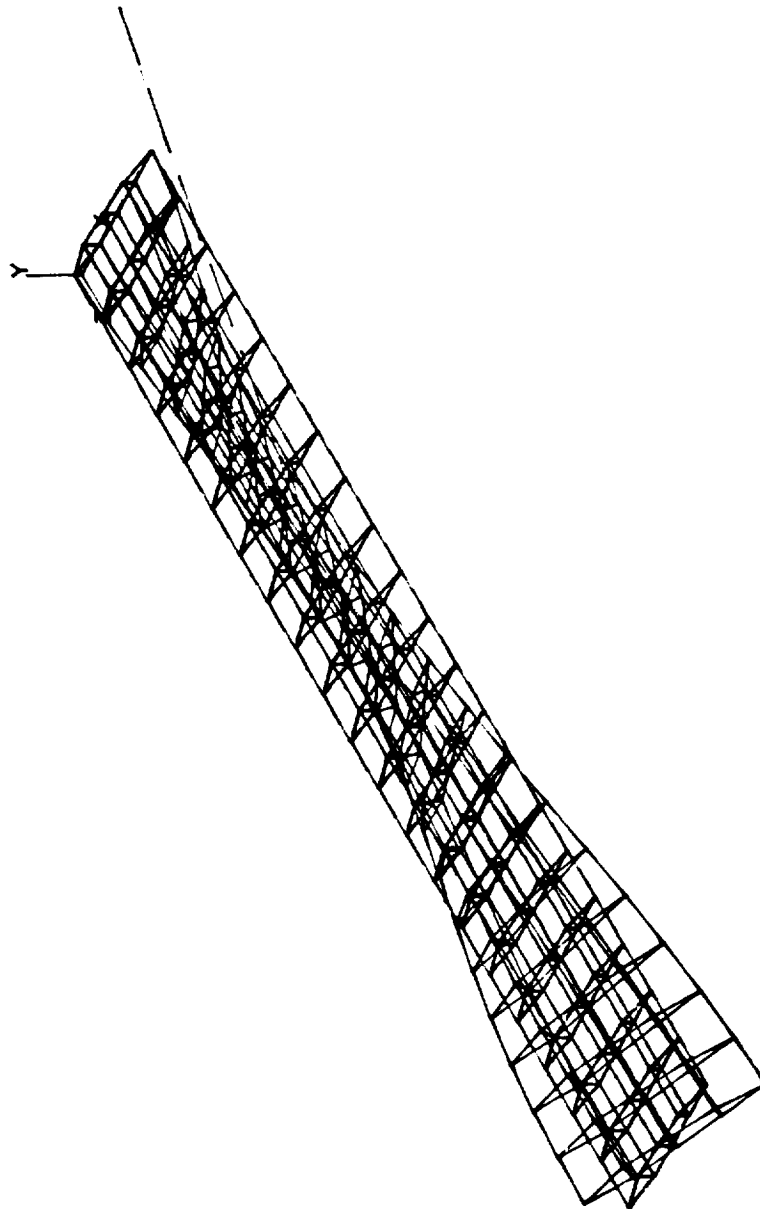


FIGURE 6.2.46

Mode 5 Revised Design w/Brace
2nd Torsion

ANSYS 4.3A2
MAR 29 1990
17: 1: 4
DISPL.
STEP=1
ITER=5
FREQ=20.91

XV -1
YV -1
ZV -1
DIST=700
XF -255
YF -120
ZF -690



WING3

ANSYS 4.3A2
MAR 29 1990
17:55:15

DISPL.

STEP=1

ITER=5

FREQ=20.91

DMX =1.935

XV =1

DIST=759

XF =255

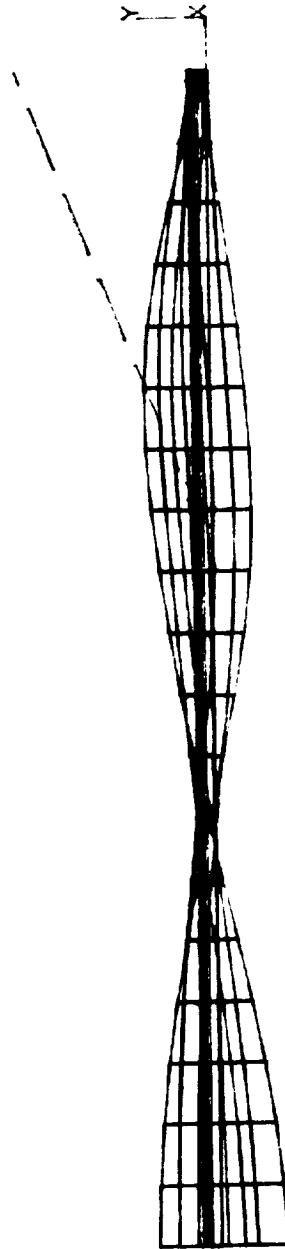
YF =120

ZF =690

FIGURE 6.2.47

Mode 5 Revised Design w/Brace

2nd Torsion



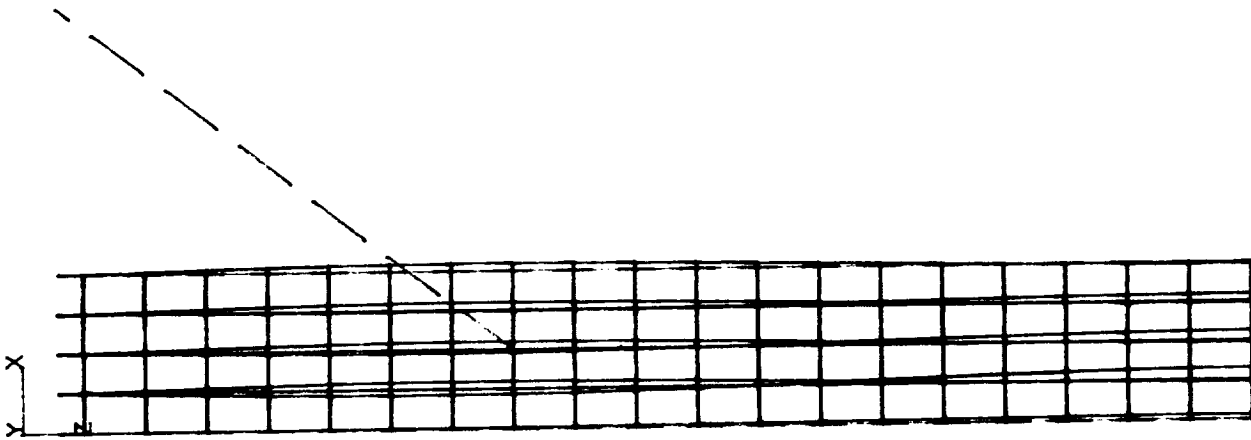
WING3

FIGURE 6.2.48

Mode 5 Revised Design w/Brace
2nd Torsion

ANSYS 4.3A2
MAR 29 1990
17:46:34
DISPL.
STEP=1
ITER=5
FREQ=20.91
DMX =1.935

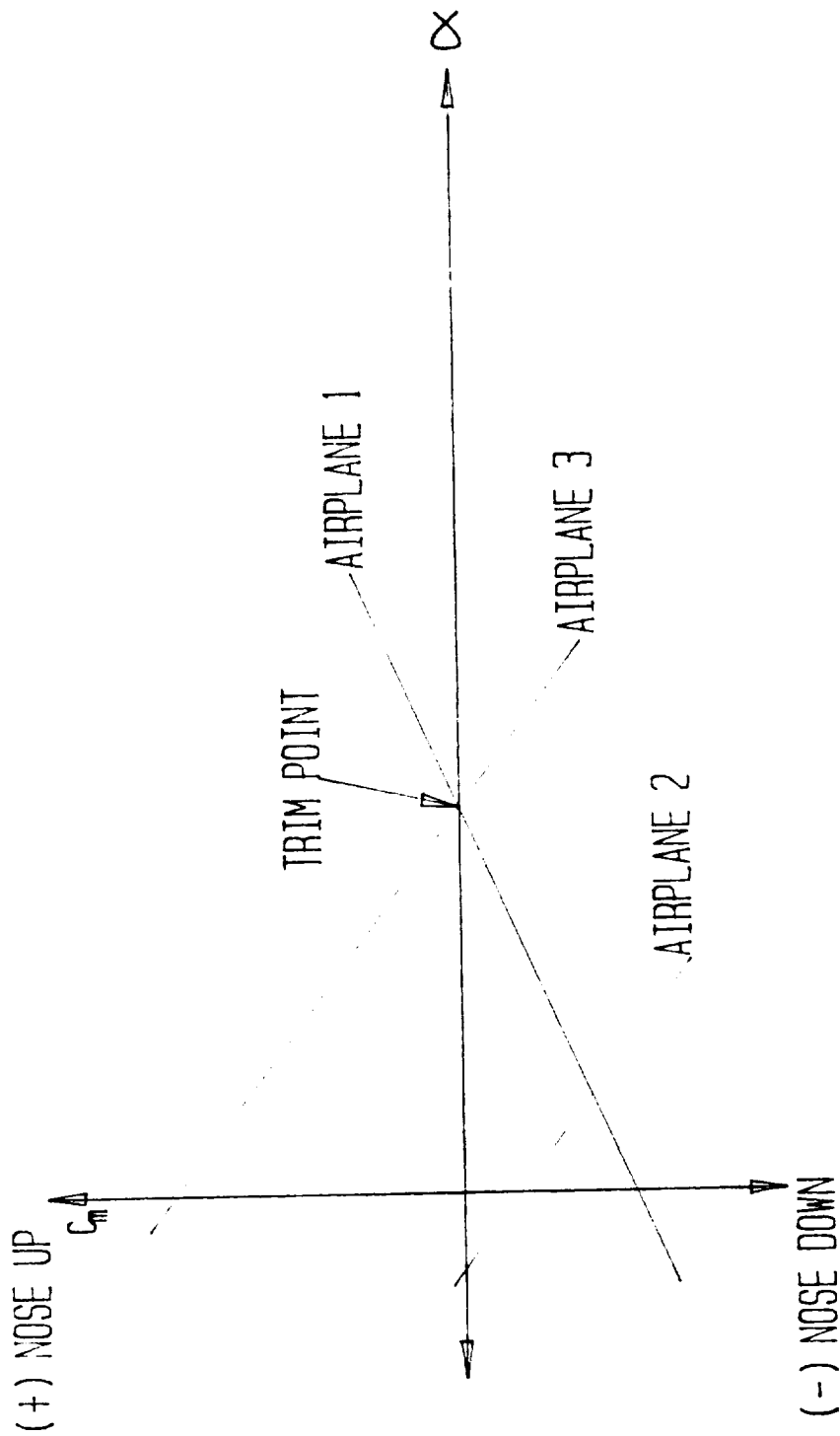
YV =1
DIST=759
XF =255
YF =120
ZF =690



WING3

Figure 7.1.1
CMcg vs. Alpha for three
Arbitrary Airplanes

ORIGINAL PAGE IS
OF POOR QUALITY



Component Contributions to Static Stability

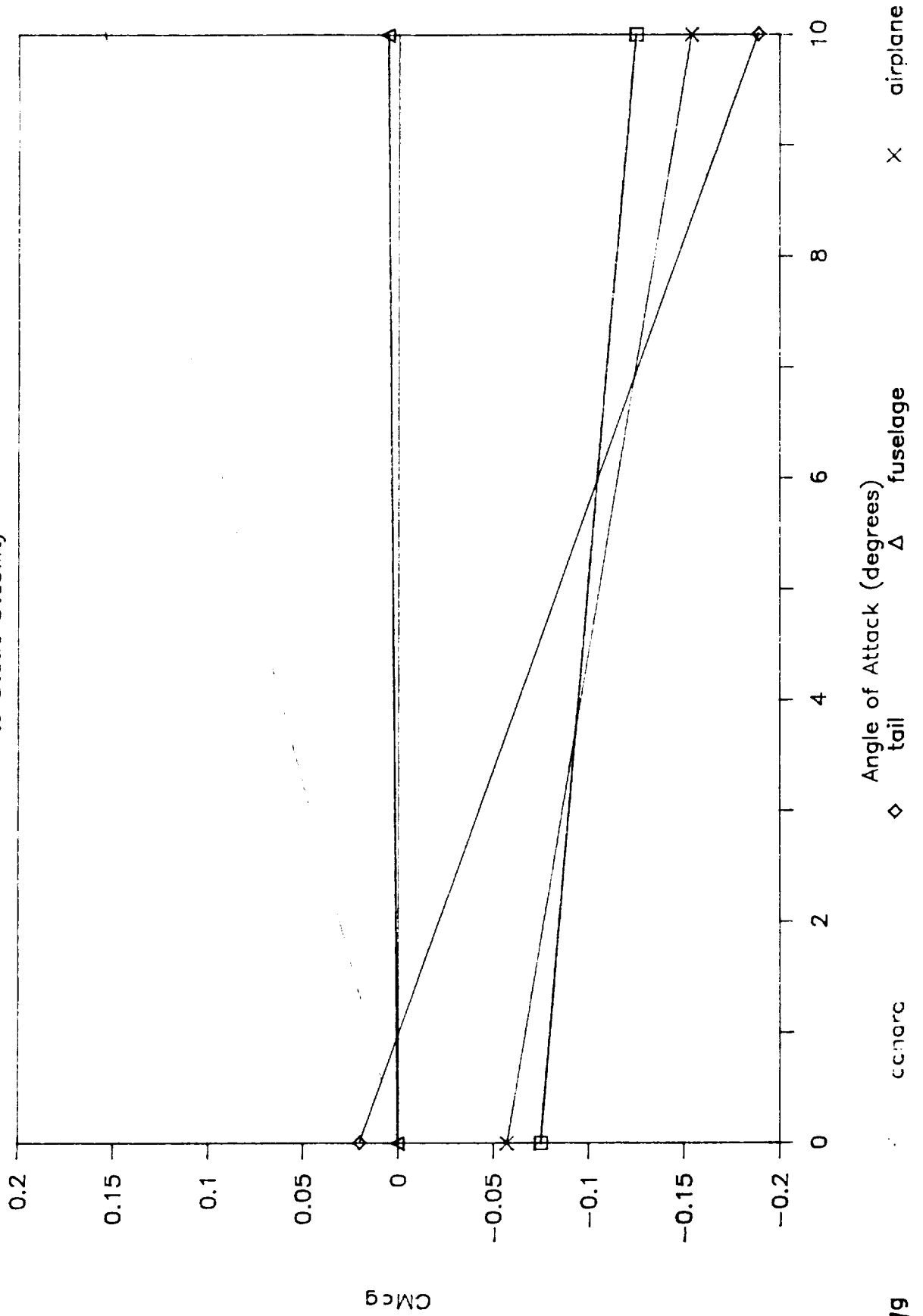
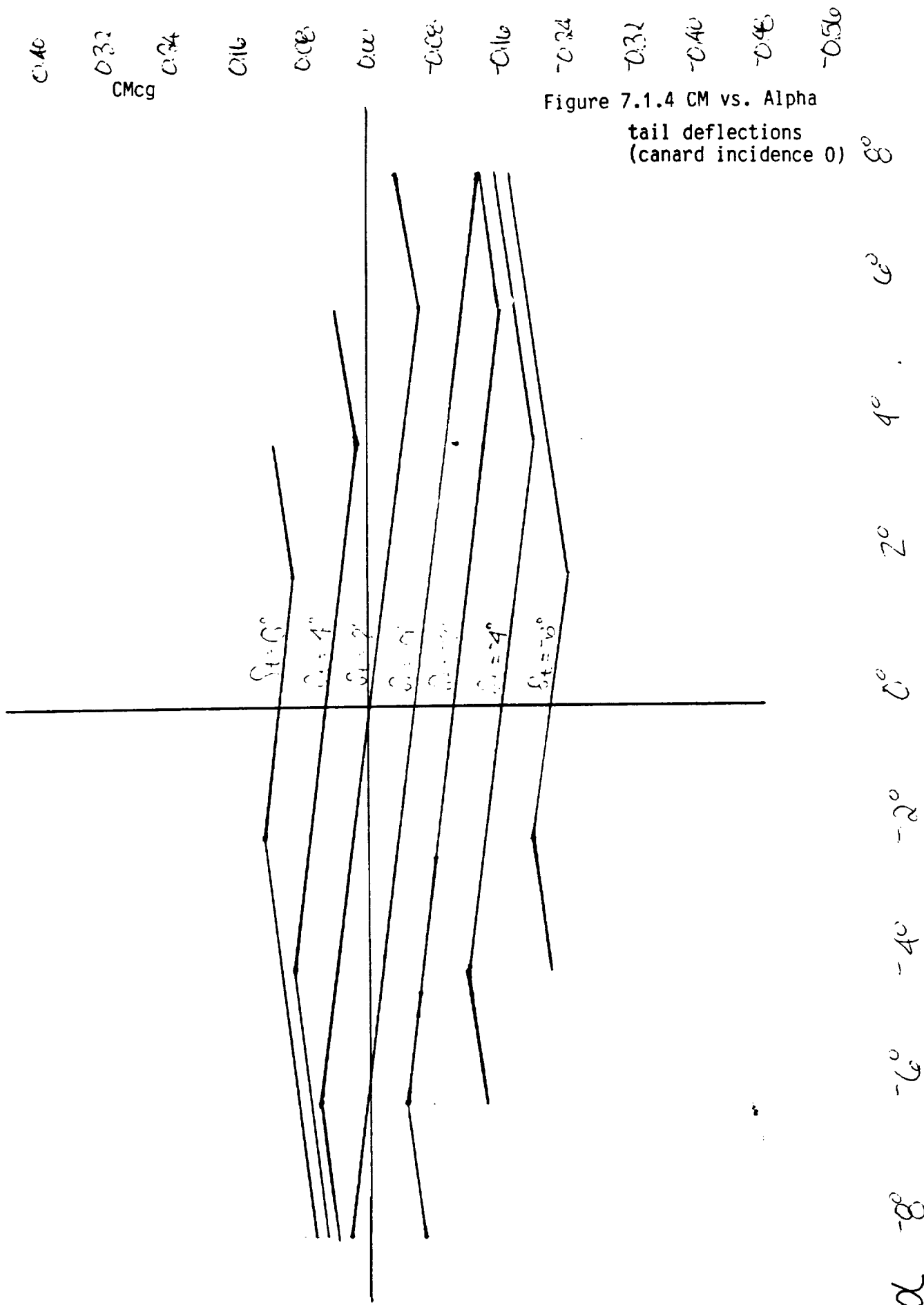


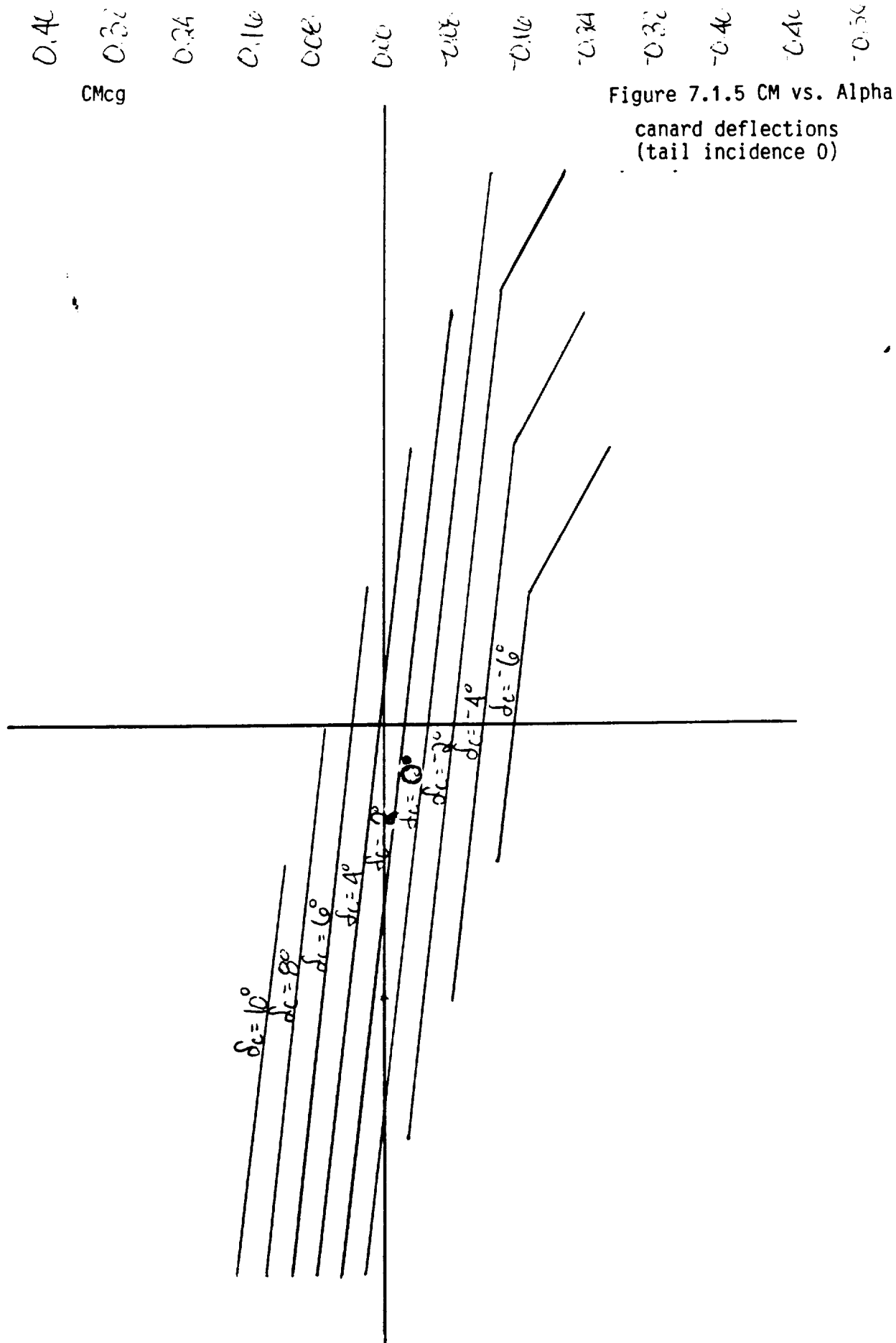
FIGURE 7.1.3

Static Stability Analysis Data

<u>Symbol:</u>	<u>Description:</u>	<u>Value:</u>
c	wing mean aerodynamic chord	15.36 ft.
S_w	wing planform area	3594.3 sq. ft.
AR_w	wing aspect ratio	15.23
S_t	tail planform area	520 sq. ft
AR_t	tail aspect ratio	5.2
S_c	canard planform area	470 sq. ft.
AR_c	canard aspect ratio	4.7
L_t	CG to tail AC distance	36.50 ft.
L_c	CG to canard AC distance	23.66 ft.
X_{ac}	CG to wing AC distance	3.84 ft.
X_{cg}	CG to neutral point dist.	3.05 ft.
n	wing/tail effective vel. ratio	1
C_{L0w}	wing lift coeff. at 0 AOA	0.302
$C_{m_{ac}^w}$	wing moment coeff. at 0 AOA	-0.0596
$dC_l/d\alpha$	wing section lift curve slope	2π



ORIGINAL PAGE IS
OF POOR QUALITY



ORIGINAL PAGE IS
OF POOR QUALITY

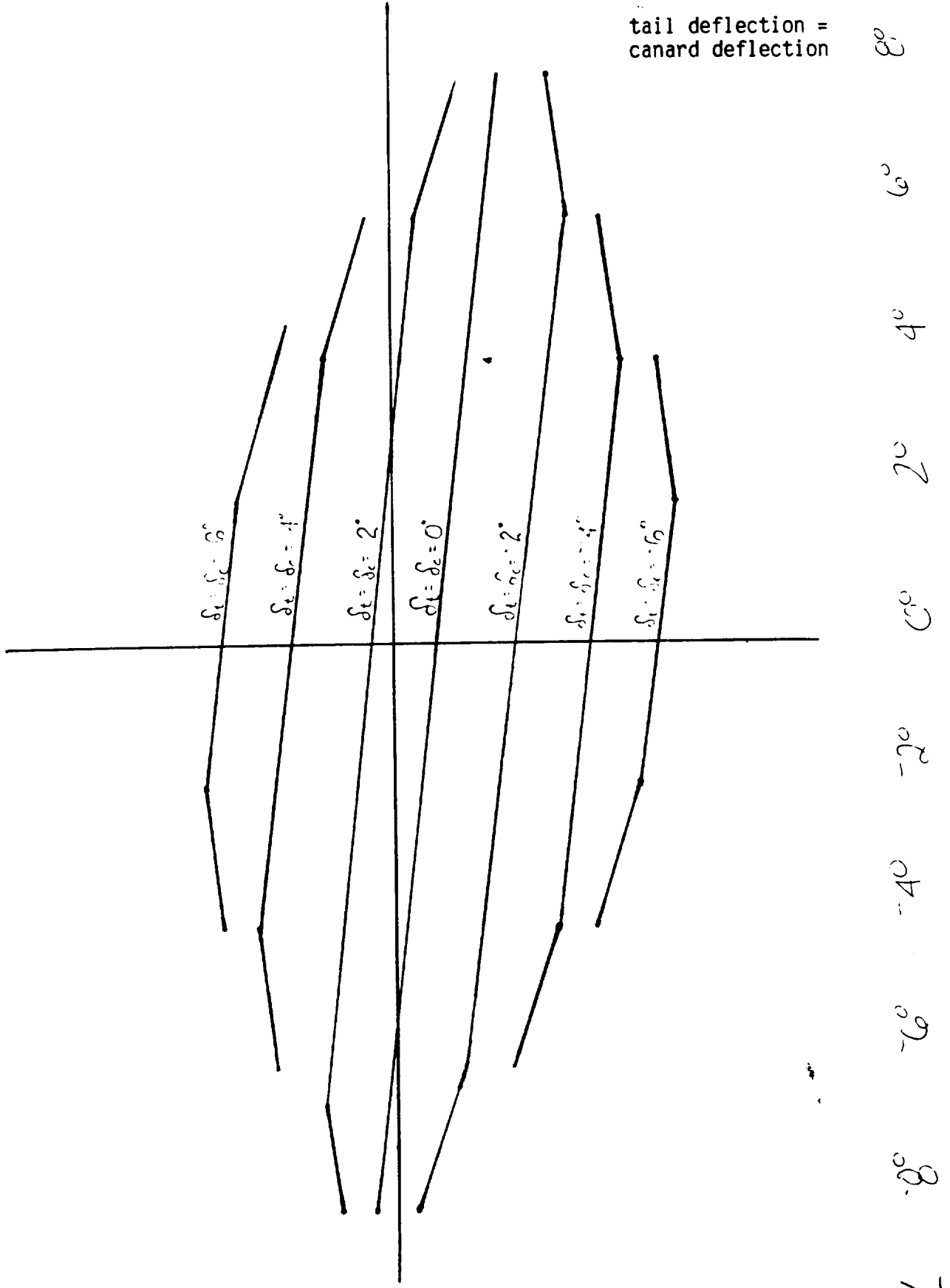
α -8° -6° -4° -2° 0° 2° 4° 6° 8°

0.40
0.32
0.24
0.16
0.08
0.00
-0.08
-0.16
-0.24
-0.32
-0.40
-0.48
-0.56

CMcg

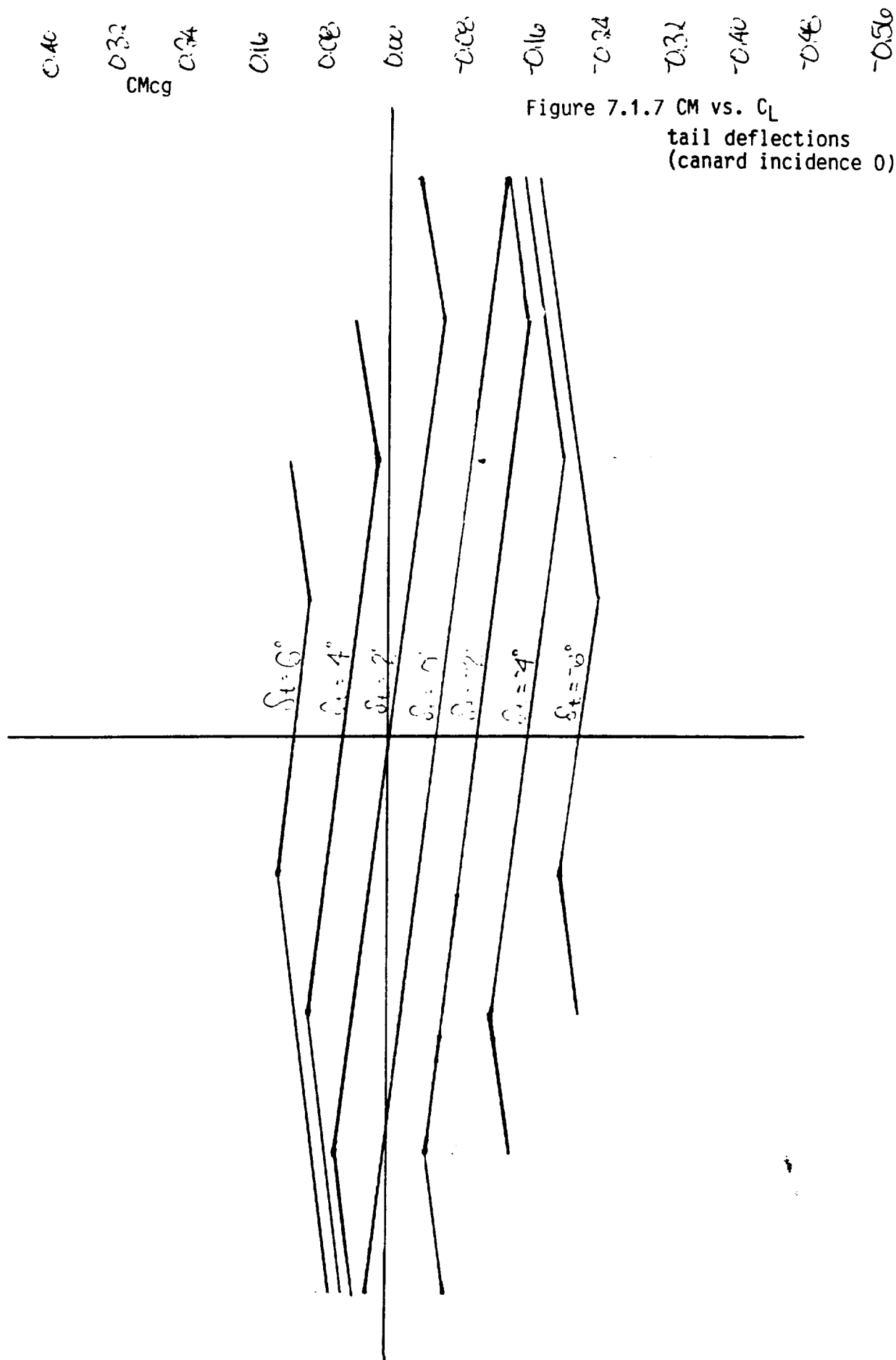
Figure 7.1.6 CM vs. Alpha

tail deflection =
canard deflection



ORIGINAL PAGE IS
OF POOR QUALITY

α



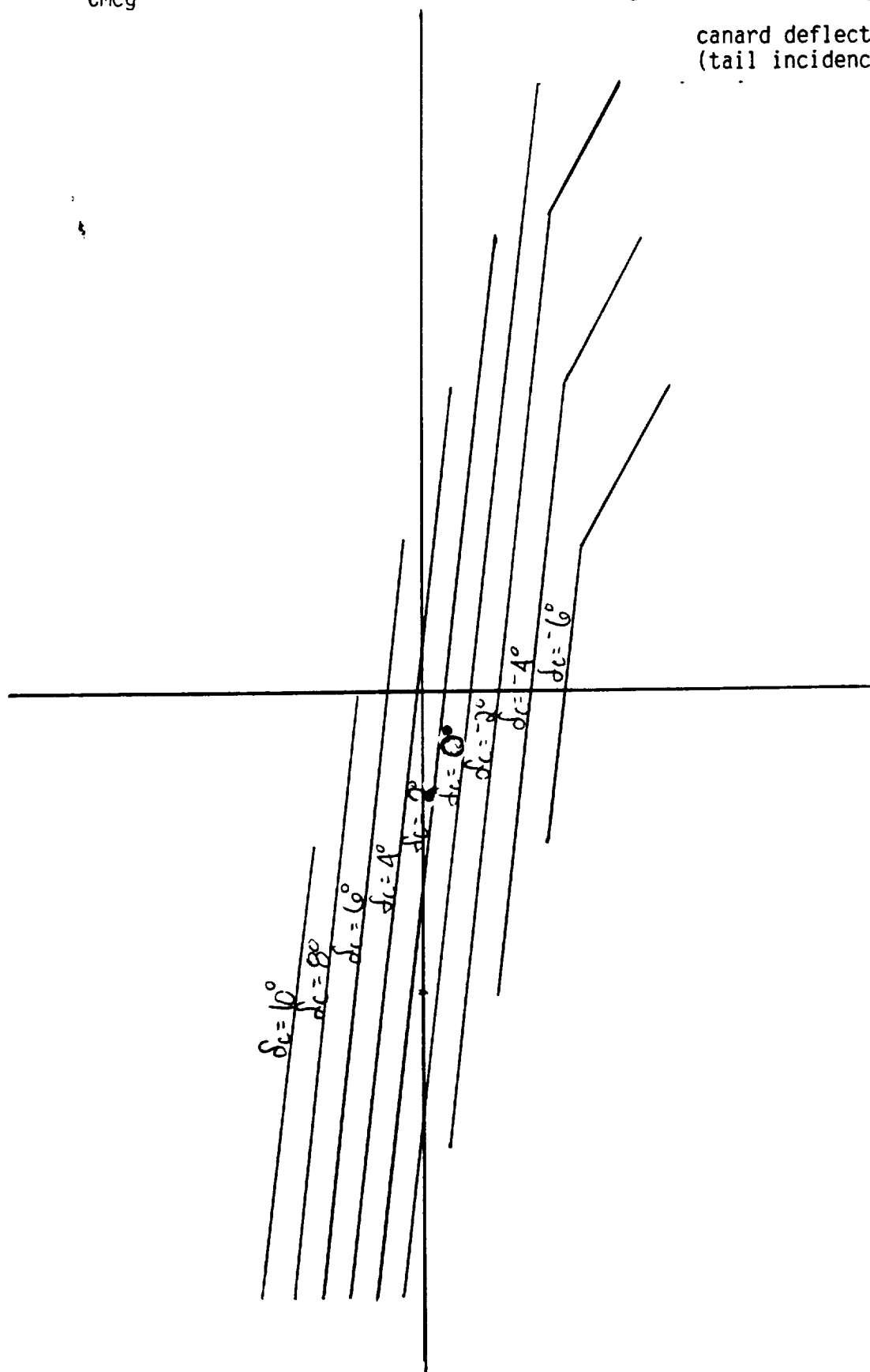
ORIGINAL PAGE IS
OF POOR QUALITY

0.40
0.32
0.24
0.16
0.08
0.00
-0.08
-0.16
-0.24
-0.32
-0.40
-0.48

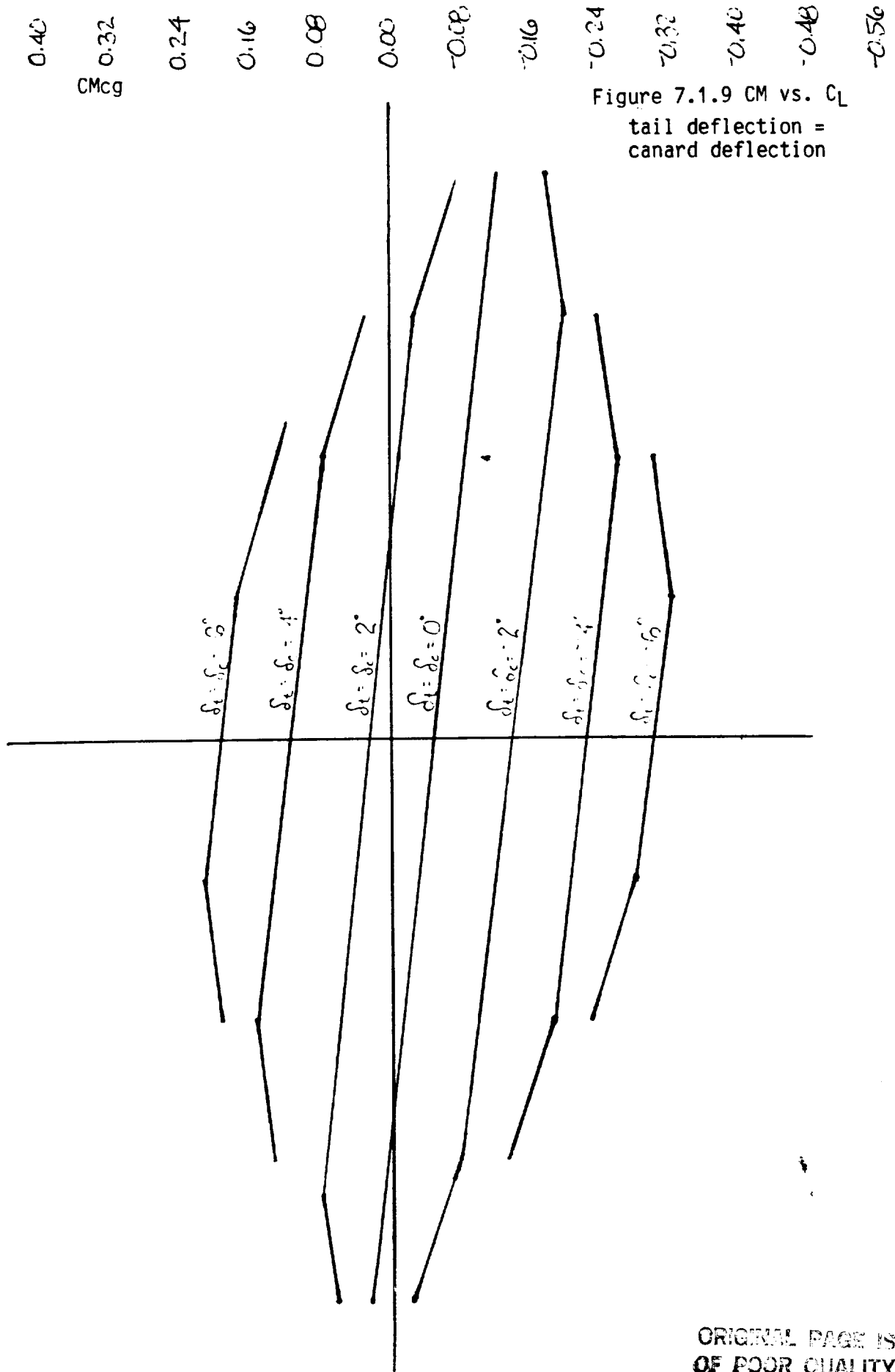
CMcg

Figure 7.1.8 CM vs. C_L

canard deflections
(tail incidence 0)



-0.603 -0.3609 -0.1301 0.1067 0.3435 0.5803 0.8170 1.0539 1.2907



ORIGINAL PAGE IS
OF POOR QUALITY

Figure 7.2.1

$$X_D = \frac{-(C_{D0} + 2C_{D\alpha}) * S * S}{m * u_0}$$

$$X_W = \frac{-(C_{D0} - C_{D\alpha}) * S * S}{m * u_0}$$

$$Z_D = \frac{-(C_{L0} + 2C_{L\alpha}) * S * S}{m * u_0}$$

$$Z_W = \frac{-(C_{L0} + C_{L\alpha}) * S * S}{m * u_0}$$

$$M_W = \frac{C_{m0} * S * S * C}{u_0 * I_y}$$

$$M_C = [(-2 * C_{L\alpha} * V_H * 1/c) + (2 * C_{L0} * V_H * 1/c + C_{D0})] * c/2u_0 * SSc/I_y$$

$$M_W = [(-2 * C_{L\alpha} * V_H * 1/c + c^2/c\alpha)] * c/2u_0 * SSc/u_0 I_y$$

where:

$$C_{D0} = cC_D/cu = 0$$

C_{D0} = reference drag coefficient at
cruise altitude

$$C_{D\alpha} = cC_D/c\alpha$$

C_{L0} = reference lift coefficient at
cruise altitude

$$C_{L0} = cC_L/cu = 0$$

$$C_{L\alpha} = cC_L/c\alpha$$

I_y = mass moment of inertia about
the y axis

The calculated values are:

	<u>100,000 feet</u>	<u>25,000 feet</u>
X_D	-.00543	-.0356
X_W	.160	1.11
Z_D	-.148	-.713
Z_W	-.911	-6.26
M_D	0	0
M_W	-.00495	-.0345
M_C	-.0579	-.398
M_W	-.000248	-.00823

ORIGINAL PAGE IS
OF POOR QUALITY

Figure 7.2.2
Combined Mode Block Diagram

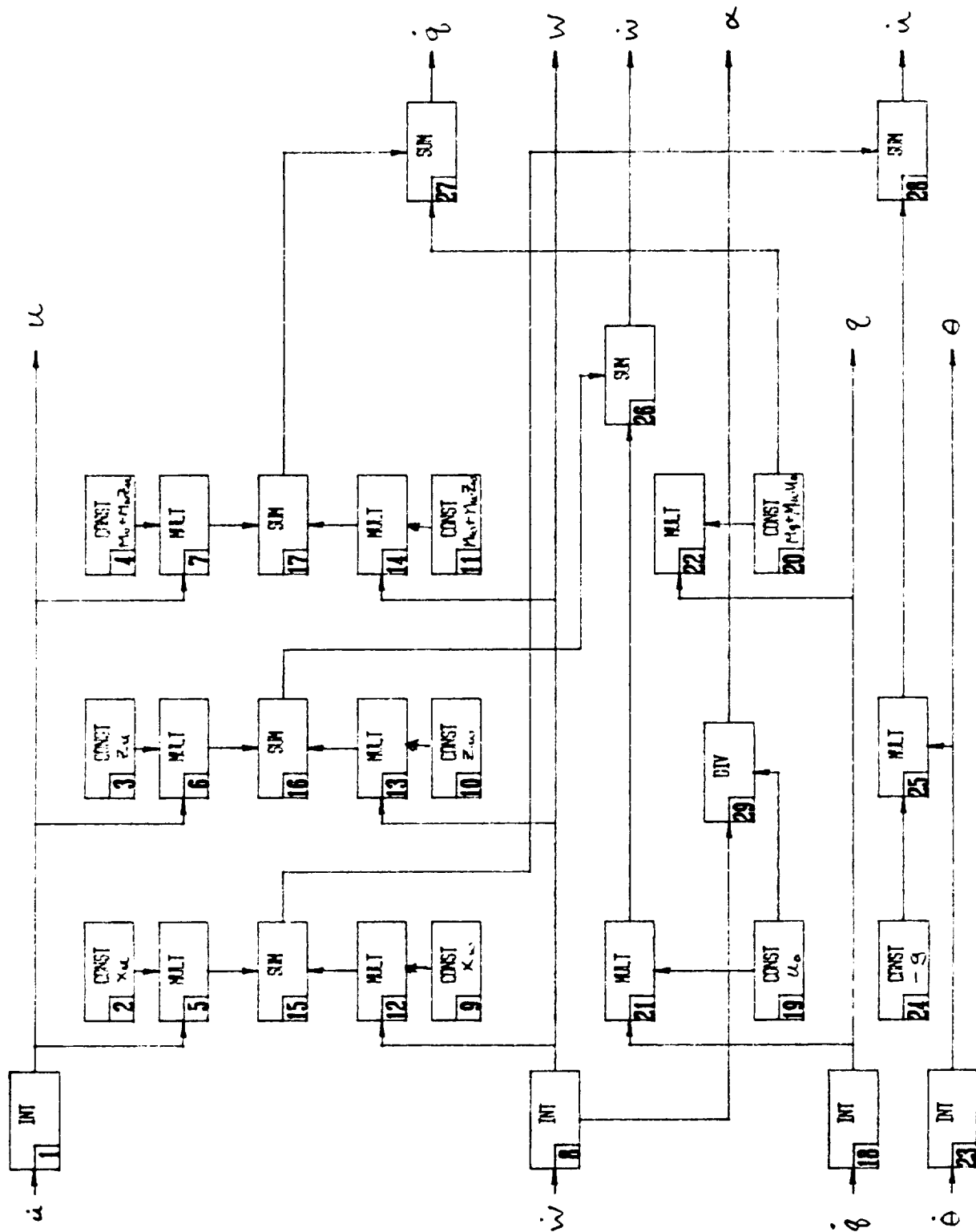
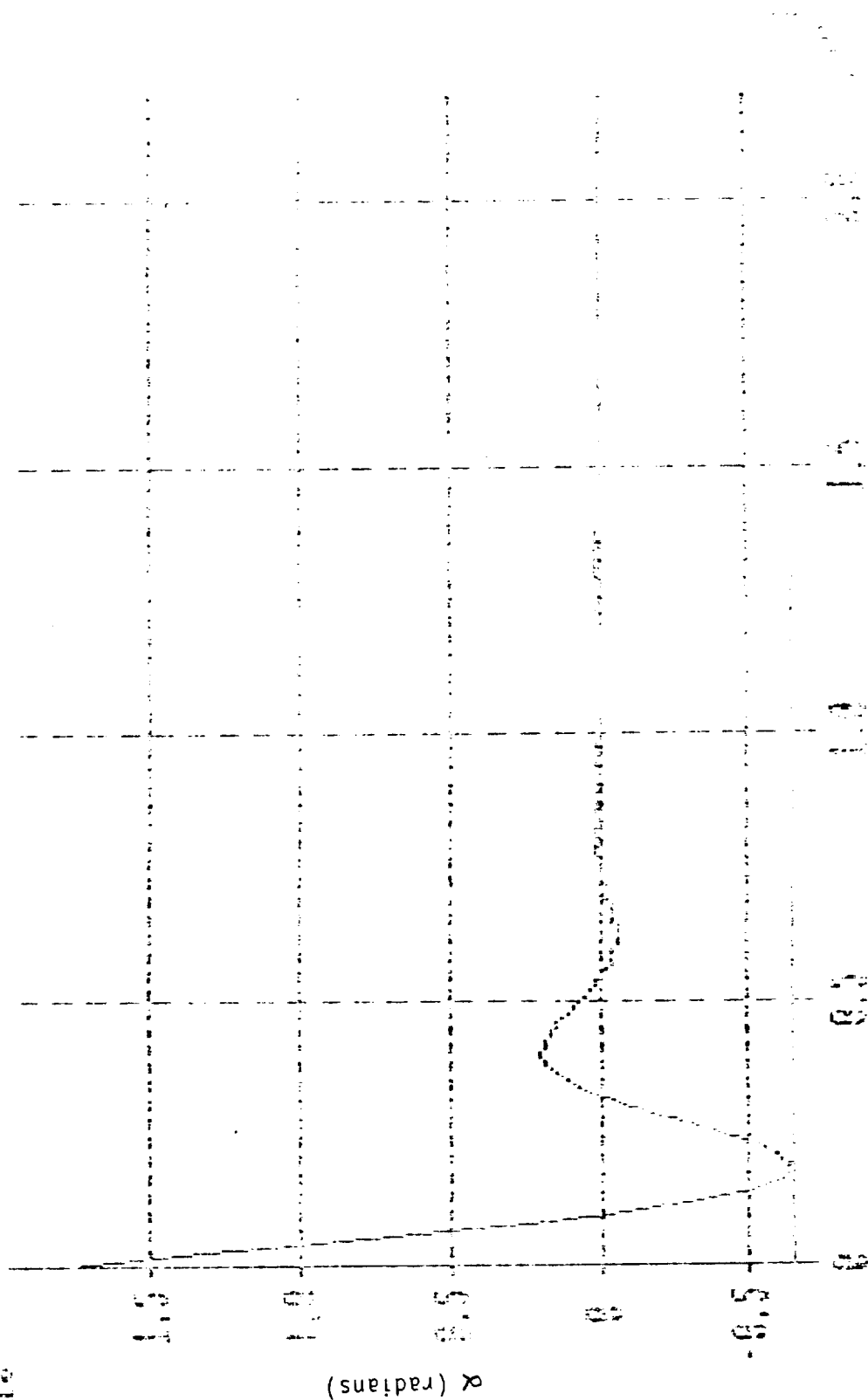


Figure 7.2.3

Short Period Mode - 100,000 ft

ASREQ v2.00
 FILE: DYN100
 -2
 x10

alpha(rad.) (Y-axis) vs TIME (seconds)



Time (seconds)

Figure 7.2.4
Long Period Mode - 100,000 ft

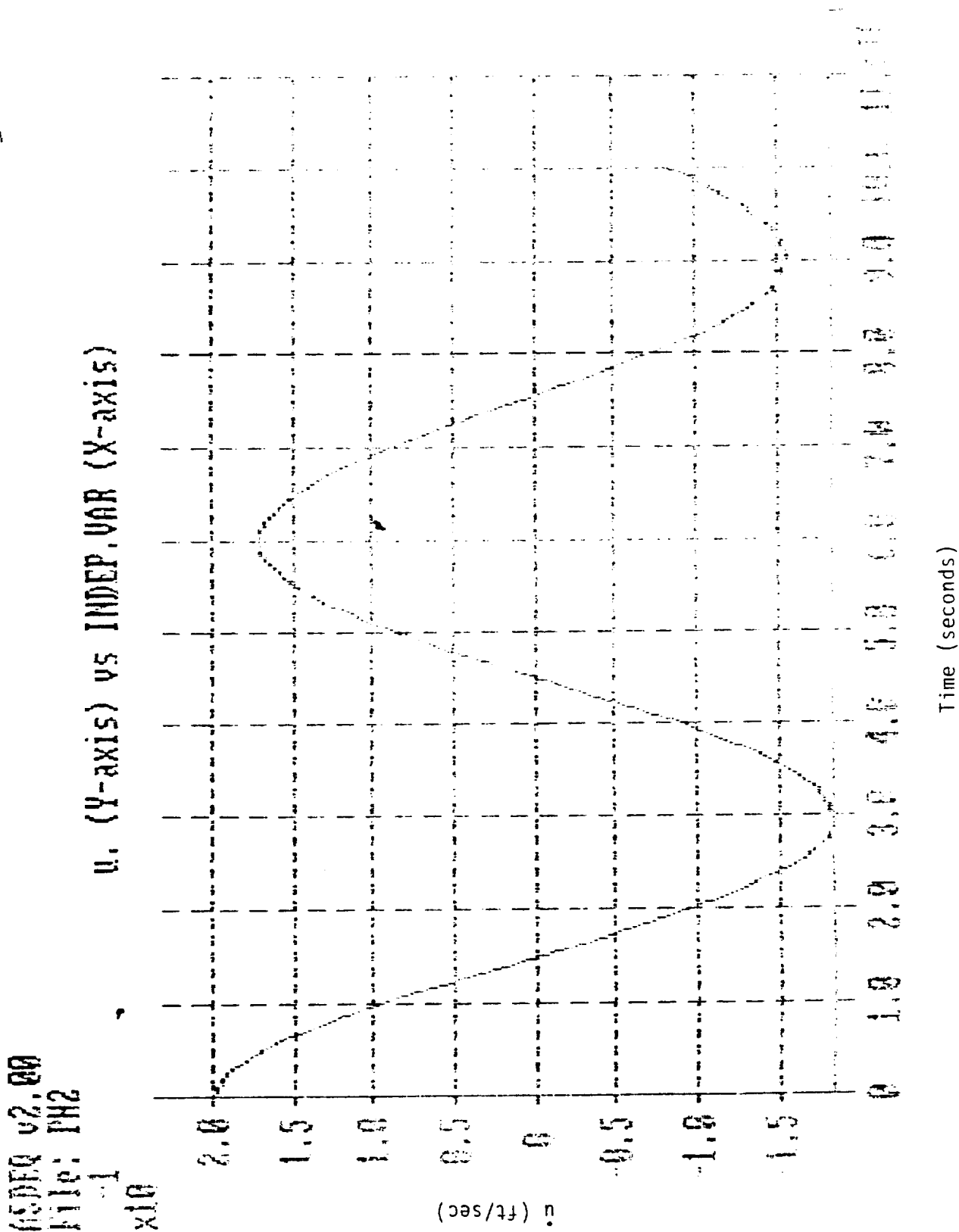
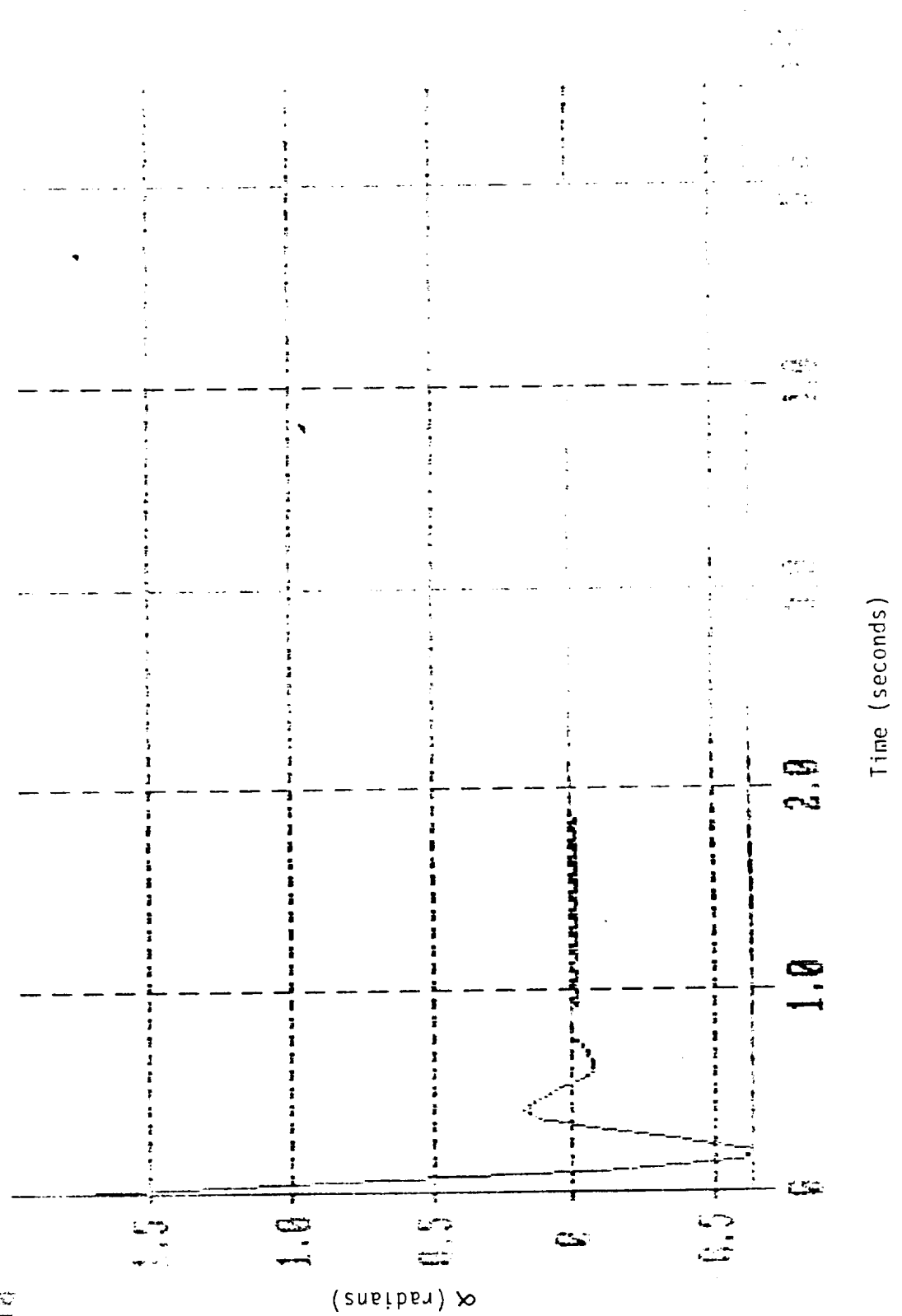


Figure 7.2.5
 Combined Mode - 100,000 ft

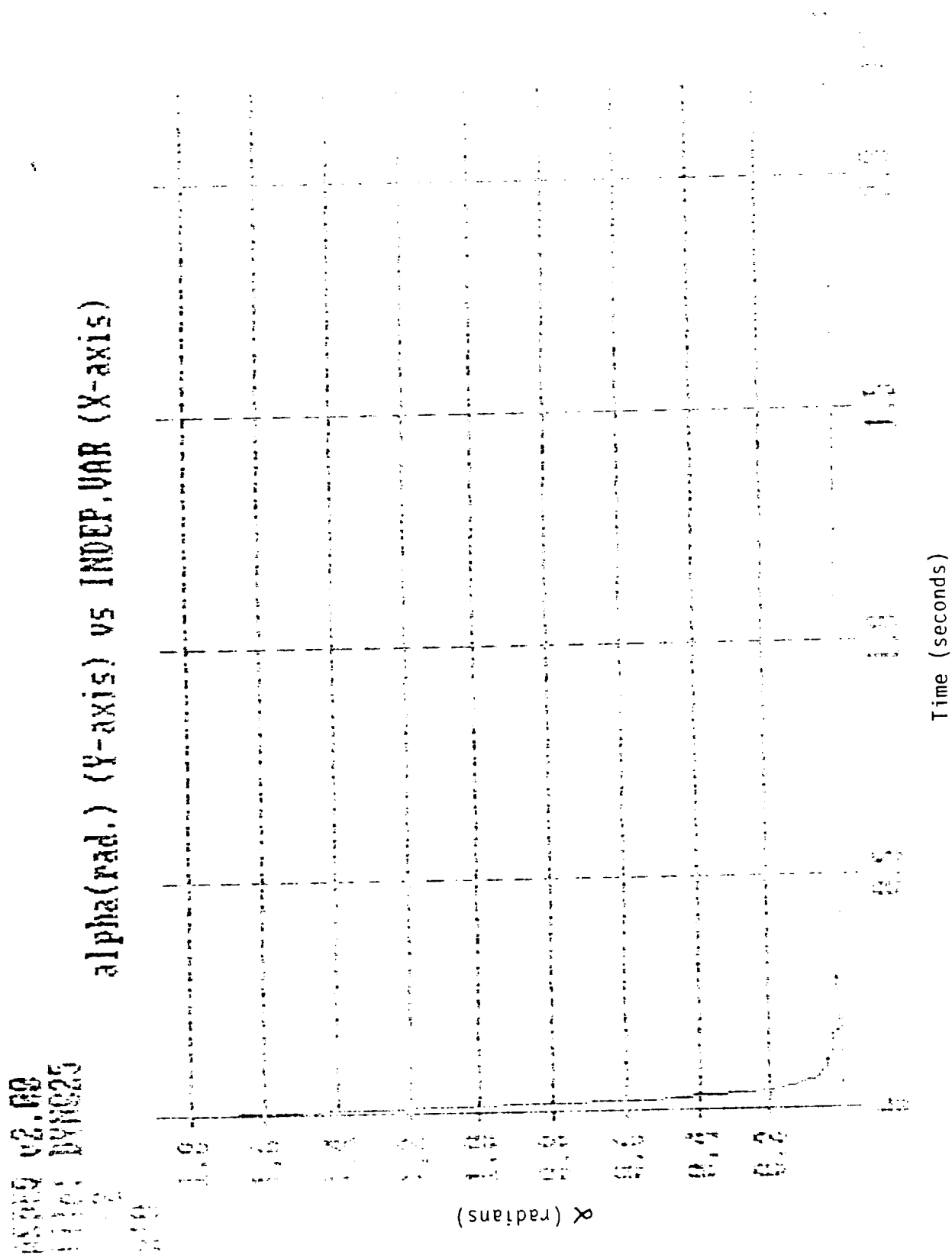
ASDFG v2.00
 FILE: DYN100
 7
 Y10

alpha(rad.) (Y-axis) vs INDEP.VAR (X-axis)



ORIGINAL PAGE IS
 OF POOR QUALITY

Figure 7.2.6
Short Period Mode - 25,000 ft



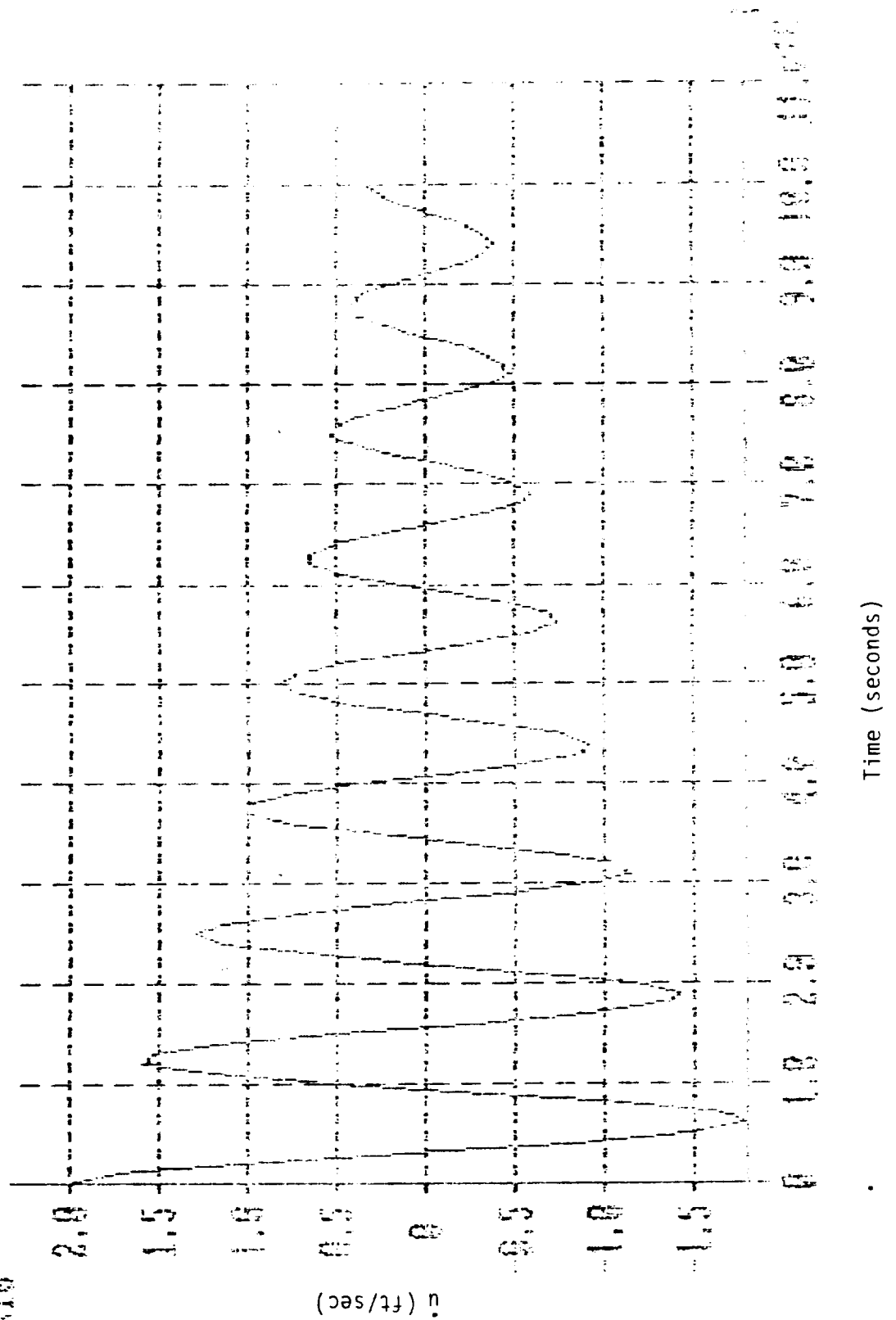
ORIGINAL PAGE IS
OF POOR QUALITY

Figure 7.2.7

Long Period Mode - 25,000 ft

ASDER v2.00
File: PH2
-1
x10

u. (Y-axis) vs INDEP.VAR (X-axis)

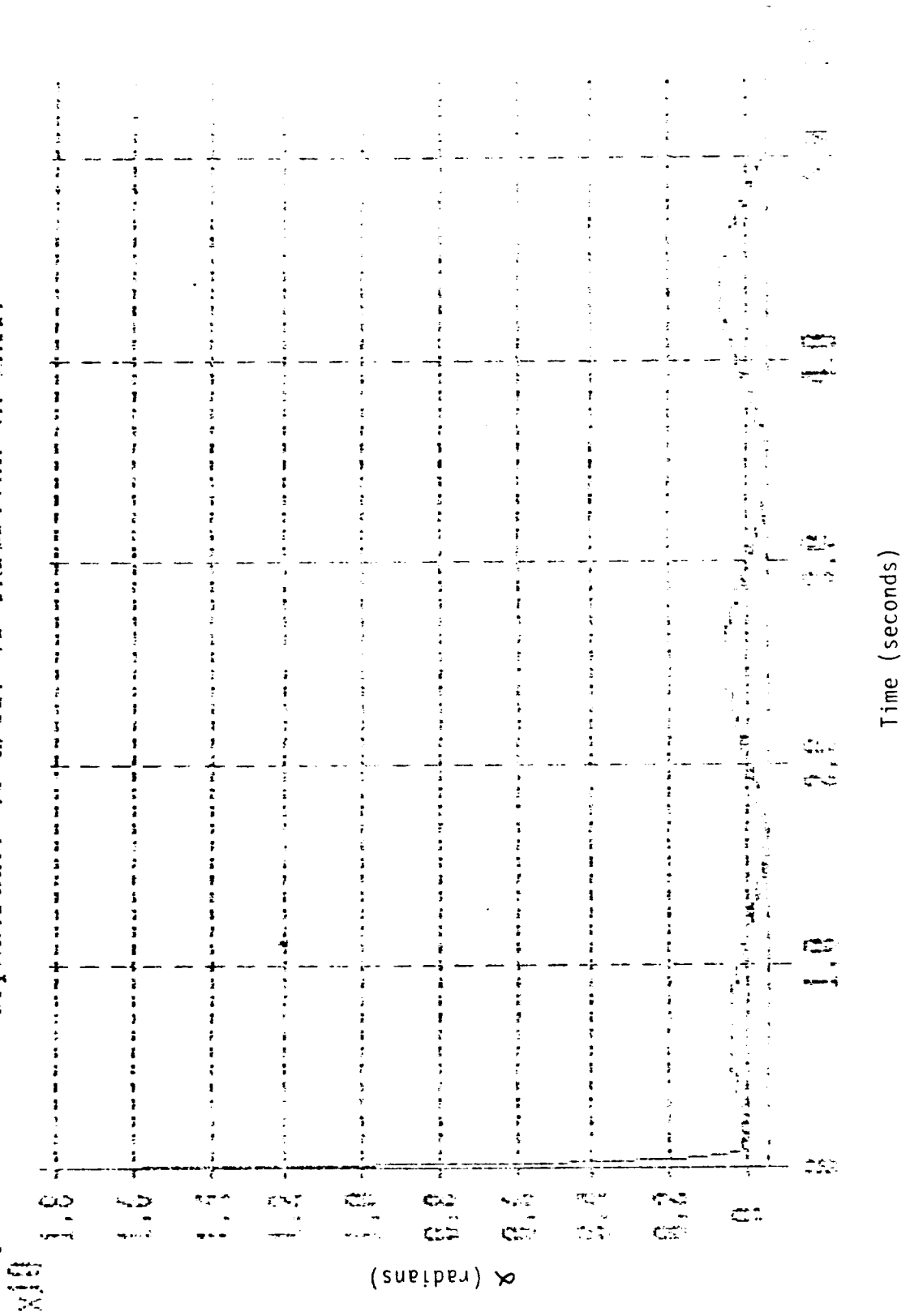


ORIGINAL PAGE IS
OF POOR QUALITY

Figure 7.2.8
Combined Mode - 25,000 ft

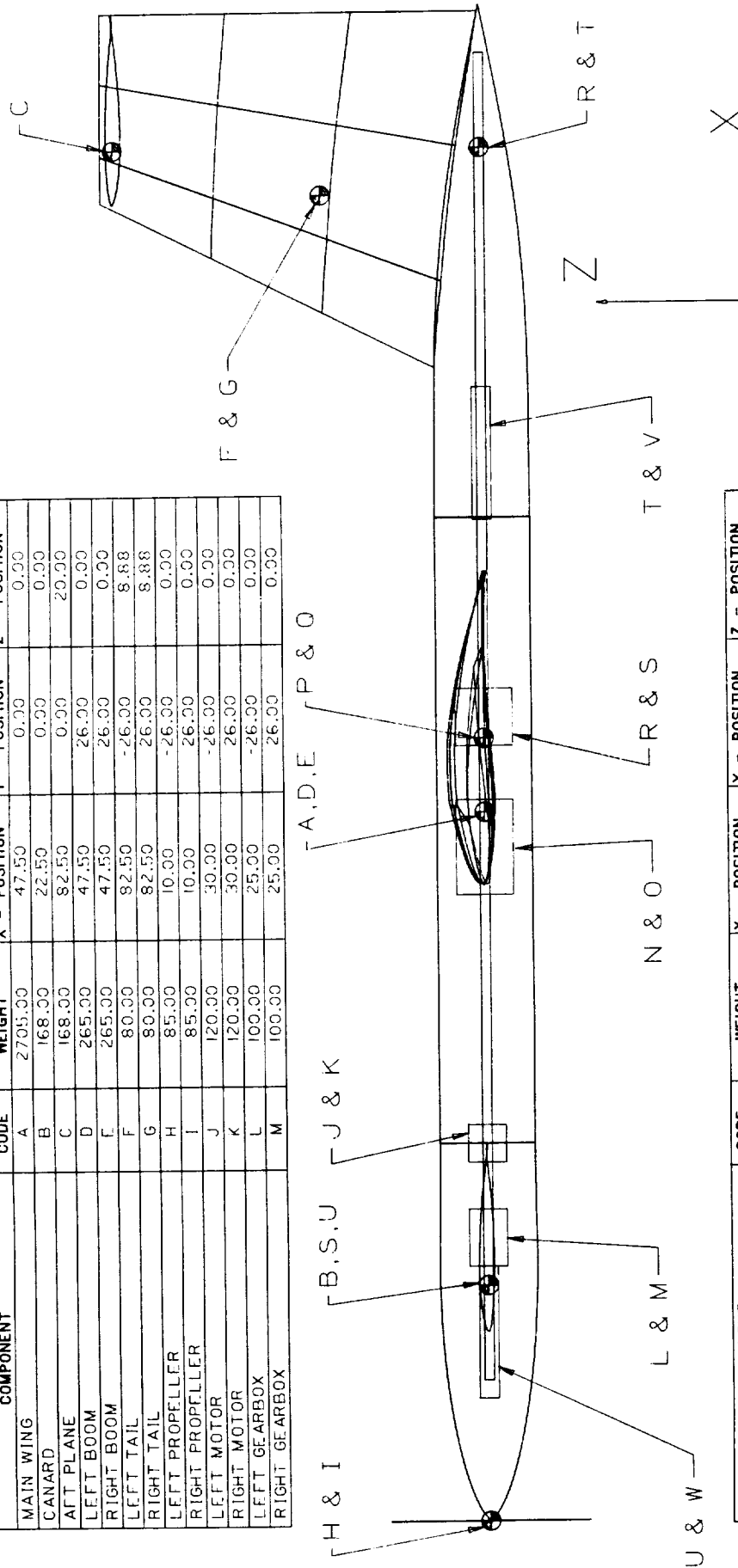
65000 v2.00
File: DYN025

alpha(rad.) (Y-axis) vs INDEP.VAR (X-axis)



ORIGINAL PAGE IS
OF POOR QUALITY

COMPONENT	CODE	WEIGHT	X - POSITION	Y - POSITION	Z - POSITION
MAIN WING	A	2705.00	47.50	0.00	0.00
CANARD	B	168.00	22.50	0.00	0.00
AFT PLANE	C	168.00	82.50	0.00	20.00
LEFT BOOM	D	265.00	47.50	26.00	0.00
RIGHT BOOM	E	265.00	47.50	26.00	0.00
LEFT TAIL	F	80.00	82.50	-26.00	8.88
RIGHT TAIL	G	80.00	82.50	26.00	8.88
LEFT PROPELLER	H	85.00	10.00	-26.00	0.00
RIGHT PROPELLER	I	85.00	10.00	26.00	0.00
LEFT MOTOR	J	120.00	30.00	-26.00	0.00
RIGHT MOTOR	K	120.00	30.00	26.00	0.00
LEFT GEARBOX	L	100.00	25.00	-26.00	0.00
RIGHT GEARBOX	M	100.00	25.00	26.00	0.00



COMPONENT	CODE	WEIGHT	X - POSITION	Y - POSITION	Z - POSITION
LEFT PAYLOAD	N	500.00	45.65	-26.00	0.00
RIGHT PAYLOAD	O	500.00	45.65	26.00	0.00
RECTENNA	P	275.00	51.40	0.00	0.00
ELECTRICAL SYSTEM	Q	354.00	51.40	0.00	0.00
LEFT CONTROL SYSTEM	R	275.00	52.50	-26.00	0.00
RIGHT CONTROL SYSTEM	S	275.00	52.50	26.00	0.00
LEFT-REAR LANDING GEAR	T	50.00	66.40	-26.00	0.00
LEFT-FRONT LANDING GEAR	U	50.00	20.00	-26.00	0.00
RIGHT REAR LANDING GEAR	V	50.00	66.40	26.00	0.00
RIGHT FRONT LANDING GEAR	W	50.00	20.00	26.00	0.00

WPI CAD LABORATORY

TITLE: COMPONENT LOCATIONS

DRAWN BY: TOM JUTRAS

SCALE: .015 DATE: 4/3/90

NO: I SHEET: I

Figure 8.2

Component Locations and Mass Properties

Component Name	Code Name	Weight Pounds	X-Pos. Ft.	Y-Pos. Ft.	Z-Pos. Ft.	Y-Moment Ft.-Lbs	X-Moment Ft.-Lbs	Iyy Blg.-Ft ²	Ixx Blg.-Ft ²	Iyy Blg.-Ft ²	Ixx Blg.-Ft ²	Iyy Blg.-Ft ²	Ixx Blg.-Ft ²	Iyy Blg.-Ft ²	Ixx Blg.-Ft ²
Main Wing	A	2705.00	47.50	0.00	0.00	1.28E+05	0.00E+00	1.73E+03	3.85E+05	3.87E+05	0.00E+00	0.00E+00	0.00E+00	0.00E+00	0.00E+00
Canard	B	168.00	22.50	0.00	0.00	3.78E+03	0.00E+00	3.10E+03	3.81E+02	1.00E+03	0.00E+00	0.00E+00	0.00E+00	0.00E+00	0.00E+00
Aft Plane	C	168.00	82.50	0.00	20.00	1.39E+04	0.00E+00	6.73E+03	3.26E+03	1.23E+03	0.00E+00	0.00E+00	2.77E+05	0.00E+00	0.00E+00
Left Fuselage	D	265.00	47.50	26.00	0.00	1.26E+04	1.24E+03	4.40E+03	5.53E+03	4.40E+03	3.27E+05	0.00E+00	0.00E+00	0.00E+00	0.00E+00
Right Fuselage	E	265.00	47.50	26.00	0.00	1.26E+04	-1.24E+03	4.40E+03	5.53E+03	4.40E+03	-3.27E+05	0.00E+00	0.00E+00	0.00E+00	0.00E+00
Left Vert. Tail	F	80.00	82.50	-26.00	8.88	6.60E+03	2.15E+03	3.51E+03	1.95E+03	4.91E+03	1.72E+05	0.00E+00	0.00E+00	-1.85E+04	0.00E+00
Right Vert. Tail	G	80.00	82.50	-26.00	8.88	6.60E+03	-2.15E+03	3.51E+03	1.95E+03	4.91E+03	-1.72E+05	0.00E+00	0.00E+00	1.85E+04	0.00E+00
Left Propeller	H	85.00	10.00	-26.00	0.00	8.50E+02	2.60E+02	3.58E+03	1.82E+03	1.82E+03	2.21E+04	0.00E+00	0.00E+00	0.00E+00	0.00E+00
Right Propeller	I	85.00	10.00	-26.00	0.00	8.50E+02	-2.60E+02	3.58E+03	1.82E+03	1.82E+03	-2.21E+04	0.00E+00	0.00E+00	0.00E+00	0.00E+00
Left Motor	J	120.00	30.00	-26.00	0.00	3.60E+03	7.80E+02	1.05E+03	2.52E+03	5.00E+00	-3.36E+04	0.00E+00	0.00E+00	0.00E+00	0.00E+00
Right Motor	K	120.00	30.00	-26.00	0.00	3.60E+03	-7.80E+02	1.05E+03	2.52E+03	5.00E+00	3.36E+04	0.00E+00	0.00E+00	0.00E+00	0.00E+00
Left Gearbox	L	100.00	25.00	-26.00	0.00	2.50E+03	6.50E+02	1.47E+03	2.10E+03	4.00E+00	-6.50E+04	0.00E+00	0.00E+00	0.00E+00	0.00E+00
Right Gearbox	M	100.00	25.00	-26.00	0.00	2.50E+03	-6.50E+02	1.47E+03	2.10E+03	4.00E+00	6.50E+04	0.00E+00	0.00E+00	0.00E+00	0.00E+00
L. side Payload	N	500.00	45.65	-26.00	0.00	2.28E+04	1.18E+03	6.54E+01	1.05E+04	2.00E+01	-5.92E+03	0.00E+00	0.00E+00	0.00E+00	0.00E+00
R. side Payload	O	500.00	45.65	-26.00	0.00	2.28E+04	-1.18E+03	6.54E+01	1.05E+04	2.00E+01	5.92E+03	0.00E+00	0.00E+00	0.00E+00	0.00E+00
Rectenna	P	275.00	51.40	0.00	0.00	1.81E+04	0.00E+00	3.59E+02	3.92E+04	3.93E+04	0.00E+00	0.00E+00	0.00E+00	0.00E+00	0.00E+00
Elect. Wiring	Q	354.00	51.40	0.00	0.00	1.44E+04	-1.37E+03	7.50E+01	5.24E+03	5.52E+03	-3.75E+05	0.00E+00	0.00E+00	0.00E+00	0.00E+00
L. side Controls	R	275.00	52.50	-26.00	0.00	1.44E+04	1.37E+03	7.50E+01	5.24E+03	5.52E+03	3.75E+05	0.00E+00	0.00E+00	0.00E+00	0.00E+00
R. side Controls	S	275.00	52.50	-26.00	0.00	1.44E+04	-1.37E+03	7.50E+01	5.24E+03	5.52E+03	-3.75E+05	0.00E+00	0.00E+00	0.00E+00	0.00E+00
Landing Gear	T	50.00	66.40	-26.00	0.00	3.32E+03	-1.73E+03	6.07E+02	1.05E+03	1.66E+03	-8.63E+04	0.00E+00	0.00E+00	0.00E+00	0.00E+00
Landing Gear	U	50.00	20.00	-26.00	0.00	1.03E+03	-9.33E+02	1.11E+03	1.05E+03	2.17E+03	-8.63E+04	0.00E+00	0.00E+00	0.00E+00	0.00E+00
Landing Gear	V	50.00	66.40	-26.00	0.00	3.32E+03	1.73E+03	6.07E+02	1.05E+03	1.66E+03	8.63E+04	0.00E+00	0.00E+00	0.00E+00	0.00E+00
Landing Gear	W	50.00	20.00	-26.00	0.00	1.03E+03	9.33E+02	1.11E+03	1.05E+03	2.17E+03	-8.63E+04	0.00E+00	0.00E+00	0.00E+00	0.00E+00
Total vehicle weights:		6720.00 pounds.				3.18E+05	0.00E+00	4.41E+04	5.43E+05	5.17E+05	0.00E+00	0.00E+00	3.94E+05	0.00E+00	0.00E+00

X-Bar = Y-Moment/Weight = 46.71 ft.
Y-Bar = X-Moment/Weight = 0.00 ft.

Figure 9.2.1

Net Power Available

Wings Level Flight

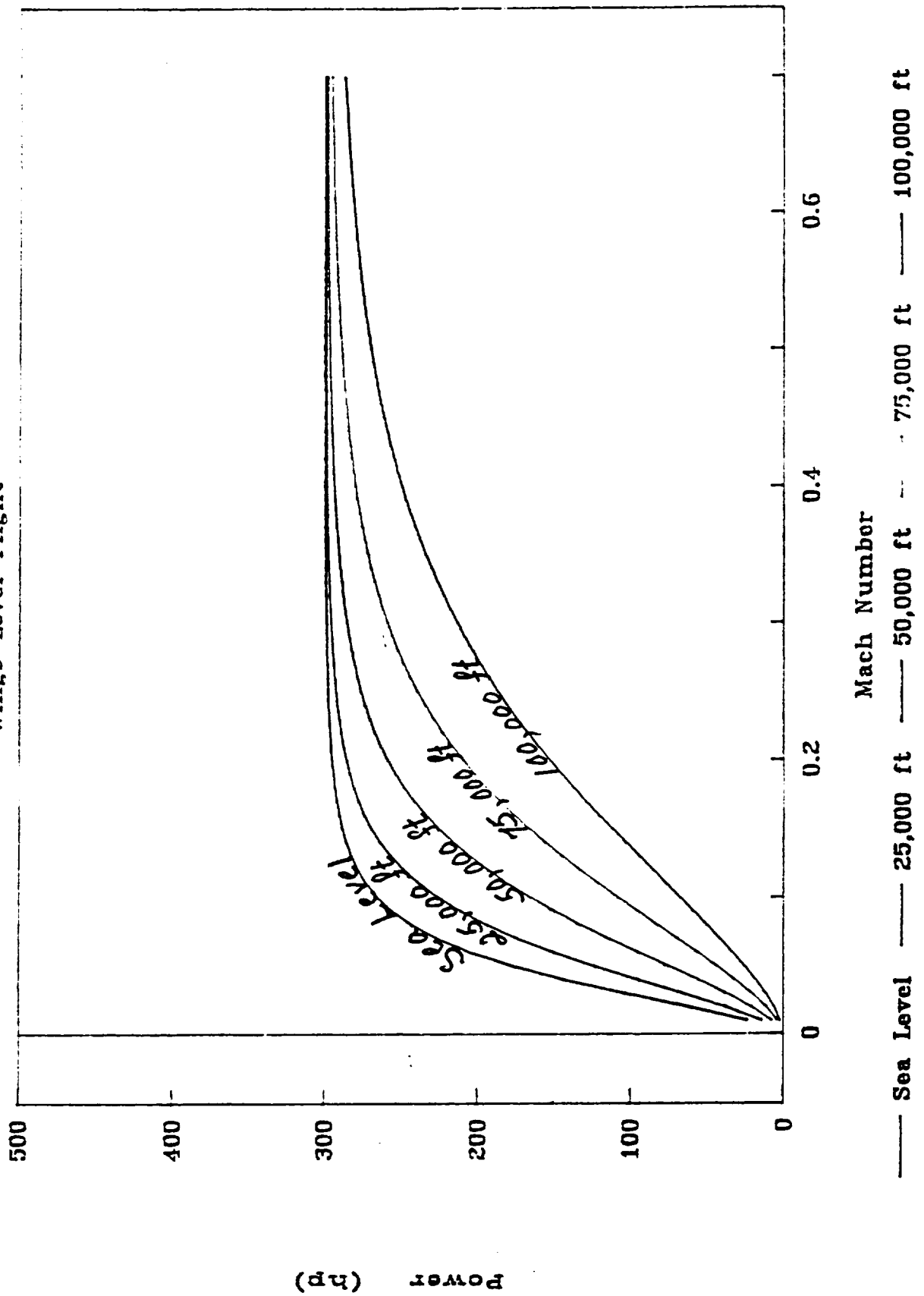


Figure 9.2.2

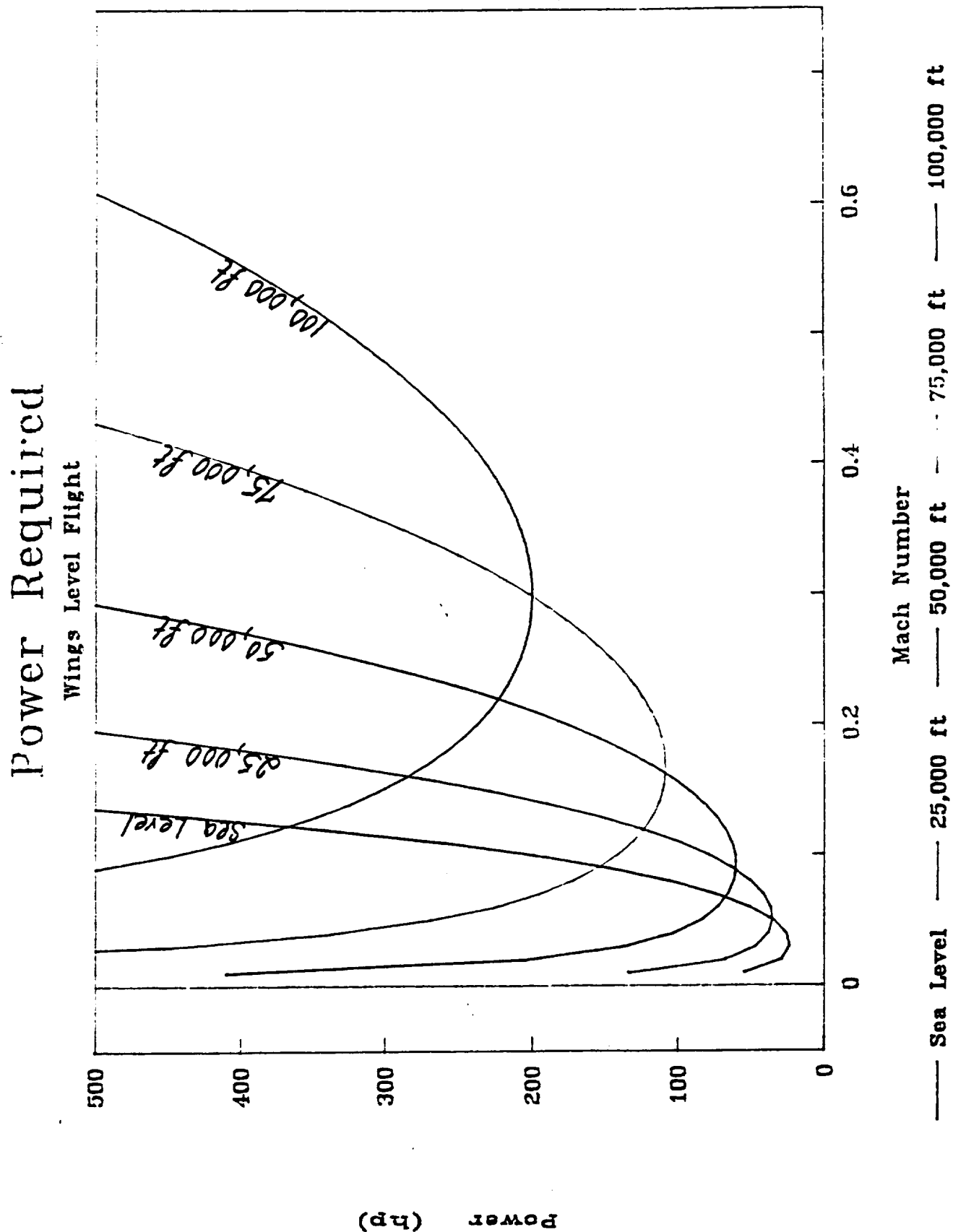


Figure 9.2.3

Power Available and Required

Altitude - Sea Level (level flight)

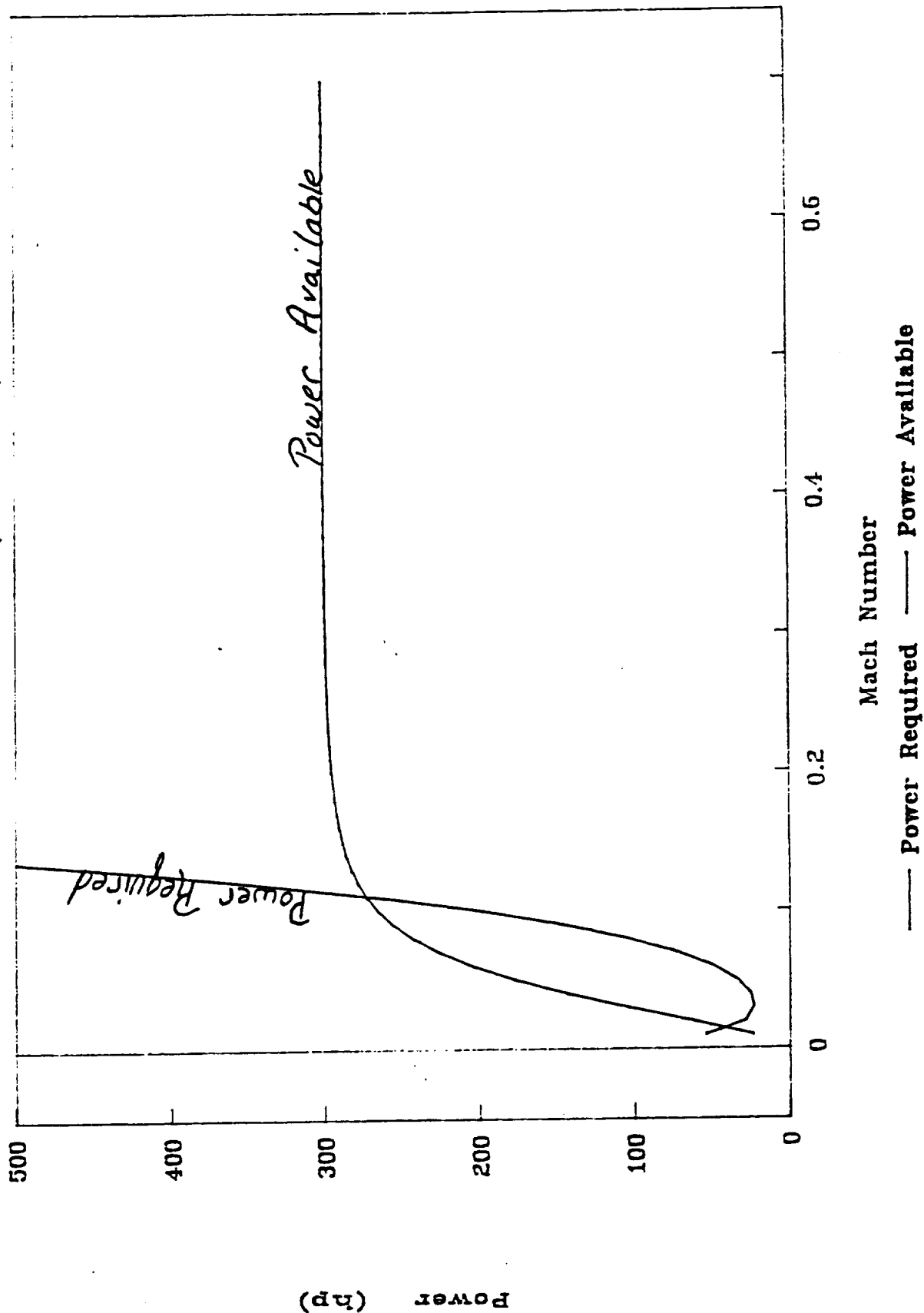


Figure 9.2.4

Power Available and Required

Altitude - 25,000 feet (level flight)

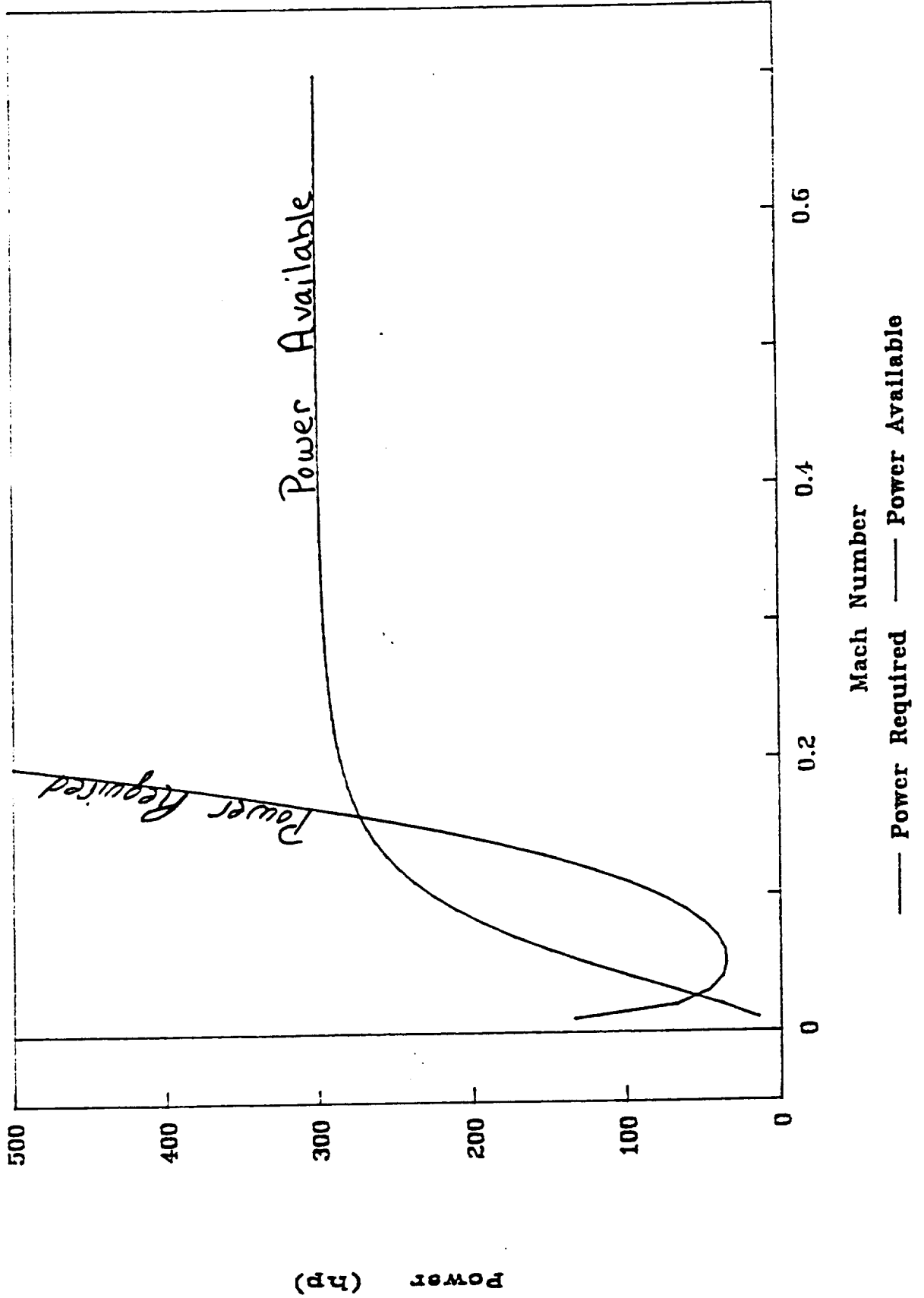


Figure 9.2.5

Power Available and Required

Altitude - 50,000 feet (level flight)

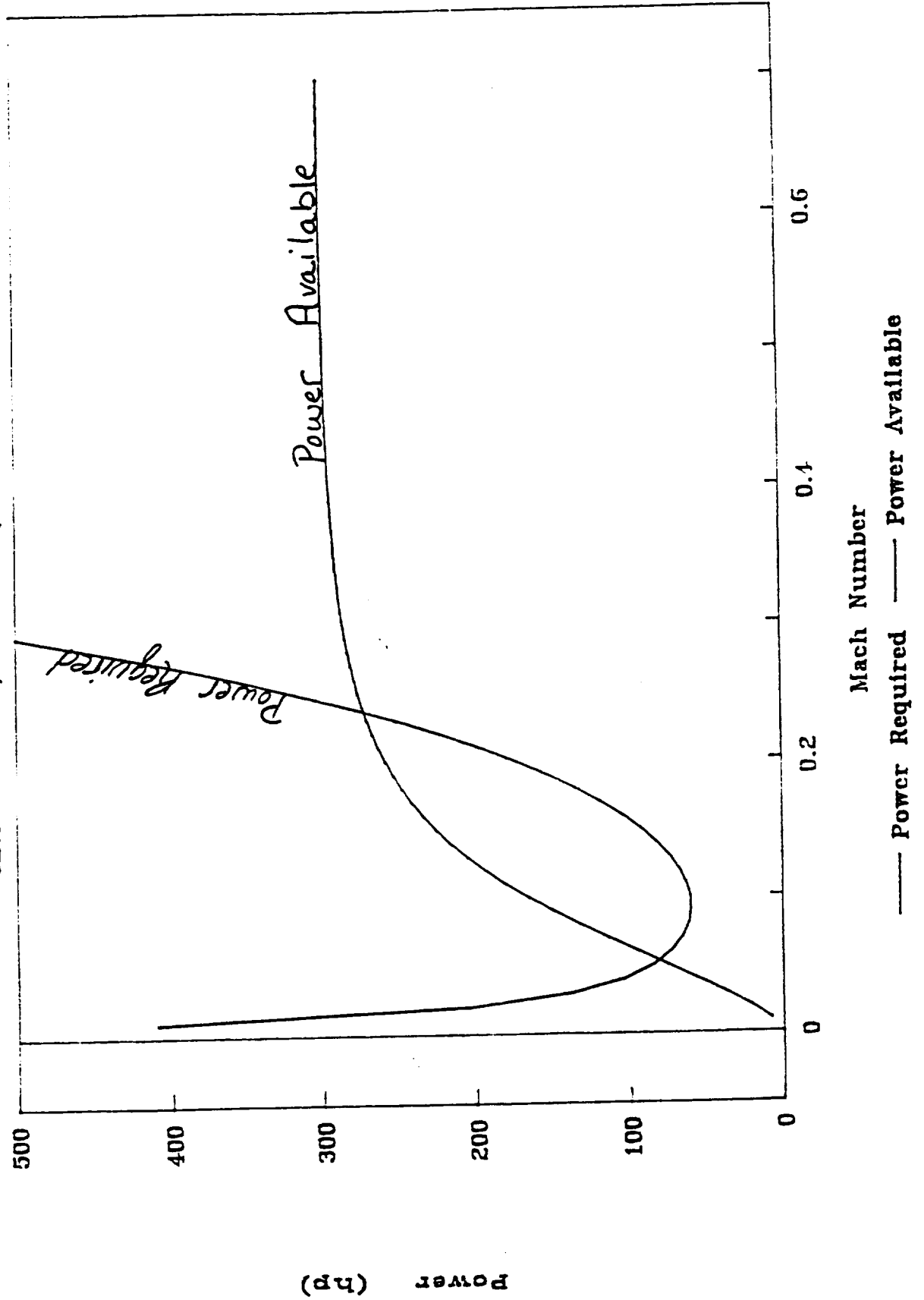


Figure 9.2.6

Power Available and Required

Altitude - 75,000 feet (level flight)

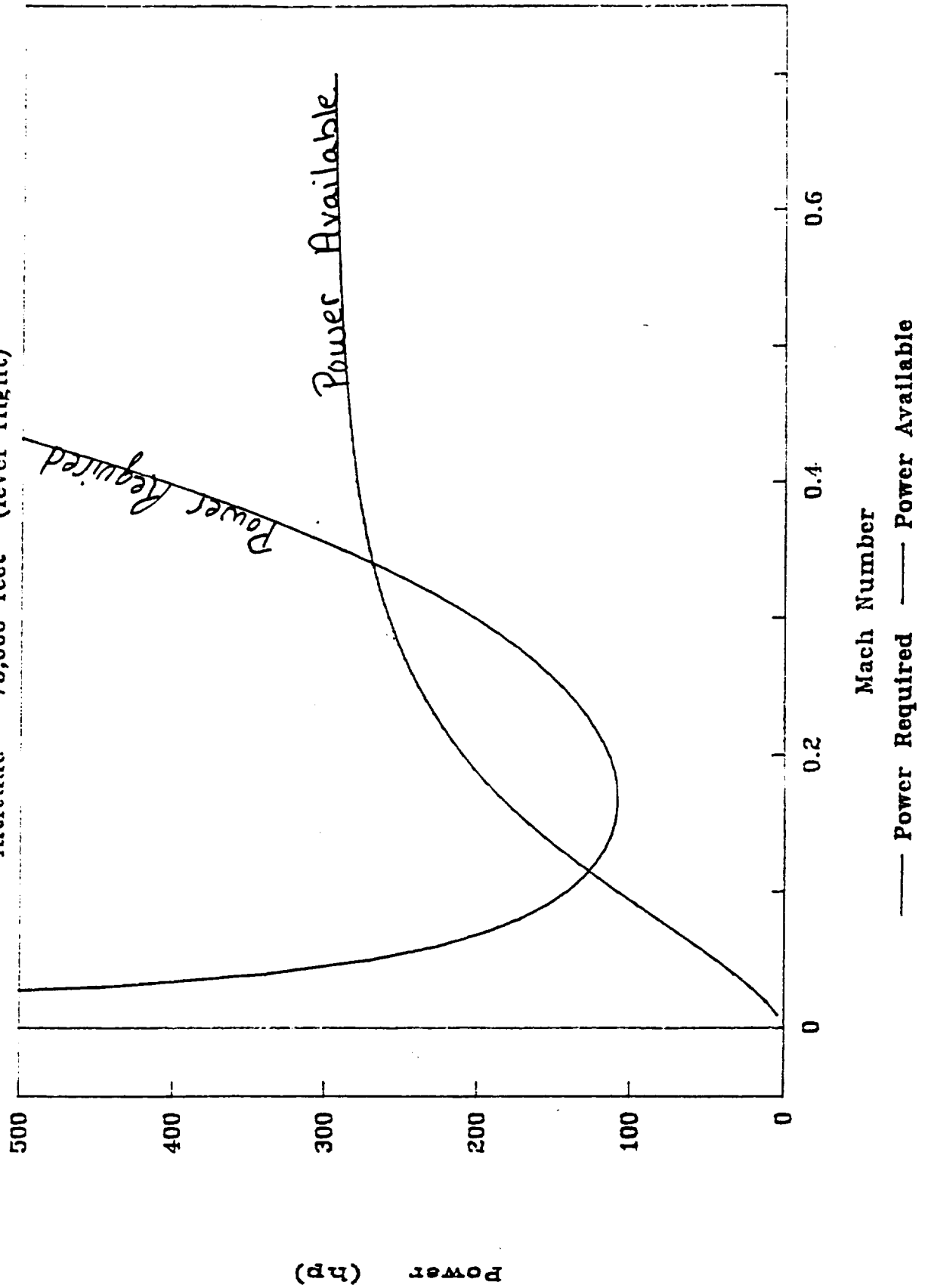


Figure 9.2.7

Power Available and Required

Altitude - 100,000 foot (level flight)

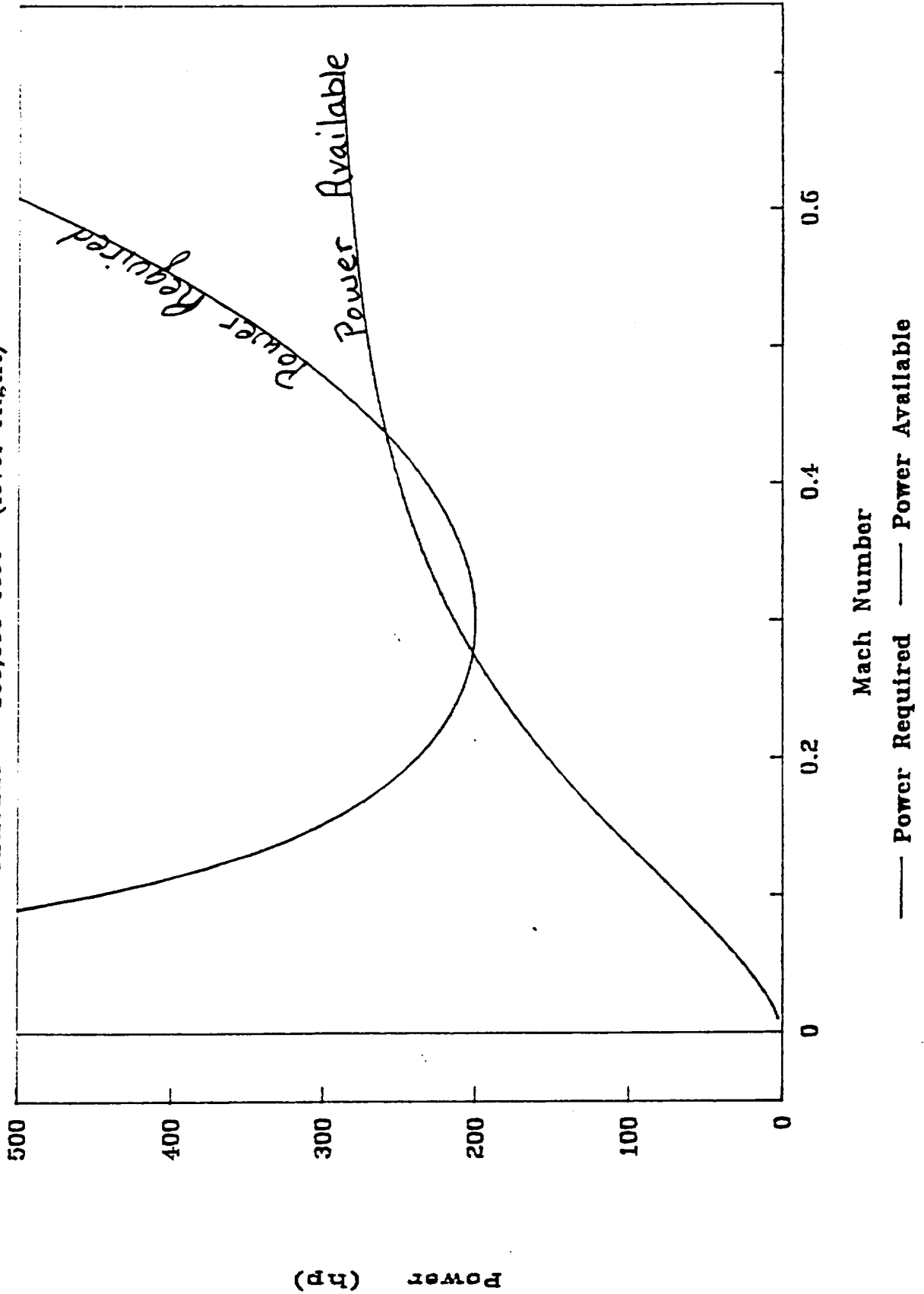
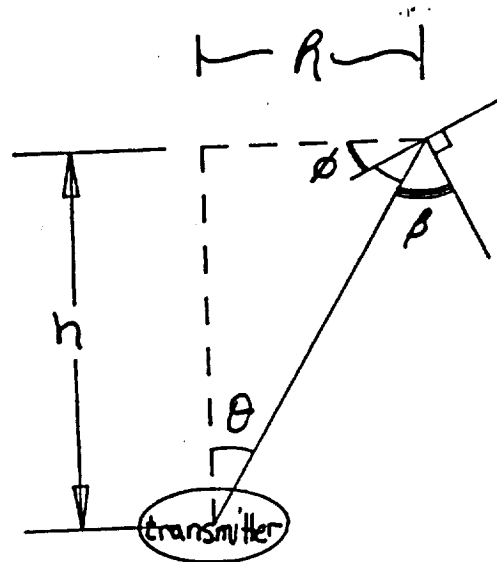


Figure 9.2.8

Angle of Incidence



- θ bank angle
- φ beam angle
- β incidence angle
- h altitude
- R flight radius

$$\beta = \varphi + \theta$$

$$\theta = \tan^{-1} (R/h)$$

$$\varphi = \tan^{-1} (V^2 / (g * R))$$

$$\beta = \tan^{-1} (R/h) + \tan^{-1} (V^2 / (g * R))$$

Angle of Incidence

Figure 9.2.9

Flight Radius Increases

$$\lim \theta = 90^\circ$$

$$R \rightarrow \infty$$

$$\lim \varphi = 0^\circ$$

$$R \rightarrow \infty$$

$$\lim \beta = 90^\circ$$

$$R \rightarrow \infty$$

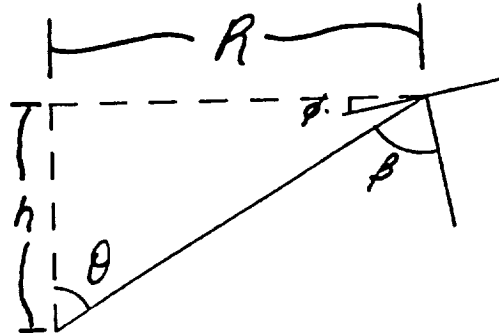


Figure 9.2.10

Flight Radius Decreases

$$\lim \theta = 0^\circ$$

$$R \rightarrow \infty$$

$$\lim \varphi = 90^\circ$$

$$R \rightarrow \infty$$

$$\lim \beta = 90^\circ$$

$$R \rightarrow \infty$$

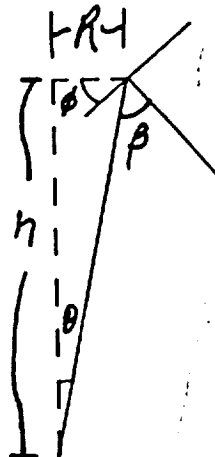
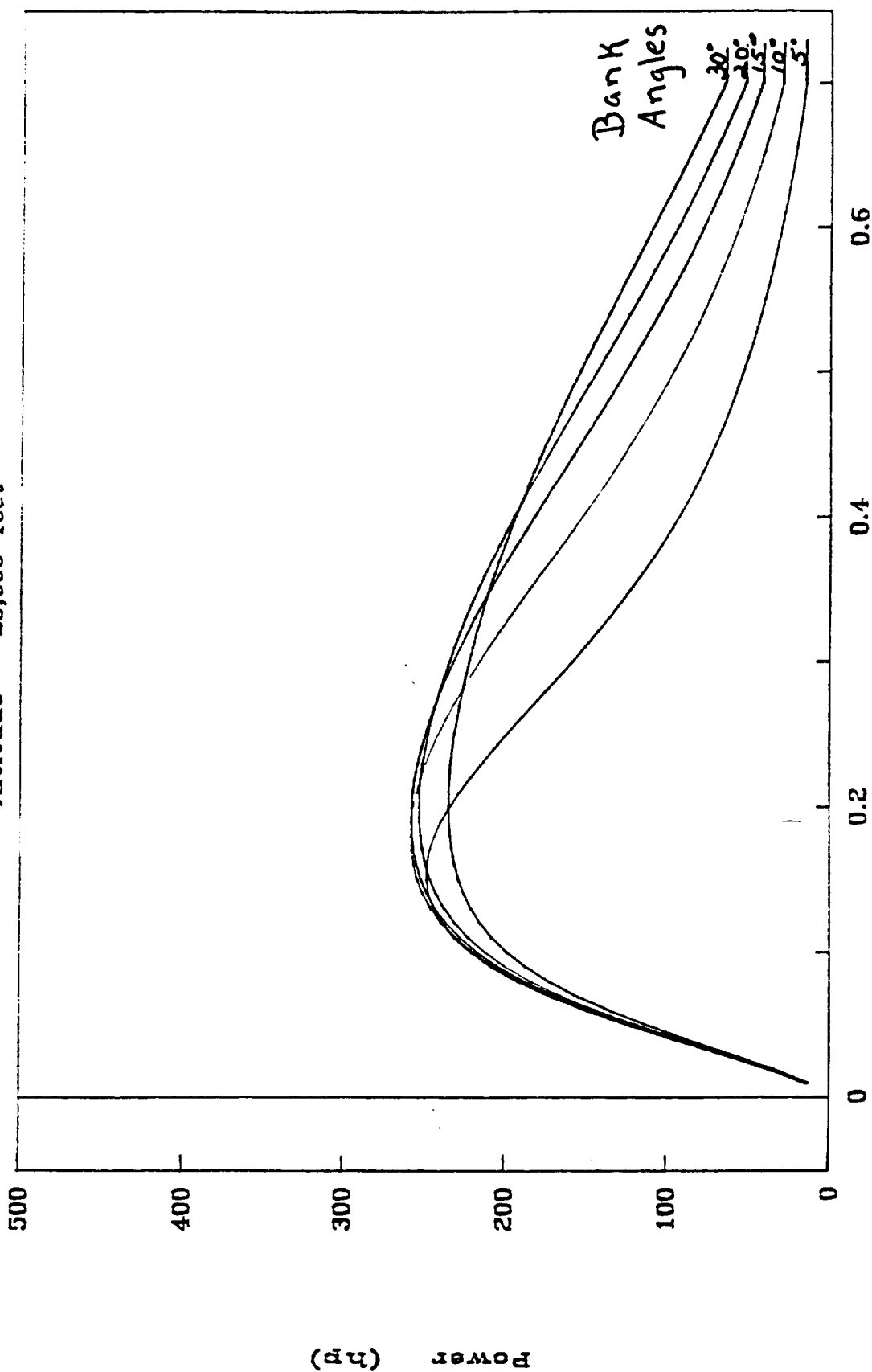


Figure 9.2.11

Net Power Available

Altitude - 25,000 feet



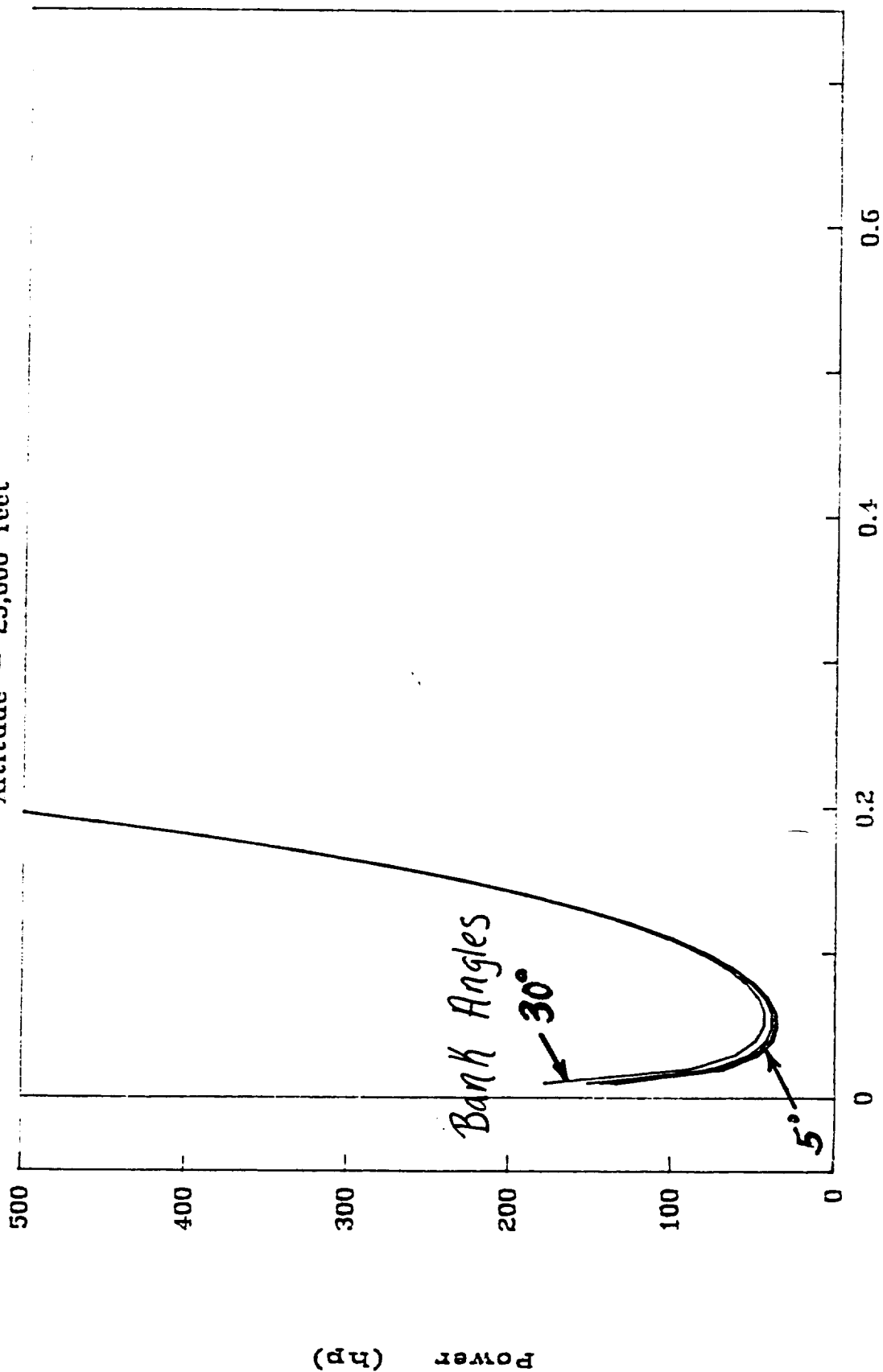
Mach Number

— Bank = 5 — Bank = 10 — Bank = 15 — Bank = 20 — Bank = 30

Figure 9.2.12

Power Required

Altitude - 25,000 feet



Mach Number

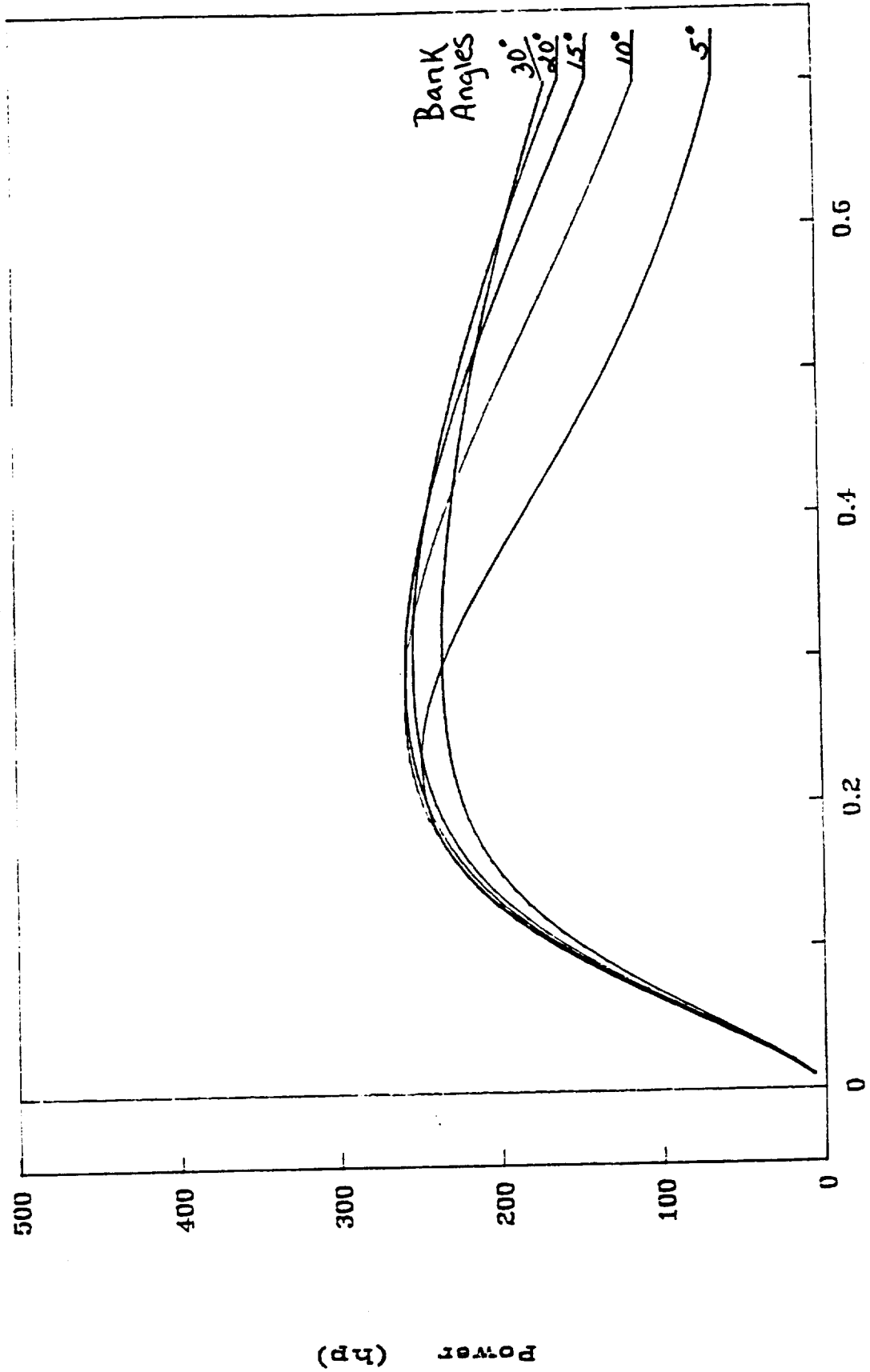
— Bank = 5 — Bank = 10 — Bank = 15 — Bank = 20 — Bank = 30

Power (hp)

Figure 9.2.13

Net Power Available

Altitude - 50,000 feet



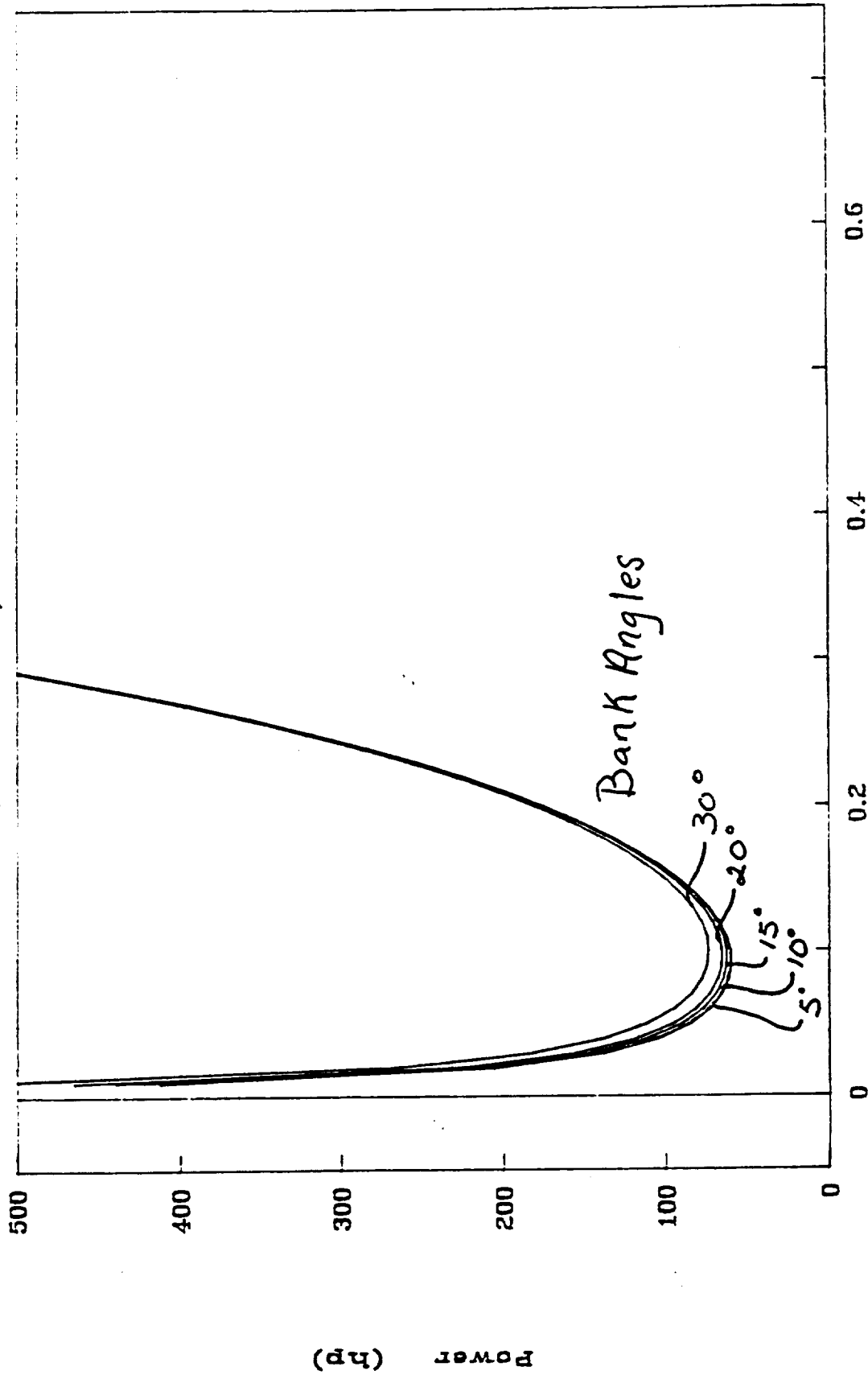
Mach Number

Bank = 5 Bank = 10 Bank = 15 Bank = 20 Bank = 30

Figure 9.2.14

Power Required

Altitude - 50,000 feet



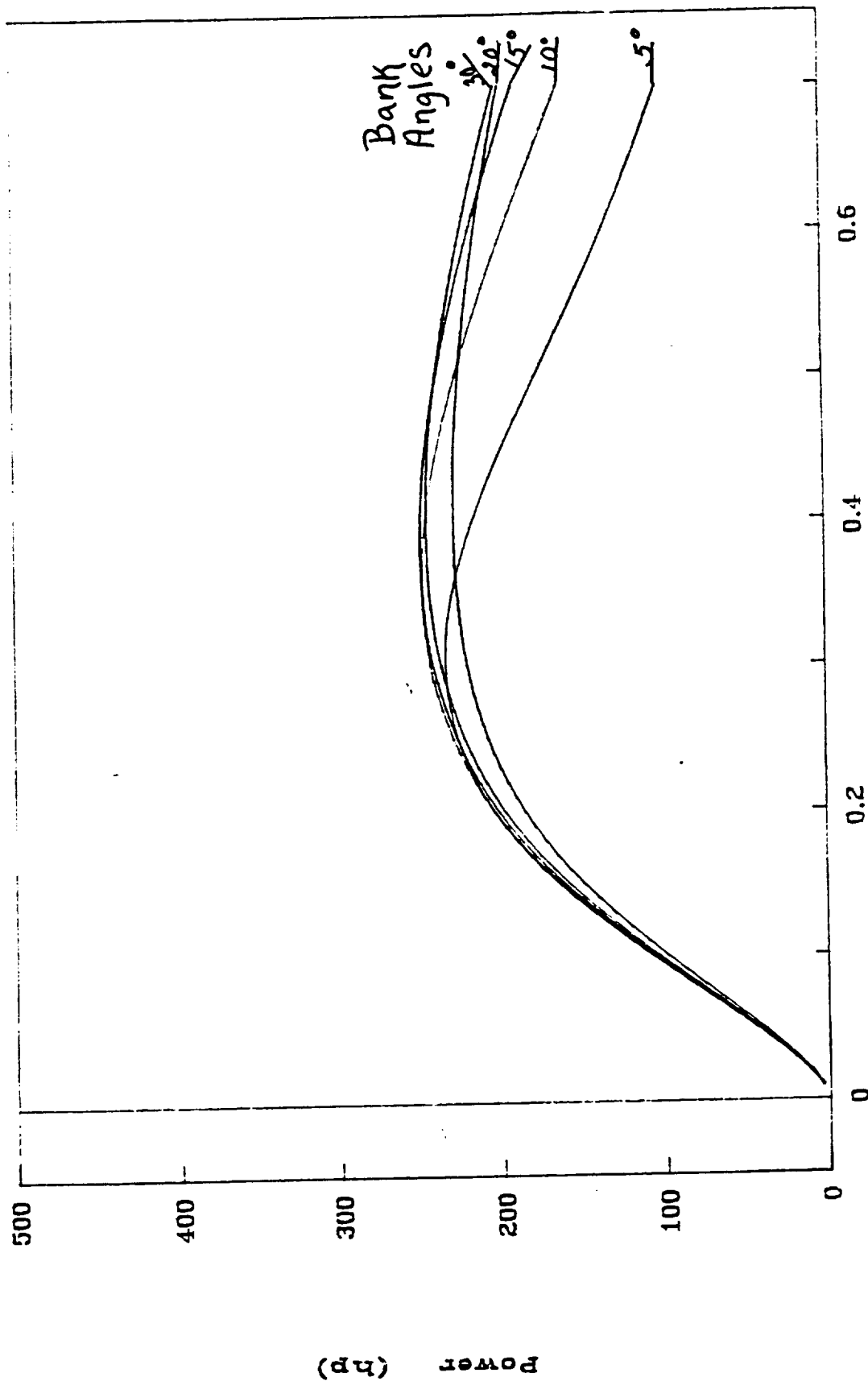
Mach Number

— Bank = 5 — Bank = 10 — Bank = 15 — Bank = 20 — Bank = 30

Figure 9.2.15

Net Power Available

Altitude - 75,000 feet



Mach Number

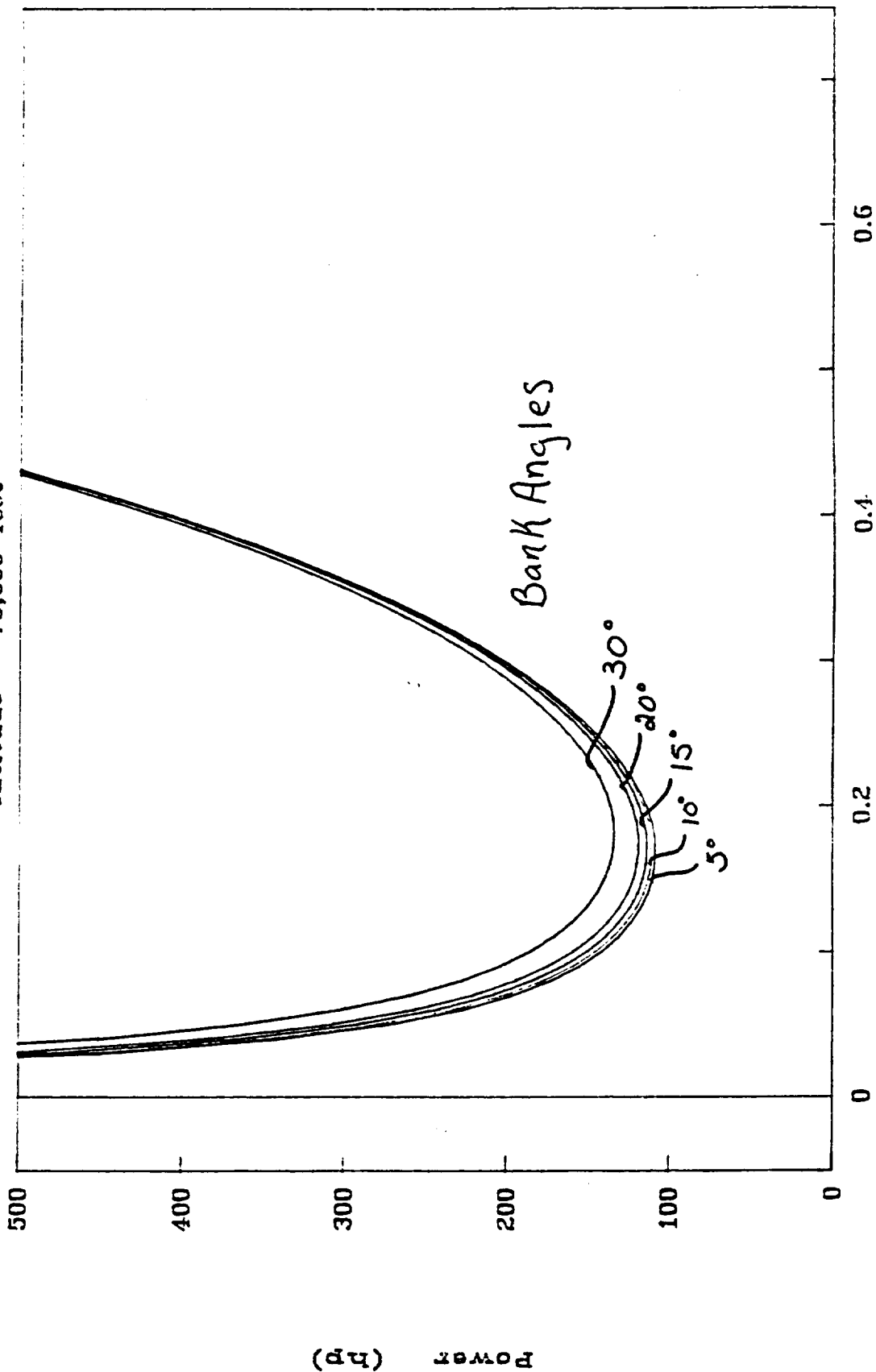
— Bank = 5 — Bank = 10 — Bank = 15 — Bank = 20 — Bank = 30

Figure 9.2.16

49

Power Required

Altitude - 75,000 feet



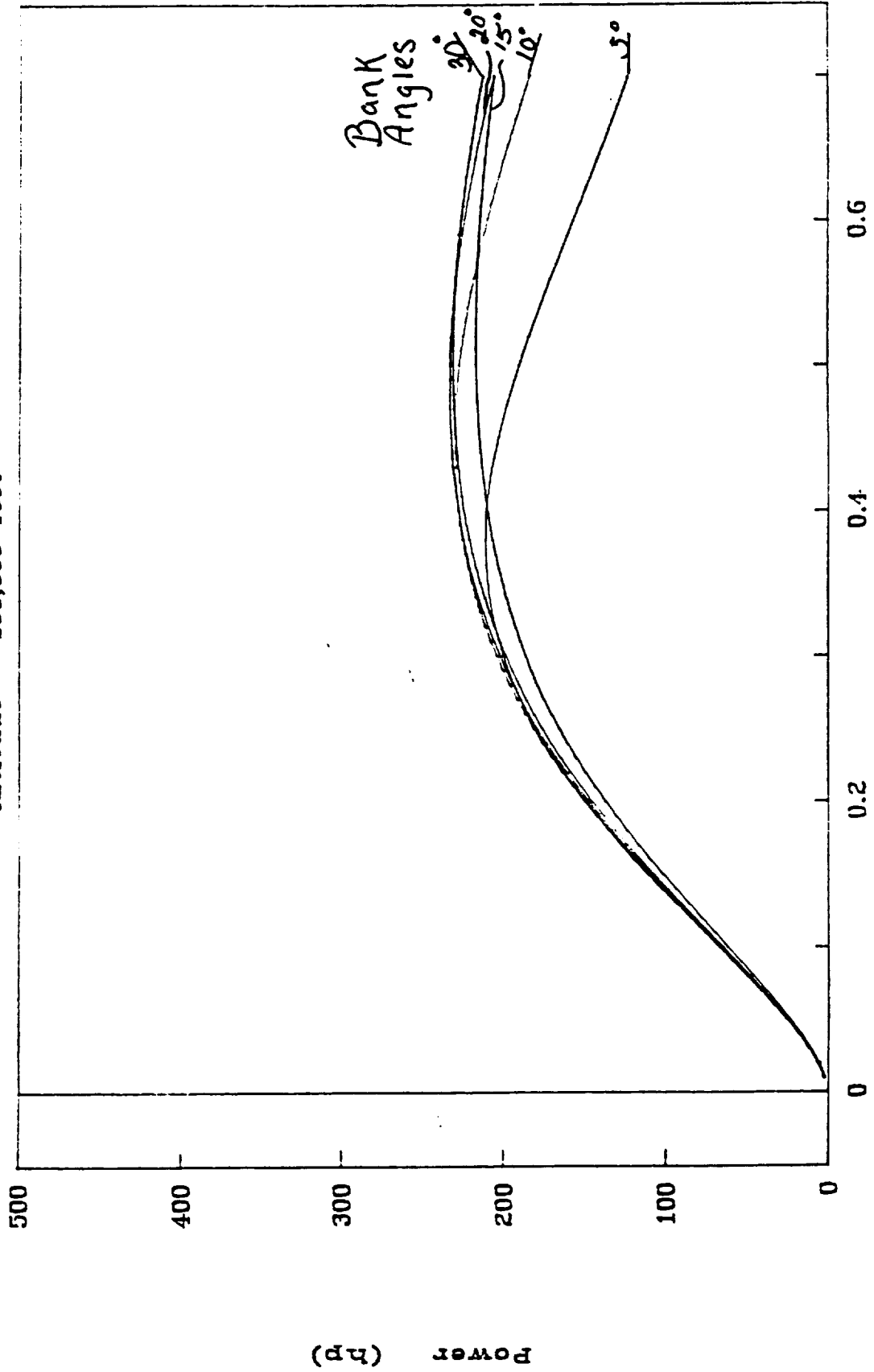
Mach Number

— Bank = 5 — Bank = 10 — Bank = 15 — Bank = 20 — Bank = 30

Figure 9.2.17

Net Power Available

Altitude - 100,000 feet



Mach Number

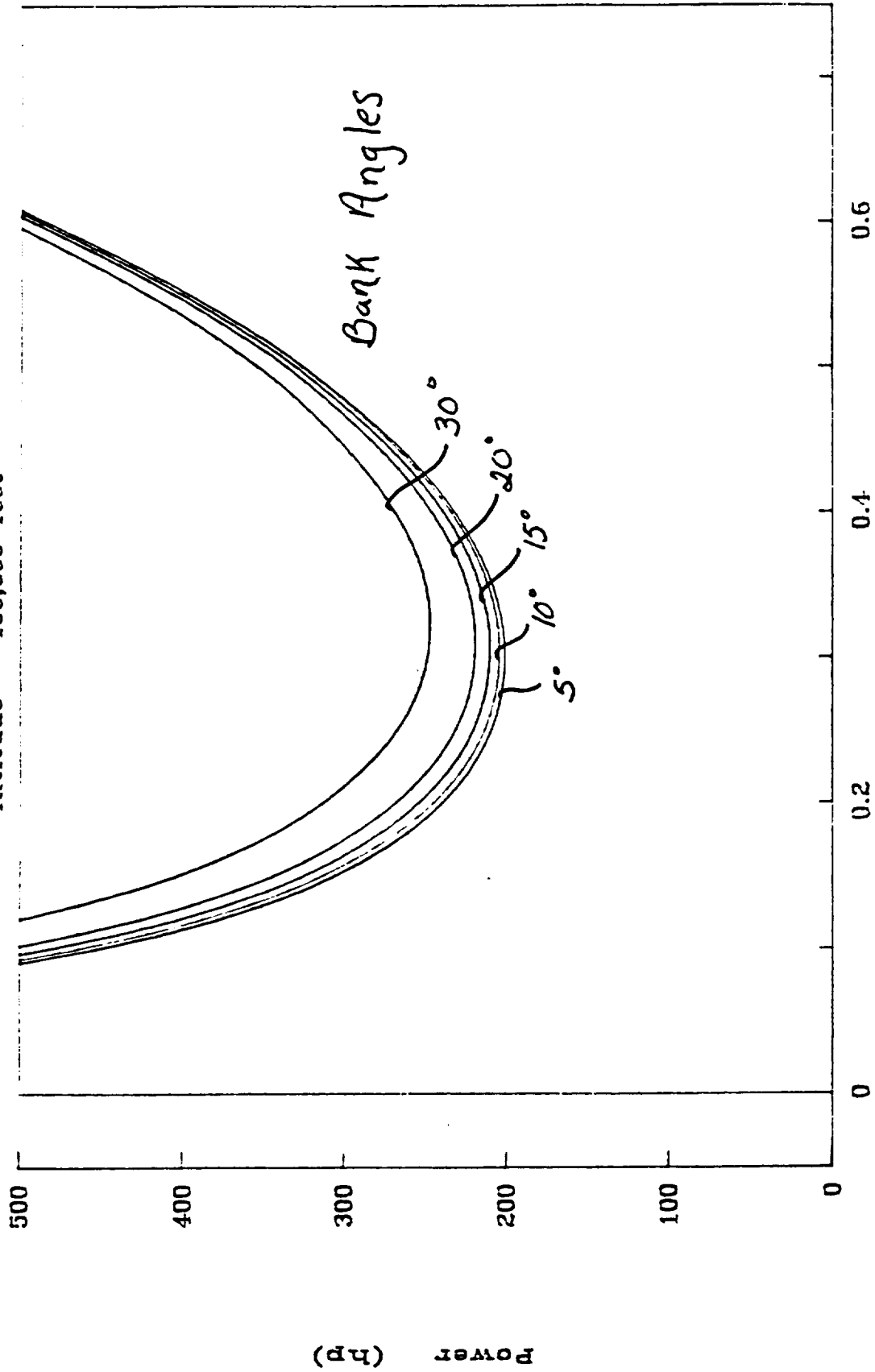
—— Bank = 5 —— Bank = 10 —— Bank = 15 —— Bank = 20 —— Bank = 30

Power (hp)

Figure 9.2.18

Power Required

Altitude - 100,000 feet

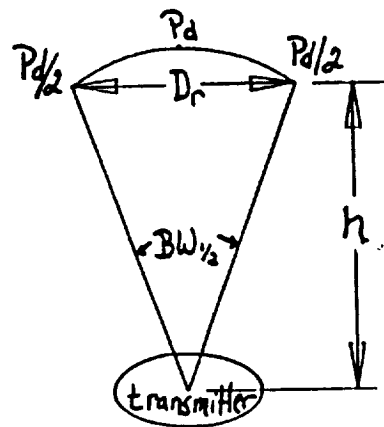


Mach Number

— Bank = 5 — Bank = 10 — Bank = 15 — Bank = 20 — Bank = 30

Figure 9.2.19

Transmitted Power Distribution



P_d power

density

A_t transmitter

area

D_t transmitter

diameter

D_r receiver

diameter

$BW_{1/2}$ $\frac{1}{2}$ beam

h altitude

$$BW_{1/2} = \frac{50 * \text{wavelength} * (2\pi/360)}{D_t}$$

$$D_t = \frac{50 * \text{wavelength} * (2\pi/360)}{BW_{1/2}}$$

Geometric Relationship

$$\tan (BW_{1/2}/2) = \frac{1}{2} D_r/h$$

$$BW_{1/2} = 2 * \tan^{-1}(\frac{1}{2} D_r/h)$$

Solving for D_t in terms of D_r :

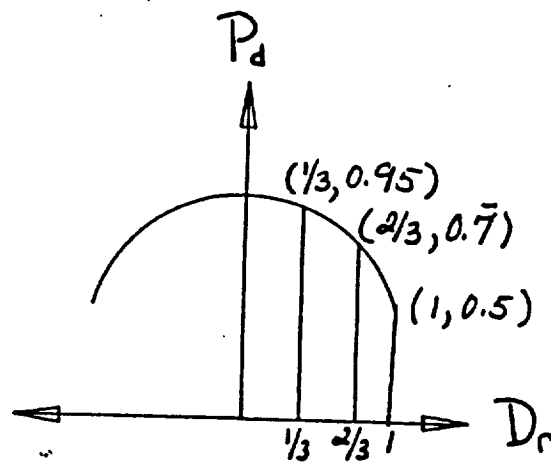
$$D_t = \frac{25 * \text{wavelength} * (2\pi/360)}{\tan^{-1}(\frac{1}{2} D_r/h)} = \frac{10 * \text{wavelength} * \pi}{36 * \theta}$$

Figure 9.2.20

Parabolic Power Density Distribution

Y fraction of Pd

X ratio of
span to Dr



Parabolic Distribution Described by :

$$Y = -\frac{1}{2}X^2 + 1$$

Figure 9.2.21

Total Transmitted Power Calculation

(at cruising altitude) θ BW

$$P_t = \frac{P_d * \text{wavelength}^2 * h^2}{A_t * n} \quad (9.9)$$

Dr(ft) tan($\theta/2$) θ (rad) Dt(m) At(m²) Pd(W/m²) P(MW)

250	1.25E-3	2.5E-3	42.761	1436.1	123.74	15.016
300	1.50e-3	3.0E-3	35.624	997.27	1002.3	17.514
350	1.75E-3	3.5E-3	30.540	732.69	899.27	21.388
400	2.00E-3	4.0E-3	26.725	560.97	843.02	26.188
500	2.50E-3	5.0E-3	21.380	359.01	785.26	38.117

Figure 9.3.1

Rate of Climb vs Altitude

Wings Level Flight

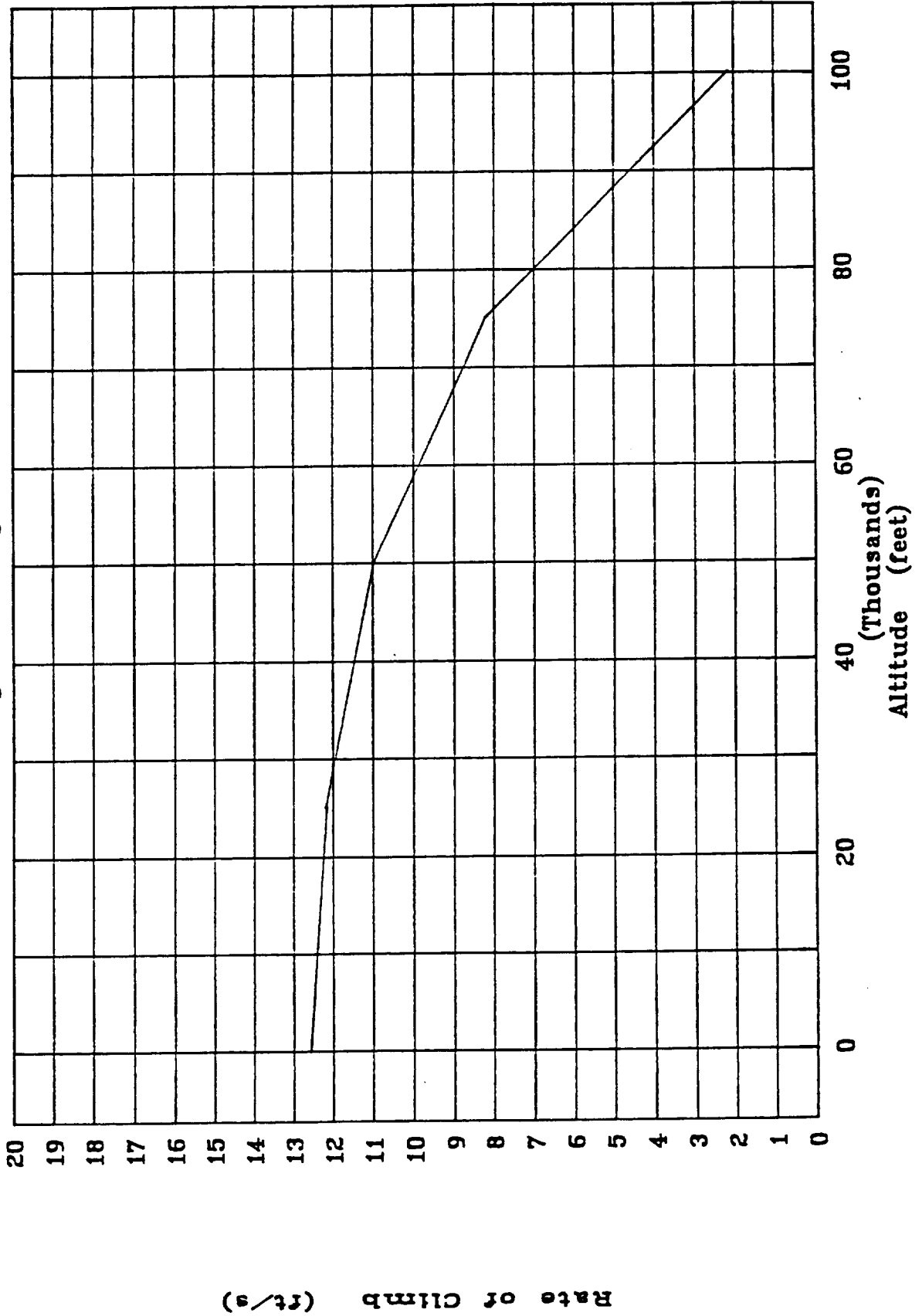


Figure 9.3.2

Rate of Climb vs Mach Number

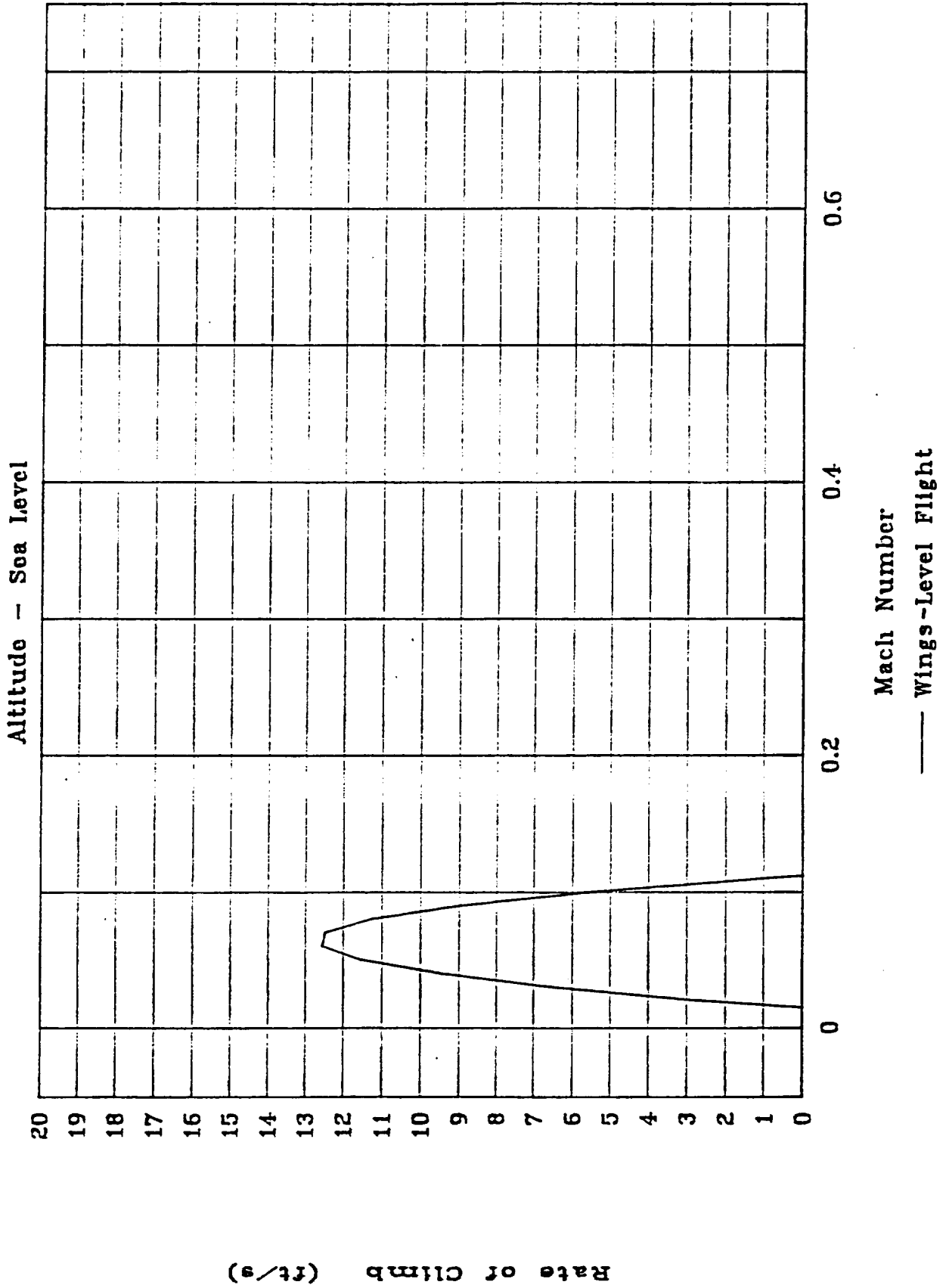
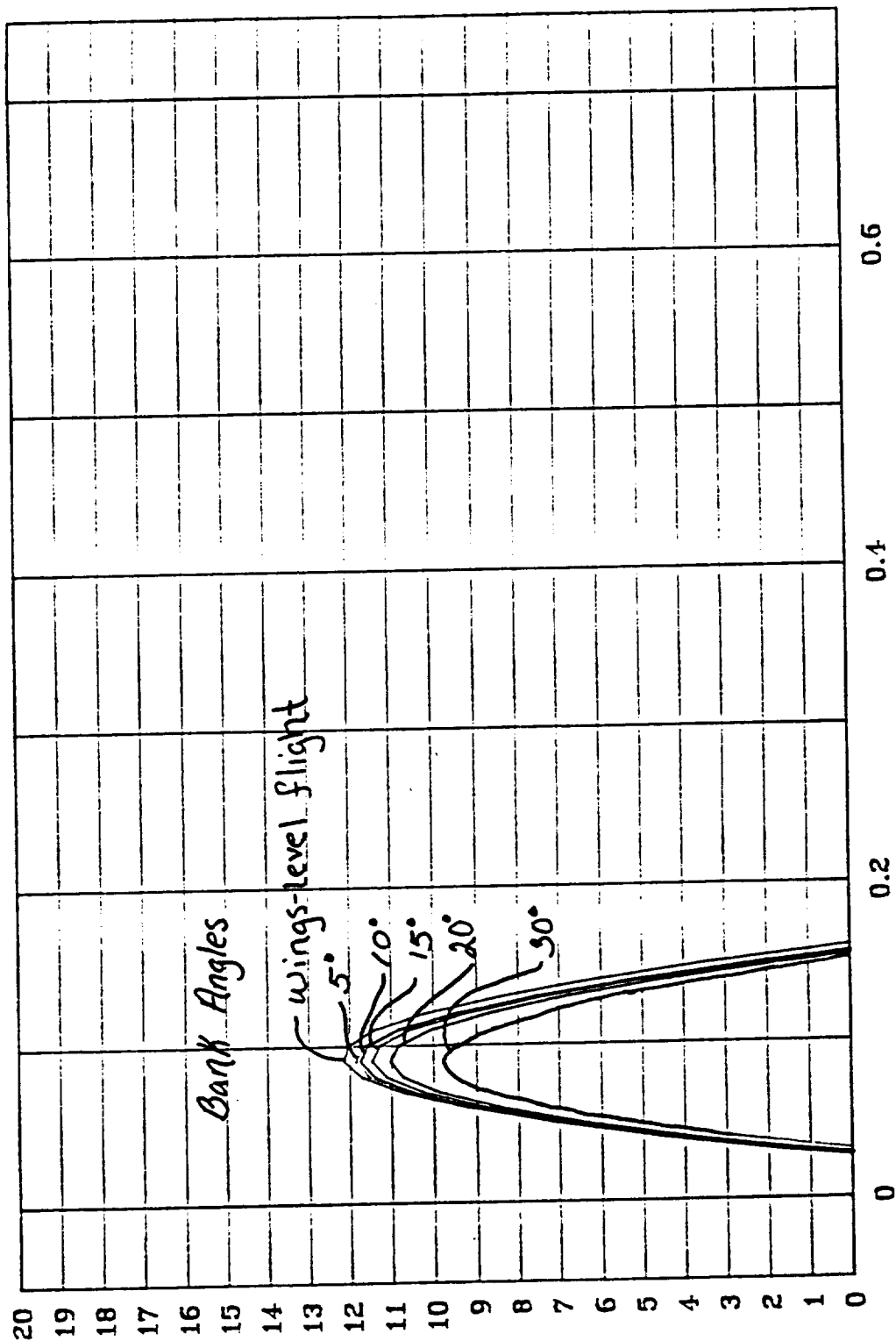


Figure 9.3.3

Rate of Climb vs Mach Number

Altitude - 25,000 feet



Mach Number

— Level flight — Bank = 5 — Bank = 10 — Bank = 15 — Bank = 20
 . . . Bank = 30

Rate of Climb (ft/s)

Figure 9.3.4

Rate of Climb vs Mach Number

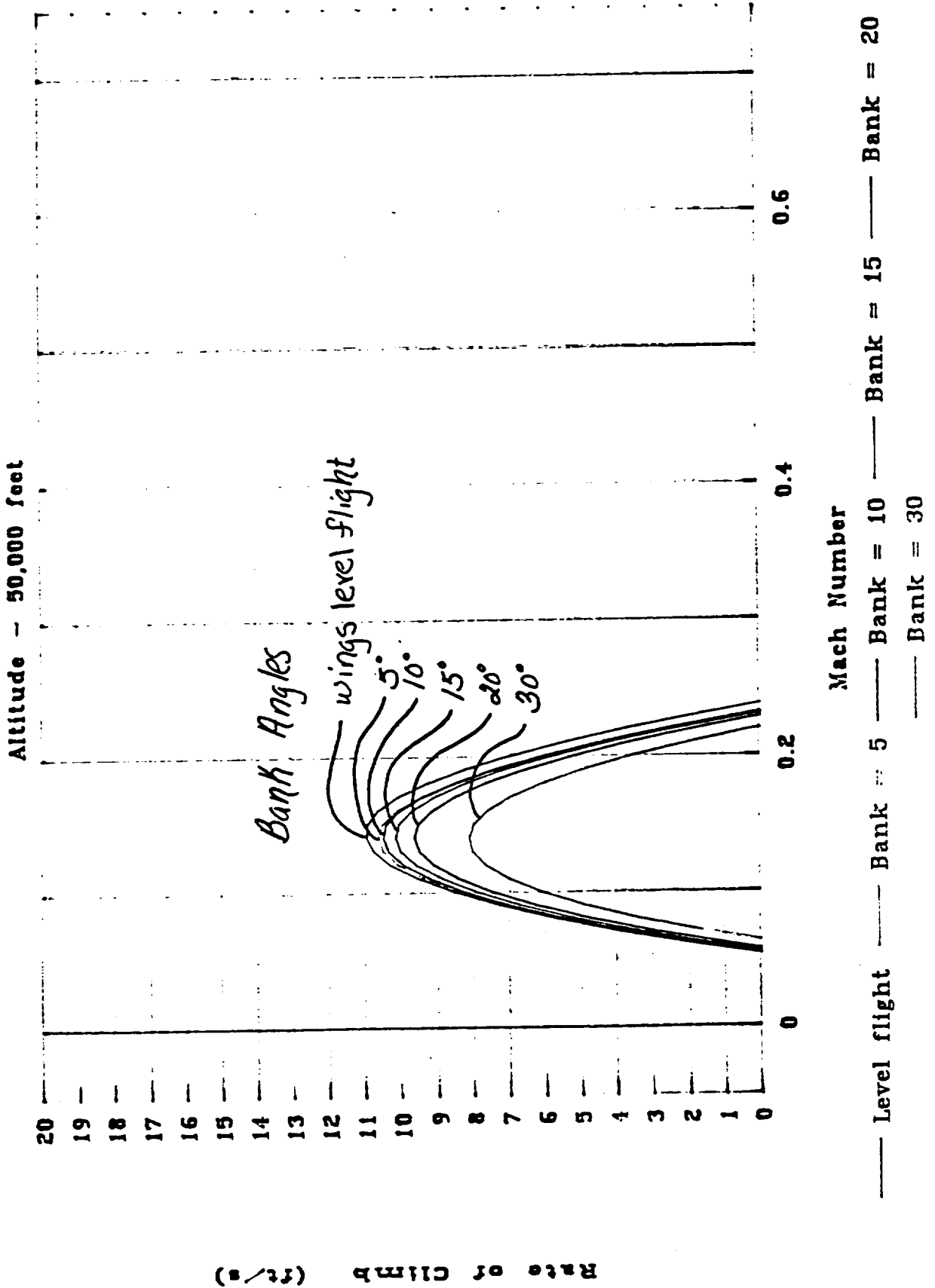


Figure 9.3.5

Rate of Climb vs Mach Number

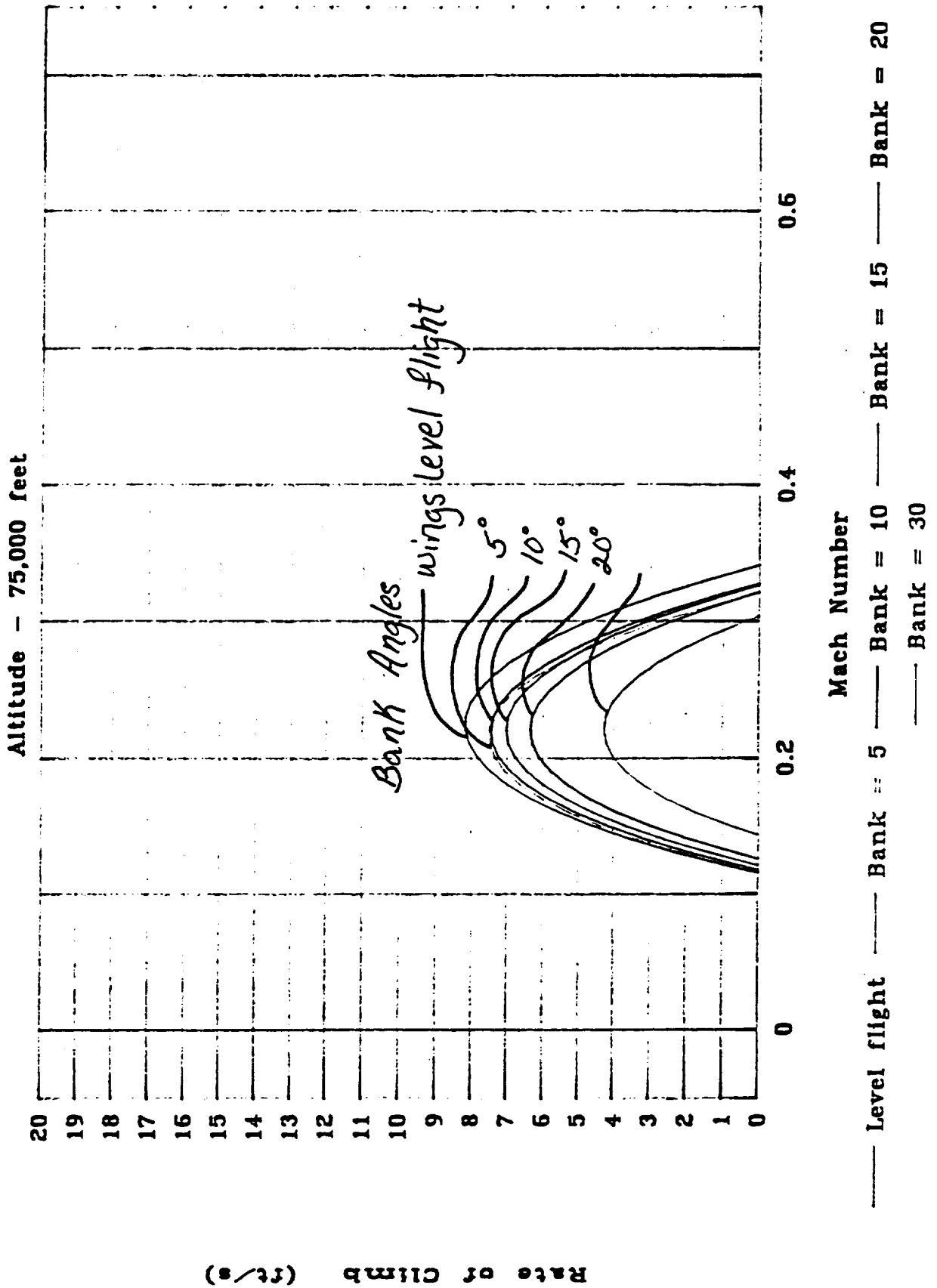


Figure 9.3.6

Rate of Climb vs Mach Number

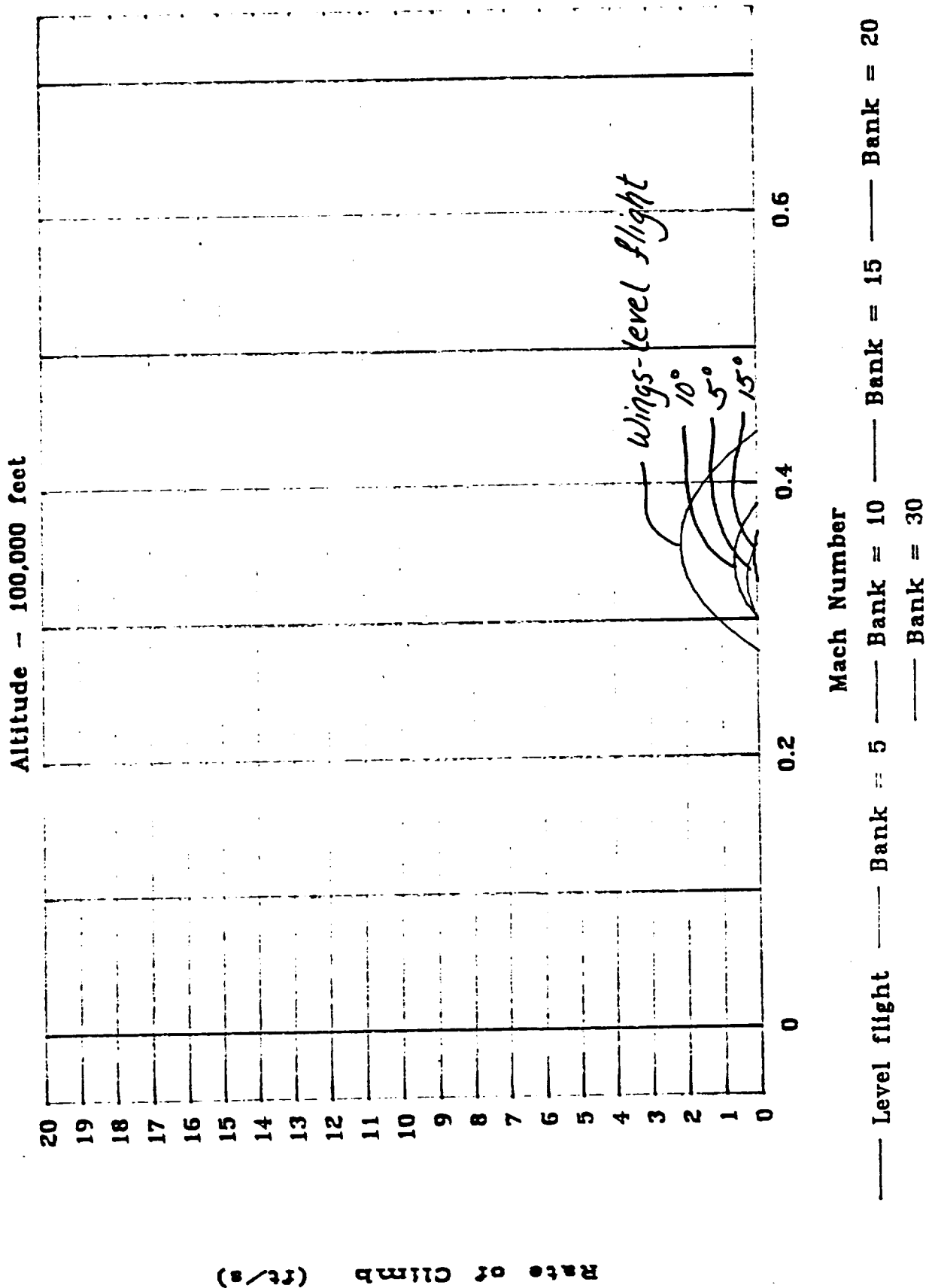


Figure 9.3.7

Time to Climb
Wings Level Flight

altitude	$dh/dt(f/s)$	$dh/dt(f/s)-1$	seconds	minutes
Sea Level to 25,000 ft	12.381	0.080772	2019.3	33.655
25,000 ft to 50,000 ft	11.571	0.086424	2160.6	36.010
50,000 ft to 75,000 ft	9.5839	0.10434	2608.5	43.475
75,000 ft to 100,000 ft	5.1744	0.19315	4828.7	80.478

Total time - 11,617 s - 193.62 min - 3.23 hrs

Figure 9.3.8

Time to Climb

Turning Flight

altitude	dh/dt(f/s)	dh/dt(f/s)-1	seconds	Time minutes
Sea Level to 25,000 ft	11.742	0.085168	2129.2	35.487
25,000 ft to 50,000 ft	11.254	0.088855	2221.4	37.0227
50,000 ft to 75,000 ft	9.1012	0.10988	2746.9	45.781
75,000 ft to 100,000 ft	3.8418	0.26029	6507.3	108.46

Total time - 13.605 s - 226.75 min - 3.78 hrs

Figure 9.4.1

Altitude vs Flight Radius

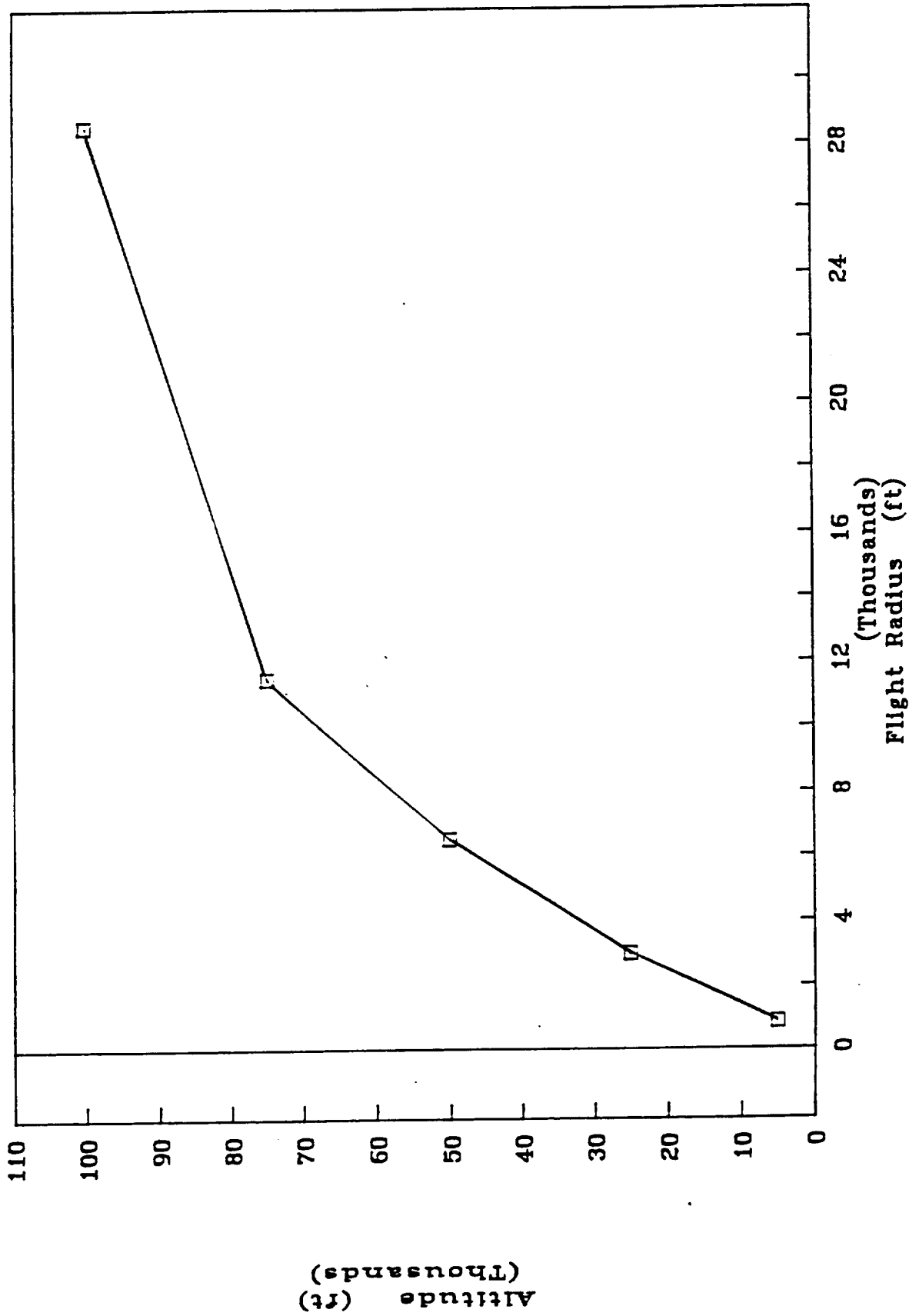


Figure 9.4.2

Mach Number vs Altitude

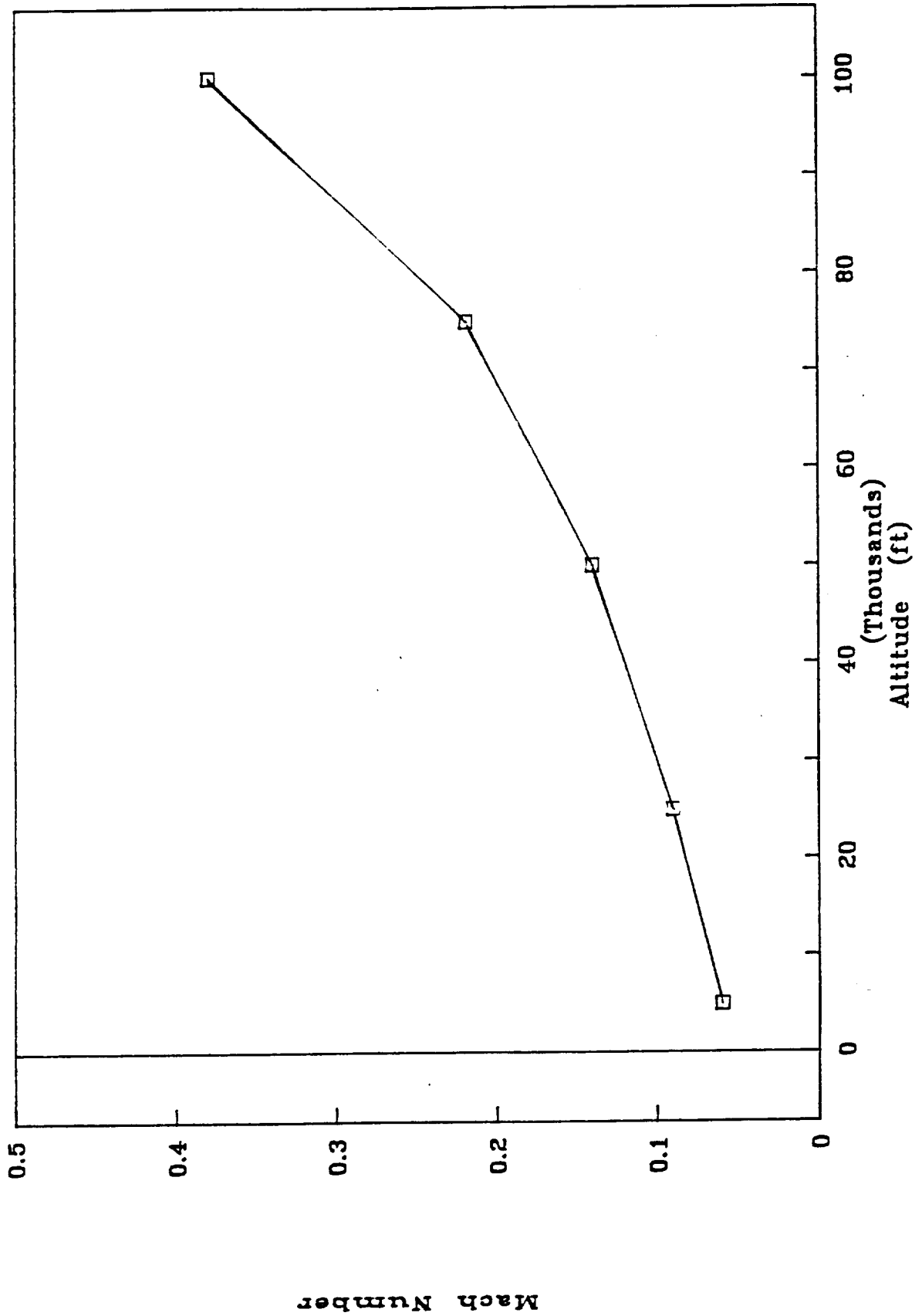


Figure 9.4.3

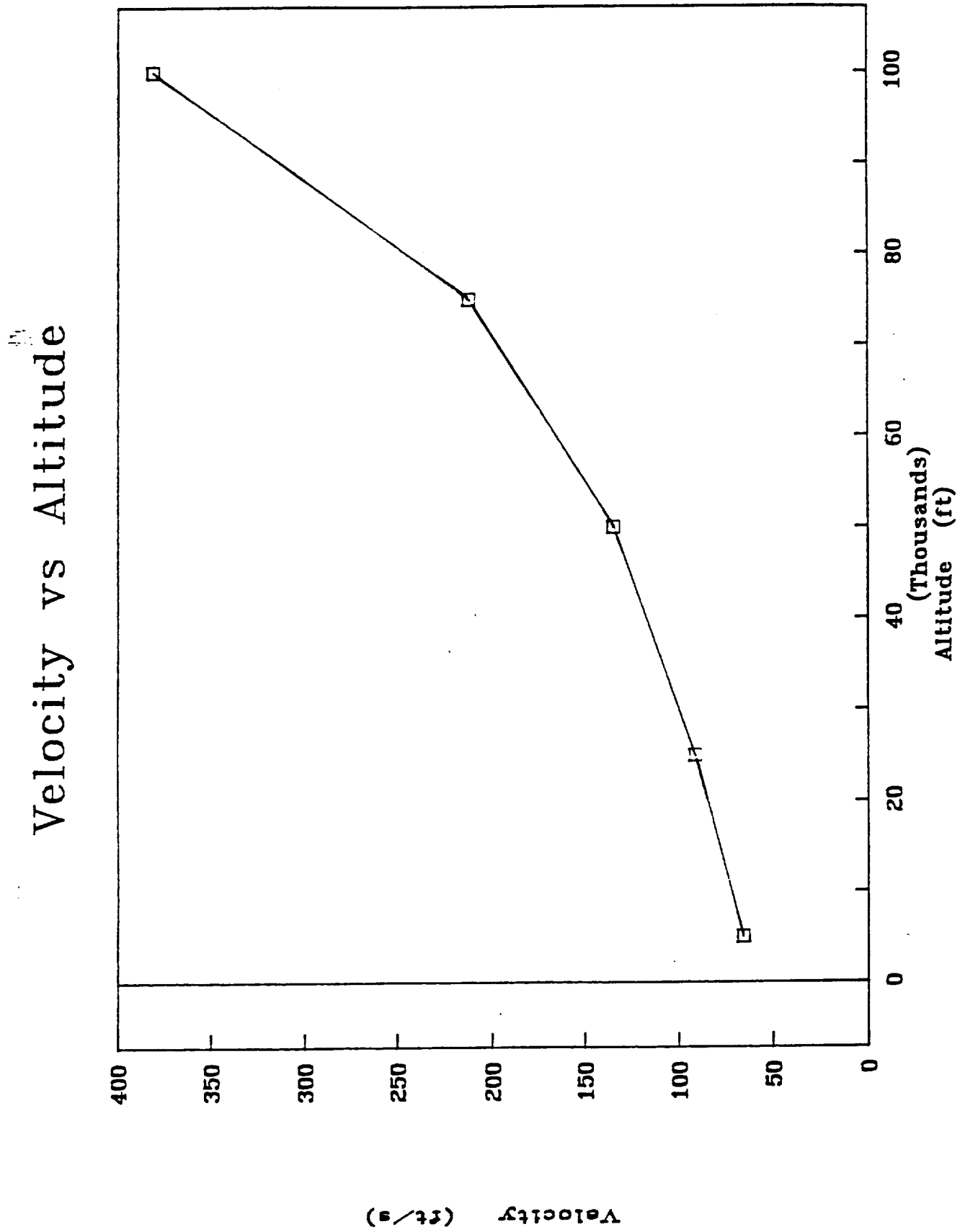


Figure 9.4.4

Coefficient of Lift vs Altitude

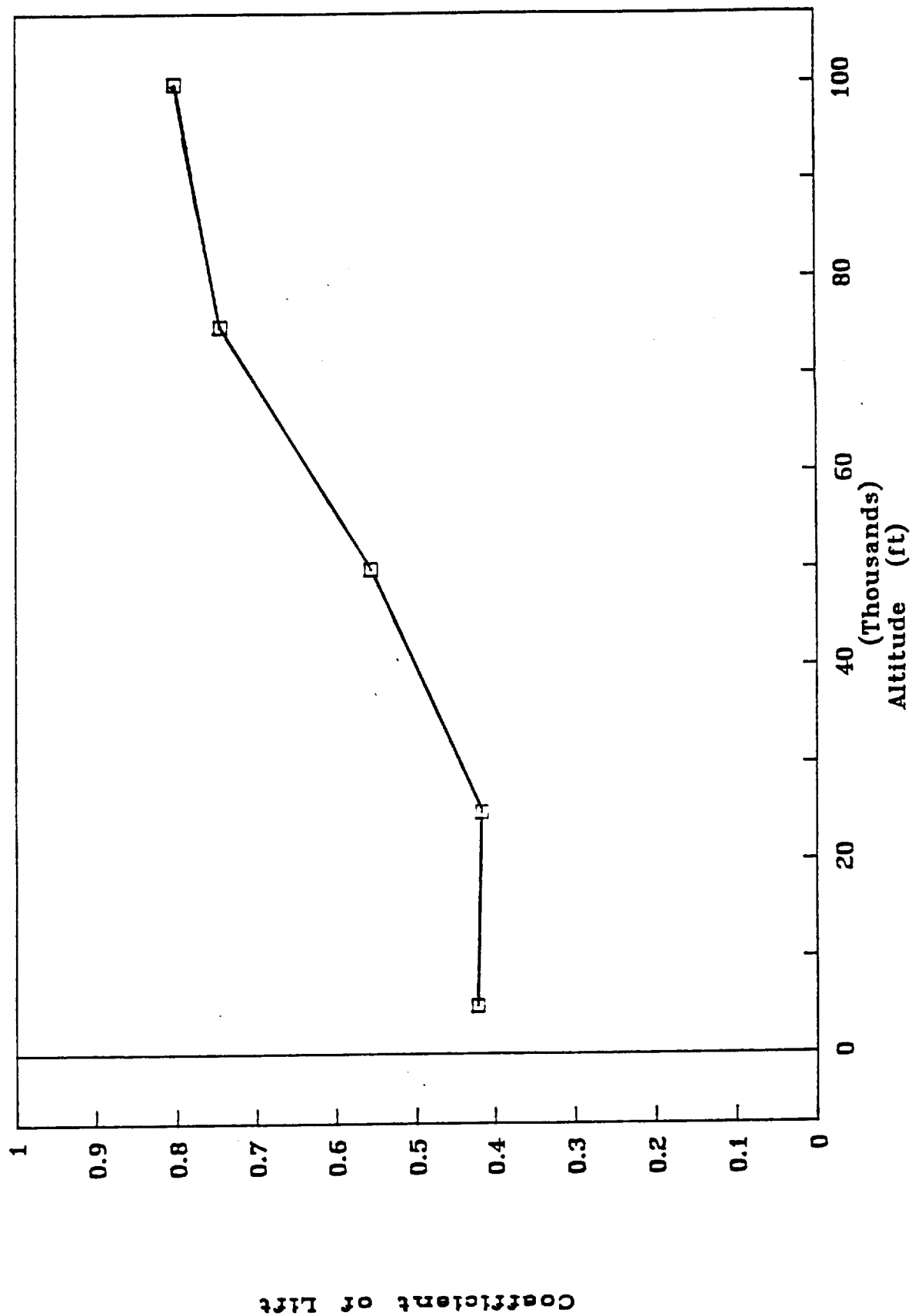


Figure 9.4.5

Bank Angle vs Altitude

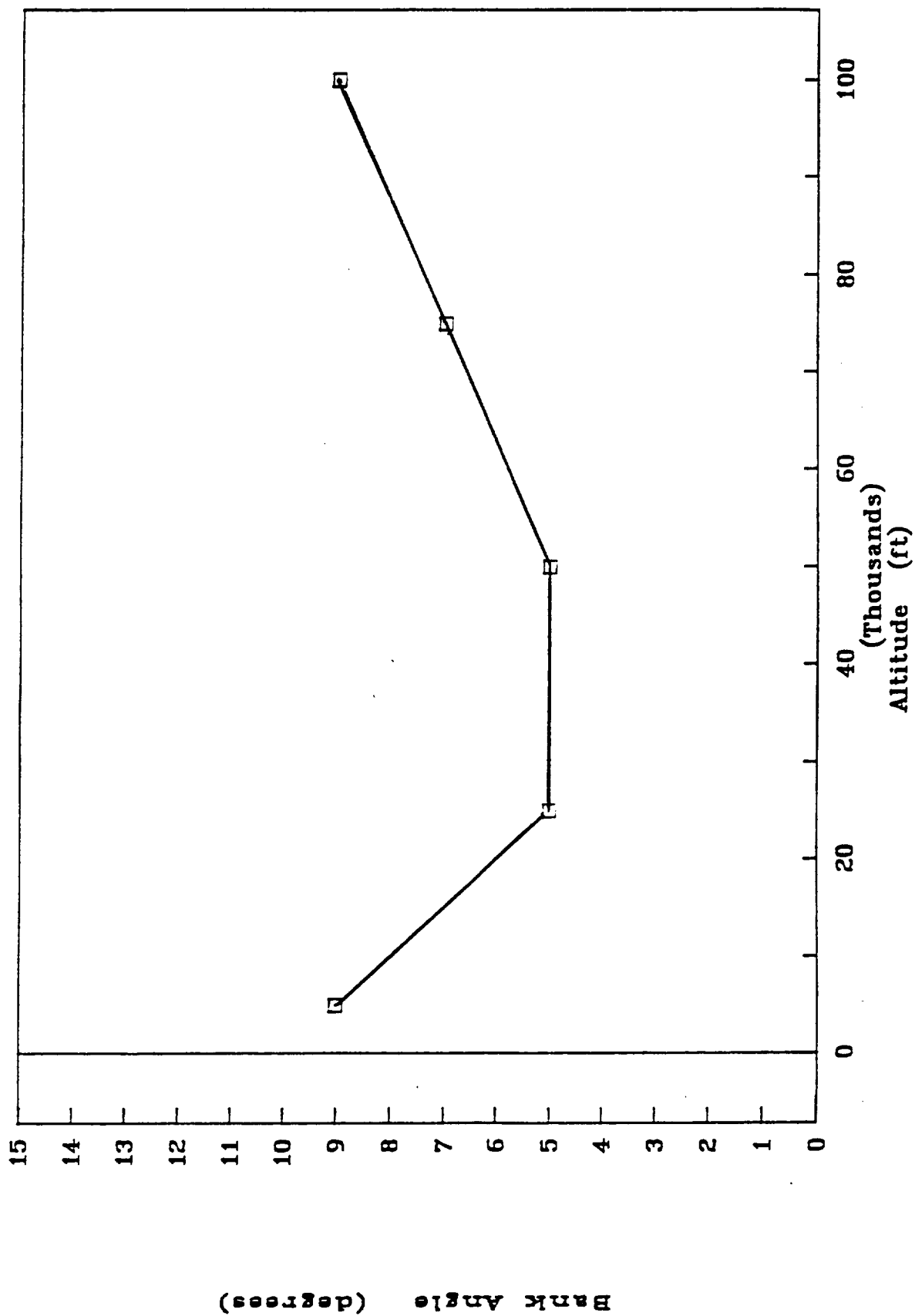


Figure 9.4.6

Flight Radius vs Altitude

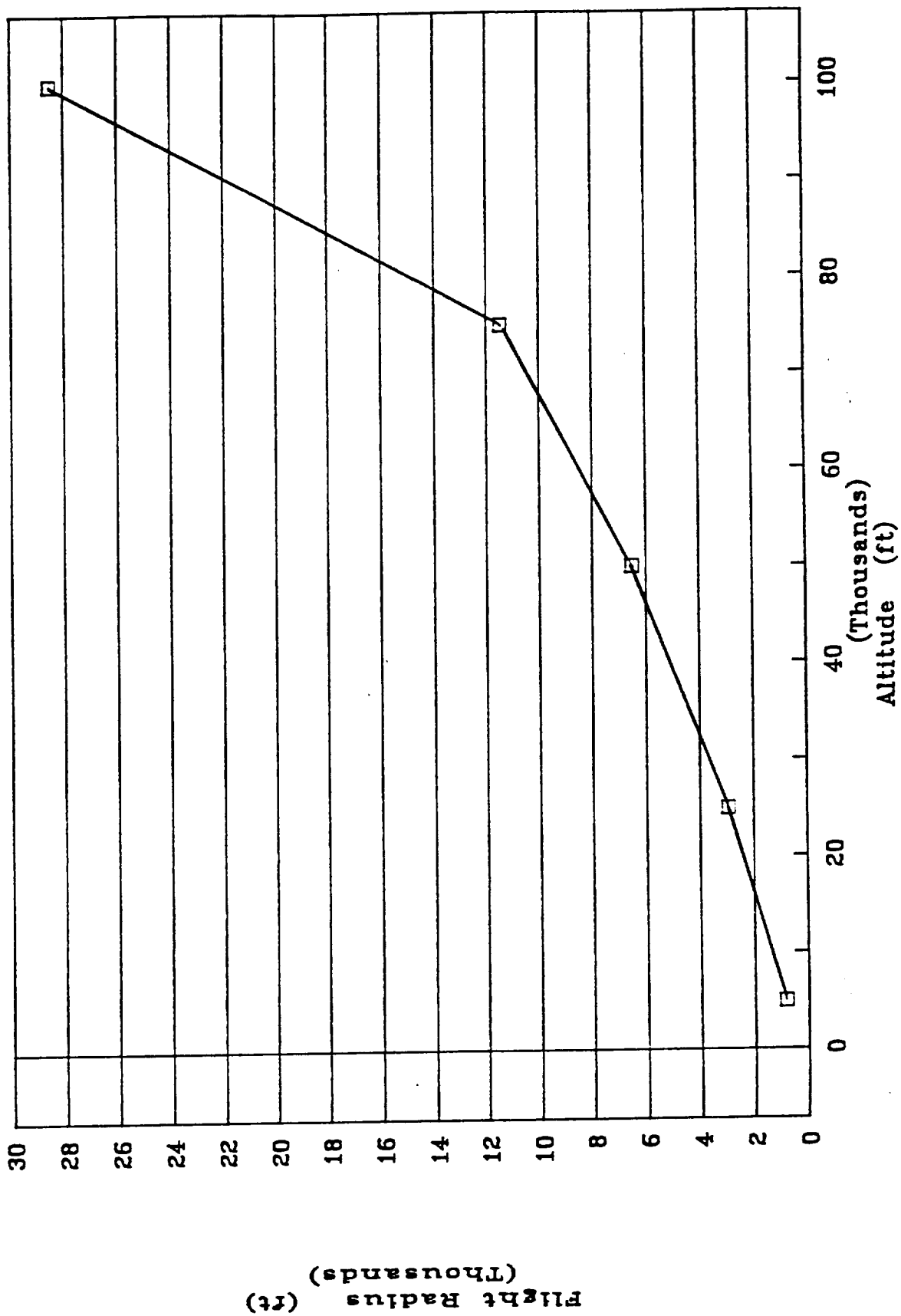


Figure 9.4.7

Climb Rate vs Altitude

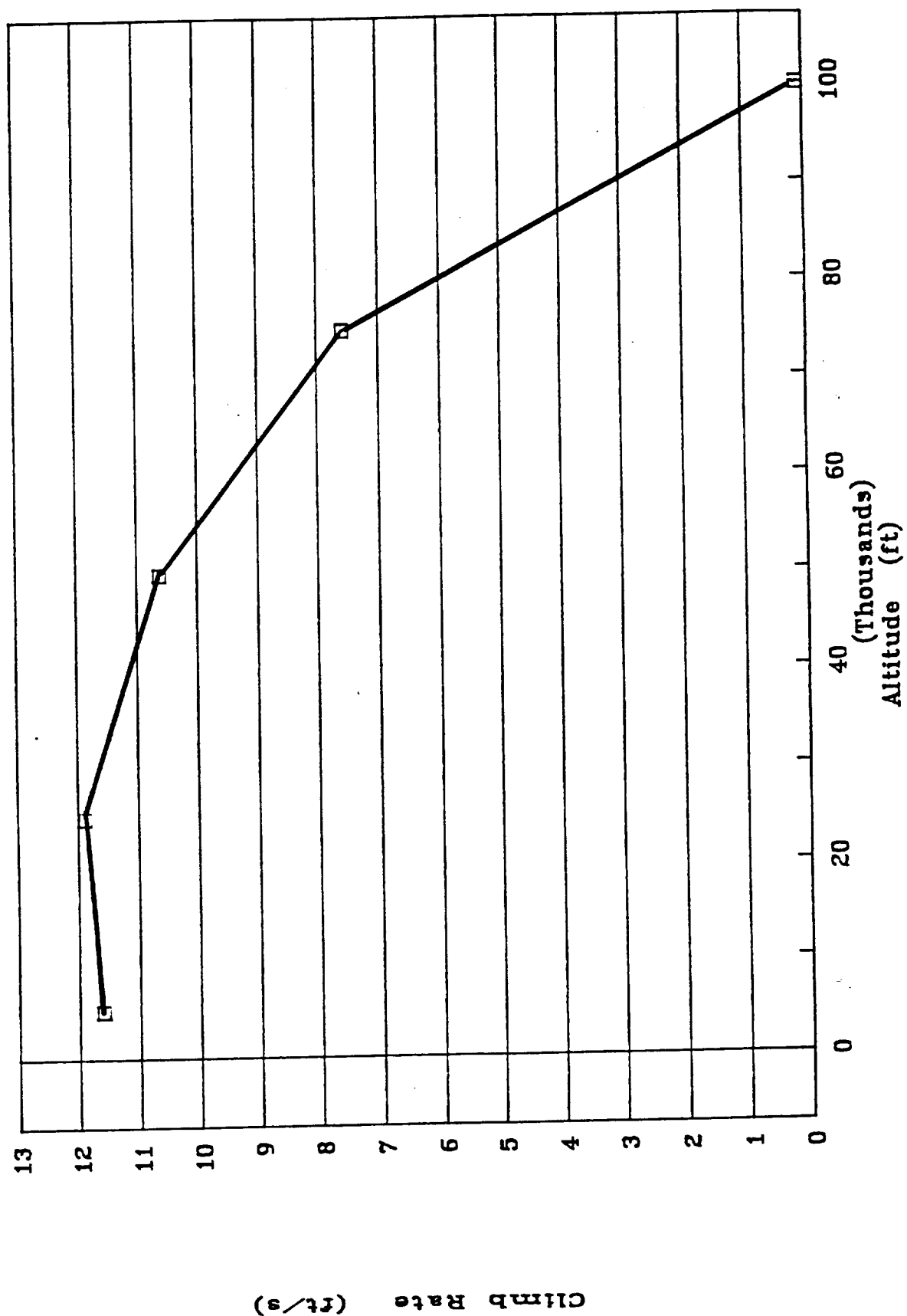


Figure 9.4.8

Altitude vs Flight Radius

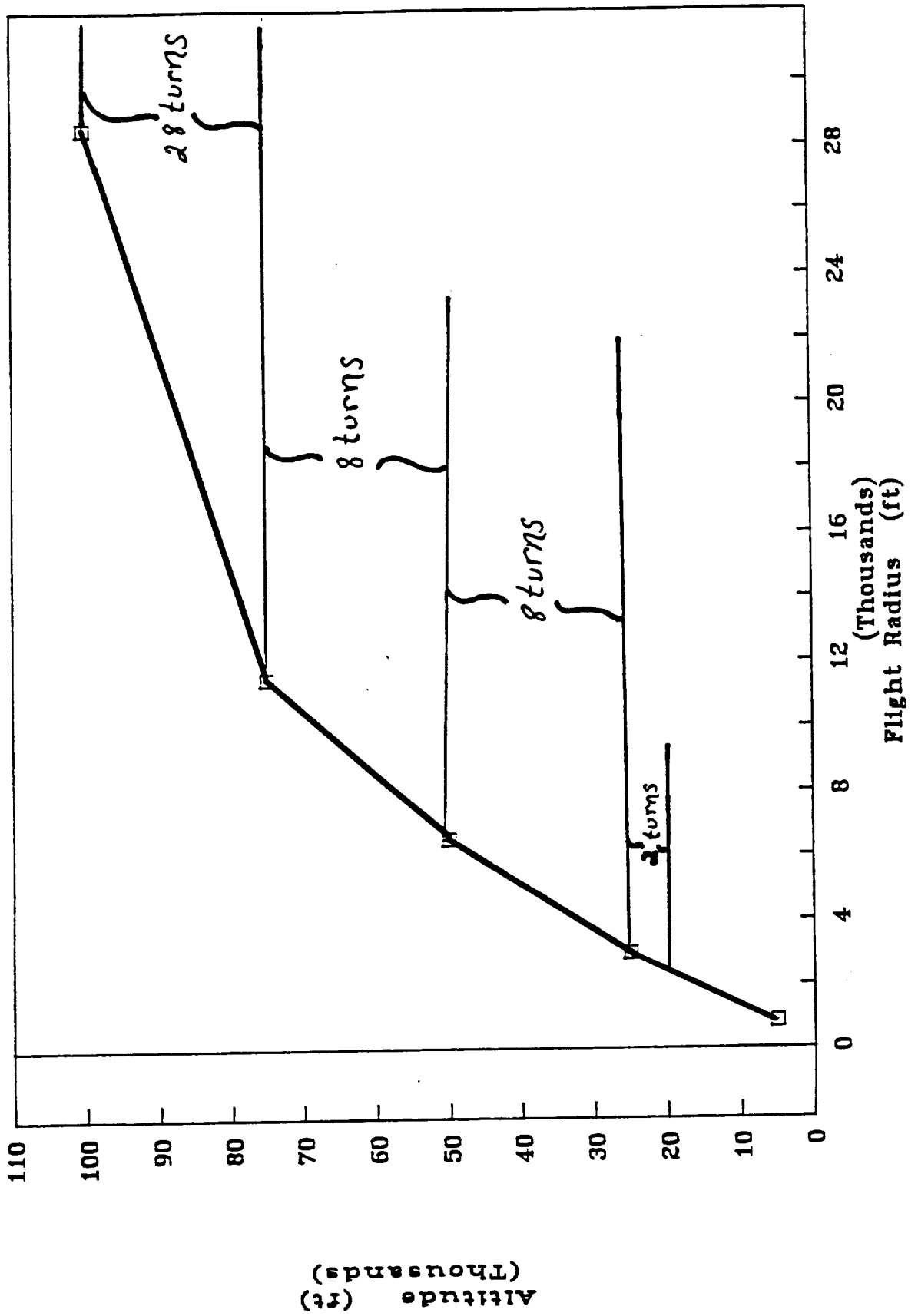
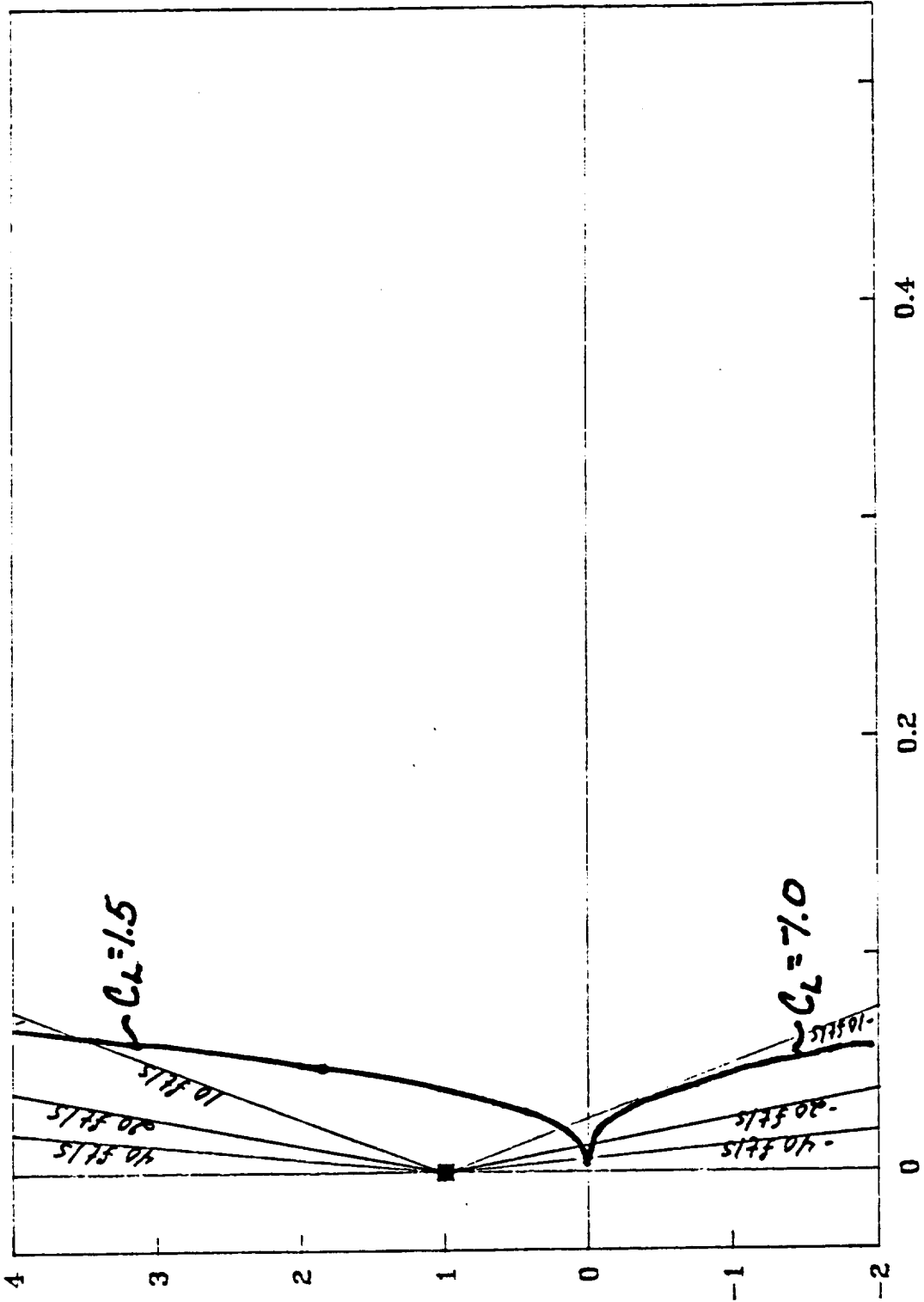


Figure 9.5.1

V-n Diagram

EFFECT OF WIND GUST

ALTITUDE - SEA LEVEL



MACH NUMBER

□ 40 FT/S + 20 FT/S ◇ 10 FT/S △ -10 FT/S X -20 FT/S V -40 FT/S

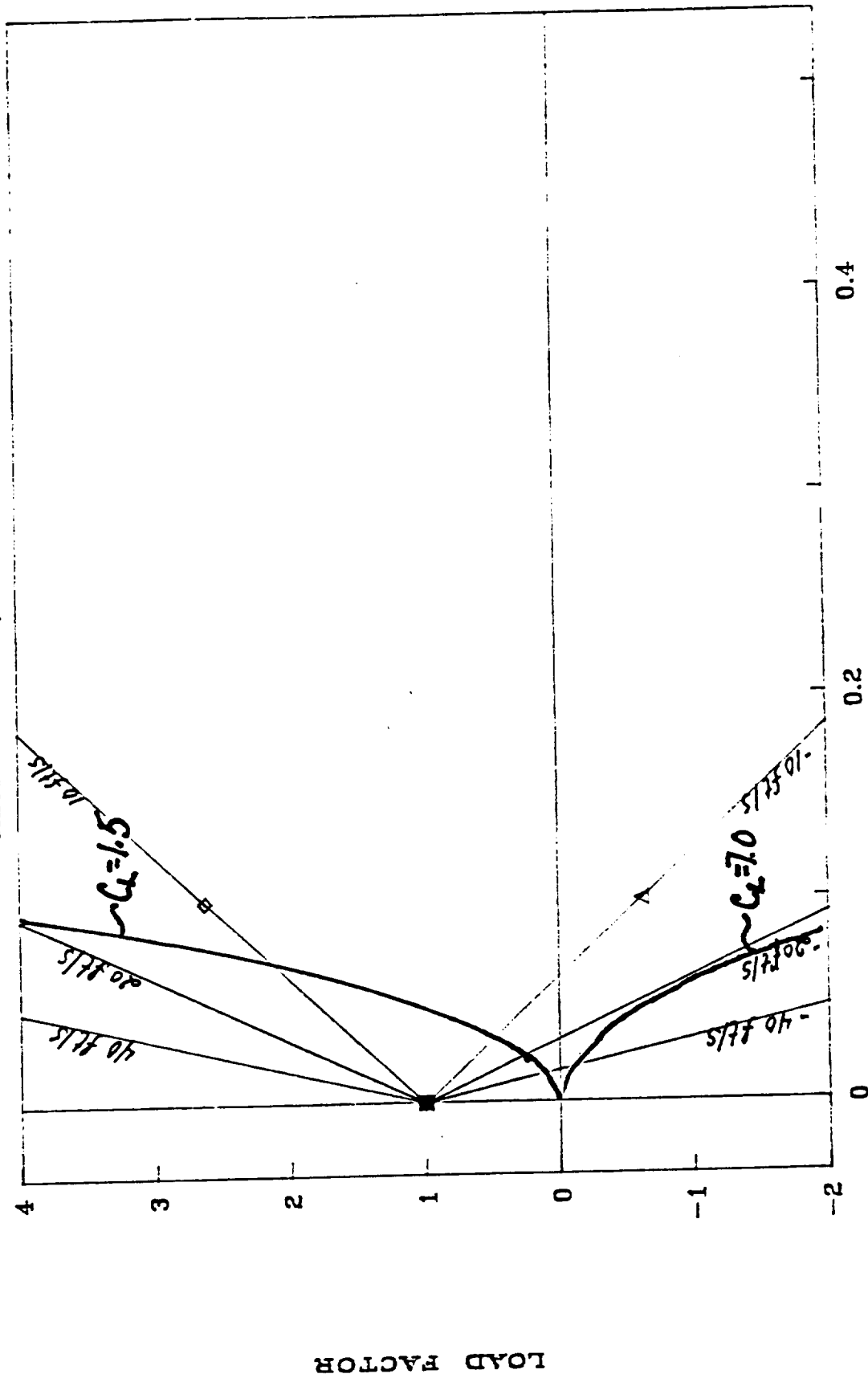
LOAD FACTOR

Figure 9.5.2

V-n Diagram

EFFECT OF WIND GUST

ALTITUDE - 25,000 FEET



MACH NUMBER

□ 40 FT/S + 20 FT/S ◇ 10 FT/S △ -10 FT/S × -20 FT/S ▽ -40 FT/S

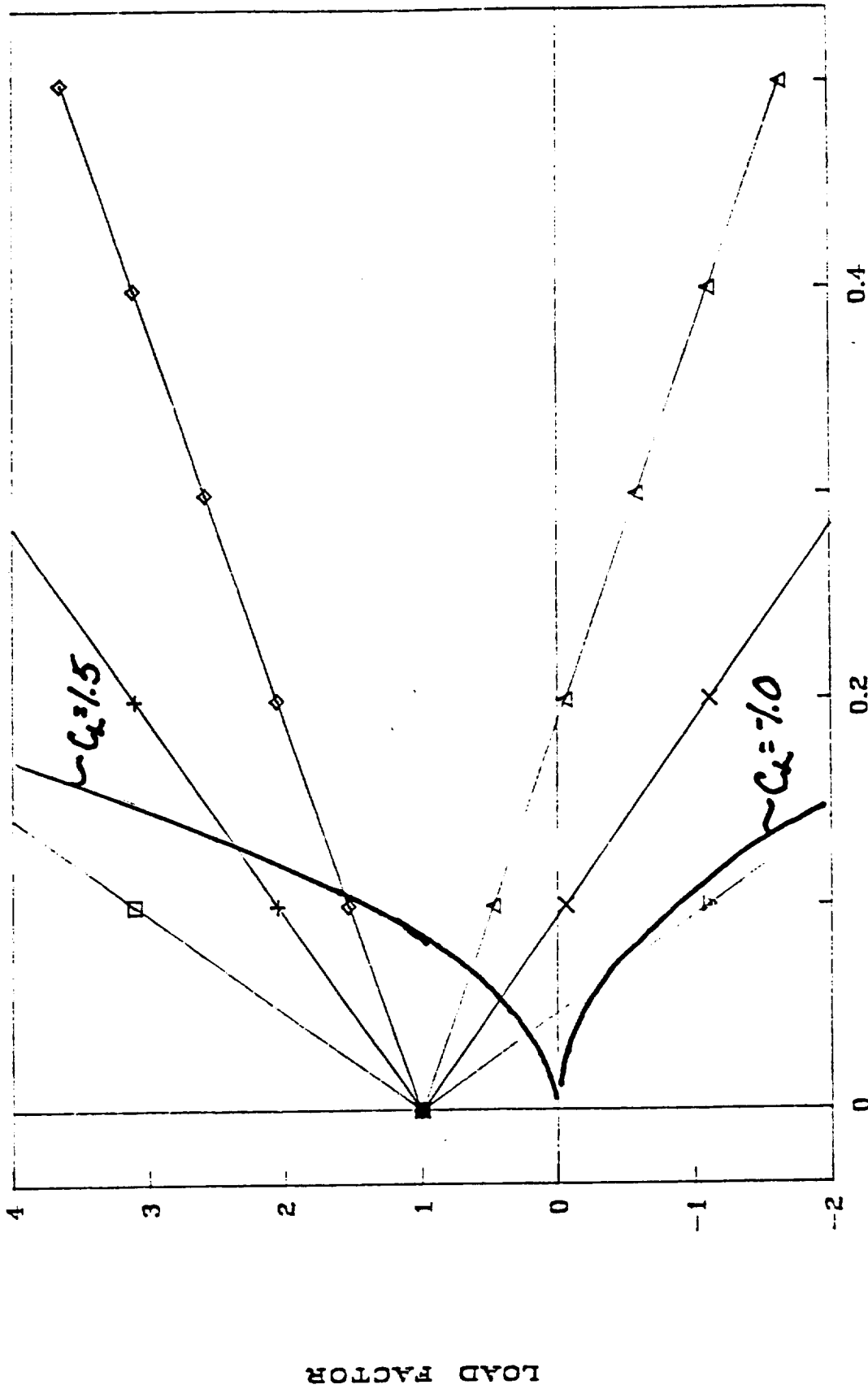
LOAD FACTOR

Figure 9.5.3

V-n Diagram

EFFECT OF WIND GUST

ALTITUDE - 50,000 FEET



MACH NUMBER

□ 40 FT/S + 20 FT/S ◇ 10 FT/S △ 0 FT/S × -10 FT/S -20 FT/S V -40 FT/S

Figure 9.5.4

V-n Diagram

EFFECT OF WIND GUST

ALTITUDE - 75,000 FEET

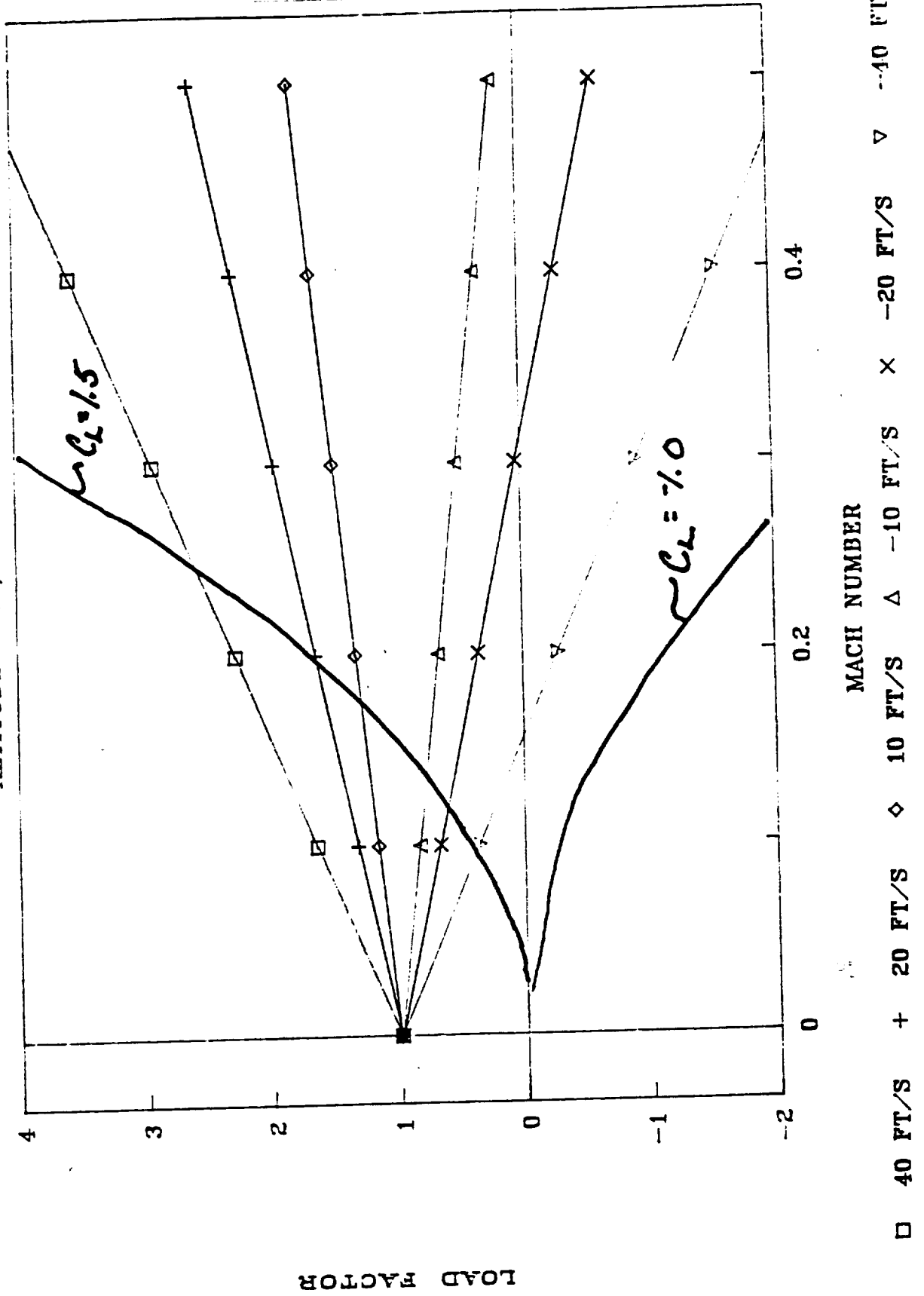
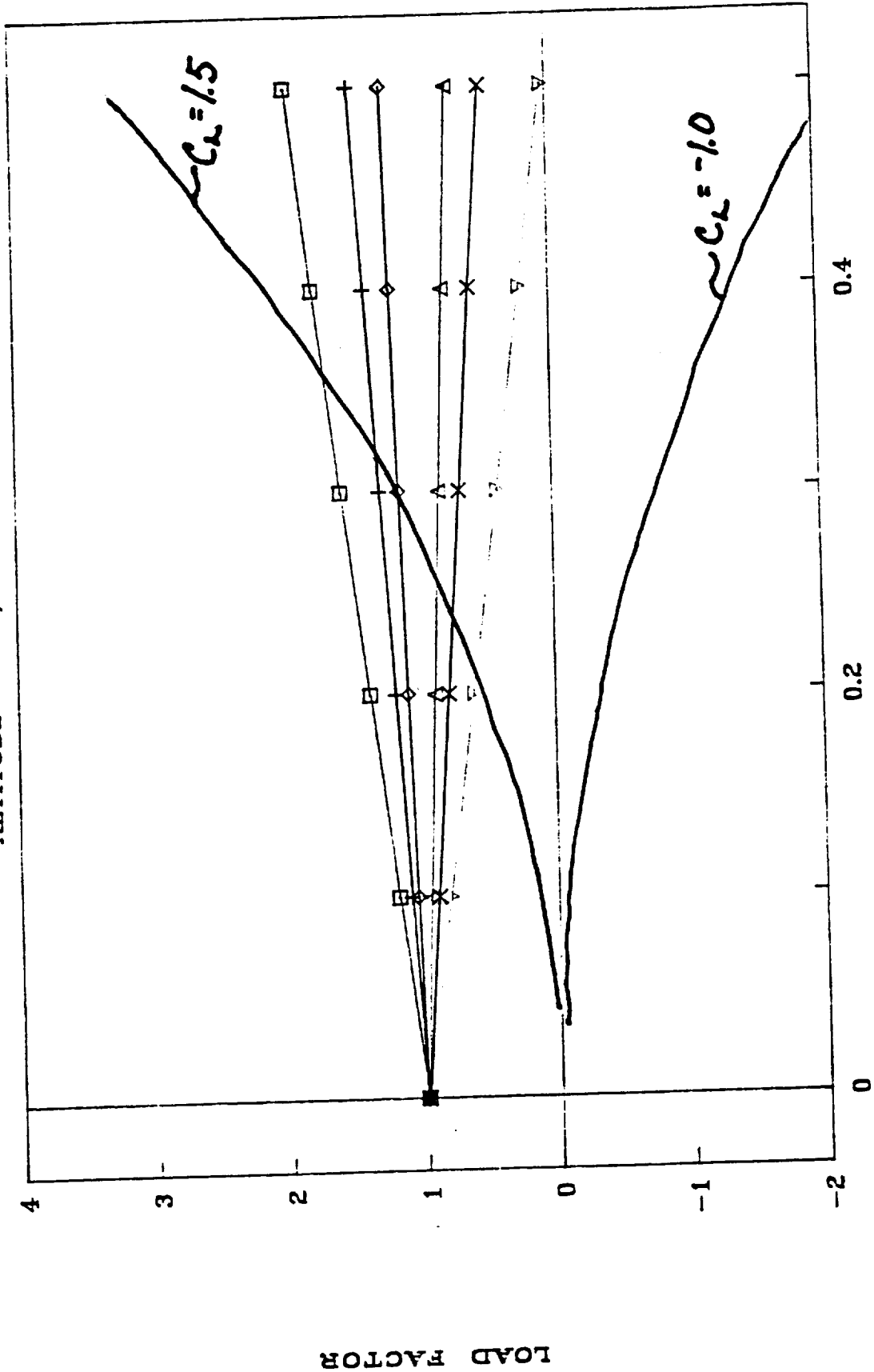


Figure 9.5.5

V-n Diagram

EFFECT OF WIND GUST

ALTITUDE - 100,000 FEET



MACH NUMBER

40 FT/S

+ 20 FT/S

◇ 10 FT/S

Δ -10 FT/S

× -20 FT/S

▽ -40 FT/S

LOAD FACTOR

Figure 9.5.6

V-n Diagram

EFFECT OF WIND GUST

ALTITUDE - SEA LEVEL

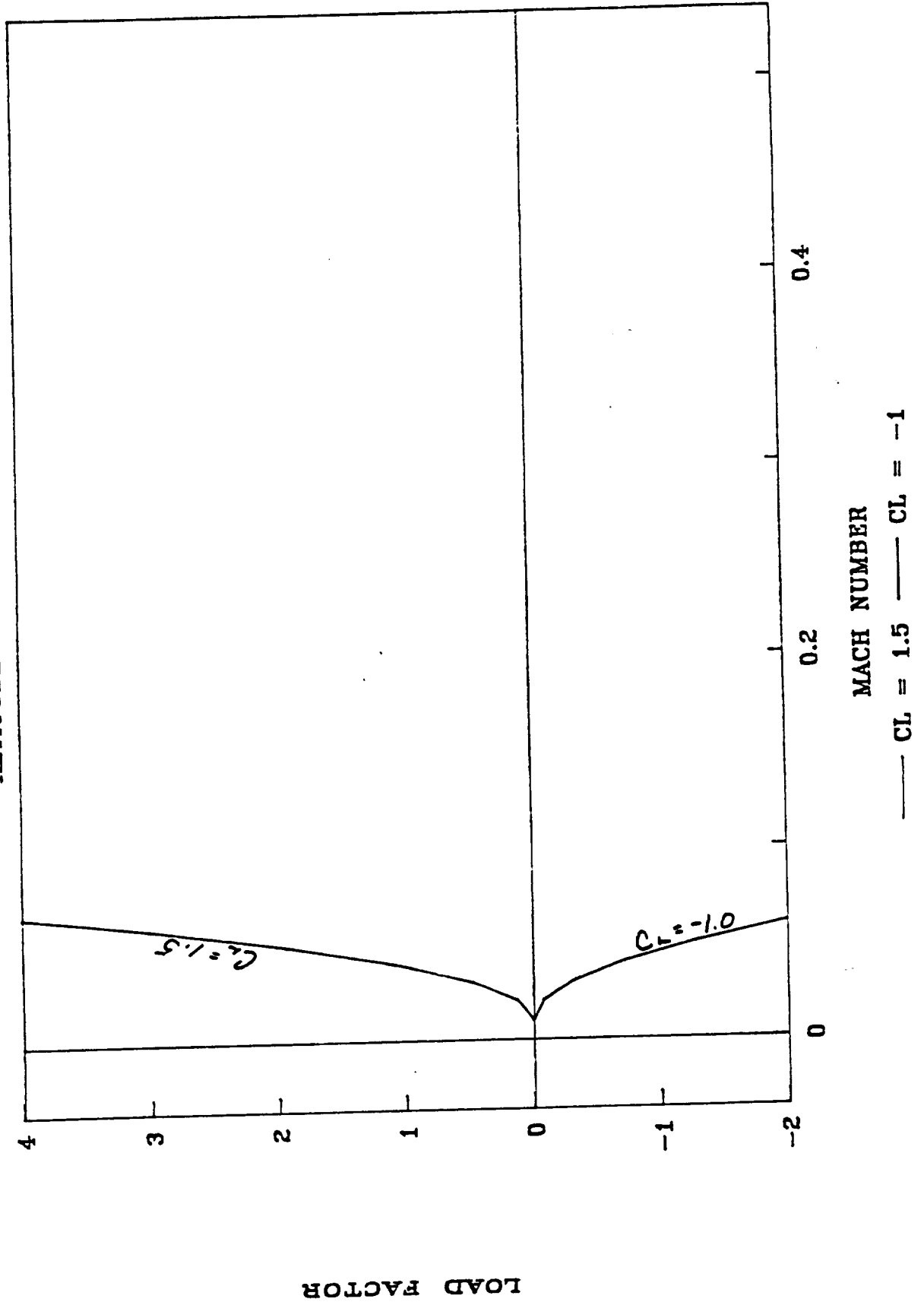


Figure 9.5.7

V-n Diagram

EFFECT OF WIND GUST

ALTITUDE - 25,000 FEET

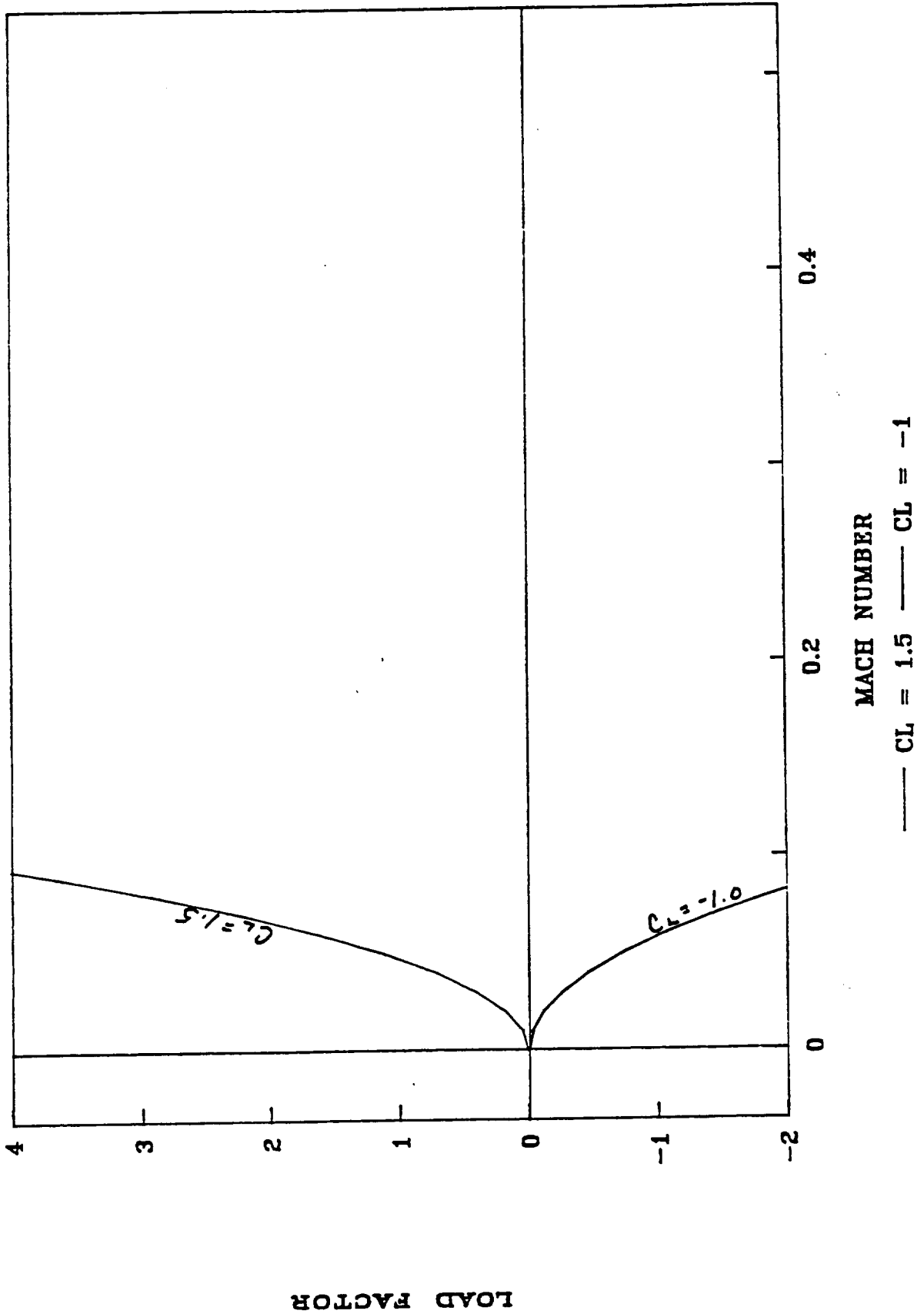


Figure 9.5.8

V-n Diagram

EFFECT OF WIND GUST

ALTITUDE - 50,000 FEET

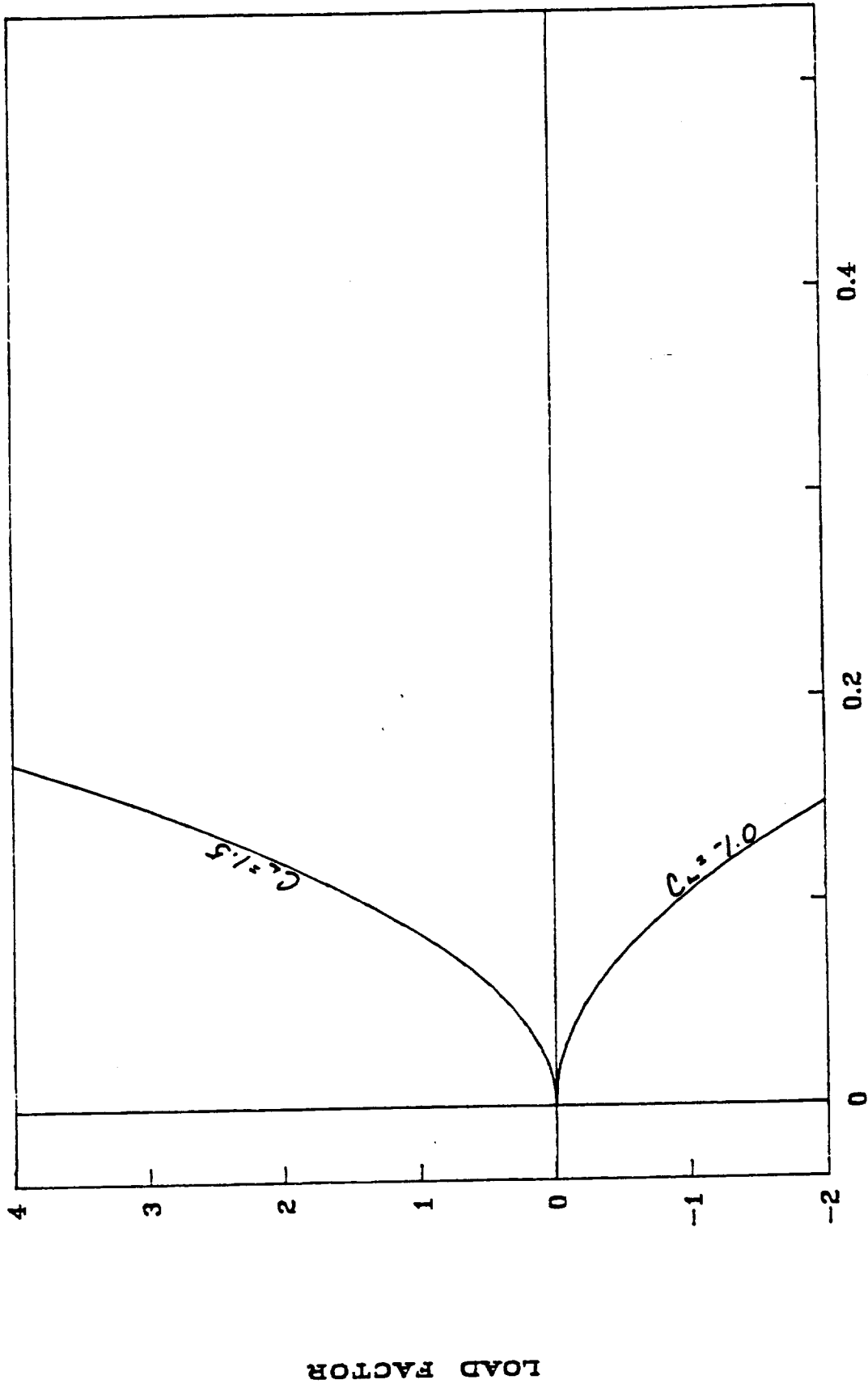
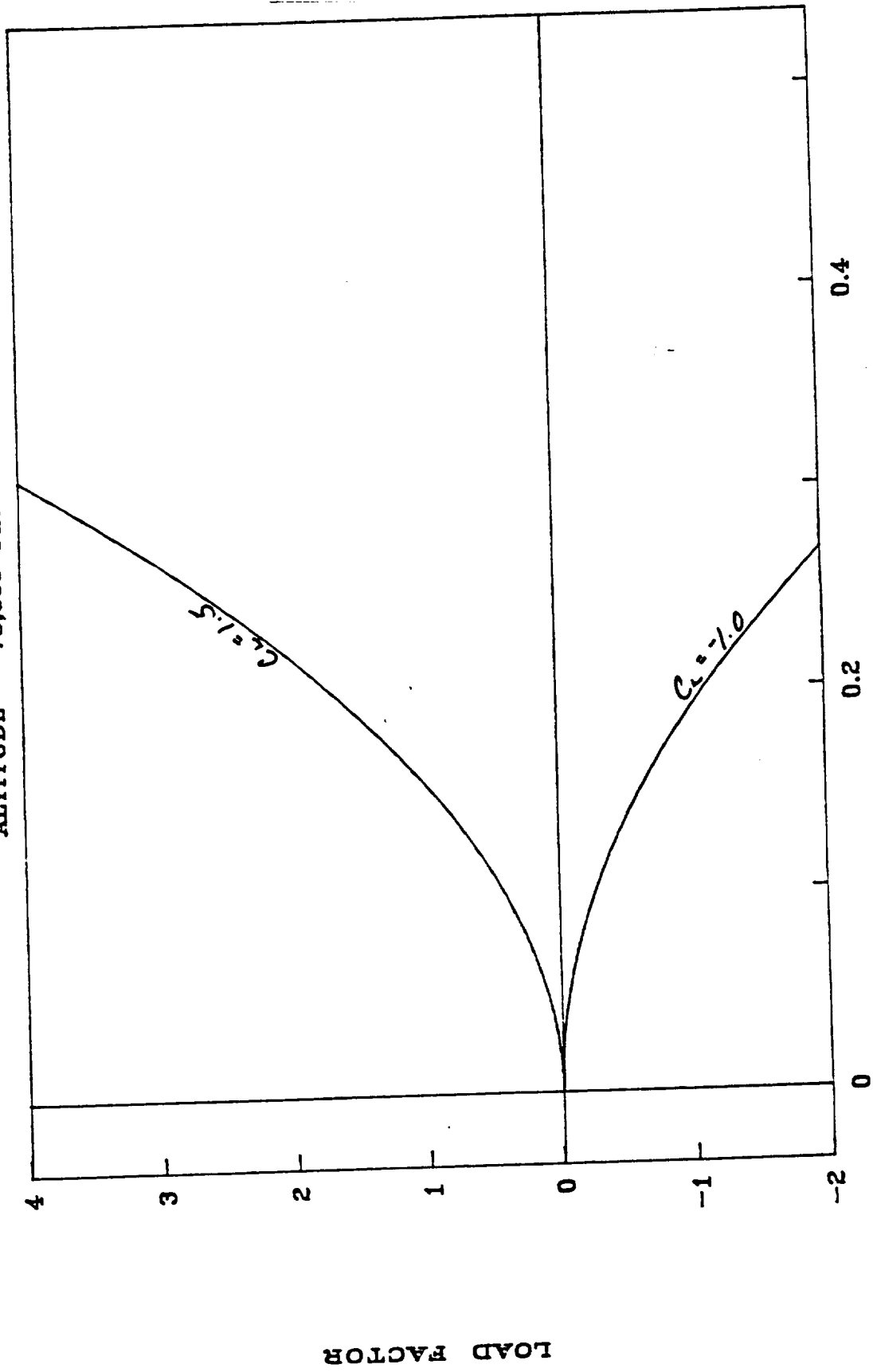


Figure 9.5.9

V-n Diagram

EFFECT OF WIND GUST

ALTITUDE - 75,000 FEET



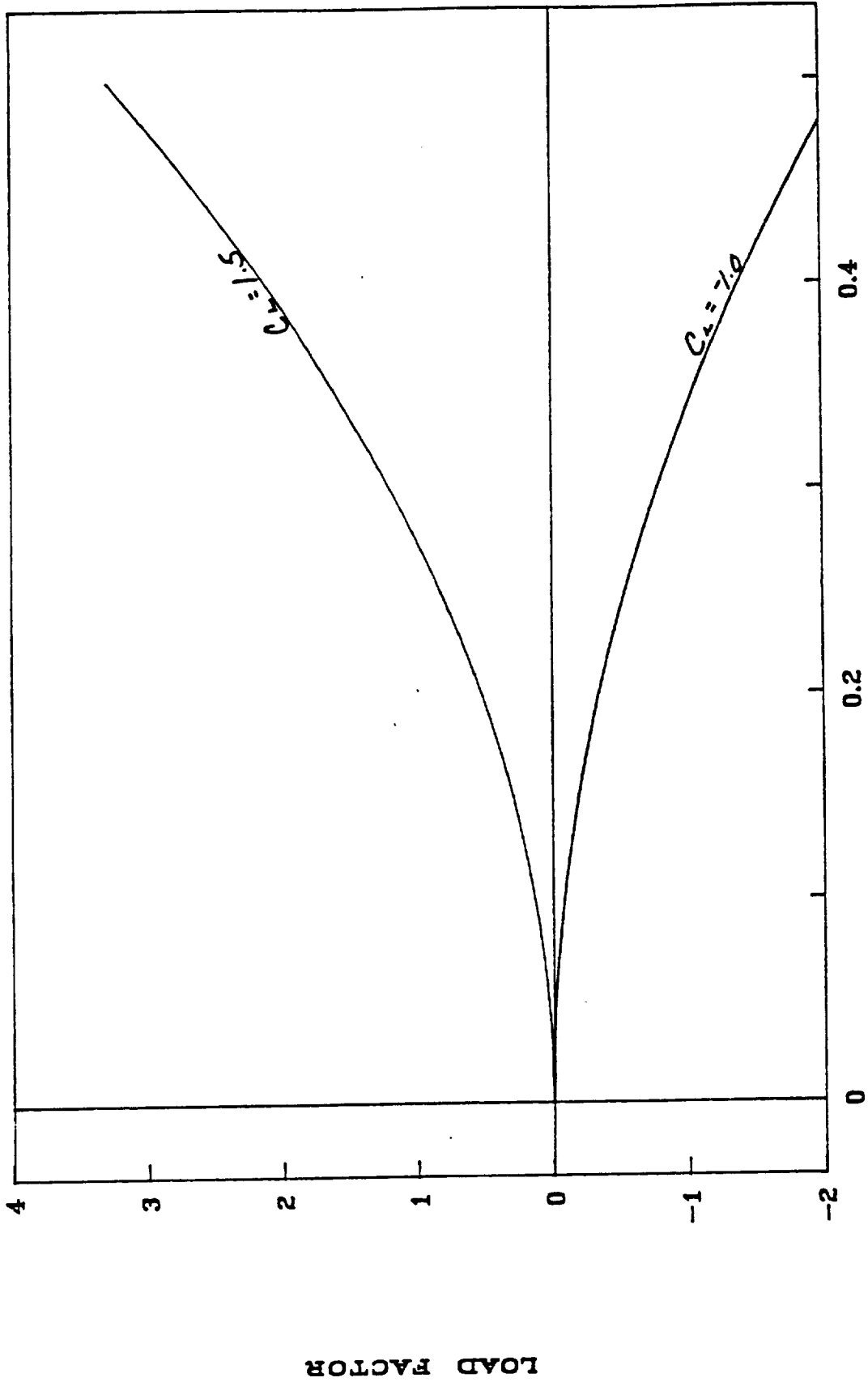
MACH NUMBER
—— $CL = 1.5$ —— $CL = -1$

Figure 9.5.10

V-n Diagram

EFFECT OF WIND GUST

ALTITUDE - 100,000 FEET



MACH NUMBER

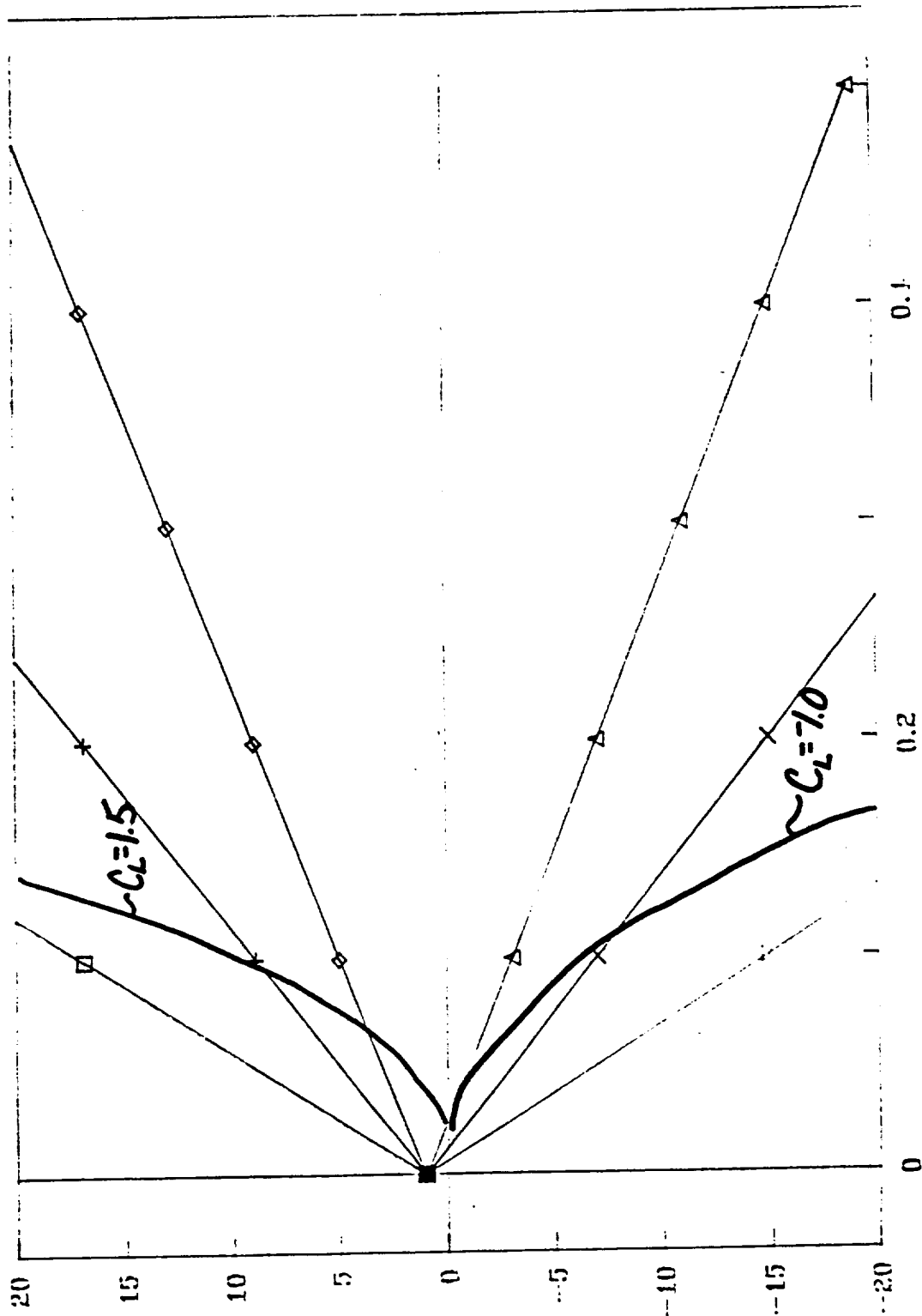
— $C_L = 1.5$ — $C_L = -1$

Figure 9.5.11

V-n Diagram

EFFECT OF WIND GUST

ALTITUDE -- SEA LEVEL



MACH NUMBER

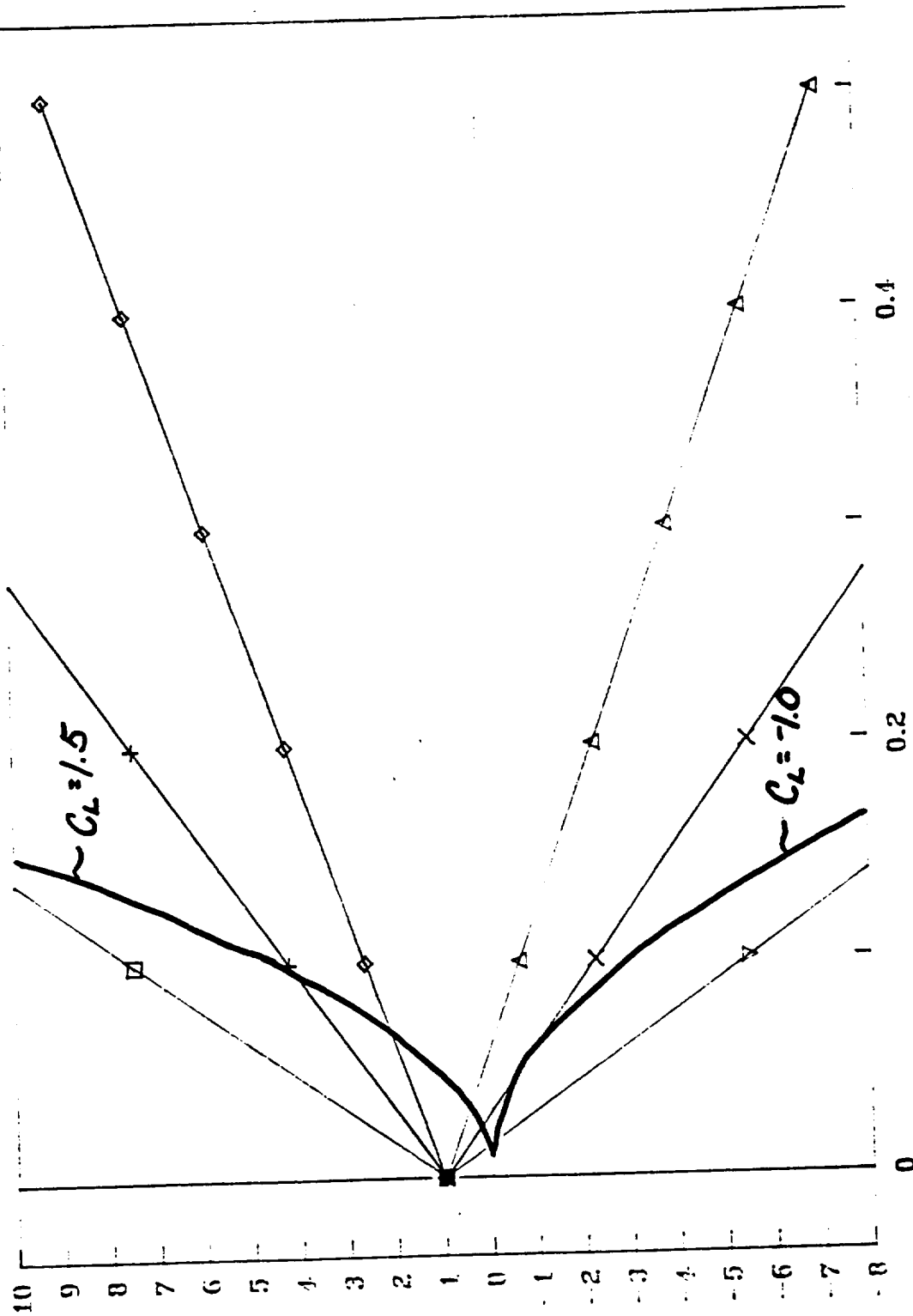
LOAD FACTOR

Figure 9.5.12

V-n Diagram

EFFECT OF WIND GUST

ALTITUDE -- 25,000 FEET



MACH NUMBER

40 FT/S
 + 20 FT/S
 ◇ 10 FT/S
 △ -10 FT/S
 × -20 FT/S
 ▽ -40 FT/S

LOAD FACTOR

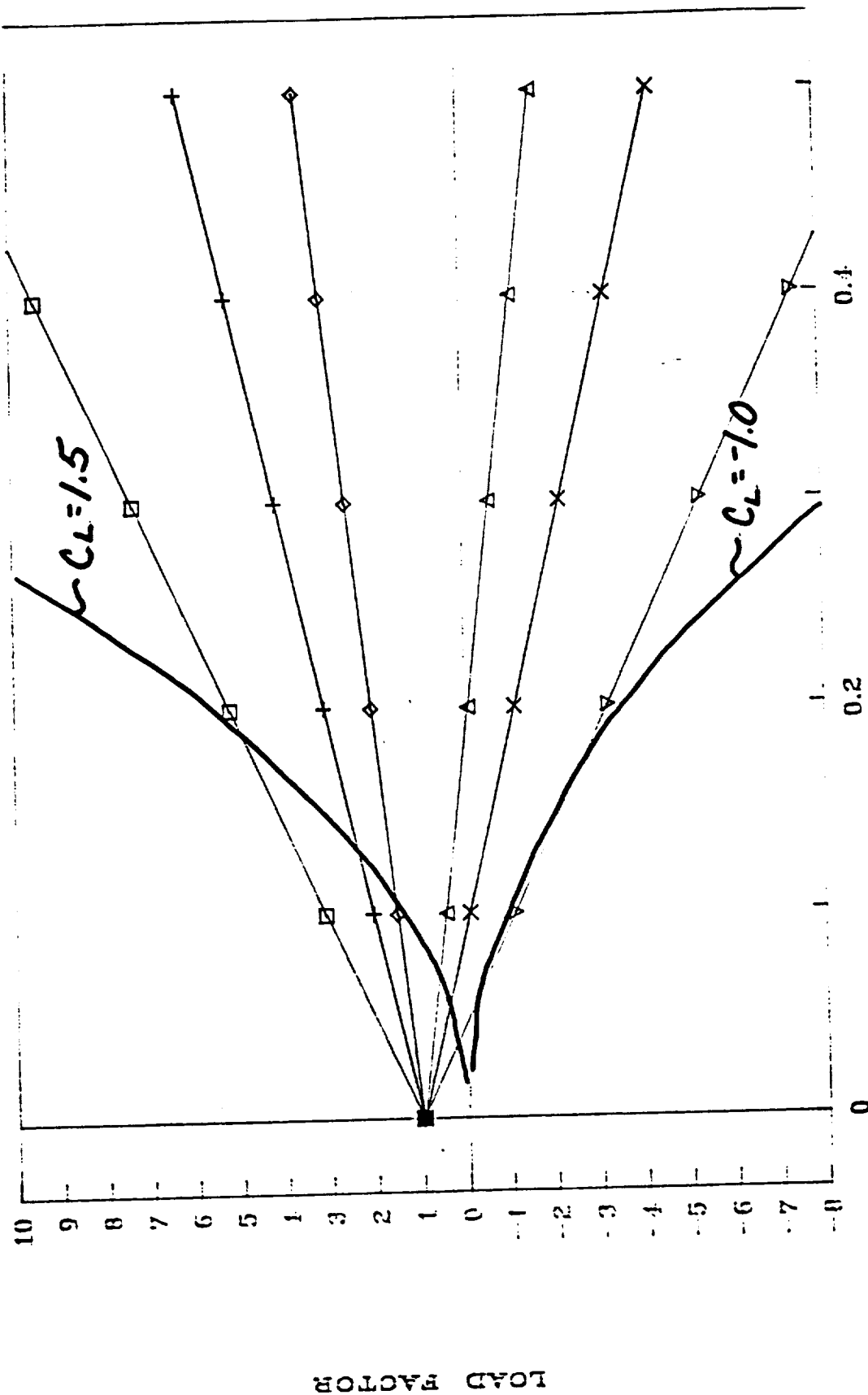
ORIGINAL PAGE IS
OF POOR QUALITY

Figure 9.5.13

V-n Diagram

EFFECT OF WIND GUST

ALTITUDE -- 50,000 FEET



MACH NUMBER

\square 40 FT/S $+$ 20 FT/S \diamond 10 FT/S Δ -10 FT/S \times -20 FT/S ∇ -40 FT/S